Search for Extra-Solar Planets with High Precision Radial Velocity Curves

Anna Brucalassi

Munich 2014

Search for Extra-Solar Planets with High Precision Radial Velocity Curves

Anna Brucalassi

Dissertation
at the Faculty of Physics
of the Ludwig–Maximilians–Universität
Munich

submitted by
Anna Brucalassi

Munich, 17th June 2014

Supervisor: P.D. Dr. Roberto Philip Saglia
Referee: Prof. Dr. Thomas Preibisch
Date of the oral exam: 28th July 2014

Contents

List of Figures

List of Tables

Acronyms

ADU Analog-to-Digital Unit

AGB Asymptotic Giant Branch

AU Astronomic Unit

BD Brown Dwarf

BF Blaze Function

BIS Bisector Spans

CMD Color Magnitude Diagram

CC Cross-Correlation

CCF Cross-Correlation Function

CCD Charge Coupled Device

CR Cosmic Rays

CV Cataclysmic Variable

DA Data Analysis

DF Dispersion Function

DFG German Science Foundation

DR Data Reduction

EW Equivalent Width

EHJ Extremely Hot Jupiters

ESO European Southern Observatory

FAP False Alarm Probability

FOCES Fiber Optics Cassegrain Échelle Spectrograph

FRD Focal Ratio Degradation

FSR Free Spectral Range

FWHM Full Width Half Maximum

Gaia Global Astrometric Interferometer for Astrophysics

GLS General Lomb-Scargle periodogram

GPI Gemini Planet Imager

HARPS High Accuracy Radial velocity Planet Searcher

HET Hobby-Eberly Telescope

HJ Hot Jupiter

HRS High-resolution Spectrograph

IAU International Astronomical Union

IF Interference Function

JD Julian Days

LC Light Curve

LM Levenberg-Marquardt method

LRS Low-resolution Spectrograph

LTE Local Thermodynamic Equilibrium

LZOS Lytkarino Optical Glass Factory

MAD Median Absolute Deviation

MPIA Max-Planck-Institut für Astronomie

MRS Medium-resolution Spectrograph

M67 Messier-67

MSSP Munich Spectrograph Stability Project

NIR Near Infrared

OC Open Cluster

OHP Observatoire de Haute-Provence

PDF Probability Density Function

PID Proportional Integral Derivative

PPD Proto-planetary Disk

PSF Point Spread Function

RMS Root Mean Square

RGB Red Giant Branch

RV Radial Velocity

SDSS Sloan Digital Sky Survey

SE Super Earth

SHS Shack-Hartmann Sensor

SOPHIE Spectrographe pour l'Observation des Phénomènes des Intérieurs stellaires et des Exoplanètes

SNDM Solar Nebular Disk Model

SNR Signal-to-Noise Ratio

SS Solar System

ThAr Thorium-Argon

TIR Total Internal Reflection

TTV Transit Timing Variation

USM Universitäts-Sternwarte München

UV Ultra Violet

UVES Ultraviolet and Visual Echelle Spectrograph

VHJ Very Hot Jupiters

VLT Very Large Telescope

WD White Dwarf

WGESP Working Group on Extrasolar Planets

Zusammenfassung

Die vorliegende Dissertation behandelt die Suche von extra-solaren Planeten mit der Radialgeschwindigkeits Methode und zwar sowohl in Bezug auf die dafür notwendige Instrumentierung als auch auf die Beobachtung. Die Arbeit ist in zwei Teile gegliedert. Im ersten Teil werden die vorgenommenen Verbesserungen des hochauflösenden Spektrographen FOCES beschrieben, der im kommenden Jahr am Wendelstein Observatorium installiert werden wird. Der zweite Teil handelt von der Suche nach Gasplaneten im offenen Sternhaufen M67.

Die Radialgeschwindigkeits-Methode ist eine der erfolgreichsten Methoden bei der Suche nach extra-solaren Planeten. Dabei wird nach periodischen Dopplerverschiebungen in Sternspektren gesucht, die durch die gravitative Wechselwirkung mit einem Begleiter verursacht werden. Projekte dieser Art benötigen Spektrographen mit einer sehr hohen Genauigkeit und Langzeitstabilitaet.

Der Spektrograph FOCES ist ein Echelle Spektrograph fuer das neue 2m Fraunhofer Teleskop am Wendelstein Observatorium. Das Instrument befindet sich seit 2010 im Labor der Universitätssternwarte der LMU wo es bis zum Abschluss des Teleskop-Betriebnahme verbleiben wird.

Die neue Integration des Instruments sowie die Konstruktion und Performance-Analyse im Bezug auf Druck- und Temperatur Stabilität des Spektrographen sind ein Hauptbestandteil dieser Dissertation. Des Weiteren beschreibt die Arbeit eine Vielzahl von Messungen mit unterschiedlichen Glasfasern verschiedenster Hersteller einschliesslich hexagonaler und octagonaler Glasfasern. Die gewonnen Daten emöglichten zu dem Schluss, dass die neue FOCES Konfiguration der Druck- und Temperaturstabilitaet es erlauben werden, Radialgeschwindigkeits-Messungen mit einer Genauigkeit von bis zu 1 m/s durchführen zu können. Basierend auf diesen Ergebnissen wird die finale Konfiguration des FOCES Spektrographen gewählt werden, in der er am Wendelstein Observatorium betrieben werden wird.

Der zweite Teil dieser Dissertation widmet sich der Suche nach massereichen Planeten um Hauptreihensterne und Sterne in späteren Entwicklungsstadien im offenen Sternhaufen M67. Dafür wurden Radialgeschwindigkeits-Messungen mit mehreren Spektrographen durchgefuehrt, nämlich mit HARPS am La Silla Obervatorium der ESO (Chile), mit SOPHIE am OHP (Frankreich) und mit dem HRS am McDonald Observatorium (Texas). Zusätzliche Messungen mit dem CORALIE Spektrographen wurden am Euler Swiss Telescope am La Silla Observatorium gewonnen. Das Ziel der Kampagnen war/ist es, eine

Langzeitstudie der Entstehung von Gasplaneten in offenen Sternhaufen durch zu führen und dabei zu bestimmen, in wie weit diese von der Sternmasse und deren Zusammensetzung abhängt.
Die Analyse der Radialgeschwindigkeits-Messungen ermöglichte die Enteckung der ersten drei Planeten im Sternhaufen M67. Zwei davon kreisen jeweils um einen G-Zwerg (YBP1194 und YBP1514) und der dritte um einen weiter entwickelten Stern S364. Interessanterweise ist YBP1194 ein Stern, der sehr ähnlich zu unserer Sonne ist. Zuvor wurde noch kein Planet um einen sog. Sonnen-Zwilling in einem offenen Sternhaufen gefunden.
Die Arbeit schliesst mit einer Effizienzstudie, die mit Hilfe von Monte-Carlo Simulationen durchgeführt wurde, und welche die Bestimmung der Planetenhäufigkeit
des Radialgeschwindigkeits-Surveys ermoeglicht. Im Gegensatz zu frueheren Veroeffentlichungen aber in Übereistimmung mit jüngeren Ergebnissen zeigt die vorliegende Dissertation, dass massereiche Planeten im offenen Sternhaufen M67 genauso häufig sind wie Planeten um Feldsterne ($\sim$9%).

Summary

After centuries of speculations about the presence of other worlds outside our Solar System, the first extrasolar planets were discovered at the end of the twentieth century (about twenty years ago). Since then, as the number of discoveries increased rapidly, an extraordinary diversity of planetary systems has been revealed. A diversity in the physical properties (mass, size, orbital periods..) as well as in the architecture of the systems of those new worlds appeared. This has changed completely our idea of planets and planetary systems and strongly influenced subsequent theories of planet formation and orbital evolution.

As I write these words, the number of known extrasolar planets is between 1700 and 1800. In addition the satellite Kepler has announced thousands candidates, of all sizes. The rate of discovery continues to increase. Those worlds continue to surprise us by the immense diversity they have and many more surprises probably await us.

This Ph.D. Thesis has as general subject the study of extrasolar planets using the radial velocity technique from both, instrumental and observative, points of view. Two main parts compose the work: the upgrade of the spectrograph FOCES, a high resolution spectrograph that will be installed next year at the Wendelstein Observatory, and the search of giant planets around stars in the open cluster Messier-67 (M67).

The radial velocity method is one of the most efficient means to search for planets and specifically, it consists in monitoring periodic Doppler shifts in the spectra of stars due to gravitational influence of an orbiting companion.

High-accuracy radial velocities for exoplanet detection are typically acquired using échelle spectrographs with high spectral resolving power (typically $R=\lambda/\Delta\lambda \sim 50000 - 100000$) and operated in the optical region (450−700 nm). Several diffraction orders are cross-dispersed, and recorded simultaneously on rectangular format CCDs providing large numbers of resolved absorption lines.

Over these past years the sensitivity of this technique has increased continuously, opening the possibility of exploring the domain of low-mass planets down to Earth masses, to discover and characterize multiple planetary systems, to perform surveys to find long period planets, to establish the planetary nature and to characterize the transiting candidates of photometric surveys. Radial velocities projects for exoplanet require high-precision spectrographs and long term stability to minimize effects of gravitational and thermal telescope flexure, and other instrument drifts.

The Ludwig-Maximilian-Univesität München (USM) operates an astrophysical obser-

vatory on the summit of Mt.Wendelstein, in the Bavarian Alps. Since August 2011 the integration in a new 8.5m dome of a new 2m Fraunhofer robotic telescope and competitive astronomical instruments has started. The Échelle spectrograph FOCES is a fiber-fed bench-mounted échelle spectrograph intended to be operated at the 2.0m Fraunhofer Telescope at the Wendelstein Observatory. The spectrograph was built in collaboration with the Max-Planck-Institut für Astronomie (MPIA, Heidelberg) and was successfully operated at the Calar Alto 2.2m telescope between 1995 and 2009. After the decommissioning in early 2010 the instrument has been returned to Munich and located at the laboratories of the Munich University Observatory, where it will remain until the telescope is fully commissioned.

The new integration of the instrument setup after the arrive from the Calar Alto Observatory, the total alignment and fine-tuning of the different optical parts, the complete construction, performance measurements and analyses of a new system for the environmental stability of the spectrograph have been one of the major parts of this PhD project. Furthermore, a variety of measurements with a selection of fibers from different vendors, including state-of-the-art octagonal and hexagonal fibers is described. Finally, different fiber sections were combined and proved on their capability as the next generation of mode scramblers and eventually as a potential solution for the new FOCES fiber-link. The values obtained in the different measurements leaded to the conclusion that with the new FOCES configuration and in this regime of environment stability, it is possible to do RV spectroscopy in the m/s region. All these preliminary investigations form the subject of the first part of the dissertation and will help in choosing the final setup of the spectrograph FOCES at the Wendelstein Observatory. The aim is to obtain a competitive high-resolution optical spectrograph able to answer to the requirements of a wide range of topics as search for extra-solar planets, asteroseismological studies and stellar abundances analysis.

The second part of this Ph.D. Thesis is focused on the search for massive planets around main sequence and evolved stars in the open cluster (OC) M67 using radial velocity (RV) measurements obtained with HARPS at the European-Southern-Observatory (ESO) 3.6-m telescope (La Silla, Chile), SOPHIE at the 1.93-m telescope of the Observatoire de Haute-Provence (France) and the High-Resolution Spectrograph (HRS) at the 9.2-m Hobby-Eberly Telescope (HET, USA). Additional RV data come from CORALIE at the Euler Swiss Telescope (La Silla, Chile).

Considering the planet formation a by-product of the stellar formation process, several researchers looked for correlations between the presence of planets and different stellar properties, like stellar mass, age, chemical composition, activity, and rotation. Such correlations could either provide clues about the requirements for planet formation and evolution, or be the result of some kind of planet feedback on the star. In this context, a very significant observational effort has been devoted to search for planets in Galactic open clusters and globular clusters with transit surveys and with lesser extent RV campaigns. Stars in cluster indeed share age and chemical composition (Randich et al., 2005), so it is possible to control strictly the sample and to limit the parameter space in a better way than when studying field stars.

The goal of our campaign is to study the formation of giant planets in open clusters

(OCs) to understand whether a different environment, such as a rich cluster like M67, might affect the planet formation process, the frequency, and the evolution of planetary systems with respect to field stars. In addition, searching for planets in OCs enables us to study the dependence of planet formation on stellar mass and to compare the chemical composition of stars with and without planets in detail.

A complete description of the stars sample and the cluster characteristics is presented. Technical details of the different facilities used and their configurations are discussed. The description of the reduction of the high-resolution spectra and their subsequent analysis for the computation of the RVs is also given. Finally, the estimation of the offset for all the RV values with respect to the HARPS data, the radial velocity distribution of the stars, and how the most likely planetary host candidates have been individuated are outlined.

The analysis of the radial velocities allowed the detection of the first three exoplanets in this cluster: two in orbit around the two G dwarfs YBP1194 and YBP1514, and one around the evolved star S364. The orbital solution for YBP1194 yields a period of 6.9 days, an eccentricity of 0.24, and a minimum mass of 0.34 M_J. YBP1514 shows periodic RV variations of 5.1 days, a minimum mass of 0.40 M_J, and an eccentricity of 0.39. The best Keplerian solution for S364 yields a period of 121.7 days, an eccentricity of 0.35 and a minimum mass of 1.54 M_J. A study of Hα core flux measurements as well as of the line bisectors spans revealed no correlation with the RV periods, indicating that the RV variations are best explained by the presence of a planetary companion. Remarkably, YBP1194 is one of the best solar twins identified so far, and YBP1194b is the first planet found around a solar twin that belongs to a stellar cluster.

The detection of these 3 planets sheds new light on our understanding of the planet formation in open clusters and its dependence of on stellar mass. For several years this has been an open question and the lack of detected planets with previous exoplanet surveys, in both open and globular clusters, triggered the hypothesis that the frequency of planet-hosting stars in clusters was lower than in the field. With our discovery in M67 (Brucalassi et al., 2014), the detection of two hot-Jupiters in the Praesepe open cluster in 2012 (Quinn et al., 2012) and of two sub-Neptune planets in the cluster NGC6811 (Meibom et al., 2013) and the announcement of a hot-Jupiter in the Hyades (Quinn et al., 2013), it is now clear that giant planets can form and migrate in a dense cluster environment.

Finally a series of simulations based on a similar Monte Carlo approach have been carried out to evaluate the detectability and the occurrence of giants planets in our Radial Velocity Survey. In contrast with early reports and in agreement with recent findings, our study show that massive planets around stars of open clusters are as frequent as those around field stars. For short-period giant planets, we derived a frequency of $\sim$2%, which is slightly higher than the value for field stars. Considering also giant planets with long periods, our simulations give a rate of $\sim$9% for the whole sample, that is quite in agreement with the rate of giant planets found by Cumming et al. (2008) and Mayor et al. (2011) for field stars. However, this fraction is a lower limit that has to be better constrained with the follow-up of some other candidates (see Pasquini et al., 2012), which reveal suggestive signals for additional planetary companions.

Preface

This Thesis is organized as follow. An introduction to the study of the extrasolar planets is given in Chapter 1. The major detection methods are described. The most commonly accepted models of formation and evolution of the planets are shown too. Several and controversial studies regarding the correlations between the presence of planets and different stellar properties and a brief introduction to the status of the search for planets in clusters are also presented. Tools and algorithms used for the analysis of the RV measurements are described at end of the chapter.

The new 2m Fraunhofer robotic telescope operated by the Ludwig-Maximilian-Univesität München (USM) on the summit of Mt.Wendelstein, in the Bavarian Alps, is presented in Chapter 2. An accurate description of the Échelle spectrograph FOCES intended to be operated at the 2.0m Fraunhofer Telescope at the Wendelstein Observatory is then given.

After a introduction to the theory and the description of the components of an optical spectrograph, the construction, the test and the performance of a new system for the environmental stability of the FOCES spectrograph are presented at end of Chapter 2 and in Chapter 3. A variety of measurements with a selection of fibers from different vendors, including state-of-the-art octagonal and hexagonal fibers is also described.

Chapter 4 reports a complete description of the M67 stars sample and the cluster characteristics. Technical details of the different facilities used, the observing strategy, the pipelines for the reduction of high-resolution spectra and the algorithms involved in the analysis of radial velocity data are also given. Finally, the chapter presents the estimation the offset of all the RV measurements with respect to the HARPS data, the radial velocity distribution of the stars, and how the most likely planetary host candidates have been individuated.

Chapter 5 presents the detection of the first three exoplanets in the M67 cluster: two in orbit around the two G dwarfs YBP1194 and YBP1514, and one around the evolved star S364. The complete analysis of the RV measurements and the scientific results are outlined.

Conclusions, perspective and future developments are summarized in Chapter 6.

Chapter 1

Introduction and Basic Principles

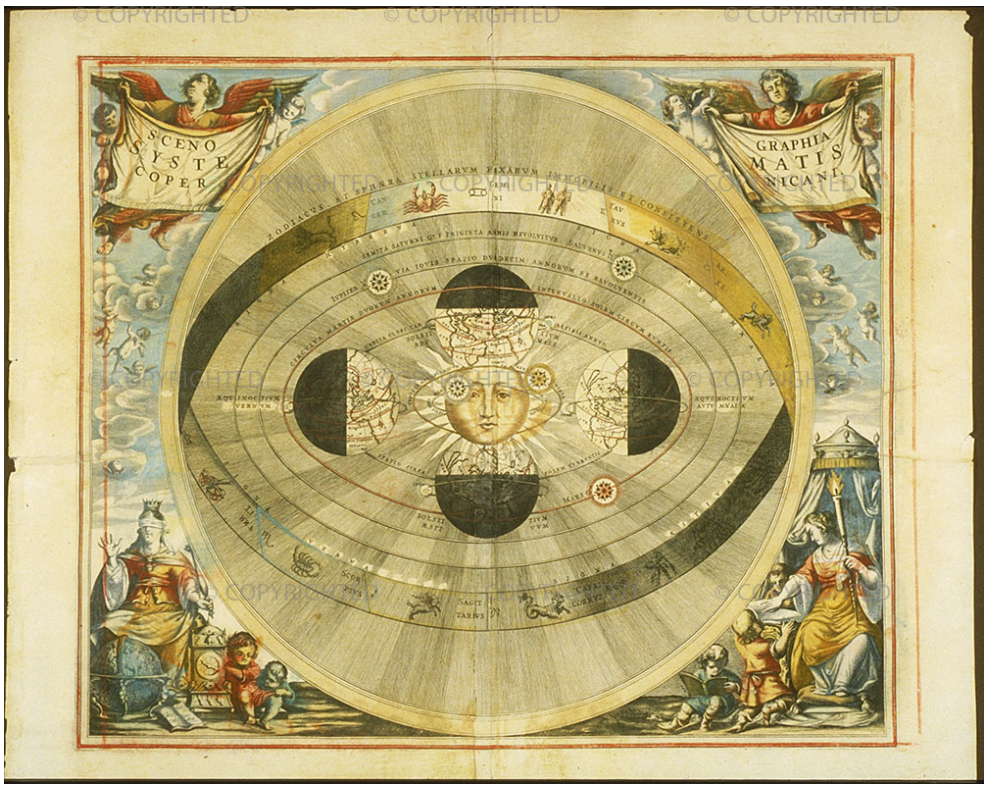

Figure 1.1: *Atlas coelestis seu Harmonia Macrocosmica.* Andreas Cellarius (1596-1665)

1.1 Extrasolar Planets

Surrounded by an ocean of stars, humanity has long hypothesized about the existence of planetary systems other than our own, and the possibility of life existing elsewhere in the Universe. For more than 2000 years people opinions have been pervaded by extremes of thinking ranging from "There are infinite worlds both like and unlike this worlds than one"(Epicurus, 341-270 BCE) to "There cannot be more worlds than one" (Aristotele, 384-270 BCE). Then, in the quest of answering if life is omnipresent in the Universe or not, it was logical to search for planets. Furthermore, other problems connected to the uniqueness of our Solar System and the position of Earth in the Universe, needed an explanation. In agreement with the universality of physical laws, nothing should preclude planets formation around other stars, but also this had to be demonstrated under the principles of the scientific method. In addition, as it usually happens, the more one search, the more one can discover. Nature gives a lot of surprises. Those surprises are what help us to define theories most efficiently and then to answer the dispute on our origins. Thus, since one has to start somewhere, a good starting point for this thesis could be to consider it in the slow and long attempt of our understanding of the Universe.

In this context, it is only recently that scientific evidence has confirmed what many had before speculated: planets do exist and are common outside the Solar System (SS). The first clear detections of planetary mass bodies over the SS came in the early 1990s using indirect methods, based on the dynamical perturbation of the star by an orbiting planet. The discovery of two planets orbiting the pulsar PSR 1257+12 (Wolszczan & Frail, 1992) was announced in 1992. High-accuracy radial velocity (Doppler) measurements obtained the first suggestions of planetary-mass objects surrounding main sequence stars in 1988 (Campbell et al., 1988), with the first clear detection reported by Mayor & Queloz (1995).

This result came as a real surprise and strongly influenced subsequent theories of planet formation and orbital evolution. The detection of a Jupiter-like planet orbiting the star 51-Pegasi in 4 days period was the first object in a new planet class, absent in our SS: the Hot Jupiters. This discovery led to a change of mentality amongst the astronomical community. Since then, the number of detections has increased rapidly year after year due to improved observational techniques, and the search of exoplanets, and their characterization, rapidly became a respectable domain for astronomy research.

As of the cut-off date for this work, March 31^{st}, 2014, a total of 1708 extrasolar planets have been identified, with more than 170 multiple systems[1].

Some statistics, according to the discovering methods are listed in Table 1.1.

On February 26, 2014, NASA announced the discovery of 715 newly verified exoplanets around 305 stars by the Kepler Space Telescope (Lissauer et al., 2014; Rowe et al., 2014). In addition, more than 3000 planetary candidates, several of them being nearly Earth-sized and some located in the habitable zone, have been identified.

Prior to the Kepler spacecraft's 2014 results, most of the known exoplanets were gas

[1] *http://exoplanet.eu/catalog/*

Table 1.1: Exoplanet detection statistics, from exoplanet.ue, March 31^{st}, 2014.

Detection methods	Systems	Multiple	Planets
Radial velocity	419	98	558
Transit	614	350	1133
Microlensing	26	2	28
Timing	11	2	14
Imaging	43	2	47
Total number of planets	1113	454	1780
Unconfirmed Kepler candidates			3705

giant planets similar to Neptune or Jupiter, since massive planets are more easily observed. However, 95% of the discovered exoplanets by Kepler are mostly between the size of Neptune and the size of Earth (known by the term Super-Earth, SE), and four of them show surface temperatures suitable for liquid water (Lissauer et al., 2014; Rowe et al., 2014). These results seem to confirm previous statistical studies indicating that the number of SE is actually larger than that of gas-giant planets (Borucki & for the Kepler Team, 2010).

At the same time, the improvement of the observational techniques has allowed increasing interest in the search for extraterrestrial life, particularly for those planets that orbit in the host star's habitable zone where liquid water (and therefore life) can exist on the surface. Thus, the study of planetary habitability, which considers several factors connected to the suitability for hosting life, is pushed by the search for extrasolar planets. The most Earth-like planets in a habitable zone to have been discovered, as of April 2014, are Kepler-186f, Kepler-62e and Kepler-62f which have 1.11, 1.61 and 1.41 Earth radii respectively (Quintana et al., 2014; Borucki et al., 2013). Furthermore, recent discoveries of Earth-sized (or smaller) planets show properties similar to the Earth (Fressin et al., 2012). In November 2013 it was announced that 22±8% of Sun-like stars harbor an Earth-sized planet in the habitable zone (Petigura et al., 2013).

Planetary-mass objects were discovered also around Brown Dwarfs (BDs) and several *free-floating objects* have been detected specifically in star forming regions and young clusters (Marsh et al., 2010). It is thought that such isolated objects were probably expelled from their original planetary system, but in this case they are not always classified as *planets*.

1.1.1 Definition of extrasolar planet

An extrasolar planet, or exoplanet, is usually considered a planet outside the SS orbiting a star different from the Sun. The official definition of planet adopted by the International Astronomical Union (IAU) actually covers the SS only (Shaver, 2006) and it is not valid for extrasolar planets. Concerning the latters, the only statement delivered by the IAU is an old working definition of SS planet issued in 2001 and modified in 2003 accordingly to the new discovered extrasolar planets. The IAU 2003 recommendation, by the Working

Group on Extrasolar Planets (WGESP, IAU 2003), is [2]:

Rather than try to construct a detailed definition of a planet which is designed to cover all future possibilities, the WGESP of the IAU has agreed to restrict itself to developing a working definition applicable to the cases where there already are claimed detections. The following criteria are considered in the newer definition:

- *objects with true masses below the smallest mass required for the ignition of the deuterium-burning (13 M_J for solar metallicity objects) orbiting stars (or stellar remnants) are 'planets'. The different formation processes are not considered;*
- *sub-stellar objects with true masses above the limiting mass for thermonuclear fusion of deuterium are 'BD'. The different formation processes and the position of such objects within their own systems are not considered;*
- *free-floating objects in young star clusters with masses below the limiting mass for thermonuclear fusion of deuterium are not planets, but are 'sub-BD'.*

However, the IAU working definition is not generally accepted. Another alternative formulation is that, planets and BD should be distinguished on the basis of the formation process. In the paradigm of the core accretion model (see Sec. 1.3), it is believed that gas-giant planets process may sometimes produce planets with masses higher than the value of mass required for the ignition of the deuterium-burning (Mordasini et al., 2007; Baraffe et al., 2008). Such scenario also admits the existence of sub-BDs, which have planetary masses but form through the direct collapse of clouds of gas like stars (see Sec. 1.3). Moreover, no precise physical significance is connected to the 13 M_J limit, since nuclear fusion where the deuterium is destroyed can occur inside the core of objects with mass below that cut-off, with a rate of this fusion that can also depend on the composition of the object (Spiegel et al., 2010) . Thus, attempts to formulate a precise definition of a planet are confronted by a number of difficulties, that are well summarized in the work of Basri & Brown (2006). In this treatment, the IAU definition is consider as valid.

[2] *http://astro.berkeley.edu/ basri/defineplanet/IAU-WGExSP.htm*

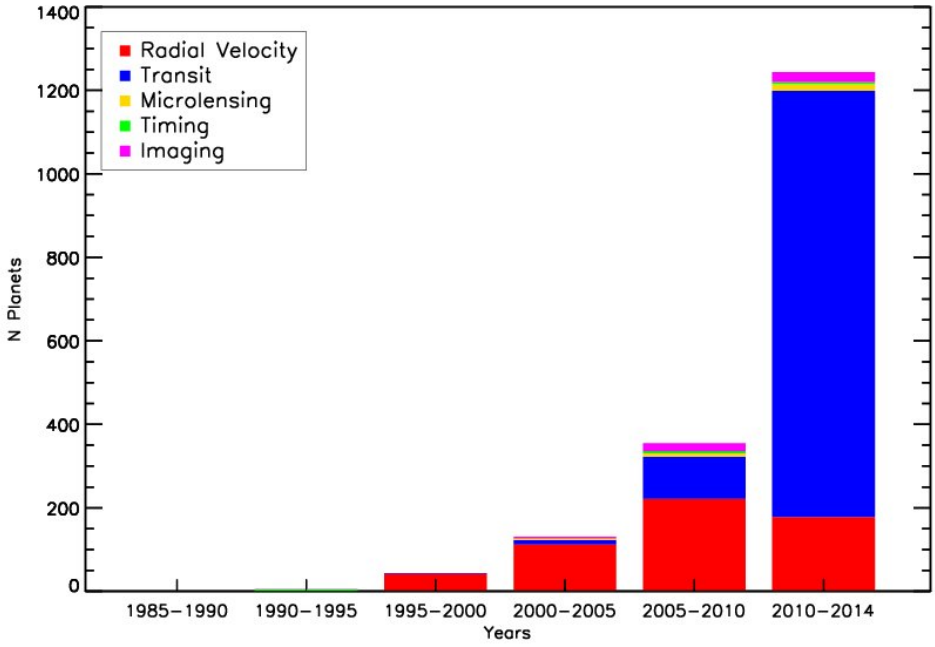

Figure 1.2: Number of extrasolar planet discoveries until March 2014 using different detection methods: radial velocity (red), transit (blue), microlensing (yellow), timing (green), direct imaging (magenta). From *www.Exoplanet.eu*.

1.2 Detection methods

In this section a description of the main detection techniques for extrasolar is given [3]. Figure 1.2 summarizes the various extrasolar planet discoveries until March 2014 using different detection methods (from *www.Exoplanet.eu*). Nowadays the investigative tools used to spot hidden exoplanets are generally divided in *Direct* and *Indirect* detection methods.

1.2.1 Direct detection method

The most simple method one can suppose in order to search for planets is to image them directly. This technique, working well within the Solar System, is nevertheless probably one of the more difficult to use in the context of extrasolar planets, due to the extreme contrast between the light emitted by the star and the light reflected by the planet. Exoplanets with size comparable to our system planets, shining by reflected starlight, result roughly billions times fainter than their host stars, and moreover, they are observed at angular separations from their host star of, at most, a few second of arc, depending on their distance. These two effects make direct detection extraordinarily hard, especially at optical wavelengths where the planets/star intensity ratio is very small and in particular from the ground due to the

[3]Based on M. Perryman, *The Exoplanet Handbook*, Cambridge Univ.Press, 2011

perturbation of the Earth's atmosphere. For Jupiter-Sun system, this ratio is $\sim 10^{-9}$ at maximum elongation, with an angular separation of 0.5 arcsec at 10 pc. For the earth-sun it is $\sim 10^{-10}$. In general, values for exoplanets of primary interest are expected to range from $\sim 10^{-5}$ in the infrared to $\sim 10^{-10}$ in the optical (Burrows et al., 2004).

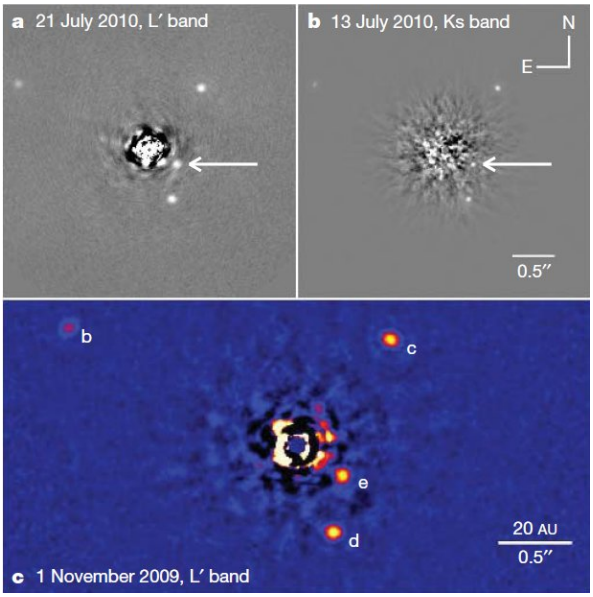

Figure 1.3: Direct detection of four planets around the star HR8799. Figure obtained from Marois et al. (2010)

To date, this technique is only sensitive to massive planets (several Jupiter masses) at large orbital distances of the order of tens AUs. The most representative objects are probably the quadruple planet system around HR8799 (Marois et al., 2008, 2010) and the planet candidates around Beta-Pictoris (Lagrange et al., 2009, 2010) and Fomalhaut (Kalas et al., 2008). The detection of exo-Earths remains out of reach of any of imaging facilities currently under development.

Different techniques are being used in order to image exoplanets at the highest angular resolution and contrast: the use of large telescopes to increase signal to noise and resolution; adaptive optic or imaging from space to correct or completely avoid the effects of the atmospheric turbulence, coronagraphic masks or null interferometry to eliminate the stellar light; interferometers to improve angular resolution and contrast between planet and star by observing at longer wavelengths. Moreover, observations in the infrared are facilitated by the simultaneous decrease in emission from the star, the increased thermal emission from the planet due to their high temperature (Absil & Mawet, 2010) and by the better performance of adaptive optics at longer wavelengths.

New designed direct-imaging instruments are the Gemini Planet Imager (GPI, Macintosh et al. (2006)) for the 8 meter Gemini South telescope and the SPHERE project at the Very Large Telescope. These instruments will survey several hundred, nearby young stars achieving sensitivities to image planets with masses a few times that of Jupiter. Information on the detected exoplanets spectrum and any polarized light they may emit, will be also available.

1.2.2 Indirect detection methods

The majority of the known extrasolar planets have been detected by means of indirect methods. These are based on the fundamental principle that the existence of a planet may be deduced by analyzing changes in some observable properties of the parent star that will be affected by the presence of a planet in an exoplanetary system. The following are the

major indirect methods applied for the detection and/or the confirmation of the extrasolar planets.

Radial velocities [4]

The radial-velocity method, also known as Doppler spectroscopy, was by far the most productive technique used by planet hunters until 2014 when NASAs Kepler satellite released 715 newly verified exoplanets discovered via the transit method, and a host of planets candidates. Nevertheless, the radial velocity method remains one of the most efficient means to search for planets and the most sure and accepted manner with which one can check results from other methods.

Specifically, Doppler spectroscopy consists in monitoring potential Doppler shifts in the spectra of stars with numerous absorption lines. The visible portion of the spectra of F, G, K and M dwarfs contains a large number of metal absorption lines. These lines form a convenient tool to measure wavelength shifts through the Doppler effect. In the absence of other phenomena capable of shifting the stellar lines or of modifying their profile, measured Doppler shifts are converted into radial (line-of-sight) velocity variations (RV) and interpreted as the motion of the star due to an orbiting companion (planet, brown dwarf, or star). Thus, measuring the motion of the parent star along the line of sight gives informations about some orbital parameters and characteristics of the companion.

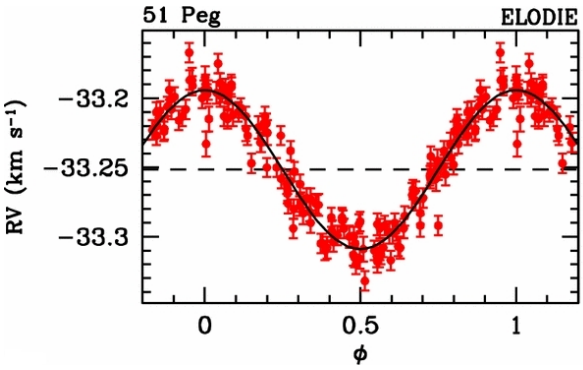

Figure 1.4: Radial velocity announcing the detection of 51Peg-b, the first extrasolar planet, the first hot Jupiter. Figure obtained from Mayor & Queloz (1995).

In particular, a planet in a Keplerian orbit induces on its parent star a perturbation of the form (using the formalism presented in Beaugé et al. (2007)):

$$V_r(t) = K \cdot [cos(\nu(t) + \omega) + e \cdot cos(\omega)] + \gamma \tag{1.1}$$

where K is the velocity semiamplitude:

$$K = \frac{m_p sin(i)}{(M_\star + m_p)} \frac{2\pi a}{P\sqrt{1-e^2}} \tag{1.2}$$

a is the semi-major axis of the orbit of the planet, P is the orbital period, m_p is the mass of the planet, $M_\star$ is the mass of the star, i is the inclination of the orbital plane, e is the eccentricity of the orbit, $\nu(t)$ is the true anomaly, ω is the argument of the periastron and

[4] Based on Eggenberger (2010)

γ is the systemic velocity off-set of the star-planet system.
Eq. 1.2 reduces to the expression of the planet minimum mass

$$m_p sin(i) \simeq \left(\frac{P}{2\pi G}\right)^{1/3} K M_\star^{2/3} \left(1-e^2\right)^{1/2} \tag{1.3}$$

under the assumption that $m_p \ll M_\star$ (G is the universal gravitational constant). Introducing the same approximation into Keplers third law yields an expression for the semimajor axis of the relative orbit:

$$a \simeq a_p \simeq \left(\frac{G}{4\pi^2}\right)^{1/3} M_\star^{1/3} P^{2/3} \tag{1.4}$$

For a more detailed explanation of the derived equations, consult the Appendix B.
Used alone, unfortunately this method suffers from two difficulties: that a stellar mass, a notably hard quantity to accurately determine for field stars, needs to be assumed in order to get to the companion mass. Then, only a minimum mass, $m_p sin(i)$ is determined. However, although the true mass of the planet can be significantly different from the minimum mass, the two values agree within a factor of 2 ($m_p \leq 2 m_p sin(i)$) in 87% of cases. Furthermore, if the RV of both the star and the planet itself can be measured, then the true masses of both can be determined (Rodler et al., 2012).

Since the probability of detecting a planetary signal depends essentially on the value of the velocity semi-amplitude, this expression indicates that Doppler measurements favor the detection of planetary systems with massive and short-period planets. Applied to the Solar System, Eq. 1.2 shows that Jupiter induces on the Sun a radial-velocity perturbation with a semi-amplitude of 12.5 m s^{-1}, while the Earth causes a perturbation with a semi-amplitude of 9 cm s^{-1}. Thus, obtaining radial velocities at this level of precision is not easy. Nowadays, extremely small RV variations can be observed, of the order of 1 m s^{-1}or even somewhat less (Pepe et al., 2011). The next generation of ESO exoplanets hunter will be ESPRESSO, the Echelle SPectrograph for Rocky Exoplanets and Stable Spectroscopic Observations (Pepe et al., 2010). It will be installed on ESO's VLT in order to achieve a gain of two magnitudes with respect to its predecessor HARPS, and the instrumental RV precision will be improved to reach cm s^{-1}level. The main scientific goals will be the search and characterization of rocky exoplanets in the habitable zone of quiet, nearby G to M-dwarfs, and the analysis of the variability of fundamental physical constants. In this contest, another example of high-accuracy radial velocity instrumentation is the echelle spectrograph FOCES whose upgrade was one of the main parts of this Phd work. This instrument, introduced in the next sections, will be placed at the Wendelstein telescope and with an RV precision of m s^{-1}level, it will be an useful facility for the search and the follow-up of extrasolar giant planets, asteroseismological studies and stellar abundances analysis.

Transit method

The transit method consists in detecting the periodic attenuation of the light curve (LC) from the host star by the transit of a planet across its surface, given a suitable alignment geometry (Moutou & Pont, 2006). Only after the discovery 51 Peg b, this method was really considered. Prior to that, the knowledge about the presence of planets near to their stars was absent.

A posteriori, this method is conceptually one of the easiest with which one can search for exoplanet candidates: one only needs to observe a planet transit in front of its host star using a light detector with enough precision to obtain good photometry, a large number of stars (by observing a small, deep field, or a wide and shallower field), time, and the capacity of analyzing the photometric timeseries. However, the probability of observing such transit for any given star, seen from a random direction and at random time, is extremely small. Because of geometrical constraints, this method is mostly dedicated to the discovery of short-period planets. It also suffers from quite a number of false positives: a significant number of eclipsing binaries false-positives can contaminate the detections, and confirmation from a different method is usually required. The observable effect is also quite small. The signal measured, indeed, is a drop in flux F, and it can be described from the radii of the transiting planet R_p and of the host star $R_\star$ as:

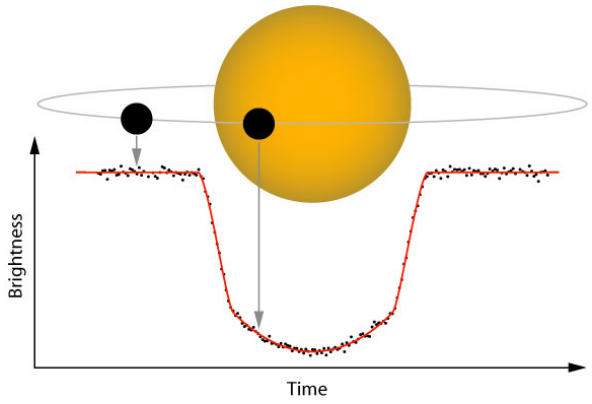

Figure 1.5: Diagram showing the change of flux received from the detector as a planet transit the parent star. The amount by which the stellar flux drops depends on both the stellar and planetary sizes.

$$\frac{\Delta F}{F} = \frac{\pi R_p^2 B_\star}{\pi R_\star^2 B_\star + \pi R_p^2 B_p} \simeq \left(\frac{R_p}{R_\star}\right)^2 \sim \frac{1}{100}\left(\frac{R_p}{R_J}\right)^2 \left(\frac{R_\odot}{R_\star}\right)^2 \tag{1.5}$$

where B_p is the planets brightness, and $B_\star$ the star's brightness. A planet with R$\sim 1R_J$ transiting a star of 1 $R_\odot$results in a drop of the stellar flux of (ΔF/F)$\sim 1.1\cdot 10^{-2}$, or around 0.01 mag. For planets of Earth or Mars radius (ΔF/F)$\sim 8.4\cdot 10^{-5}$ and $3\cdot 10^{-5}$ respectively. The first transit HD209458 was observed by Henry et al. (1999) and independently by Charbonneau et al. (2000). Since then, the number of known transiting planets has grown and different surveys from the ground (e.g. HAT, OGLE, WASP) and from space (e.g. Corot, Kepler) were set up to carry out detections of new planets from their periodic transit signature. After the advent of the Kepler satellite, this has become the first most productive method of detection (1137 planets as of March 31th, 2014). In general, ground-based searches are able to discover transits with depths up to about (ΔF/F)$\sim$1%, revealing gas-giant plants around stars frequently bright enough for RV confirmation. Surveys from

the space, beyond the effect of the atmospheric seeing and scintillation, are discovering planets with transit depths of a few times 10^{-4}, extending detectable exoplanet masses down to just a few $M_{\oplus}$. The transiting method is of particular importance because it is not only a detection tool, but also provides an estimate of the planetary radii and gives us physical informations about the planets. The planet's structural atmospheric properties indeed are accessible from photometry and spectroscopy during the transit and the secondary eclipse when the planet passes behind the star. Furthermore, once the planetary mass is obtained, it is possible to estimate the density, which in turn gives a first estimate of planet's composition.

Gravitational microlensing

Gravitational microlensing occurs when a foreground star is almost exactly aligned to a more distant background star along our line of sight. The foreground star acts as a lens, splitting the light from the background source star into two images, which are typically unresolved. However, these images of the source are also magnified, by an amount that depends on the angular separation between the lens and source. The relative motion between the lens and source therefore results in a time-variable magnification of the source: a microlensing event.

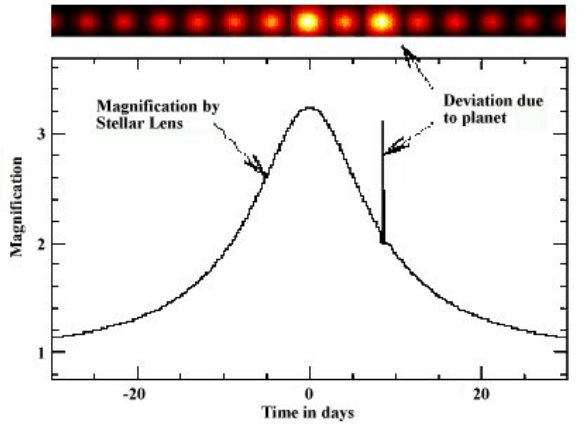

Figure 1.6: Example of magnified microlensing light curve with planetary deviations. NASA©, courtesy A. Feild.

If the foreground star hosts a planet with projected separation near the paths of these images, the planet will also act as a lens, further perturbing the images and resulting in a characteristic, short-lived signature of the planet. Carefully monitoring over several hours of the light curve, as the alignment changes, allows the additional lensing effects of a planetary companion to be identified. By the end of March 2014, 28 extrasolar planets have been detected. This method is most sensitive to detecting planets around 1-10 AU away from Sun-like stars. Unfortunately, the objects that have been found with this method are also useless for further studies, notably, because the short time events do not allow to measure orbital motion and get constrains on eccentricity.

Astrometry

This method concerns the precise measurement of the star position in the sky and the monitoring of variations in that position over the time (Unwin et al., 1997). The observable displacement of the star can be due to the gravitational perturbation of an orbiting planet. The big advantage of this method is to obtain information on the semimajor axis and the inclination of the planet orbit. Another very important point of interest is that its higher sensitivity is for gas giants orbiting at a few AU from their star. Despite this

method has been used to study the properties of planets detected with other techniques, only 1 planet has been discovered as of March 31th, 2014, due to the smallness of the displacements caused by a planet and to the limited accuracy of the surveys. New important results are expected with the 'Global Astrometric Interferometer for Astrophysics' (Gaia) survey (Sozzetti, 2012) which measure billions of stars to V$\sim$20mag at accuracies of $\sim$20-25μarcsec.

Transit Timing Variation (TTV)

Considering a planetary system with more than one planet, each object introduces small perturbations in the orbits of the others. This can produce small variations in the times of transit of a planet suggesting the presence of a new unknown companion, which itself may not transit. Successful detections of multiplanetary systems have been found using the Kepler satellite: for example, the non-transiting Kepler-19c has been identified by variations in the transits of the planet Kepler-19b (Ballard et al., 2011) Alternatively, this method can detect the presence of outer planets that orbit binary systems perturbing the eclipses in an eclipsing binary star. As of March 2014, numerous planets have been confirmed with this method.

Pulsar timing

Pulsars are understood to be fast rotating neutron star, ultradense supernova remnant, emitting radiation in a focused beam at the object magnetic poles. We can detect this emission for those objects whose beam is sometimes directed towards Earth. If an unseen body is in orbit around such an object will cause it to oscillate around the barycenter and slight variations in the timing of its observed pulses in the radio domain. The precision of those instruments, the otherwise regularity of the pulses and the number of events one gets thanks to the rapidity of pulsars rotation allows very fine measurements. The first confirmed detection of an extrasolar planet was made using this method (Wolszczan & Frail, 1992). Although it was the first discovery, the impact of this was never as big as that of 51 Peg b because of the unusual nature of the central-most object, i.e. a supernova remnant. It is thought those planets may have formed from dust ejected during the supernova event and reorganized into a disc later. A few other scenarios have been investigated (see Wolszczan & Kuchner, 2011, for references).

Variable star timing

Similar to pulsar timing is the detection of a variable signal in the oscillations of V391 Peg compatible with a gas giant giant orbiting at a few AU (Silvotti et al., 2007). The planet yield from these techniques is small, but interesting as they explore the future of planetary systems, after stars evolved off the main sequence. Like pulsars, there are some other types of stars which exhibit periodic activity. Deviations from the periodicity can sometimes be caused by a planet orbiting it.

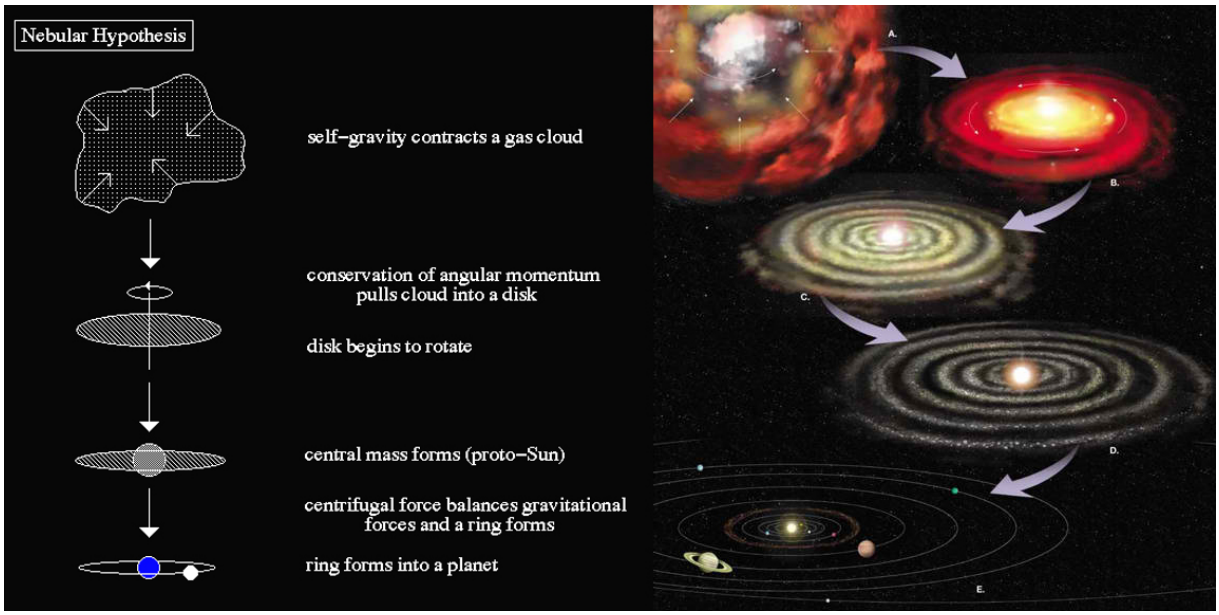

Figure 1.7: Schematic representation of The Nebular Hyphothesis. From abyss.uoregon.edu ©

1.3 Planet formation

1.3.1 Overview

The *Solar Nebular Disk Model* (SNDM) or simply *Solar Nebular Model* (Woolfson, 1993) is the widely accepted modern theory explaining the formation and evolution of planetary systems (Montmerle et al., 2006). It finds origins as modern variant and extension of the solar nebula theory, or *Nebular Hypothesis* (see Fig. 1.7), advanced by Swendenborg, Kant, Laplace, and others since the 18th century to describe the planet formation in the Solar System. In this paradigm, planetary systems, including our solar system, are believed to form as part of the common process of star formation. According to SNDM, stars form within gravitational unstable regions inside massive and dense clouds of molecular hydrogen, called giant molecular clouds. These clouds then collapse and form stars. A sun-like star usually takes around 10^8 yrs to form. Gas and dust in the collapsing molecular clouds carry some angular momentum which prevent the direct falling onto the protostar, and reside in a relative long-lived accretion disk, the Proto-planetary Disk (PPD), which provides, under the right circumstances, the environment for the subsequent stages of planet formation. The PPD is an accretion disk which continues to feed the central star. The quantity of the dust and gas falling onto the disk rather than directly onto the star is connected to the angular momentum of the collapsing cloud. The lifespan of the accretion disks is about 10 million years.

By the time the star reaches the classical T-Tauri stage, the disk, at the begin very hot, becomes thinner and cools. In the inner part of the PPD, terrestrial mass-planets

are formed through a progressive agglomeration of material denoted, as it grows in size, as dust, rocks, planetesimals and protoplanets. The temperature is too high for volatile molecules like water and methane to condense, so only less volatile materials with high melting points, start to condense, forming purely rocky grains that contain crystalline silicates or metals (like iron, nickel, and aluminum). A more detailed description of rocky formation is given in the sec. 1.3.2.

The formation of giant planets is described by a more complicated process. It is believed to occur further out in the disk, beyond the so-called *snow line* (see Fig. 1.8), where planetary embryos are mainly made by various ices. The material is cool enough for volatile icy compounds to remain solid. The ices that form the Jovian planets are more abundant than the metals and silicates that form the terrestrial planets, allowing the Jovian planets to grow several times more massive than in the inner part of the PPD. Although the following process is not completely clear, it seems that some embryos can continue to grow and eventually reach 5-10 $M_{\oplus}$, threshold value to start the capture of hydrogen and helium from the disk. Initially, the accumulation of gas by the rocky-icy core proceeds slowly with time scales of several million years, but after the protoplanet mass reaches about 30 Earth masses, it accelerates and goes on in a runaway manner. The accretion process terminates when the gas is dissipated. A phase of migration then can occur over long distances for the formed planets. The ice giants, like Uranus and Neptune, are sometimes referred to as failed cores, which formed too late when the disk had almost disappeared. Gaseous planets formation and migration is presented more accurately in sec. 1.3.3

In general, the SNDM of planet formation works well to explain the origin of what we see in our solar system today. It is possible to obtain a disk-shaped solar system with planets in nearly circular orbits revolving in a common direction around the Sun. The condensation sequence explains why there are two groups of planets in the solar system: large, low-density Jovian planets in the outer parts and small, high-density Terrestrial planets in the inner parts. At the core of this theory is the idea that planets form as a natural byproduct of star formation. Thus, it suggests that planets should be common in our universe. However, a number of stages and their related time scales remain quite uncertain, amongst them the coagulation of the dust and other particles over several orders of magnitude in size and mass, the role of turbulence, some problems of the angular momentum transport, and the contribution of gravitational fragmentation in the formation of planetesimals and in the growth of giants planets.

1.3.2 Terrestrial planets formation

In the paradigm of the SNDM, terrestrial planets form in the inner part of the protoplanetary disk [5], within the frost line, where the condensation of water ice and other substances into grains is prevented by the high temperature (Raymond et al., 2007). Such conditions are thought to exist in the inner 34 AU part of the disk of a sun-like star (Montmerle et al., 2006). The planet formation process occurs in a number of successive sub-stages char-

[5]Based on *Astrophysics of Planet Formation* (Armitage, 2010)

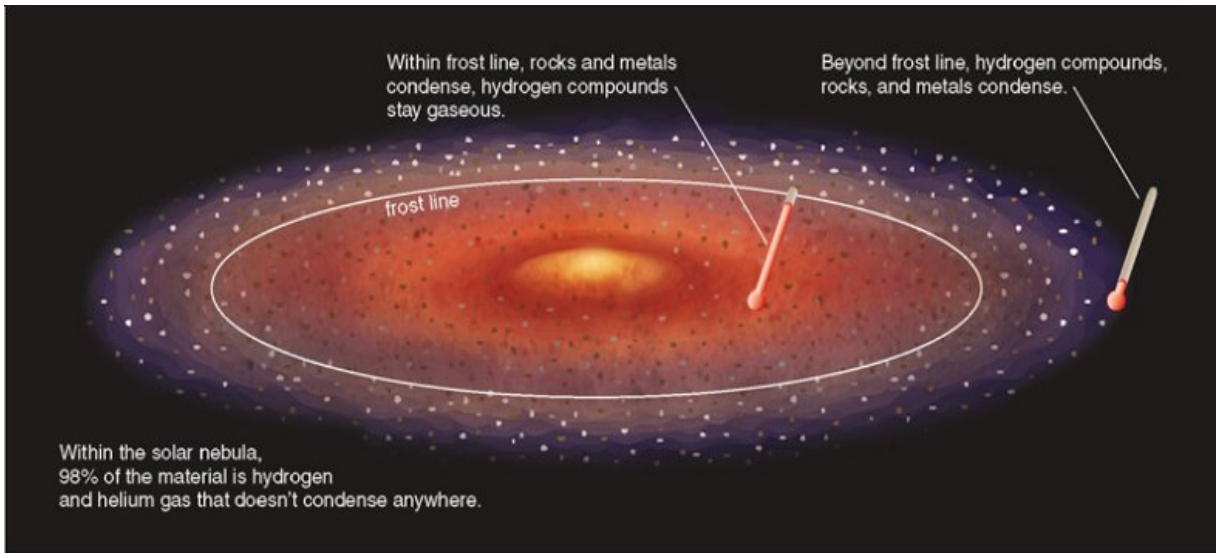

Figure 1.8: Inside the frost line where temperatures are higher, rocks and metallic materials can condense. Instead hydrogen compounds, such as water and methane, that typically condense at low temperatures, remain gaseous. Thus, the inner planets are made almost entirely of rocks and metals. Courtesy Pearson Education Inc.©.

acterized by different particle interactions (Safronov & Zvjagina, 1969; Goldreich & Ward, 1973; Ruden, 1999). First, the dust grains settle into a dense layer in the mid-plane of the disk, where they start to collide and stick together forming macroscopic objects, or *rocks*, with sizes of order 0.01-10 m, all orbiting the protostar in the same direction and in the same plane, probably similar to the thick rings around Saturn (Esposito, 2002; Nicholson et al., 2008). In a second stage, over the next 10^4 to 10^5 yrs, further collisions result in the formation of *planetesimals*, objects of size $\sim$1 km or above, moving by gravitational interactions, and accumulating in particular orbits, with nearly empty gaps between them. In the third phase, due to the mutual gravitational interaction between planetesimals, small changes in their Keplerian orbits happen, resulting in subsequent collisions, most of which occur at velocities producing a single larger object. In case planetesimals have sufficient mass, runaway growth of embryos occurs (Kokubo & Ida, 2002) with a mass growth rate proportional to $R^3 \cdot M^{4/3}$, where R and M are the radius and mass of the growing body, respectively (Thommes et al., 2003). The specific object growth accelerates as the mass increases and a few larger bodies rise rapidly at the expense of smaller ones. Runaway accretion for these bodies requires between 10^4 to 10^5 yrs to exceed approximately 10^3 km in diameter. As the mass of the largest bodies grows, they cause gravitational perturbations on the remaining planetesimals. This leads to a slowdown in the accretion rate and the end of further growth of smaller bodies.

The next stage is called *oligarchic accretion* and it is characterized by the predominance of several hundred of the largest bodies, named *oligarchs*. No other body than the oligarchs can grow, but the accretion continues more slowly and roughly at the same rate (Kokubo

& Ida, 2002). This slowdown occurs because, although the feeding zone expands as the planets mass grows, with a rate of accretion proportional to R^2, which is derived from the geometrical cross-section of an oligarch (Thommes et al., 2003), the number and mass of available planetesimals decrease and thus the specific accretion rate is proportional to $M^{-1/3}$. As it decreases with the mass of the body, smaller oligarchs can merge into larger ones.

The oligarchs continue to accrete until planetesimals are not anymore available in the disk around them (Kokubo & Ida, 2002). The final mass of an oligarch depends on surface density of planetesimals and on the distance from the star (Thommes et al., 2003). For the terrestrial planets it is up to $0.1\,M_\oplus$ or one Mars mass (Montmerle et al., 2006). The resulting picture of the oligarchic stage is the formation in a $\sim 10^5$ yrs (Kokubo & Ida, 2002), of about 100 Moon- to Mars-sized planetary *embryos*. They are thought to settle inside gaps in the disk and to be separated by rings of remaining planetesimals.

The final stage of rocky planet formation, starts when embryos become massive enough to gravitationally perturb each other and only a small number of planetesimals remains (Montmerle et al., 2006). The phase is characterized by violent collisions and mergers, due to chaotic orbits of the embryos (Raymond et al., 2006) and where the remaining planetesimals are expelled from the disk or collide with each other. This process takes from 10^7 to 10^8 yrs and leads to the formation of a limited number of Earth-sized bodies. From numerical simulations it seems that the number of surviving planets is on average from 2 to 5 (Montmerle et al., 2006; Raymond et al., 2006; Bottke et al., 2005; Petit et al., 2001). In this paradigm, Earth and Venus should represent the result of this merging phase in the SS (Raymond et al., 2006). Their formation required the merging of approximately 10-20 embryos, while an equal number of them were probably ejected from the SS (Bottke et al., 2005). Applied to the solar system, simulations suggest moreover that Earth reached half its mass in 10-30 Myr and its current mass in $\sim$100 Myr, with an exponential decreasing of the growth rate. The longer duration inside this final stage, the larger is the possibility to accrete material from different regions of the inner disk. Some of the embryos indeed, which originated in the asteroid belt, are thought to have brought water to Earth (Raymond et al., 2007). Mars and Mercury maybe be embryos that survived this phase failing to grow. (Bottke et al., 2005). The final configuration of terrestrial planets in term of size and spacing depends on several factors, in particular, the initial conditions, the viscosity (still not well understood) of the protoplanetary disk, and the existence and migrations of giants planets (see following section). For this last point indeed simulations show that in the SS the oligarchic and post-oligarchic stages are influenced by the presence of the giants Jupiter and Saturn.

1.3.3 Gas giant planets formation

The term *giant planets* refers to large planets, typically $\gtrsim 10\,M_\oplus$, that are not composed primarily by rocky or other solid matter. When orbiting close to the host star with period of less than 10 days they are referred to as *Hot Jupiter*.

There are two proposed models to account for the formation of the massive planets

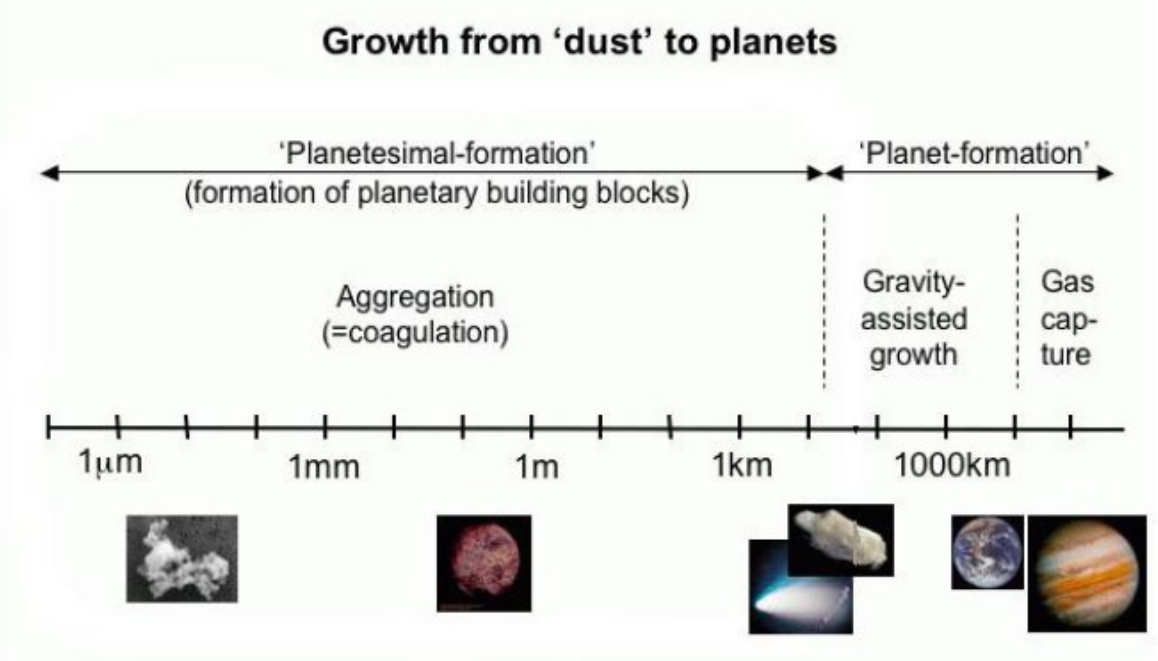

Figure 1.9: Illustration of planet formation, following the core-accretion model. Courtesy C. Dullemond.©.

[6]: *core accretion model* (Pollack et al., 1996; Rice et al., 2003; Alibert et al., 2004) and *gravitational disk instability model* (Boss, 1997; Mayer et al., 2002).

The most commonly accepted mechanism for the formation of Jupiter-like planets is the core accretion model. The same mechanism is considered valid for the solar system gas and ice giants, and for the exoplanet giant, at least for those orbiting within 10-50 AU. In this model the gas giant planets formation is described by a two-stage process. The first stage is closely similar to the formation of terrestrial planets (Kokubo & Ida, 2002). A massive core of $\sim$10-20 $M_\oplus$ forms through the coagulation of planetesimals. The second phase is characterized by a progressively more rapid accretion of a gaseous envelope from the PPD (Montmerle et al., 2006).

As described in the previous section, such process starts with the run-away growth of planetesimals, followed by the slower oligarchic stage (Thommes et al., 2003). However, a merging phase is not predicted in this case, due to the low probability of collisions between planetary embryos in the outer part of planetary systems (Thommes et al., 2003). In addition, at larger orbital radii, beyond the snow line, the temperature is low enough that ices as well as rocky materials can condense. This extra solid material, combined with the reduced gravity of the central star, allows large solid cores to form more easily in the outer regions of a disk with composition consisting mainly of ice. Typically, there is not enough solid material to form bodies this massive in the inner region of a protoplanetary disk.

[6]Based on *Astrophysics of Planet Formation* Armitage (2010)

Once the cores are of sufficient mass (5-10 $M_\oplus$), they begin to accrete gas from the surrounding disk (Montmerle et al., 2006). Initially a core is enclosed by a low mass envelope in hydrostatic equilibrium, which grows slowly more massive as the gas cools and contracts onto it (Inaba et al., 2003; Fortier et al., 2007). Over a period of a few million years, the core can eventually exceed a critical core mass of up to 30 $M_\oplus$ beyond which hydrostatic equilibrium is no longer possible, and a phase of extremely rapid gas accretion occurs. The remaining 90% of the mass is accumulated in approximately 10^4 yrs (Fortier et al., 2007). The accretion process ends when the planetesimals and gas terminate, either due to the opening of a gap in the PPD (Papaloizou et al., 2007), or because the gas dissipates. In this model, giants planets like Uranus and Neptune can be explained as failed cores that started too late the gas accretion stage, when almost all gas had already disappeared.

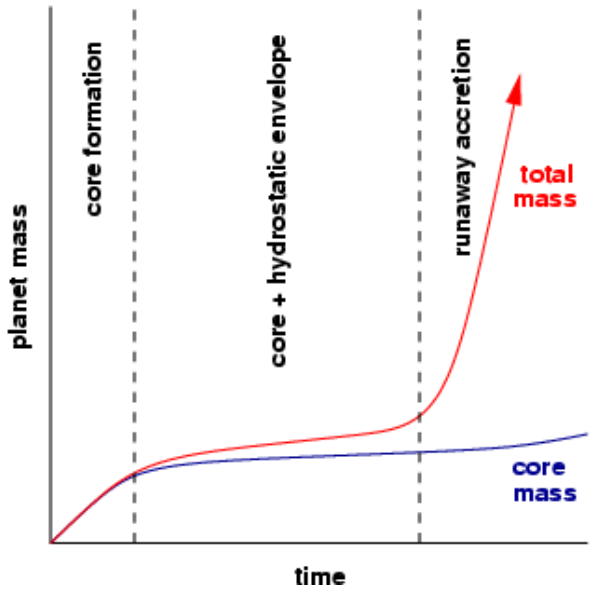

Figure 1.10: Schematic illustration showing how the core mass (blue line) and the total mass (core + envelope: red line) grow in a calculation of giant planet formation via core accretion. The formation of a ∼10 $M_\oplus$ core is followed first by slow quasi-static growth of an envelope, before finally run-away gas accretion ensues. The time scale of the slow phase of growth is a few million years. Courtesy P. Armitage.

There are, however, a number of issues with this model. Considering a PPD with a minimum mass capable of terrestrial planet formation, simulations show that only a 1-2 $M_\oplus$ cores at the distance of Jupiter (∼5 AU) can be formed within 10^7 yrs (Thommes et al., 2003). However, the value of 10^7 yrs corresponds to the average lifetime of gaseous disks around Sun-like stars (Haisch et al., 2001). Therefore, since the inner gas disks of PPDs disperse on timescales of 3- 5 Myr, the process of planet formation is a race against time (e.g. Pickett & Lim 2004). Several solutions were proposed to reduce the time-scale of the accretion: for example the possibility of a disk with increased mass (Thommes et al., 2003); the migration of the proto-planet, so that the embryos could accrete more planetesimals (Inaba et al., 2003); the influence on the accretion of gas drag in the gaseous envelopes of the embryos (Inaba et al., 2003; Fortier et al., 2007). Thus, the core formation of a gas giant planet (such as Jupiter and perhaps Saturn) is explained by a combination of the previous reported possible solutions.

The understanding of planets formation like Uranus and Neptune remains instead problematic. Indeed, the formation in situ of their cores at the distance of 20-30 AU from the central star results unlikely for any proposed theory (Montmerle et al., 2006). A possible solution is that they initially accreted in the Jupiter-Saturn region, to be then scattered to their present location after a migration phase (Thommes et al., 1999).

The second theory for gas giant formation, gravitational disk instability, also remains under study. According to this model, giant planets form in massive protoplanetary disks by gravitational instability within the disk itself, which leads to its fragmentation into clumps (Boss, 2003). Some of them, if they are sufficiently dense, can collapse and carry to rapid formation of gas giant planets and even brown dwarfs on the timescale of 10^3 years. However this scenario is only possible in massive disks, more massive than 0.3 solar masses, while, in comparison, typical disk masses are $0.01-0.03\,M_{\odot}$. Because the massive disks are rare, this mechanism of the planet formation is thought to be infrequent. On the other hand, this mechanism may play a major role in the formation of brown dwarfs. Thus the core accretion scenario seems to be the most promising one as it can explain the formation of the giant planets in relatively low mass (less than $0.1\,M_{\odot}$) disks (Janson et al., 2011).

Another important point to consider is that the presence of gas-giant planets can significantly influence the formation of terrestrial planets. Their existence tends indeed to increase eccentricities and inclinations of planetesimals and embryos in the terrestrial planet region (inside 4 AU in the SS) via Kozai mechanism (Bottke et al., 2005; Petit et al., 2001). The Kozai mechanism, or the LidovKozai mechanism, refers to the orbit of a satellite that is perturbed by another body orbiting farther out. Due to the perturbation, the orbit of the satellite experiences a periodic evolution (libration, oscillation about a constant value of its argument of pericenter) that drives it to lower inclination but very high eccentricity. This dynamical mechanism is particularly active in hierarchical triple systems (Ford et al., 2000), the inner orbit being subject to a similar evolution under the secular perturbations by the outer body. Moreover, if the giant planets formation occurs too early, the planet accretion in the inner part of the PPD can be reduced or even prevented. If their formation occurs roughly at the end of the oligarchic stage, as probably happened in the SS, the planetary embryos merging phase will be more violent (Bottke et al., 2005) and, as consequence, a minor number of terrestrial planets, but more massive, can evolve (Levison & Agnor, 2003).

1.4 Orbital migration

The relatively large number of close-in Hot-Jupiters, discovered after `51 Peg-b` (Mayor & Queloz, 1995), has focused attention on some earlier predictions (Goldreich & Tremaine, 1980) that Jupiter-Mass planets could experience planetary migration. The existence of hot Jupiters in fact could not be explained in the regime of only the core accretion model, since the lack of material at so short distances from the star could not allow the formation of so close-in giant planets. Nowadays at least three mechanisms are believed to lead to substantial orbital evolution once the planets have formed: i) the interaction between the planet and the residual gaseous protoplanetary disk (*gas disk migration*); ii) the interaction with the remnant planetesimals (*planetesimals disk migration*); iii) planet-planet scattering. The basis for each of the processes is summarized in the following sections. [7]

[7] Based on Armitage (2010)

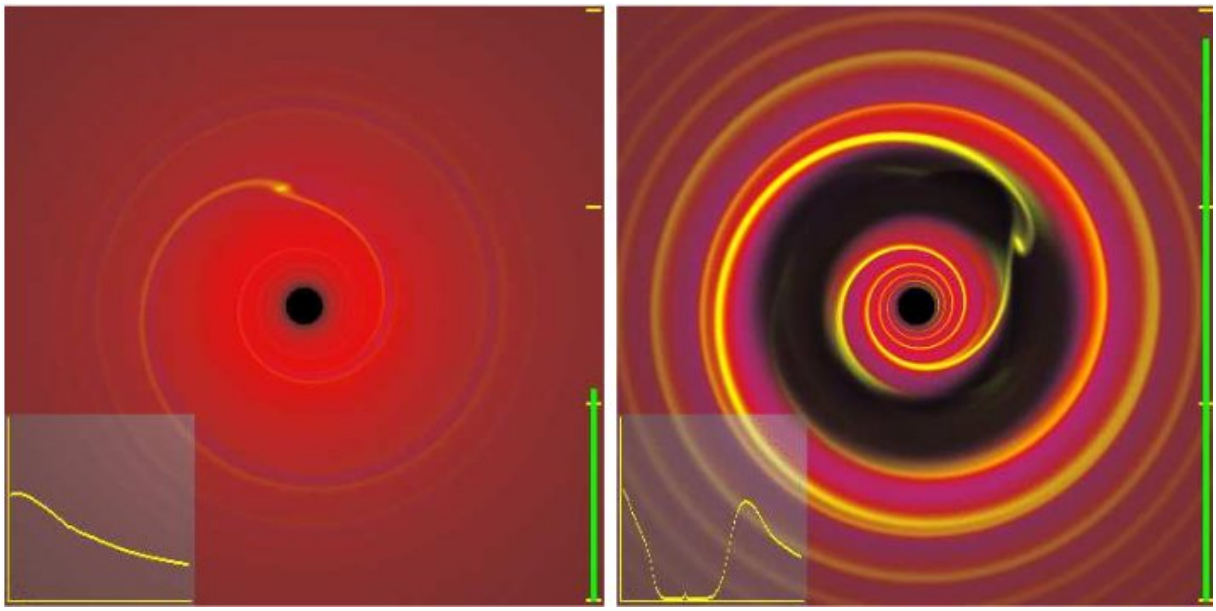

Figure 1.11: Type I and type II migration. Simulations of the interaction between a planet in circular orbit with a non-turbulent protoplanetary disk: (a) In Type I migration, a relatively low-mass planets excites a wave in the gas disk, but does not significantly perturb the azimuthally-averaged surface density profile (inset). (b) In type II migration, a more massive planet (here of $10\,M_{\odot}$) clears an annular gap, within which the surface density is a small fraction of the unperturbed value. As the disk evolves the planet follows the motions of the gas (inward or outward) while remaining within the gap. Courtesy P. Armitage.©.

1.4.1 Gas disk migration

The runaway, oligarchic and the early post-oligarchic stages of planet formation are followed by the continuing presence of residual gas within the disk. A planet moving through the PPD along its orbit gravitationally perturbs this gas and can generate spiral density waves at orbital radii where the gas is in resonance with the planet. The planet experiences a torque, energy and angular momentum are hence transferred between the planet and the surrounding gas through such waves. This results in a variation of the semi-major axis (causing the planetary migration) and possibly orbital eccentricity. Two main scenarios of gas disk migration have been identified. (Goldreich & Tremaine, 1980; Lin & Papaloizou, 1986; Ward, 1997).

Evolution of the planet orbit that weakly perturbs the surface density profile of the gas disk, is referred as *Type-I migration*. Analytical and numerical simulations show that this conditions hold for low-mass planets ($M_p \leq 10\,M_{\oplus}$) and the migration rate is proportional to the planetary mass. Since the planet remains entirely embedded within the gas, the most important resonances are those closer to the planet. The interactions with the gas disk located interior to the planetary orbit add angular momentum to the planet, while the

interactions with the exterior disk remove angular momentum. The net balance of these two effects causes radial planet migration inward or outward. Theoretical calculations suggest that inward planet migration is favored and potentially with a short time scale: a migration time scale of only $\sim 10^6$ yrs is estimated by Tanaka et al., 2002 for a $1\,M_\oplus$ planet at 5 AU. Furthermore, considering a highly turbulent disk, type-I migration can be described more as a random walk than as a smooth inward migration. Type-I migration has likely an important role in the formation of giant planets in the core accretion model (see Section 1.3) while it may be a relatively minor effect for terrestrial planets, due to their low masses. Type-I migration is illustrated in Figure 1.11a.

Concerning the other scenario, for larger planet masses, the surface density profile of the gas disk is strongly perturbed by the presence of the planet. The exchange of angular momentum between the planet and the disk tends to remove gas from the vicinity of the planet orbit, creating an annular gap with a lower surface density of the gas. The resulting orbital evolution, in direction and rate, depends on how rapidly the gas of the disk tries to fill again the gap on the base of its angular momentum transport processes. This regime is known as *type-II migration* (see Figure 1.11b) and the orbit of the planet and the viscous evolution of the disk are directly connected. In the regions of the disk where the gas is flowing inward, the planet moves inward too and vice versa. Planets that have formed a gap continue to accrete some gas via narrow streams of material that cross the gap. However, as the planet grows more massive and the gap becomes deeper, the rate of gas accretion decreases. Type-II migration is typically slower than type-I migration. The boundary between type-I and type-II migration is not sharp. In between these regimes, non-linear effects become important.

There is no direct observational evidence for gas disk migration, but it is widely believed that this mechanism explains the existence of Hot Jupiters, such the planet orbiting `51 Pegasi`. Furthermore, it has been supposed that gas disk migration may also excite planetary eccentricity, providing a simultaneous explanation for the wide spread of eccentricity observed among extrasolar planets, but this remains a still open question. Another important point is connected to the halting processes. Conditions which drive inward migration should provide some halting mechanisms, if the planet is not to fall onto the host star. Several scenarios have been hypothesized, but none of which have fully accepted. Migration would be stopped also at any radius when the disk dissipates (Trilling et al., 2002), although this appear to require too many constrains on the mass and disk lifetime to explain the observed population. A slightly different picture would follow if the close-in planets reached their current configurations by tidal circularization after scattering into eccentric orbits. For the close-in planets, tidal decay could continue, even after the circularization and the very hot Jupiters observed might simply be those next for tidal destruction (Jackson et al., 2009). More direct evidence for this scenario will come from increased statistics on semi-major distribution and spin-orbit alignment. Ford & Rasio (2006) used the observed distribution of Hot-Jupiters to constrain the location of the inner edge in the mass-period diagram. In a population still dominated by inward migration, the inner edge of the mass-period distribution should correspond to the Roche limit. They found instead that the edge corresponds to a separation close to twice the Roche limit, as

expected if the planets started on highly eccentric orbits that were later circularized.

1.4.2 Planetesimal-disk migration

After formation of the terrestrial and gas/ice giants, and the dispersal of the gas disk, some planet migration is still expected as a result of gravitational scattering between the planets and any remaining planetesimals. By conservation of angular momentum, an inward scattering of the planetesimal will be accompanied by an outward movement of the planet and vice versa. A significant change of the planet orbit will occur if the mass of interacting planetesimals and the mass of the planet are comparable. Given that the mass of the condensed matter is $\sim$5 times larger than the gas mass in typical PPD, ice giants, which have accreted relatively modest gaseous envelopes, will be favored to undergo planetesimal-disk migration than very massive gas giant planets (Hahn & Malhotra, 1999; Kirsh et al., 2009; Bromley & Kenyon, 2011; Capobianco et al., 2011).

Planetesimal migration appear to had significant effect on the architecture of SS. A strong evidence for the early occurrence of this mechanism in our system comes from the distribution of trans-Neptunian objects. Observations show that Pluto itself and a large population of other objects (called *Plutinos*) are in 3:2 resonance with Neptune. Some of these bodies have eccentricities high enough that they cross Neptune's orbit. This particular distribution is thought to be the final result of the outward migration of Neptune (Malhotra, 1995), following the scattering of a disk of planetesimals. Simultaneously, these planetesimals, moving inward, may eventually experience encounters with Jupiter and ejected from the SS. As Neptune slowly migrated outwards, it could have captured Pluto and other bodies into the 3:2 resonance (a process referred as resonant capture) and increased their eccentricity.

More generally and with less direct evidence, Tsiganis et al. (2005) proposed a model where all the gas-giant planets in the SS originated in a more compact configuration, which then evolved through a phase of planetesimal scattering to its current configuration. In this so-called *Nice model*, a crossing of the 2:1 resonance between Jupiter and Saturn is hypothesized and associated to the *late heavy bombardment* (a temporary peak in the cratering rate, Gomes et al., 2005) on the Moon.

1.4.3 Planet-planet scattering

Planet-planet scattering, resulting from gravitational interactions with other orbiting planets in the same system, can also continue after both the gas and planetesimal disks have been lost or depleted (Rasio & Ford, 1996; Lin & Ida, 1997; Ford et al., 2001; Marzari & Weidenschilling, 2002; Ford et al., 2003). Evolution of an initially unstable multiple planetary system can result in the ejection of one or more planets (typically the lightest); an increase in the orbital separation of the planets, toward a more stable configuration; planet-planet or planet-star collisions. The relative probability of these processes is determined by the initial orbital radii, masses, orbital eccentricities, and numerical N-body simulations are needed to study the evolution of such systems. However, typically the final

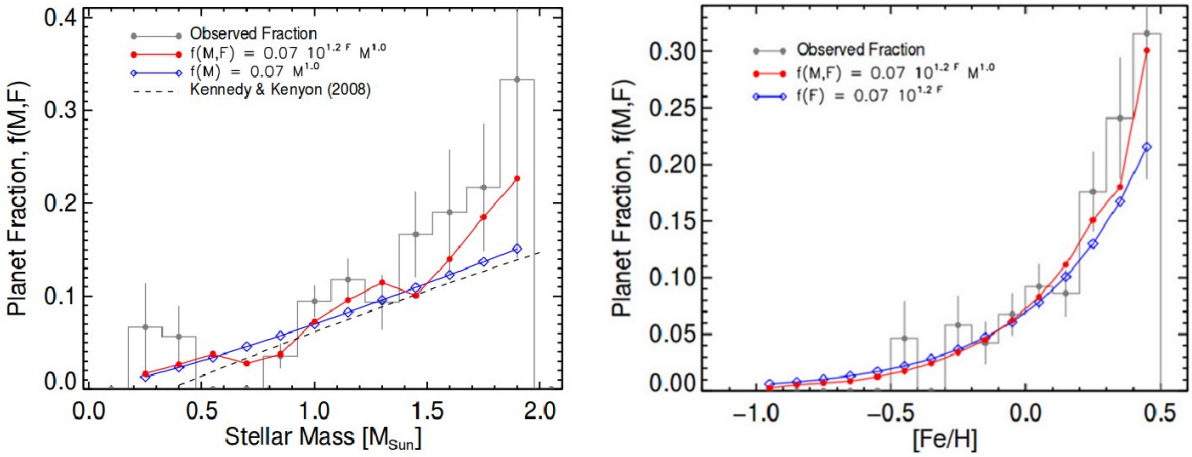

Figure 1.12: *Left panel*: Planet fraction ($f = N_{planets}/N_{stars}$) as a function of mass for the stellar sample. The red filled circles show the planet fraction predicted by Eq. $f(M, F) = CM^{\alpha}10^{\beta F}$ for the masses and metallicities of the stars in each bin. The dashed line shows the stellar mass relationship predicted by Kennedy & Kenyon (2008). *Right panel*: Planet fraction ($f = N_{planets}/N_{stars}$) as a function of metallicity for the stellar sample. The blue open diamonds show the best-fitting relationship between planet fraction and stellar metallicity for $M_{\star} = 1\,M_{\odot}$. Adapted from Johnson et al. (2010).

result of scattering is a modest migration of the surviving planet often with a significant gain in eccentricity (Adams & Laughlin, 2003; Veras & Armitage, 2006; Ford & Rasio, 2008; Raymond et al., 2011). The planet-planet scattering is a promising scenario for explaining the occurrence of non-circular orbits, with numerical simulations that can well reproduce the observed eccentricity distribution of massive extrasolar planets.

1.5 Properties of the planet-host stars.

Given that planet formation is a by-product of the stellar formation process, a close investigation of the planet-host stars is also expected to provide important clues about the formation of planetary systems. In this context, several researchers looked for correlations between the presence of planets and different stellar properties, like stellar chemical composition, mass, age, activity, and rotation. Such correlations could either provide evidence about the requisites for planet formation, or be the result of some kind of planet feedback on the star. While it is clear that stellar mass has a great impact on the frequency of giant planets (Bonfils et al., 2007; Lovis & Mayor, 2007; Johnson et al., 2010), the precise dependence of the planet rate on stellar mass is not yet known. Moreover, the precise role of metallicity and stellar chemical composition is also still to be fully understood. Several studies (Santos et al., 2004; Fischer & Valenti, 2005; Udry & Santos, 2007; Sousa et al., 2011; Mortier et al., 2013) have shown that the probability of giant planets depend

strongly on metallicity. Fig. 1.12 shows the empirical relationship derived by Johnson et al. (2010), describing the planet occurrence as a function of stellar mass and metallicity, according to the equation: $f(M, F) = CM^{\alpha}10^{\beta F}$ where $F = [Fe/H]$ and $M = M_{\star}/M_{\odot}$. Current number, based on RV samples, suggest that around 25% of the stars with twice the metal content of the Sun harbor a giant planet, against only ∼3% for solar-metallicity stars (Sousa et al., 2011; Mayor et al., 2011). The correlation between metallicity and occurrence appears to extend to the close-in giant planets discovered by transit photometry (Guillot et al., 2006). However this trend is not present for stars which host lower mass objects, as Neptunians and Earth-like planets (Udry & Santos, 2007; Sousa et al., 2011; Mayor et al., 2011) and for giant host stars (Pasquini et al., 2007; Döllinger et al., 2011; Mortier et al., 2013). It is thus likely that both metallicity and stellar mass impact the occurrence and the properties of giant planets. Larger samples will be needed to confirm this observation and to disentangle the two effects.

Most analyses suggest that the overall mass-metallicity correlation observed in planet-host stars has a primordial origin and reflects the characteristics of the protoplanetary disk (e.g. Livio & Pringle, 2003; Santos et al., 2003; Fischer & Valenti, 2005). This conclusion favors the core accretion model for the formation of giant planets (Ida, 2004; Udry & Santos, 2007; Mordasini et al., 2012) because the higher the grain content of the disk, the easier to build the cores that will later accrete gas, before the gas disk dissipates. According to the disk instability model, instead, the presence of planets would be apparently insensitive to stellar metallicity (Boss, 2003).

Another important point is related to the chemical abundances analysis of the planet-host stars. The last 10 years of spectroscopic observations dedicated to the search of extrasolar planets have provided an unprecedented set of high-quality spectra. Several studies are trying to understand the effects of the formation of planets and planetary systems on the atmospheric Litium (Li) abundance of planet host stars. It is still under discussion if planet hosting stars are more Li depleted with respect to stars non-hosting planets. This result was also supported by Takeda & Kawanomoto (2005); Israelian et al. (2009); Takeda et al. (2010) and Gonzalez et al. (2010). Doubts about the proposed Li-planet connection have been raised in several works Baumann et al. (2010); Ghezzi et al. (2010); Ramírez et al. (2012) and argue that the observed behaviour of Li abundances could be associated to age, mass, or metallicity differences between stars with and without planets. A recent work instead seems to confirm the amount of depletion of Li in planet-host solar-type stars and that this is higher when the planets are more massive than Jupiter (Delgado Mena et al., 2014).

Moreover, it is still not clear if there is a possible correlation between chemical abundances of the volatile-refractory elements of the hosting stars and the presence of rocky planets. Recently, Meléndez et al. (2009) noticed that the Sun shows a deficiency in refractory elements (i.e. with a relatively high equilibrium condensation temperature or a very high melting point) with respect to the volatile content (i.e. materials with relatively low equilibrium condensation temperature) when comparing with the mean abundance pattern of the other solar twins (see fig. 1.13). They found a decreasing trend of the mean abundance differences, $\Delta[X/Fe]_{Sun-Star}$ versus the condensation temperature T_C and suggested

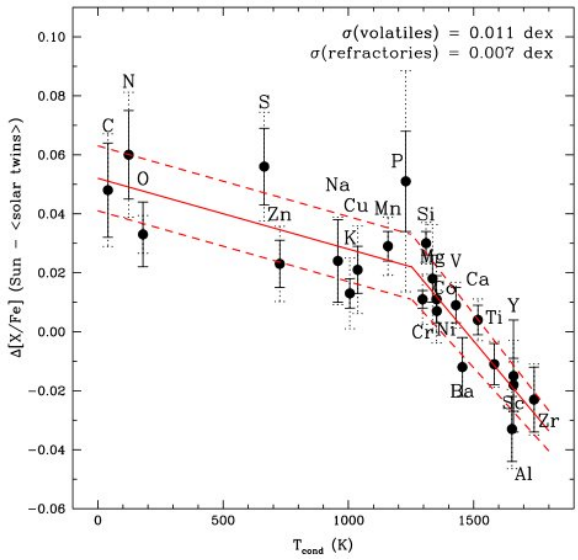

Figure 1.13: Mean abundance differences $\Delta[X/Fe]_{Sun-Star}$ between the Sun and the mean values in the solar twins as function of T_C . The abundance pattern shows a break at T_C ∼1200 K. Volatile elements (with low T_C) are more abundant in the Sun relative to the solar twins, while elements that easily form dust (i.e. refractories, with high T_C) are underabundant. Adapted from Meléndez et al. (2009).

that this behaviour was connected to the presence of terrestrial planets in the solar system: probably refractory elements were trapped in the terrestrial planets in our solar system. A particularly circumstance is that the inner solar planets and meteorites are enriched in refractories compared to volatiles, with abundance pattern being almost a mirror image of the solar pattern relative to the solar twins (Ciesla, 2008). The same conclusion has also been reached by Ramírez et al. (2009, 2010) who analyzed several solar twins and analogs. However, recent results by González Hernández et al. (2013) and Adibekyan et al. (2014) strongly challenge the relation between the presence of planets and the abundance peculiarities of the stars (fig. 1.14). They have shown that there is no statistically significant difference in T_C slopes for planet-hosting stars (in particular for rocky planet hosts) and stars without any detected planetary companion. They conclude that the age and probably the Galactic birth place are determinant to establish the star's chemical properties. Old stars (and stars with inner disk origin) have a lower refractory-to-volatile ratio.

Despite the huge progress in developing instrumentation and observational techniques during the past decade, the study of extrasolar planets properties via direct observations is still a very difficult task, and the precise study and characterization of known extroplanets cannot be dissociated from the study of planet host stars.

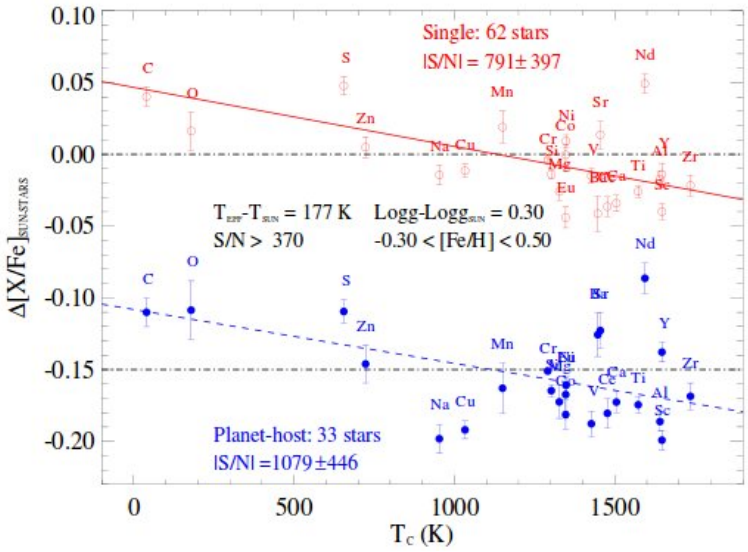

Figure 1.14: Mean abundance differences $\Delta[X/Fe]_{Sun-Star}$ between the Sun, and 33 planet-host stars (blue filled circles) and 62 non-hosting stars (red open circles) of the whole sample of solar analogues. An arbitrary shift of -0.15 dex has been applied to the abundances of the planet-host stars, for the sake of clarity. González Hernández et al. (2013) found very similar behaviour in the mean abundance pattern of stars with and without planets, irrespective of the number of planets, and mass and orbital period of the planets, suggesting that there is no clear signature of terrestrial planets in these mean patterns. Adapted from González Hernández et al. (2013).

1.6 Search for planets in clusters

Since the search of giant planets in the open cluster M67 was one of the main parts of this PhD project, in this section a brief introduction of the status of the search for planets in clusters is given.

A very significant observational effort has been devoted to search for planets in Galactic open clusters and globular clusters with transit surveys and with lesser extent RV campaigns. The scientific motivation includes establishing the effect of stellar mass and metallicity on planet occurrence (Ida et al., 2000; Kobayashi & Ida, 2001), determining time scale of formation and migration, and modeling the effects of stellar encounters on formation and destruction (Fregeau et al., 2006; Malmberg et al., 2007). Stars in cluster share age and chemical composition (Randich et al., 2005), so it is possible to control strictly the sample and to limit the parameter space in a better way than when studying field stars. The observation of large samples of bright and nearby field stars has given the possibility of studying the dependence of planet formation on stellar parameters. However, detailed comparisons are affected by the composite nature and population of the stars and biases in the samples, so that conclusions are often controversial. Instead the possibility to study planets around stars in cluster can provide the perfect sample to answer still open

questions about the frequency of planets with respect to stellar properties. Indeed the planet-metallicity correlation and the stellar mass planet occurrence are crucial topics still under discussion with important influence on models of planet formation (see sec. 1.5).

Furthermore, if we examine the current distribution of the Jupiter mass planets for RV surveys around FGK stars at solar metallicity we find an exoplanet host-rate higher than 10% for planets with a period of up to a few years and 1.20±0.38%, for very close-in hot-Jupiters with a period shorter than ten days (Cumming et al., 2008; Mayor et al., 2011; Wright et al., 2012). Despite most stars form in clusters and stellar associations, this rate around field stars has been in contrast to the lack of detected planets in both open and globular cluster for several years. Before 2012, the detections with the RV technique were limited to a long-period giant planet around one of the Hyades clump giants (Sato et al., 2007) and to a substellar-mass object in NGC2423 (Lovis & Mayor, 2007). No evidence of short-period giant planets has been presented in the study of Paulson et al. (2004) around main sequence stars of the Hyades. Furthermore, no transiting planets were confirmed by several transit campaigns in open clusters (Bruntt et al., 2003; Street et al., 2003; Bramich et al., 2005; Mochejska et al., 2005; Burke et al., 2006; Aigrain et al., 2006; Hartman et al., 2009), neither in globular clusters (Gilliland et al., 2000; Weldrake et al., 2005, 2008; Nascimbeni et al., 2012). The paucity of detected planets triggered the hypothesis that the frequency of planet-hosting stars in clusters is lower than in the field. To explain the dichotomy between field and cluster stars, it has been suggested that the cluster environment might have a significant impact on the disk-mass distribution. Eisner et al. (2008), studying disks around stars in the Orion Nebula Cluster (ONC), proposed that most of these stars do not posses sufficient mass in the disk to form Jupiter-mass planets or to support an eventual inward migration. Other scenarios may be attributed to post-formation dynamics, in particular to the influence of close stellar encounters (Spurzem et al., 2009; Bonnell et al., 2001) or to tidal evolution of the hot-Jupiters (Debes & Jackson, 2010) in the dense cluster environment. However, a study of van Saders & Gaudi (2011) found no evidence in support of a fundamental difference in the short-period planet population between clusters and field stars, and attributed the non-detection of planets in transit surveys to the inadequate number of stars surveyed. This seems to be confirmed by the recent results. Indeed, we can list the discovery of two hot-Jupiters in the Praesepe open cluster in 2012 (Quinn et al., 2012) and of two sub-Neptune planets in the cluster NGC6811 as part of The Kepler Cluster Study (Meibom et al., 2013), the new announcement of a hot-Jupiter in the Hyades (Quinn et al., 2013) and the detection in M67 (Brucalassi et al., 2014) of three Jupiter-mass planets that will be presented as a part of this Phd project.

1.7 Tools for RV data analysis

Since the work during my PhD was mainly focused on the study of extrasolar planets using the RV velocity technique from both, instrumental and observative, points of view, I thought it could be useful to dedicate a section of this chapter to describe some tools and

algorithms that I used for the analysis of the RV measurements.

1.7.1 Measurement principles

What we usually measure is an instantaneous values of the stellar velocity on our line of sight, the so-called radial velocity. This is given by the small, systematic Doppler shift in wavelength of the many thousands of absorption lines present in the high-resolution optical spectrum of the stars. Doppler's equation can be written in the classical form as

$$f_{obs} = \left(1 - \frac{v_{em} - v_{obs}}{c}\right) \cdot f_{em} \tag{1.6}$$

where, f_{obs} is the observed frequency; v_{em} is the velocity of the star, or the source; v_{obs} is the velocity of the observer; c, is the velocity of light and f_{em} is the initially emitted frequency. This equation can be be rearranged to get the velocity of a star as a function of wavelength in the observer reference frame as

$$v_r = \left(\frac{\Delta\lambda}{\lambda_{em}}\right) c \tag{1.7}$$

where $\Delta\lambda = \lambda_{obs} - \lambda_{em}$ and λ_{obs}, λ_{em} are the observed and emitted wavelengths. Conventionally, positive values of v_r indicate recession. Thus a redshift is caused by an object receding from our point of view. It has to be noted that one needs to take into account the radial velocity of the observer. In order to get precise and accurate radial velocities we therefore need to know well the motion of the Earth around the barycenter of the solar system.

High-accuracy radial velocities for exoplanet detection are typically acquired using échelle spectrographs with high spectral resolving power (typically R=$\lambda/\Delta\lambda \sim 50000 - 100000$) and operated in the optical region (450−700 nm). Several diffraction orders are cross-dispersed, and recorded simultaneously on rectangular format CCDs providing large numbers of resolved absorption lines. High instrumental stability and accurate wavelength calibration are required to minimize effects of gravitational and thermal telescope flexure, and other instrument drifts. Large telescopes and long integration times are still important to achieve the necessary high signal-to-noise, and corresponding sub-pixel accuracies.

Radial velocities are traditionally obtained by cross-correlating (CC) the observed spectra with a template synthetic stellar spectrum or with box-shaped, binary (0 and 1 values) masks (Baranne et al., 1996; Pepe et al., 2002). The stellar masks have nonzero zones corresponding to the theoretical positions and widths of stellar absorption lines at zero velocity. Experience shows that there is no need to use a different mask for each star. Common practice is to use a few masks corresponding to the main spectral subtypes (e.g. G2, K5, and M2).

The operation of CC basically consists in the measure of how similar the stellar spectra and the template are as a function of a displacement applied to one of them. Such similarity is estimated by the value of the correlation function (CCF) as a function of the displacement (expressed in pixel).

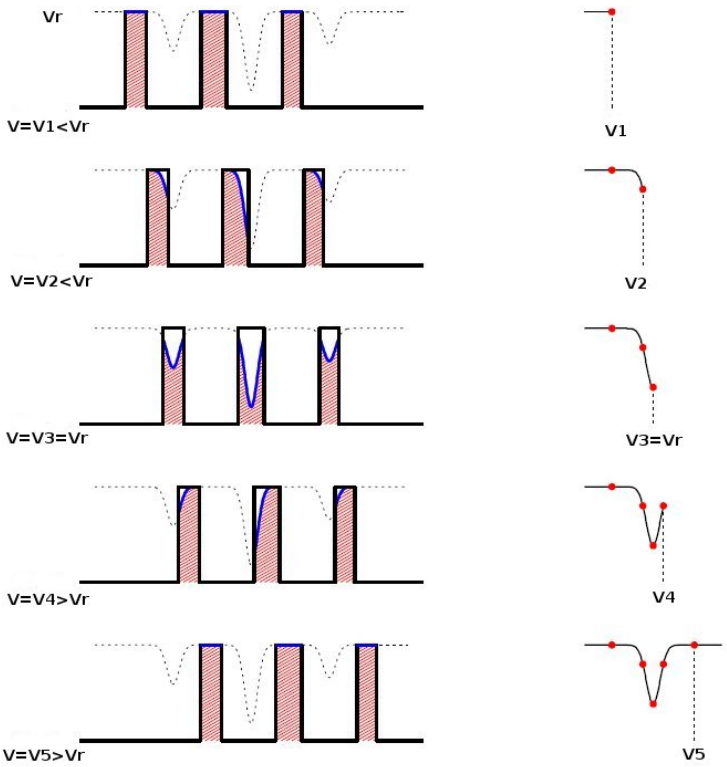

Figure 1.15: Schematic illustration of the CCF construction using a binary mask. Diagrams on the left represent the stellar spectrum (dashed lines) and the binary mask (solid lines, transmission zones shown as hatched areas). Diagrams on the right show the result of the cross-correlation process. Courtesy of Claudio Melo.

Thus the goal is to determine the velocity value ϵ minimising (or maximising depending on the analysis tool used) the function (Queloz, 1995):

$$C(\varepsilon) \propto \int_{-\infty}^{\infty} \mathrm{S}(v)\mathrm{M}(v-\epsilon)\mathrm{d}v \tag{1.8}$$

where S is the stellar spectrum and M is the mask or the synthetic template, both expressed in velocity space v. Associated errors are established from Monte Carlo modeling. Weighting according to the relative line depths further optimizes the signal-to-noise, and can also reduce the perturbing effects of telluric lines (Pepe et al., 2002).

The CCF usually follows a bell curve: it reaches its maximum (minimum) when the absorption lines in the template and in the observed spectra are aligned. Fig. 1.15 shows schematically how the cross-correlation function (CCF) in case of using a mask is obtained. The CCF is constructed by shifting the velocity of the mask by increasing amounts over a window roughly centered on the radial velocity of the star. The better the alignment between the stellar lines and their box-shaped counterparts in the mask, the lower the cross-correlation value. The CCF is thus minimal when the velocity of the mask perfectly

matches the radial velocity of the star (middle panel in Fig. 1.15).

The precise shape of the resulting cross-correlation function depends on the intrinsic spectral line shapes and on the template line widths, and overall represents a mean profile of all lines in the template. In addition to the radial velocity, the width of the CCF gives the stellar rotational velocity $v \sin i$, while the equivalent width provides a metallicity estimate if the effective temperature T_{eff} is known approximately (Queloz, 1995).

In the absence of systematic line asymmetry, the central part of the CCF is well approximated by a Gaussian function and the radial velocity of the star is measured by the center of the Gaussian best-fit.

1.7.2 Fitting planets

Once one obtains several RV measurements, it is necessary to check the presence of the planets and try to reconstruct the orbit. Referring to eq. B.2 and eq. 1.2, there are five observables related to the star's Keplerian orbit which can be fit for each orbiting planet on the basis of radial velocity measurements: e, P, t_p, ω and the combination $K = f(a, e, P, i)$. Two further terms are usually considered: a *systemic velocity* γ describing the constant component of the RV of the system's center of mass with respect to the solar system barycenter; and a linear trend parameter d, which may take into account instrumental drift as well as undetected contributions from massive, long-period companions. The calculation of the radial velocity parameters for a single orbiting planet is typically based on the search of parameters space using χ^2 minimization. Specific tools are employed for period estimates simplifying the search: an example widely used is the Lomb-Scargle algorithm (Scargle, 1982; Horne & Baliunas, 1986).

For a system of n_p planets, the first-order approach to fitting multiple systems is to ignore the effect of the planet-planets interactions and to approximate the total radial velocity signal as a linear sum of n_p eq. B.2, giving $5n_p + 1$ Keplerian parameters to be fit, including γ and optionally d. In this Keplerian fitting, the dominant planet signal is identified, its Keplerian contribution subtracted from the observational data and the process repeated until all significant signals are detected. A more rigorous multi-planets χ^2 analysis of the original data can then be applied using the previous results as starting values.

A summary of some specific techniques used for this work is detailed in Appendix B.

Chapter 2

The Munich Spectrograph Stability Project

Figure 2.1: The Wendelstein Observatory.

2.1 Introduction

The Ludwig-Maximilian-Univesität München (USM) operates an astrophysical observatory on the summit of Mt. Wendelstein, in the Bavarian Alps (see fig. 2.1). The site has an altitude of 1840 m, provides approximately 1100 clear hours per year and an exceptional good seeing (median value < 0.8").

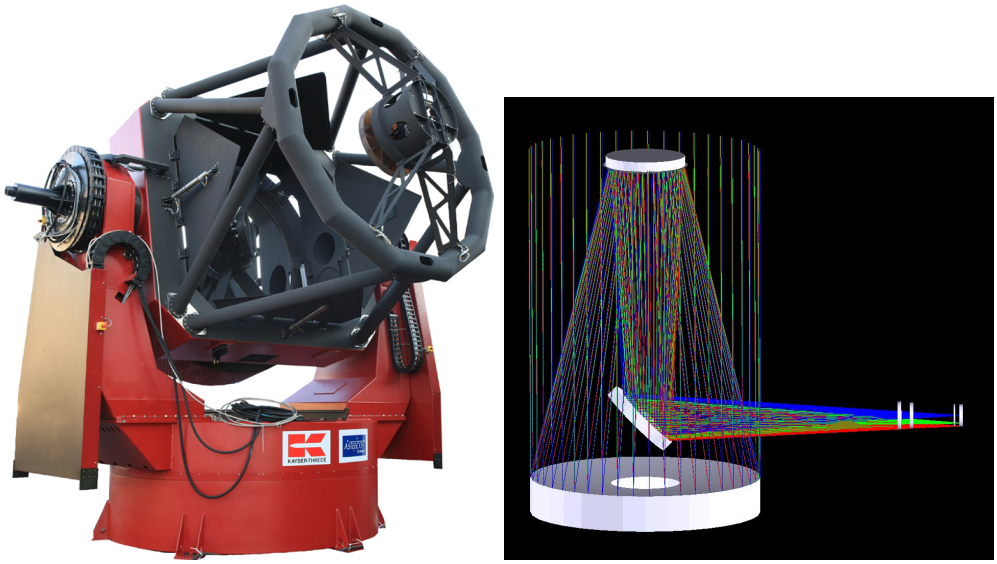

Figure 2.2: The new 2-m Fraunhofer robotic telescope (left). Ray-tracing for the Nasmyth Port 1 (right).

Since August 2011 the integration in a new 8.5-m dome of a new 2-m Fraunhofer robotic telescope (see fig. 2.2) with a very compact alt-azimuth design has started[1].
Financial support for the building comes from the *Freistaat Bayern*, while the telescope is financed together by the *Freistaat Bayern* and the *Federal Government of Germany* (BMBF). The instruments instead are funded by the *Excellence Cluster Origin and Structure of the Universe*, and the *German Science Foundation* (DFG).
The overall management of the telescope project has been done by *Kayser-Threde GmbH, Munich* and its subcontractor *Astelco GmbH, Martinsried*, which is the main contributor of the telescope mechanics. The design work for the building has been prepared by the *Staatliche Bauamt München II* with the help of the *Staatliche Bauamt Rosenheim*, while the dome has been produced by *Baader Planetarium GmbH, Mammendorf*. More details on the opto-mechanical design and the production of the telescope can be found in Thiele et al. (2012); Hopp et al. (2012).
The space available at the observatory is limited by the steepness of the mountain and thus, an alt-azimuth mounted telescope was selected with no Cassegrain station and two

[1]Based on Hopp et al. (2008, 2010); Grupp et al. (2008)

Table 2.1: Basic optical parameters of the 2-m Fraunhofer Telescope.

Parameters	**Port 1**	**Port 2**
Free system aperture [μm]	2.0	2.0
Total focal ratio	7.8	7.7
Total focal length [mm]	15600	15472
Field radius [deg]	0.35	0.1
Scale [arcsec/15μm]	0.198	0.200
Scale [μm/arcsec]	76	75
Central obscuration	13%	13%

Nasmyth stations only. To keep the system compact, a three mirror design has been developed between vendor and USM where the first two mirrors form a relatively fast Richey-Chretian system (f/7.8), while the third flat mirror is mounted on a rotation stage and selects between the two Nasmyth stations called port 1 and port 2 in the following. Both of these ports have a derotator, while only port 1 is equipped with a three lens corrector, offering a wide field mode (field of view (FOV) of 0.7° diameter). All the three mirrors of the telescope has been produced by *Lytkarino Optical Glass Factory* (LZOS,Moscow). Table 2.1 presents the basic optical data of the telescope.
Thanks to the long-term access, the Fraunhofer Telescope forms an ideal complement to large international instruments. As scientific projects, it includes the participation in follow-up observations and long-term monitoring for large surveys (like e.g. PanStarrs, HETDEX, or eROSITA), and programs in combination with other facilities where USM is a partner like e.g. the 9.2-m Hobby-Eberly-Telescope (HET). Furthermore, it will be used to support different education projects for students.

Port 1 harbors a wide-field camera (**WWFI**) with 0.5°x0.5° field of view and minimal ghosting. It is made by a mosaic of four 4kx4k e2v CCDs built by Scientific Instruments in Tucson. The camera supports standard broad band and high throughput filters in the SDSS system and allows for further filters (for details see Gössl et al. (2010)). The highest priority science projects for this instrument are the extension of the pixel lensing studies in search of compact dark matter (Riffeser et al., 2001), variability studies in nearby galaxies, and will support survey projects at other telescopes like e.g. the spectroscopic HETDEX survey (Hill et al., 2008).

Table 2.2: Basic optical parameters of the instruments at the Nasmyth Port 2.

Instruments	**Image sampling Resolving power**	**Wavelength range**	**FOV**	**Detector**
3KK	2 x VIS: 0.4″/2 pixels 1 x IR: 0.5″/2 pixels	340-970 nm 970 nm-2.3 μm	0.14° 0.20°	2x2K 15μm CCD 2x2K 18μm Hawaii CCD
FOCES	R∼70000	380-900 nm	1.35″	2x2K 13.5μm CCD
VIRUS-W	R∼2500	475-560 nm	150″x76″	2x4K 15μm CCD

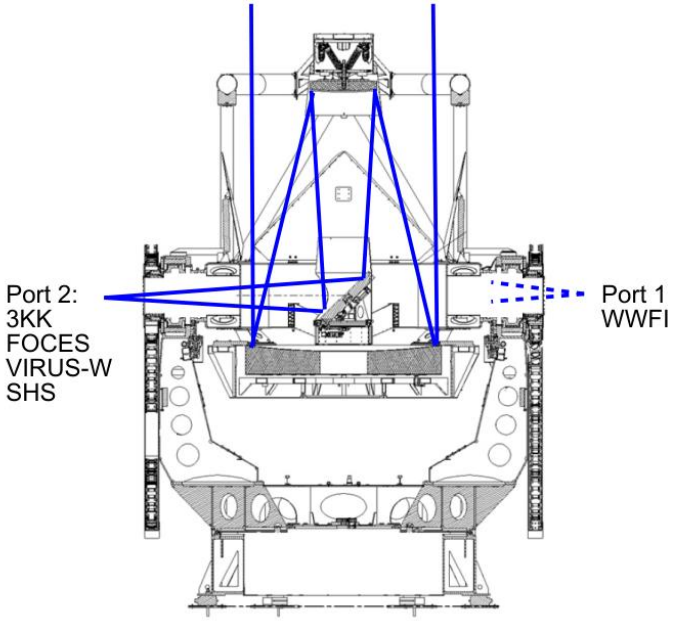

Figure 2.3: Overview of the optics integrated into the mechanical design

Port 2 has no field correction lens system and offers a field of view of 0.14°. This focal station will be equipped with a number of imaging, spectroscopic and calibration devices:

3KK: a three-channel camera (3KK) which allows simultaneous observations in two optical bands and one NIR band. It will be used for fast multi-wavelength follow-up observations of targets-of-opportunity like Gamma-Ray-bursts or efficient photometric redshift determinations of galaxy clusters identified in PanSTARRS, Planck and eROSITA surveys (for details see Lang-Bardl et al. (2010)).

FOCES: a fiber-coupled high resolution échelle spectrograph for single object spectroscopy. Offering high resolving power over the entire visible spectrum, FOCES will be optimized for stellar astronomy and high resolution spectral line analysis. For a description of the instrument see sec. 2.1.1.

VIRUS-W: an integral field spectrograph equipped by 250 fibers and working at visible wavelengths with medium and low resolution. Since 2010 the instrument is operating at the 2.7m McDonald Telescope in Texas/USA. Its primary scientific focus addresses nearby galaxy kinematics and populations studies (for details see Fabricius et al. (2008)).

SHS: A Shack-Hartmann Sensor used for telescope alignment and seeing tests.

The mechanism to change between the different focal stations is presented in Grupp et al. (2008). Basic data of the scientific instruments are summarized in Table 2.2. To calibrate the spectrographs and as reference source for the SHS, a telescope simulator with different calibration lamps is also mounted on the port. Fig. 2.3 shows the optical layout of the telescope, together with the location of the instruments at the two focal stations.

2.1.1 The Fiber Optic coupled Cassegrain Échelle Spectrograph (FOCES)

The échelle spectrograph FOCES (Pfeiffer et al., 1998) is a fiber-fed bench-mounted échelle spectrograph intended to be operated at the 2.0-m Fraunhofer Telescope at the Wendelstein Observatory. The spectrograph was built in collaboration with MPIA (Heidelberg) and was successfully operated at the Calar Alto 2.2m telescope between 1995 and 2009. After the decommissioning in early 2010 the instrument has been returned to Munich and located at the laboratories of the Munich University Observatory, where it will remain until the telescope is fully commissioned.

One important field of application for this kind of instrument is dedicated to high precision radial velocity measurements, based on Doppler effect, such as the study of extrasolar planets or stellar structural analysis requires. Over these past years the sensitivity of this technique has increased continuously, opening the possibility of exploring the domain of low-mass planets down to a few Earth masses, to discover and characterize multiple planetary systems, to perform surveys to find long period planets, to establish the planetary nature and to characterize the transiting candidates of photometric surveys. Radial velocities projects for exoplanet require high-precision spectrographs and long term stability to detect tiny velocity variations below the meter per second domain. Nowadays the best instruments are designed to recover RV signals with an accuracy better than 10 cm s^{-1}. (see for example the ESO projects of ESPRESSO (Pepe et al., 2010) and CODEX (Pasquini et al., 2010)).

The unique opportunity to use the échelle spectrograph FOCES as test bed for more than two years in Munich has inspired the *Munich Spectrograph Stability Project* (MSSP) that focuses the efforts and expertise of people working on different fields of spectroscopy, spectrograph design and quantum optics to better understand and improve on issues related to high precision and high stability spectroscopy.

MSSP is mainly dedicated to understand three fields of stability problems:

- **Spectrograph stability**: this part focuses on the mechanical stability of the spectrograph as well as the stability with respect to environmental influences such as pressure and temperature changes.

- **Illumination stability**: this field considers the issues arising from non-constant illumination of the spectrograph slit, or - as we concentrate on fiber coupled instruments - of the fiber input. Such non-constant illumination in both angular space and position space arises from natural seeing fluctuations and guiding/tracking inaccuracies of the telescope and severely affects the precision that can be achieved.

- **Fiber stability**: this studies aspects of transport phenomena when light travels through multi mode optical fibers. Fiber modes and focal ratio degradation are two main aspects analyzed.

All these preliminary investigations form the subject of this part of the dissertation and will help in choosing the final configuration of the Fiber Optic Coupled Échelle Spec-

Table 2.3: Comparison between the performance planned for FOCES at Wendelstein and the previous set up.

Calar Alto 2.2m	**Wendelstein** 2.0-m
$1997 - 2010$	$2010-$
$R = 46000/64000$ on $24/15\mu$m CCD	$R = 70000$ on 13.5μm CCD
L-N2 cooled	Peltier cooled
Moving parts (slit, grating, prisms, etc)	No moving parts
Not stabilized	Pressure and Temperature stabilized
$S/N = 100$ for G-star 10^{th} mag: 1h exp	$S/N = 100$ for G-star 10^{th} mag: 1h exp

trograph (FOCES) at the Wendelstein Observatory. The aim is to obtain a competitive high-resolution optical spectrograph able to answer to the requirements of a wide range of topics as search for extra-solar planets, asteroseismological studies and stellar abundances analysis.

2.1.2 Stability goal

According to Grupp et al. (2010), the FOCES stability goal is assumed to recover a radial velocity signal of 1 m s^{-1}. From the Doppler's law:

$$\Delta v = \frac{c}{\lambda}\Delta\lambda \tag{2.1}$$

it is possible to notice immediately the challenging aim of measuring radial velocities to an accuracy level of $\sim$1 m s^{-1}. Assuming a resolving power of a typical Échelle spectrograph of $R = \lambda/\Delta\lambda$ =70000 this corresponds to 1/4300 of a two pixel Nyquist resolution element or $\sqrt{2} \times 1/4300 \approx 1/3000$ of a single pixel. With 13.5 μm pixel size CCD this leads to a linear movement of 45Å. This example easily shows that extensive efforts are required to avoid all source of instability. Indeed crucial points in achieving such high accuracy of the instruments are the spectrograph, the illumination and the coupling stability.

Table 2.3 outlines the main characteristics planned for the FOCES spectrograph when it will be placed at the Wendelstein Observatory with respect to the previous set up at the Calar Alto Observatory.

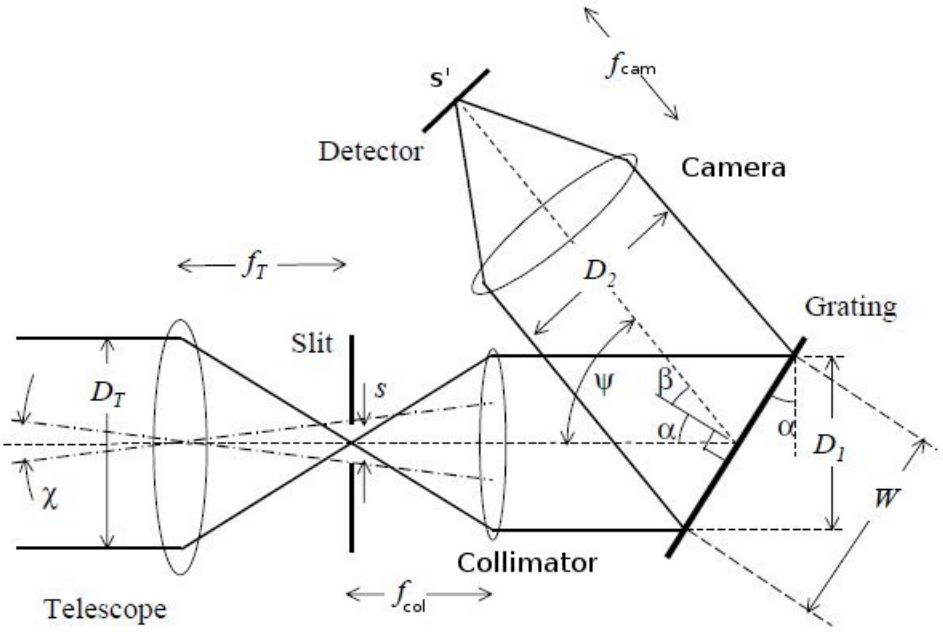

Figure 2.4: Optical layout for a typical spectrograph.

2.2 Basic concepts

In this section the theory and the fundamental spectrograph components of an optical spectrograph are presented. [2] The basic layout of an astronomical spectrograph is shown in Figure 2.4.

It consists of an entrance slit placed at the focus of the telescope, a collimator that intercepts the divergent telescope light and produces a parallel beam, a dispersing element (prism or grating) and a camera that focuses the dispersed light onto a detector. The distance between the slit and the collimator is the focal length of the collimator, f_{col} and the distance between the camera and the focused spectrum is the focal length of the camera, f_{cam}. The diffraction grating is the principal dispersion device for astronomical spectrographs. The most commonly used type is the ruled plane reflection grating with a triangularly-corrugated surface of periodic grooves. Each groove can be seen as a narrow slit, causing diffraction of the incident light. Each monochromatic

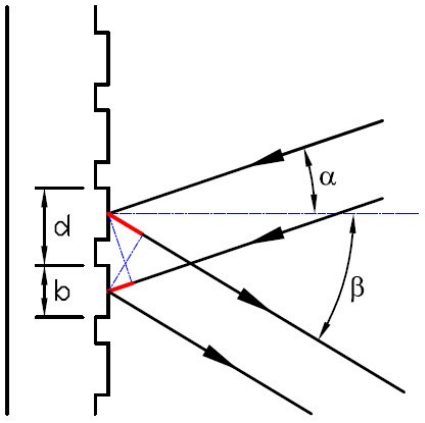

Figure 2.5: Unblazed diffraction grating.

[2] Based on *Diffraction Grating Handbook*, C. Palmer, Thermo RGL;
Dispersive Astronomical Spectroscopy, Jeremy-Allington-Smith;
The Observation and Analysis of Stellar Photospheres, D. F. Gray

beam is diffracted by grooves in a broad range of directions. The usefulness of a grating depends on the fact that there exists a unique set of discrete angles for which the light from each groves is precisely in phase with the light from all other grooves, leading to constructive interference. Each discrete angle corresponds to a different diffraction order of the grating. Fig. 2.5 shows the geometry of grating diffraction, together with the incident beam and the diffracted beam. It can be deduced from this figure that for constructive interference, the optical path difference $d\sin(\alpha) + d\sin(\beta)$ has to be an integer multiple of the wavelength λ, with α the incident angle, β the diffracted angle and d the groove spacing. From this relationship, the grating equation can be derived:

$$m\lambda = d(\sin\alpha \pm \sin\beta) \tag{2.2}$$

where the integer number m is the *diffraction order*. The plus and minus signs are for respectively reflection and transmission gratings. Only the reflection issue is considered in the following part. The case with $m = 0$ coincides with specular reflection, the wavelength are not dispersed and the grating works as a mirror. By differentiating eq. 2.2, the *angular dispersion* of a diffraction grating is obtained:

$$A = \frac{d\beta}{d\lambda} = \frac{m}{d\cos\beta} = \frac{\sin\beta + \sin\alpha}{\lambda\cos\beta} \tag{2.3}$$

and for collimated light the *linear dispersion* is then:

$$\frac{dl}{d\lambda} = \frac{dl}{d\beta}\frac{d\beta}{d\lambda} = f_{cam}A \tag{2.4}$$

where $dl = f_{cam}d\beta$. In the ideal case of diffraction limited imaging, the *spectral resolving power* of a grating $R_0 = \lambda/\delta\lambda$ (where $\delta\lambda$ is the resolution element) is defined by:

$$R_0 = \frac{mW}{d} = mN = \frac{W}{\lambda}(\sin\alpha + \sin\beta) \tag{2.5}$$

where W is the width of the grating and N is the total number of grooves. As it can be seen later, the resolving power of the whole spectrograph is usually much less than the resolving power of the grating itself and in practice is limited by the spectrograph geometry (see sec. 2.2.3).

The particular but common case in which the light is diffracted back toward the direction from which it comes (i.e. $\beta = \alpha = \delta$) is called *Littrow configuration*. It simplifies the grating equation and the relations for the dispersion and resolution to:

$$m\lambda = 2d\sin\delta \tag{2.6}$$

$$A = \frac{d\beta}{d\lambda} = \frac{m}{d\cos\delta} = \frac{2\tan\delta}{\lambda} \tag{2.7}$$

$$R_0 = \frac{2W\sin\delta}{\lambda} = \frac{2D_1\tan\delta}{\lambda}, \tag{2.8}$$

where D_1 is the diameter of the incident beam (see fig. 2.4). In general, the Littrow condition ensures tha maximum grating efficiency (see section below).

For a given pair of α and β, Eq. 2.2 can be satisfied for every wavelength for which m is an integer. This implies that many wavelengths are diffracted in the same direction, leading to the overlapping of the orders. The difference between two wavelengths λ and $\lambda^{'}$ in a given order for which there is no overlapping in an adjacent order, is:

$$\Delta\lambda = \lambda^{'} - \lambda = \frac{\lambda}{m} \tag{2.9}$$

and is called *free spectral range* (FSR). The relation 2.9 descends by imposing the overlapping condition for the wavelengths λ and $\lambda^{'}$ between successive orders, $m\lambda^{'} = (m+1)\lambda$. When m is small and thus FSR is large, filters can be used to rule out the overlapping wavelengths. For large m and short FSR, a different technique called cross-dispersion (see below) is used to separate the overlapping spectral orders.

2.2.1 Efficiency and blazing

The grating efficiency at a given wavelength is defined as the fraction of any monochromatic energy flux incident on the grating that is diffracted into a certain diffraction order. This fraction of flux is determined by the normalized intensity function of the diffracted wave (e.g. Jenkins & White 1976):

$$I(\alpha,\beta) = IF \cdot BF = \left(\frac{\sin(N\frac{\pi d}{\lambda}(\sin\beta+\sin\alpha))}{N\sin(\frac{\pi d}{\lambda}(\sin\beta+\sin\alpha)}\right)^2 \left(\frac{\sin(\frac{\pi b}{\lambda}(\sin\beta+\sin\alpha))}{\frac{\pi b}{\lambda}(\sin\beta+\sin\alpha)}\right)^2 \tag{2.10}$$

where the first term is the interference function (IF), representing the diffraction by successive grooves at spacing d and the second term is the blaze function (BF), describing the diffraction of a single groove, determined by the groove width b. Its effect is to modulate the interference pattern for a single wavelength.

The blaze function has the maximum when $\alpha = (-)\beta$, corresponding to the unusable case of specular reflection (order zero). For practical spectroscopy, the blaze peak of the grating can be shifted at a convenient higher number of diffraction order by tilting each groove with respect to the plane of the grating until specular reflection of each groove facet is obtained, maximizing thus the grating efficiency for that given order (see Fig. 2.6). This is equivalent to move the BF along the abscissa in Fig. 2.7 until the peak coincides with a maximum of the IF in the considered order. In this case BF corresponds with the direction in which the beam would be reflected in the absence of any diffraction. The

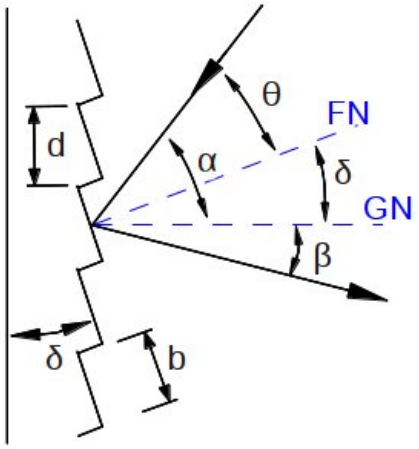

Figure 2.6: Blazed grating. FN: facet normal, GN: grating normal.

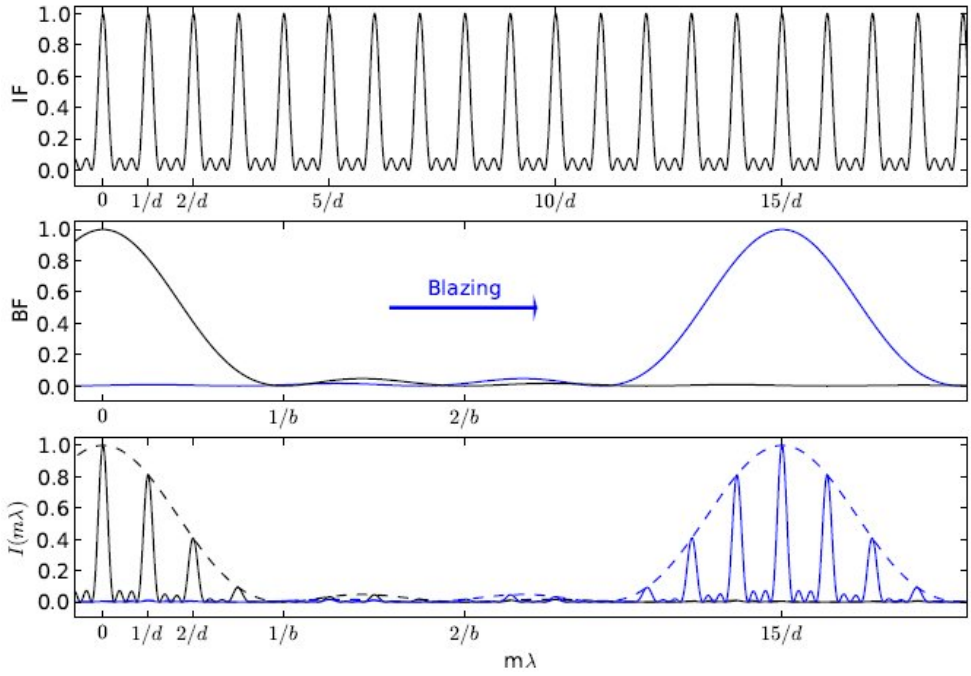

Figure 2.7: Blazing of diffraction grating.

control over the distribution of diffracted energy with wavelength, modifying the shape of the grating grooves is called *blazing*.

From Fig. 2.6, it can be seen that $\theta = \alpha - \delta$ and $r = \delta - \beta$ with the convention that α and β have the same sign if they are on the same side of the grating normal. So the blaze peak condition occurs when $\theta = r$ which is equivalent to $\alpha + \beta = 2\delta$. Making use of the identity $\sin x + \sin y = 2 \sin \frac{x+y}{2} \cos \frac{x-y}{2}$, it is possible to rewrite the grating equation at the blaze condition and obtain the *blaze wavelength* at the blaze peak:

$$\lambda_b = \frac{2d \sin \delta \cos \theta}{m} \tag{2.11}$$

where θ=0 for the Littrow configuration. It is noticed that the efficiency of a grating also depends on the polarization of the incident light. Typical diffraction gratings used in astronomy have an efficiency of $60 - 70\%$ for randomly polarized light at the blaze peak.

2.2.2 Échelle grating

According to Eqs. 2.5 and 2.8, it is possible to obtain a larger resolving power by increasing the angles α and β, or increasing the blaze angle δ of the grating. However, for technical limitations the ruling of very steep gratings is allowed only when the groove spacing is large. This type of gratings is called *échelle* gratings and is used at such a high blaze angle that the steep side of the groove becomes the optically active facet (see Fig. 2.8). Échelle gratings are often characterized by their R-number which indicates the tangent of the blaze angle. The most common type of échelle is probably R2 (δ=63°), while for large instruments, larger blaze angles up to R4 (δ=76°) are becoming quite frequent. Steeper gratings are favored since, at a given width W, they lead to a smaller beam diameter and thus allow a smaller optics. Moreover, for the same W, R_0 is proportional to sinδ (Eq. 2.8) and thus increases with δ. Therefore, Échelle gratings have to work at high spectral order numbers m (Eq.2.5), but their free spectral range is very small (Eq. 2.9) and many different orders lie on top of each other on the detector. One solution to this problem is to introduce a secondary disperser element, called *cross disperser*, to separate the overlapping orders. The cross disperser works to the direction perpendicular of the échelle dispersion with a much smaller angular dispersion. For current square or rectangular optical detectors, the resulting two-dimensional (2D) format of the double-dispersion spectrum is very useful (see Fig. 2.9). It allows to record a large number of orders, and thus a broad spectral range, with high resolution sampling on a 2D detector. The cross-dispersed échelle spectrograph have become standard instrument for astronomical high resolution optical spectroscopy.

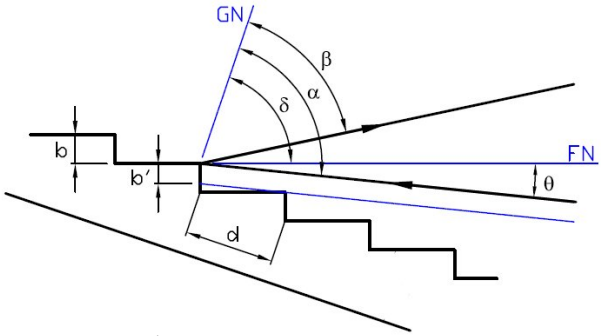

Figure 2.8: Échelle diffraction grating geometry.

Échelles generally operate close to the Littrow mode ($\theta \approx 0$) to avoid shadowing effects by previous facets, diminishing the effective groove width from b to b' (see Fig. 2.8). The net effect of moving away from the Littrow configuration is a decreasing efficiency and for high blaze angles, above 63°, this issue is particularly significant that this mode becomes mandatory.

2.2.3 Slit spectrographs and resolution

The performance of a real astronomical spectrograph in term of spectral resolution depends not only on the resolving power of the dispersing element but also on a series of different issues such as the dimensions and locations of the entrance slit, the aberrations and the magnification of the images and the pixel size of the detector.

For a high-resolution spectrograph, an entrance slit fixes the size of the spectral source and makes it constant. Spectrograph slits are usually given by their on-sky aperture, which is

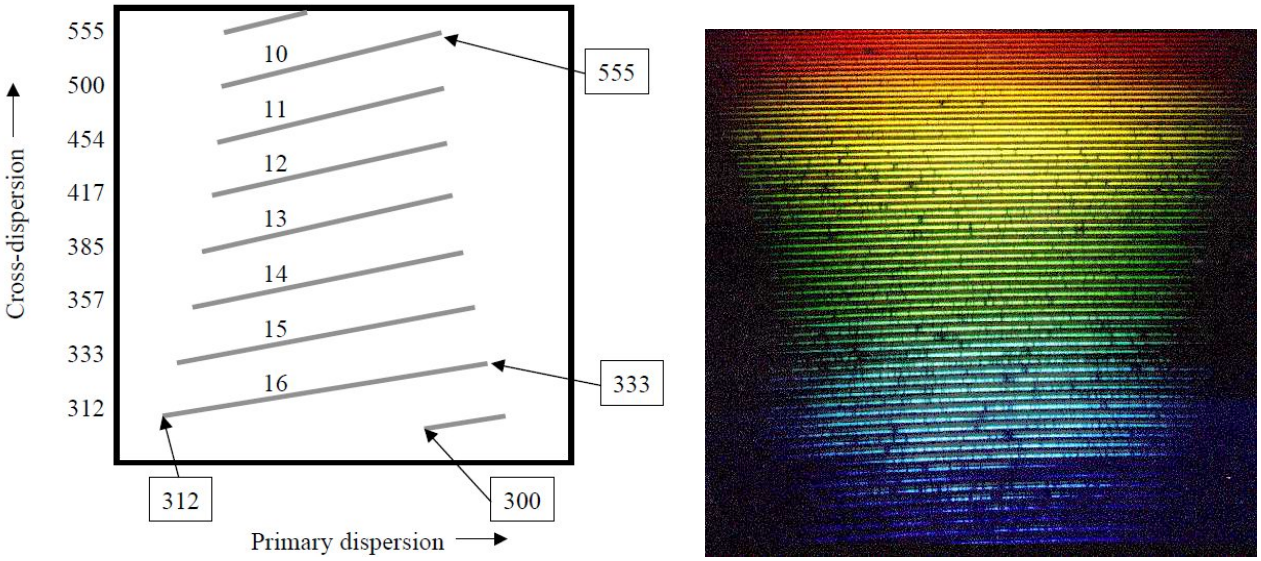

Figure 2.9: Left: Simplified layout on the detector of a cross-dispersed spectrogram. The numbers 10-16 label the different spectral orders. The numbers, that label the vertical axis, are the wavelength (nm) at the lowest end of each complete order. For simplicity the orders are shown evenly spaced in cross-dispersion.
Right: Real échelle spectrum of the Sun from the FOCES spectrograph.

related to their physical size by $\chi = s/f_{tel}$ where f_{tel} is the focal length of the telescope and s is the size of the slit (in mm). However, if the size of the object is smaller than the slit, than the appropriate size is the dimensions of the object. If the object is larger than the slit, light will be lost. This is where seeing can play an important role in spectroscopic observations.
The slit suffers from two types of magnification: spatial and spectral. So at the end, the image of the slit width projected on the detector is given by:

$$s^{'} = rs\frac{f_{cam}}{f_{col}} = r\chi f_{tel}\frac{f_{cam}}{f_{col}} \tag{2.12}$$

where f_{col} and f_{cam} are the focal lengths of the collimator and the camera, the ratio $\frac{f_{cam}}{f_{col}}$ represents the *spatial de-magnification* and r, the *anamorphic magnification* defined by:

$$r = \frac{D_1}{D^2} = \frac{\cos\alpha}{\cos\beta} \tag{2.13}$$

Fig. 2.4 shows that the beam diameter D_1, seen as aperture of the camera, increases due to the dispersion angle, to D_2. The magnification of the spectrograph changes accordingly in dispersion direction. In the direction along the slit, the beam diameter and the magnification remain constant. The resolution limit of the spectrograph is defined as the wavelength

difference $\Delta\lambda$ for which the separation between the images of two wavelengths λ and $\lambda + \Delta\lambda$ equals the width of the slit images $s^{'}$. Nothing smaller than the slit image on the detector can be resolved. Using the definition of *linear dispersion* in eq. 2.4, the resolution element (or the width of slit image) can be expressed in term of wavelength units: $\Delta\lambda = s^{'}\delta\lambda/\delta l$. When combining this with Eq. 2.12, the spectral resolution is defined as:

$$R = \frac{\lambda}{\Delta\lambda} = \frac{\lambda A f_{col}}{rs} = \frac{\lambda A}{r\chi}\frac{D_1}{D_T} \tag{2.14}$$

where D_T is the aperture of the telescope. For a grating spectrograph, this results in:

$$R = \frac{m\lambda}{d\cos\beta}\frac{D_1}{r\chi D_T} = \frac{W(\sin\beta + \sin\alpha)}{\chi D_T} \tag{2.15}$$

and simplified for the Littrow configuration ($r = 1$, $\alpha = \beta = \delta$):

$$R = \frac{2D_1\tan\delta}{\chi D_T} \tag{2.16}$$

Note that the resolution R obtained with a finite slit width is always less than the theoretical maximum which may be obtained with a infinitely narrow slit.

Finally one more issue that should be considered especially in the design phase of a spectrograph is the sampling of the spectra. The smallest resolution element for the spectrograph should be sampled at the minimum of the Nyquist Frequency, which corresponds to 2 pixels per resolution element. Therefore the detector pixel size becomes a limiting factor of the resolution.

Previously it has been shown that a good solution for a high-resolution spectrograph covering a wide spectral range is based on an échelle diffraction grating in combination with a cross disperser. In the next section, introducing the échelle spectrograph FOCES, an example how such an instrument can be configured efficiently is presented.

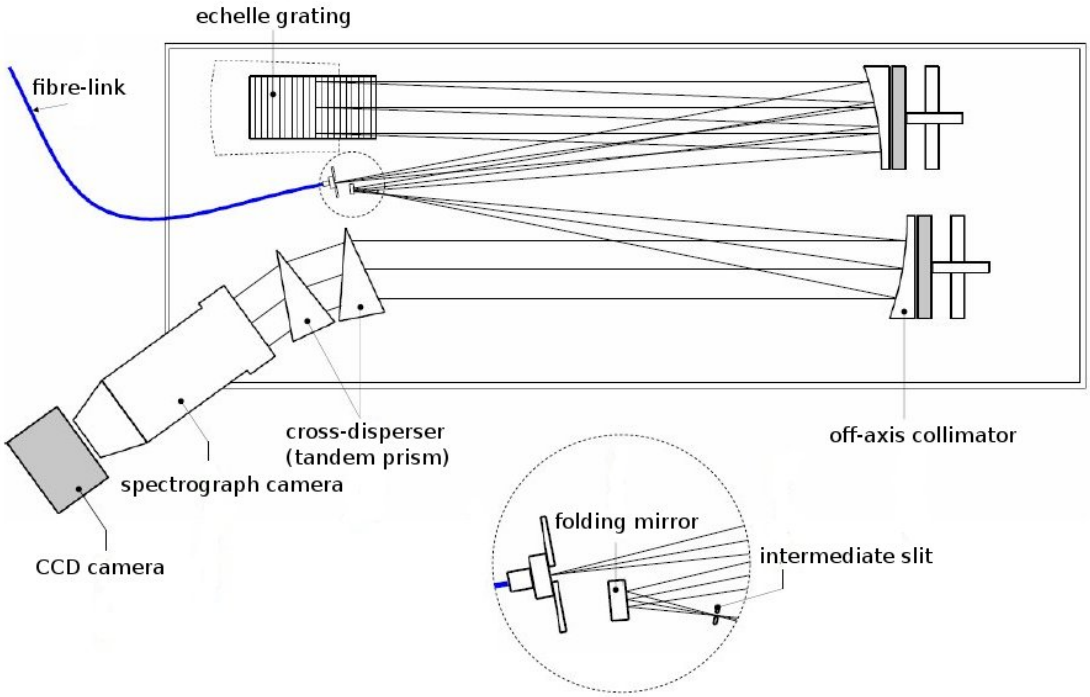

Figure 2.10: Optical design of the FOCES spectrograph (Pfeiffer et al., 1998).

2.3 FOCES optical design and working principle

Since the FOCES cross-dispersed échelle spectrograph is back to Munich, a successive refurbishing was done by replacing the old Tektronix CCD-detector and improving a few crucial subsystems to guarantee best possible opto-mechanical stability (cfr. sec. 2.4).
In this section we summarize the optical design, including the global layout of the spectrograph adopted during the series of tests at the laboratories of Munich University Observatory. We refer to Pfeiffer et al. (1998) for a more detailed description of the instrument configuration.

Figure 2.10 shows the actual optical layout of FOCES. Following the light path from the fiber entrance at the telescope focal plane to the CCD detector plane, the starlight first passes through an exchangeable circular diaphragm that defines the input light cone. A microlens placed in front of the fiber entrance converts the telescope beam into a much faster beam (e.g. f/3.5) in order to fulfill the requirement of the low focal ratio degradation. The starlight is then guided through an optical fiber over a distance of approximately 20 m. The fiber exit is with respect to its optical parameters quite similar to the fiber head. A microlens glued to the fiber exit converts the fast beam, which propagates the fiber, into a much slower beam (f/10) that fits the instrument design. The emerging light cone is then collimated through an off-axis parabolic mirror segment toward a 31.6 lines/mm

R2 échelle grating. Its ruled area is 34 mm over-filled by the 15 cm diameter beam. As clear in fig. 2.10, the spectrograph works in a so called near-Littrow mode (cfr. Schroeder, 1987), a configuration where incident beam and diffracted beam are nearly parallel oriented with respect to each other in order to double pass the collimating element and increase the efficiency of the échelle grating. According to the *white pupil* design (Baranne, 1988), after the échelle grating, the beam is re-imaged at a intermediate focus just behind a small folding mirror. This ensures two main advantages. First, the spectrum can be effectively cleaned from scattered light produced at the échelle grating and other surfaces by inserting a slit mask at the intermediate focus. As far the second one, the beam size at the cross-disperser element will be not much larger than that one leaving the échelle grating. A second off-axis parabolic mirror segment collimates the light towards a cross-dispersing tandem prism, that separates the overlapped diffraction orders perpendicular to the principal dispersion direction. The prisms are made of LF5 with a basis length of 160 mm, a width of 112.6 mm and a prism angle of 33°. The strong cross-dispersion required implies the tandem prism arrangement to avoid problems with the total reflexion that would occur on a single prism angle of 55°. After passing both prisms the light enters a transmission camera that finally images the two-dimensional échelle spectrum onto a 2K×2K CCD-detector.

The main FOCES instrument parameters are:

Resolving power: $R = 70000$

Spectral coverage: $\lambda = 3800\text{Å} \cdots 9000\text{Å}$. Orders overlap up to 7600Å.

Fiber link: Original 100μm silica-silica step index multi mode optical fiber, used in Calar Alto to connect telescope and spectrograph. Light is coupled to and from the fiber using Fabry micro lenses glued to the fiber surface.

CCD-detector: New AndorSystem 2048×2048, 13.5 μm pixel size. Maximum cooling $-100°$ C. External thermoelectric chiller (Oasis 160-Solid State) set to 18° C.

Collimator: 1524 mm (f/10), parabolic off-axis mirror.

Échelle-grating: 165×320×50 mm, blaze angle 65°, 31.6 lines/mm(R2).

Cross-disperser prism: 190×160×112.6 mm, deflection angle 33°.

Camera optics: 455 mm (f/3)

2.3.1 Current Optical Fiber link

In the last decades the use of optical fibers to connect the focus of the telescope to the spectrograph placed far away in an isolated environment has became very important. This configuration causes some transmission loss and requires additional optics to inject the telescope beam efficiently into the fiber, but it offers some clear advantages, mostly related to instrument stability:

- The optical fibers decouple the instrument from the movement of the telescope, completely avoiding gravitational flexure and mechanical vibration.
- It is possible to place the instrument in an isolated and controlled thermal chamber, protecting it from environmental changes (atmospheric pressure, temperature and relative humidity) in the telescope dome.
- Modern fibers guarantee very high transmission efficiency over a wide wavelength domain.
- The fibers property of scrambling the image at the fiber entrance reduces the effect of seeing and guiding fluctuations at input of the spectrograph.

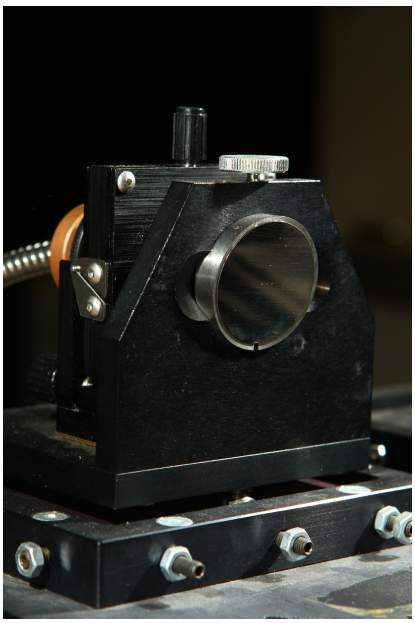

Figure 2.11: Small tilted mirror before the fiber head.

The spectrograph FOCES will be located few meters below the telescope dome in a dedicated room of the Wendelstein Observatory. To cover the distance between the telescope focal plane and the instrument, a minimum fiber length of ≈ 20 m is required. For the tests in the Munich laboratories the spectrograph has preserved the original fiber configuration present at the Calar Alto Observatory. It is in fact currently equipped with a standard step-index multi-mode circular fiber from Polymicro Technologies, with 100μm core diameter. To avoid strain and stresses, the fiber is wrapped in a smoothly teflon mantle, and then in a steel spiral. Light enters through a circular diaphragm in a small tilted mirror just before arriving to the fiber head. (see fig. 2.11). Three such entrance apertures could be originally exchanged with corresponding different input light cone and resolution (see Pfeiffer et al., 1998). The overall fiber-link consists of two important units called *fiber head* and *fiber exit*. Both units are equipped with a plan-convex lens that converts a slow beam into a fast beam and vice versa. Fig. 2.12 shows the imaging principle of

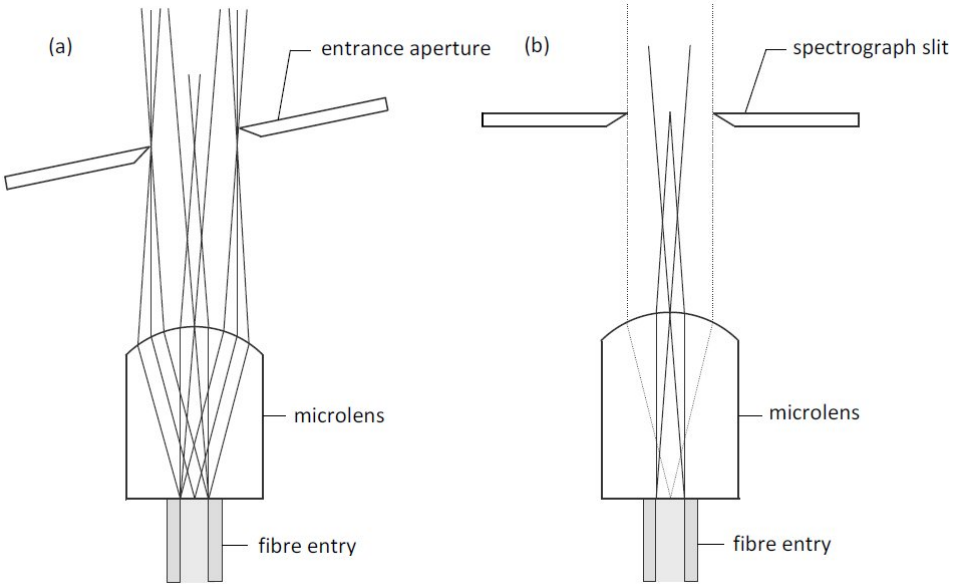

Figure 2.12: FOCES fiber head (a) and fiber exit (b) optics (Pfeiffer et al., 1998).

the fiber head and fiber exit in more detail. The telescope images the star on the surface of the tilted mirror and not directly on the fiber entrance. The fiber head is used to imaging the telescope pupil onto the real fiber input. The fiber exit instead produces a scrambled image of the entrance aperture exactly at the entrance slit of the spectrograph. The effective fiber entrance beam speed is of the order of f/3.5 to maximize the light throughput and minimize losses due to focal ratio degradation (FRD). Apart from that, such lenses also help to scramble the light on both fiber-ends by exchanging far-field and near-field light distribution (Pfeiffer et al., 1998), where near-field and far-field are respectively defined as the brightness distribution across the output face of the fiber, and as the angular distribution of the light of fiber output beam.

2.4 Mechanical Stability

Mechanical stability is guaranteed by an optical bench, where FOCES is mounted, made of ferromagnetic stainless steel with a weight of ≈300 kg. Its mechanical properties are optimized for frequencies below 50 Hz to compensate for small perturbations, while resonances near 140 Hz and higher are damped pneumatically using a system of shock absorbers to mount the bench on. As mentioned before, since the spectrograph is under lab conditions, a series of mechanical renovations have been done to improve the opto-mechanical stability. The old 1024×1024 Tektronix CCD-detector with 24 μm pixel size has been replaced by a new AndorSystem 2048×2048, with 13.5 μm pixel size. The new camera is equipped also by an external water-cooling system (Oasis 160-Solid State) with temperature set-point of 18° C. Movable and remote controlled components including the adjustable slit, grating mount and prism cross disperser were either changed or fixed permanently. A new shutter has been placed in the optical path between the second slit and the second collimator. The grism pair used to reinforce the cross dispersion in order to provide enough spacing between the diffracted orders was permanently removed. Only a focusing mechanism that enables fine adjustments of the camera optics with respect to the CCD-detector is still working. The internal heat from motors is kept negligibly small, by switching off all the active electronic components just after their utilization.

2.5 Pressure and Temperature Stability

Beside the mechanical stability, *environmental stability* is one key issue to make the spectrograph particularly useful for radial velocities work. Temperature and atmospheric pressure changes, together with relative humidity fluctuations have important direct effects on the spectrograph performance. These effects can be divided in three categories:

- Thermal expansion modifies the dimensions of the optical elements and also the relative position of the optical elements in the spectrograph.
- The refractive indices of the optical glasses change with temperature, having influence on all refractive elements (lenses and prisms).
- Air pressure perturbations and relative humidity fluctuations result in changed refractive processes on air-glass-air surfaces.

A first effect of changing environmental conditions is that the image quality of the disturbed optical system will degrade. As a first approximation, the result is a slightly defocused instrument and a decreased spectral resolution. Secondly, those perturbations can also cause the position of the spectrum on the detector to change. For accurate radial velocity measurements, this position should be as stable as possible. A signal that comes from the observed star can not be qualified anymore if these shifts are in the order of the Doppler precision required to detect a planet. The obvious method to avoid problems with changing

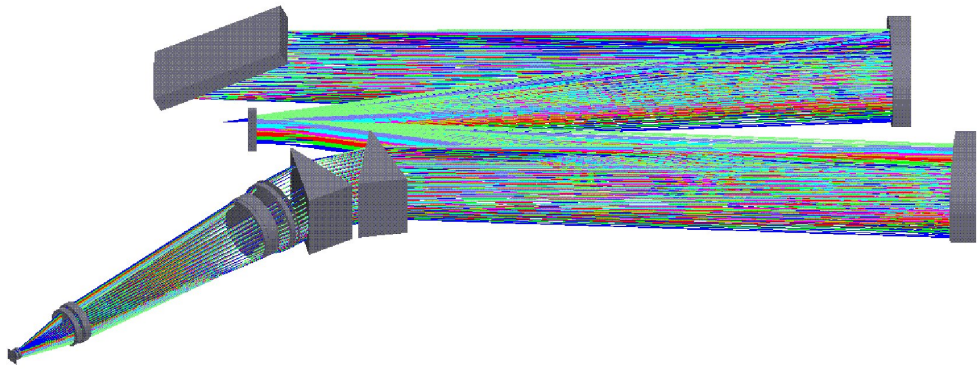

Figure 2.13: 3D model of the FOCES spectrograph. Courtesy of Frank Grupp. First surface modeled is the entrance slit, the fiber exit and the micro lens system are not taken in account. The last surface is the CCD plane.

environmental parameters is an intrinsically stable environment. Two concepts have been employed until nowadays:

- Housing the whole spectrograph (or part of it) into a vacuum chamber. This guarantees pressure stability and it makes thermal stabilization easily by preventing gas convection and conduction. The spectrograph HARPS (Mayor et al., 2003) at the ESO 3.6-m (La Silla) follows this approach.
- Setting the spectrograph in several shells of thermal and pressure stabilized "boxes", insulating it and pressurizing it. The PEPSI spectrograph (Strassmeier et al., 2008) is one example for this approach.

The second option has been chosen as the basis of the FOCES configuration, since it allows for easier maintenance and access to the spectrograph. It also avoids the use of vacuum proof materials and can be regarded as a good solution to upgrade existing instruments at relatively moderate cost.

2.5.1 Simulations and stability goal

A ZEMAX ray-tracing model of the FOCES spectrograph (see Fig. 2.13) developed by F.Grupp (Grupp et al., 2010) is used to explore the influence of temperature and pressure changes on the position of the spot centroid in the focal plane of the spectrograph. This gives the possibility to find reasonable estimates for the level of stabilization needed for accurate RV spectroscopy and provides useful theoretical results that can be compared with the real measurements.

18 spots in 6 diffractive orders from 3800 Å up to 8700 Å have been modeled to cover the CCD area of 2K×2K pixels with size of 13.5 μm (see Fig. 2.14). The centroid positions are evaluated for all 18 wavelengths for different pressure and temperature values (see

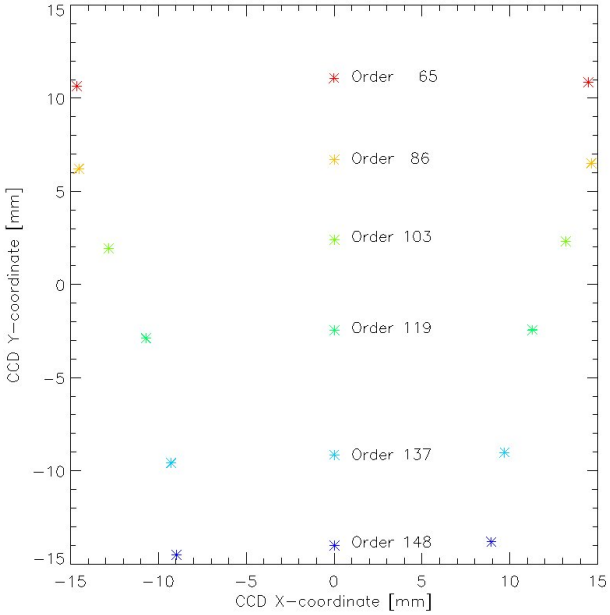

Figure 2.14: Configuration of the spots modeled: one spot at the center and two respectively at the limit of the overlapping area for each order are considered. From top to bottom the center wavelengths of the orders are: 8743 Å, 6608 Å, 5518Å, 4777 Å, 4148 Å, and 3840Å.

Table 2.4: Pressure and temperature variations modeled

Variable	Base value	Variations
Pressure	$800hPa$	±0.1hPa, ±0.2hPa, ±0.5hPa,±1.0hPa, ±10.0hPa
Temperature	20° C	±0.01° C, ±0.02° C, ±0.05° C, ±0.1° C, ±1.0° C

Tab. 2.4). The resulting spot center changes for both pressure and temperature variations are shown in fig. 2.15. It can be noted that the main movement of the a spot center is along the cross order direction (y-axes) for both pressure and temperature variations. For a pressure change of max ±10hPa the y-movements are around ±0.2pixels all over the CCD surface. Movements along the main dispersion direction (x-axes) are about 1.5 order of magnitude smaller and depend on the position on the CCD. For a temperature variation of max ±1° C, a spot center movement of around ±0.2pixels is found with strong dependence on the position on the detector surface. Again the movement along the main dispersion direction (x-axes) is smaller (by a factor 0.4) than in cross order direction.

From this analysis and according to the considerations presented in sec. 2.1.2, *it is necessary to ensure an environmental stability of better than 0.1K in temperature and better than 0.8 hPa in pressure to do RV spectroscopy in the m/s region.*
This corresponds to a maximum allowed x-movement (parallel to the main dispersion direction) of $\sqrt{2}$x1/3000≈1/2000 pixels, and a maximum y-movement (parallel to the cross-dispersion direction) of ≈1/30 pixels of the spot on the CCD plane. A gain of $1/\sqrt{2}$ is

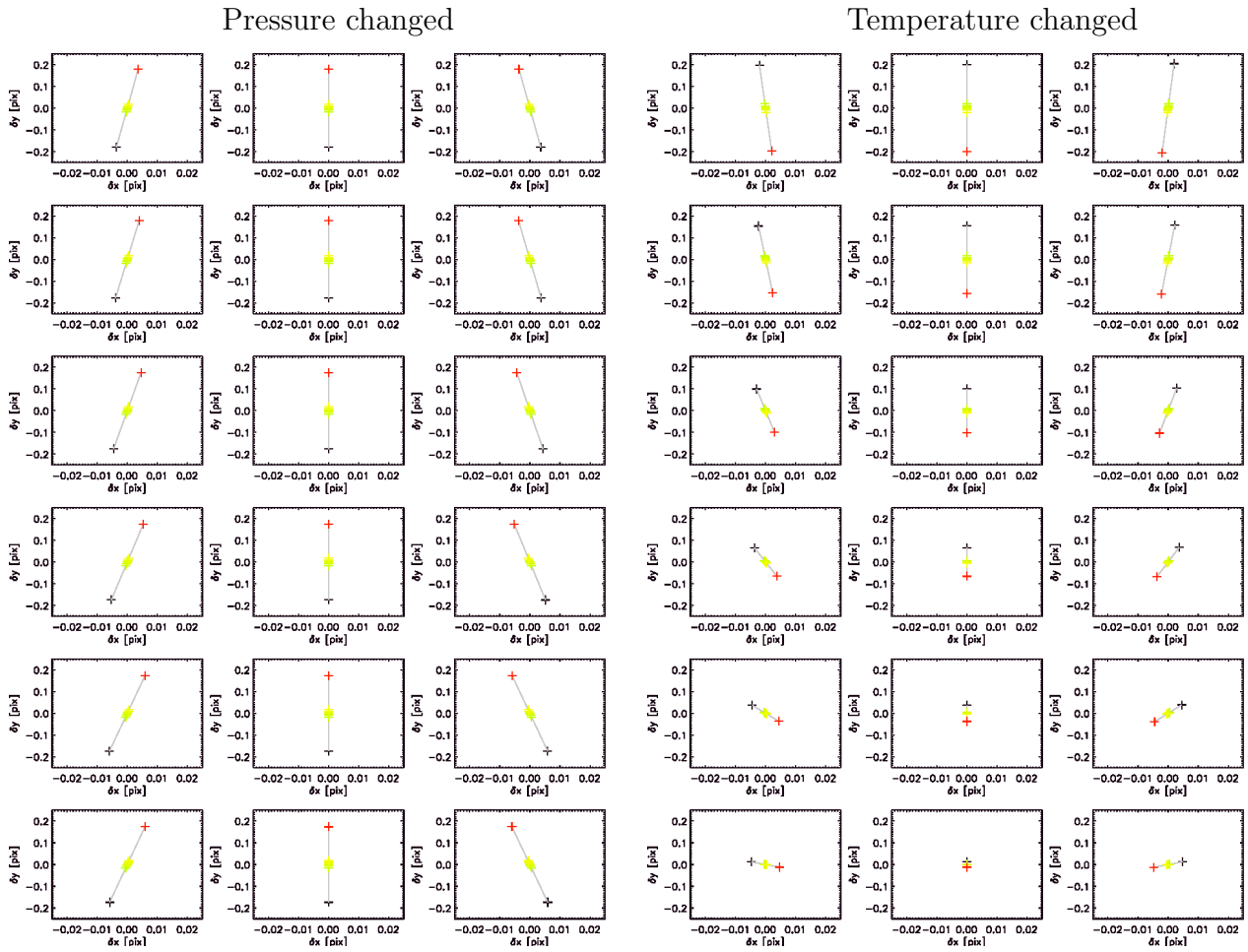

Figure 2.15: Total change corresponding to the 18 modeled spot centers when pressure (left) is varied by max $\pm 10 hPa$ and temperature (right) is varied by max $\pm 1°$. The scale of both plots is pixels. The x-axes is parallel to the main dispersion direction of the grating, the y-axes is parallel to the dispersion direction of the cross disperser prisms.

considered in x-direction due to the anti-symmetric behavior of the centroid movement with respect to central position for changes of pressure and temperature (see Fig. 2.15).

Figure 2.16: FOCES at the end of January 2010.

2.5.2 The "box in box" system

The MSSP started when FOCES was moved and re-assembled at the Munich laboratories at the end of January 2010 (see Fig. 2.16). After a pre-studies (see sec. 2.5.1) and costs evaluation phase, it was decided to place the spectrograph in two shells of thermal and pressure stabilized "boxes", following the PEPSI spectrograph (Strassmeier et al., 2008) approach.
The inner box surrounds the actual spectrograph optics and is equipped of 11 heating mats of a total 50 W power, covering the side walls and the ceiling.

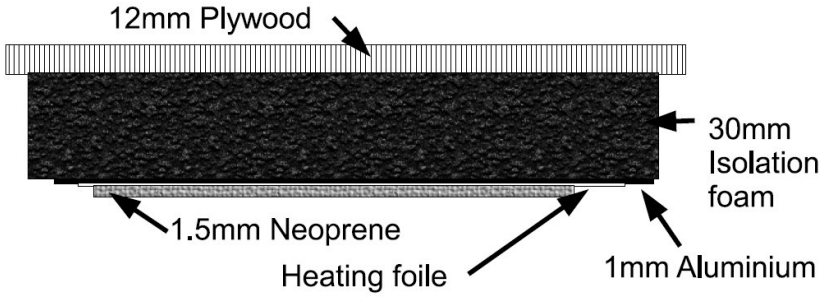

Figure 2.17: The five heating and isolation layers of the FOCES inner box.

In order to avoid thermal radiation from the hotter parts of the foils and to equally distribute the heat over a larger area the isolation and heating of the inner box consists of the five layers schematically shown in Fig. 2.17.

The outer larger box was commissioned and built directly in situ in collaboration with the workshop of the Observatory. This serves as pressure stabilization box and holds the outer volume heating system with 36 heating foils offering a total power of 900 W. This outer box consists of a wooden construction of 2.5×2.1×3.5m reinforced by an aluminum exo-skeleton. The dimensions were selected to guarantee accessibility to the spectrograph and to avoid any possibility of thermal convection inside. The thickness and the numbers

Figure 2.18: The open FOCES pressure box.

of the bars allow a maximum movement of 3 mm of the wooden structure under effect of the over pressure. The internal surface is totally covered by several layers of a special paint and one thick plastic foil to keep the box very tight and isolated. As further measure to avoid air leakages, all the edges of the external box are filled by silicon gel.

One of the box faces is removable and constitutes the only access to the inner part (see fig. 2.18).
The maximum overpressure that it is possible to reach inside the total system is ≈25 hPa and a security pressure valve ensures the safety of the environment preventing this threshold is exceeded.

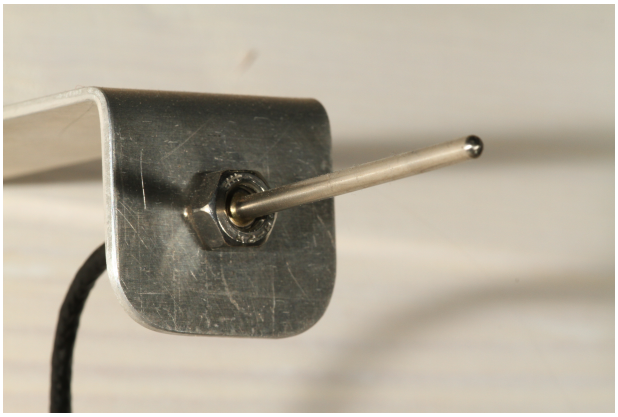

Figure 2.19: Temperature sensor.

Temperature is stabilized actively by the two heating layers in the "box in box" system. Four precise PT100 (Class AA/10) sensors record the outside and the inside temperature. They are positioned in the air volume of the inner box, in the grating holding aluminum structure, in the air volume of the outer box and in the air of surrounding laboratory respectively. A PTC10 temperature controller from Stanford Research Systems with a read noise of ∼2mK for PT100 thermometers is used to control the output to the spectrographs heating. The temperature of the surrounding room is controlled by a normal air conditioning system set to 20.0° C.

Pressure in the outer (and therefore inner) box is actively stabilized by means of a flow controller with a range of $0 \cdots 44$l/min, blowing clean, oil free and dry air into the box through a diffuser preventing strong turbulences and working against a small leakage rate. P is measured by two precision barometers, one controlling the PID loop of pressure control,

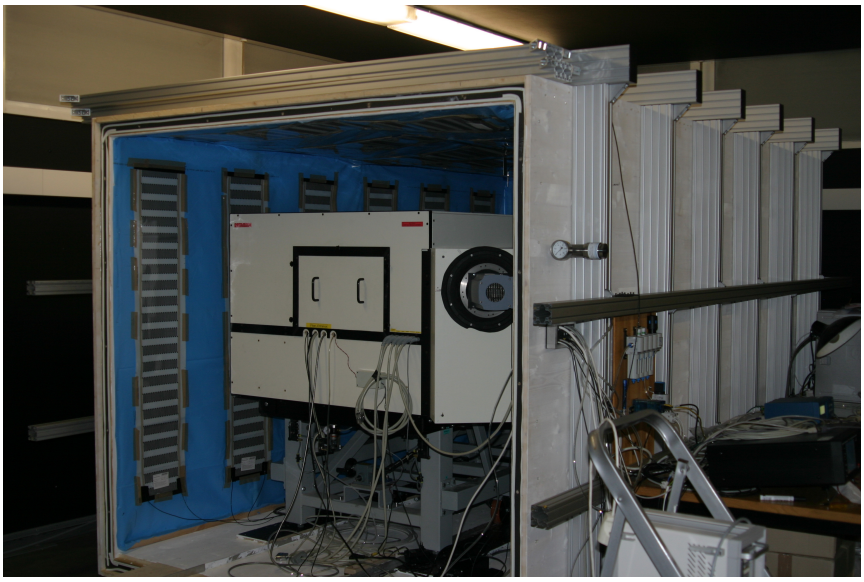

Figure 2.20: FOCES inside the pressure box, door still open. On the left the outer heating system is visible.

the other displaying the pressure for monitoring. The laboratory pressure is measured by a simple Internet Protocol (IP) Weather Station.

Fig. 2.20 shows the main structural components of the stabilization system.

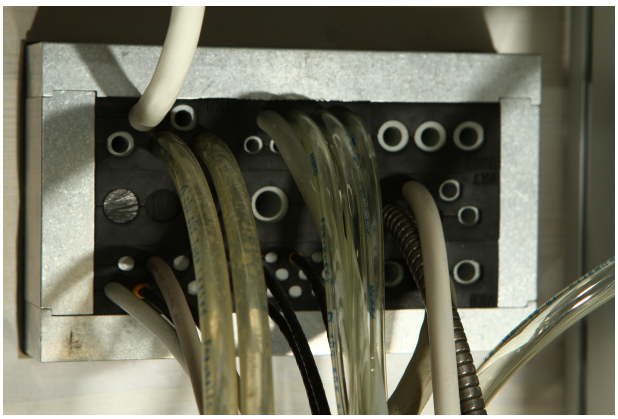

Figure 2.21: Cables connection.

The outer box with its exo-skeleton maintains the pressure and also holds the outer volume heating system. The inner light tight and also isolated (white) box surrounds the optical bench and holds the inner heating system.

A small section in the wooden wall filled by special soft material allows the cables connection between inside and outside the external box without air losses (see fig. 2.21).

In the next chapter all the results of the tests to verify temperature and pressure stability of the system here introduced will be presented.

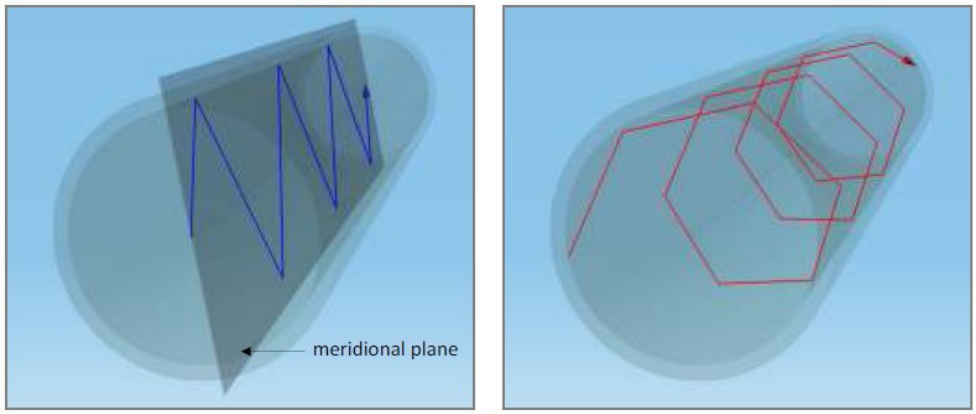

Figure 2.22: Illustration of meridional rays (left) and skewed rays (right) propagation in a circular core fiber.

2.6 Illumination and Fiber stability

Optical fibers are used to lead the light from the telescope to the entrance of the spectrograph. They have great flexibility and useful properties explained in the introduction. However, they are affected by one important issue: they are not perfect light transmitters. To better understand how light can be efficiently transported between the telescope and the instrument, an introduction into the fundamental principles of light propagation through an optical fiber is given in the Appendix A. Here only some fundamental aspects are summarized. Optical fibers consist of several layers of material with different refractive index that enable total internal reflection (TIR). Light propagation inside optical fibers generally can be described by two principal theories. The first one, called *Ray Theory*, describes light behavior in fibers using an optical ray model, based on geometrical optics. According to this theory, light can propagate into fibers following meridional or skewed trajectories. Meridional rays travel on a plane crossing the axis of the optical fiber, instead skew rays propagate in a more helical shaped without passing through the fiber axis (see fig. 2.22). The second theory, called *Mode Theory*, uses the electromagnetic wave behavior to describe the light propagation along the fiber. The light beam inside the fiber corresponds to a superposition of a set of guided electromagnetic waves called *modes* that interfere with each other at the fiber end to cause the speckle type pattern well observed when using highly temporally coherent light (see fig. 2.23). Standard fibers used in astronomy with 2-8 m class telescopes are step index optical fibers with diameters of $50 - 300\,\mu$m and usually can carry many modes. The number of modes in a thick step index fiber is described by the equation (Grupp et al., 2010):

$$M = 2\left(\frac{\pi r}{\lambda}\right)^2 \sin^2\left(\arctan\left(1/2f_{\#}\right)\right) \tag{2.17}$$

where r is the fiber radius, λ is the wavelength of the light coupled to the fiber and $f_{\#}$ the coupling f-number. When the fiber is moved with the telescope or something changes

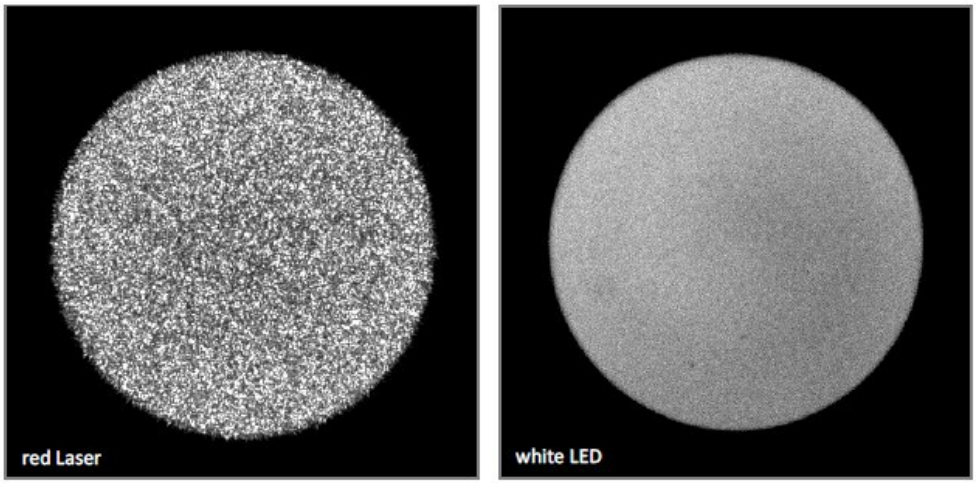

Figure 2.23: Light distribution at the fiber end using a laser source and a broad band source illumination such as a white LED.

in the fiber input illumination, this speckled patter is modified leading to a significant impact on the spectrograph throughput, called *modal noise* (see Grupp, 2003; Corbett & Allington-Smith, 2006) and influencing the stability of the spot at the detector plane (see Avila & Singh, 2008). During an observation in fact, guiding/tracking inaccuracies and the fluctuations introduced by turbulence atmosphere (seeing) produce variable illumination of the fiber entrance. Optical fibers in general scramble the light well in axial direction but less distinctive in radial direction: the position information of the telescope spot on the fiber entrance partially remains and is transferred to the fiber output and therefore to the spectrograph entrance slit. Due to the movement of the input spot on the fiber surface, the light distribution changes in both near-field and far-field. As a consequence, the Point Spread Function (PSF) on the CCD-detector of the spectrograph may shift in spectral direction and limits therefore the current RV precision. Incomplete photometrical scrambling is present in all fibers that carry more than one mode and in terms of existing and future high-resolution instruments still needs careful investigations. In order to reach the desired precision, all errors should be kept as small as possible. Beside the impossibility to use in astronomical cases single mode fibers which have core diameters less than $10\,\mu$m, this can be done using optical and mechanical scramblers. Optical scramblers basically exchange near-field and far-field, whereas mechanical scramblers continuously shake, vibrate or bend the fiber. This results either in a significant amount of light loss or high focal ratio degradation (FRD). Down to the present there are no scramblers available that can have both issues under control. However several vendors introduced new fibers with non-circular shaped profile and scrambling measurements, carried out by different groups (Chazelas et al., 2010; Avila et al., 2006; Avila & Singh, 2008; Avila, 2012; Perruchot et al., 2011) using such fibers with square and octagonal core geometry, have confirmed their outstanding performance. This gives hope to replace old techniques with single or combined fibers purely made by non-circular fiber sections.

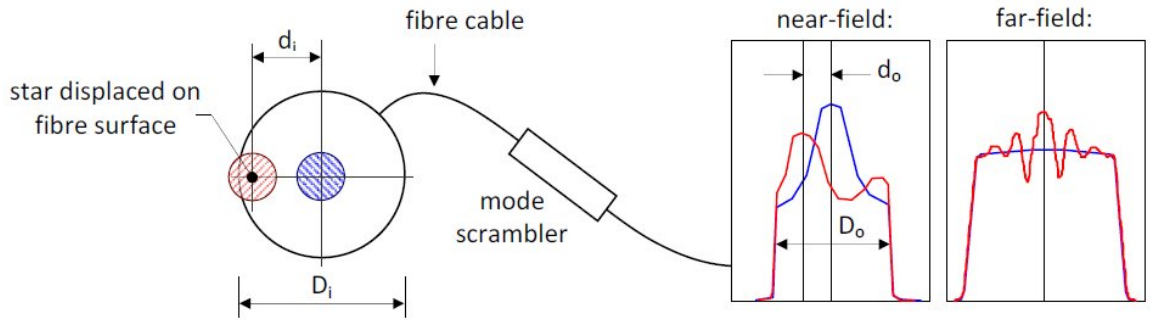

Figure 2.24: Effect of the entrance spot displacement in near-field and far-field. Adapted from Avila & Singh (2008).

Photemetrical scrambling

Power exchange in multi-mode fibers among modes is mainly governed by scrambling. Insufficient scrambling results in less power exchange and therefore residual position information remains. Fig. 2.24 shows schematically how the photometrical light distribution behaves for centered (blue) and displaced (red) entrance spots. Horizontal shifts of the telescope focal spot lead to significant changes at the fiber output. The relation between the relative displacement of the telescope spot across the fiber entrance $\Delta\phi_{fiber}$ and the relative displacement of the intensity barycenter measured in near-field with respect to the fiber core diameter ΔPSF, is called *Scrambling Gain*. Scrambling gain was introduced by Avila et al. (2006) and can be mathematically expressed by:

$$G = \frac{\Delta\phi_{fiber}}{\Delta PSF} = \frac{d_i/D_i}{d_0/D_0} \tag{2.18}$$

where d_i is the position of the entrance spot in units of the fiber input D_i and d_0 the position of the barycenter of the output intensity in units of the output diameter D_0. The barycenter displacement is computed regarding to the center image (i.e. nominal spot position). In order to qualitatively compare different measurements among themselves it was helpful to normalize the barycenter displacement. This results in very small numbers and it has been applied in previous literature to express this ratio in one-thousandth ($d/1000$) of the core diameter (Chazelas et al., 2010; Avila et al., 2006; Avila & Singh, 2008).

Focusing on the fiber-fed spectrograph FOCES, the current fiber-link does not provide sufficient good photometrical scrambling and a new fiber with better scrambling performance and eventually lower FRD is currently under investigation. The preliminary test of different fibers from several vendors will be presented in the next chapter.

Chapter 3

Stability Test: performance and first results

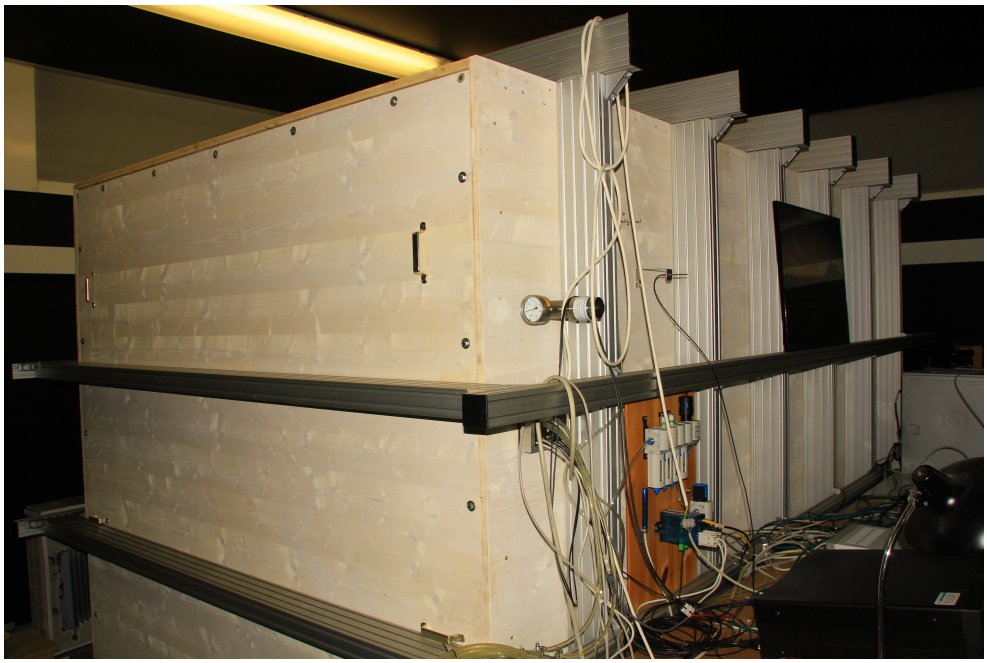

Figure 3.1: FOCES Pressure Box

In this chapter all the measurements of the spectrograph stability performance are described and discussed. The first part presents the test to verify the temperature and pressure stability of the "box in box" system. These measurements were done in several steps:

- Verification of the temperature stability only in the inner box.
- Verification of the temperature and pressure stability of the total system.
- Evaluation of the influence of changes in temperature and pressure on the stability of the system.
- Evaluation of the influence of changes in CCD temperature on the stability of the system.

The second part of the chapter manly deals with the characterization of an apparatus used to measure photometric scrambling simultaneously in near-field and far-field and then, with the scrambling measurements of circular and non-circular fibers by simulating seeing fluctuations and telescope beam defocusing that typically occur during an observation. Finally, different fiber sections were combined and proved on their capability as the next generation of mode scramblers and eventually as a potential solution for the new FOCES fiber-link at the Wendelstein Observatory. This part was done in collaboration with two master students and in this document only a summary of the work done is reported.

3.1 FOCES Inner Box Test

The first tests have been carried out using only the control system of FOCES and the inner shell heating, while the outer temperature was controlled by a normal lab air-conditioning system. Two pt100 class AA 1/10 temperature sensors in four wire configuration were recording the outside and inside temperature. The PTC10 temperature controller has been utilized to regulate the 50V/1A output for the spectrographs heating. It is important to note that the aim is to reach high long and short term relative stability, therefore absolute temperature values are of minor interest for these applications.

3.1.1 Test with alternating room temperature

For this measurement the set-point of the spectrograph inner temperature was fixed to 20.300° C. Instead the air condition was running with a set-point of 20° C. This resulted in a temperature alternating between 19.3° C and 20.7° C with a pseudo frequency of ∼700 seconds. Under these conditions the temperature became stable on an average of 20.3006° C with a standard deviation of 0.0011 K. This is already below the sensor read noise that is specified to 2 mK. Outside and inside temperature along time are shown in Fig. 3.2. The influence of the outside volume temperature oscillation on the inside temperature is visible. The amplitude of the inside temperature change is ∼1/300 of that of the room temperature

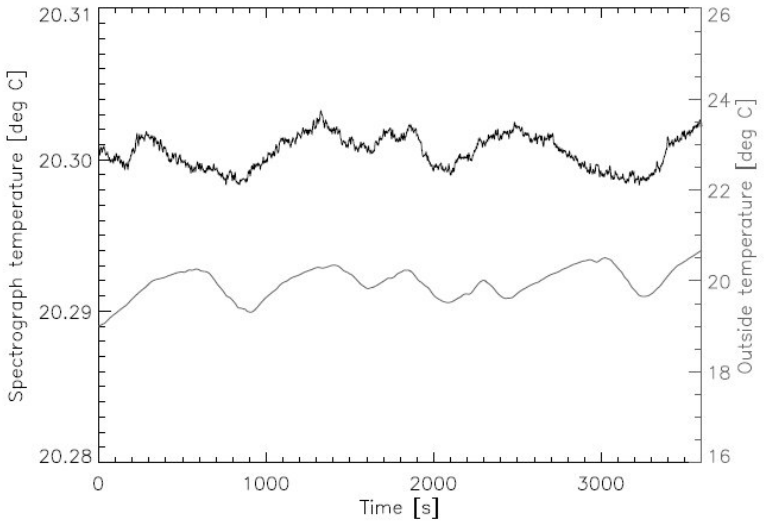

Figure 3.2: Outside and inside temperature for a test with running air-condition. Set-points: 20° C for outside and 20.300° C for the spectrograph interior.

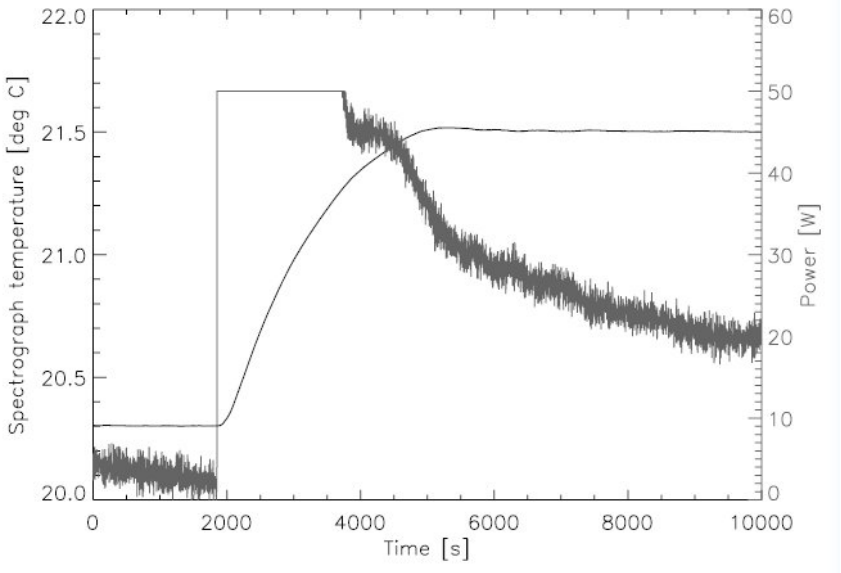

Figure 3.3: Spectrograph inside temperature and heater power for a test when changing the inside temperature from 20.300° C to 21.500° C. The transient response for both is also visible. The system became stable again after ∼4000 seconds.

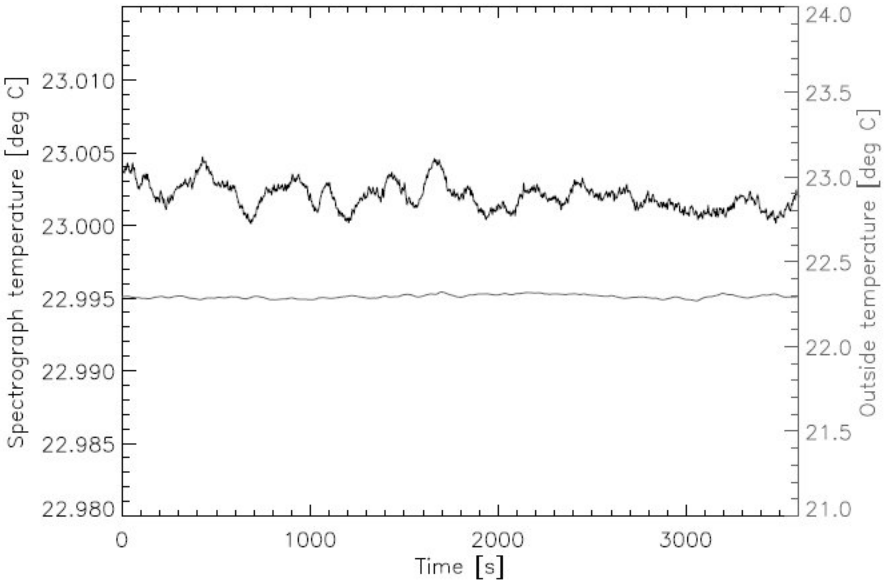

Figure 3.4: Spectrograph inside temperature and room temperature when setting the inside temperature to 23.000° C.

change. Fig. 3.3 shows the change of temperature and transient response when changing the spectrograph interior temperature from 20.300° C to 21.500° C. The system became stable again after ∼4000 seconds.

3.1.2 Test at fixed outside temperature

A test was run with a set-point of the spectrograph temperature of 23.000° C and the room temperature fixed to ∼ 22.3° C. Fig. 3.4 shows the inside and outside temperature while the heating foils inside inner volume were working. Temperature became stable on 23.0018° C. with a standard deviation of 0.00096 K.

As first promising result, the spectrograph could reached a stability of 0.00096K under quiet conditions (room temperature ±0.1K), even without the outer layer stabilization. Under much harder conditions, with the room temperature oscillating by ±1.4K, the influence of the outside temperature change was notable with respect to periodic fluctuations in the inside volume, but still a stability on 0.0011 K level could be achieved, below the design goal of 0.02 K standard deviation.

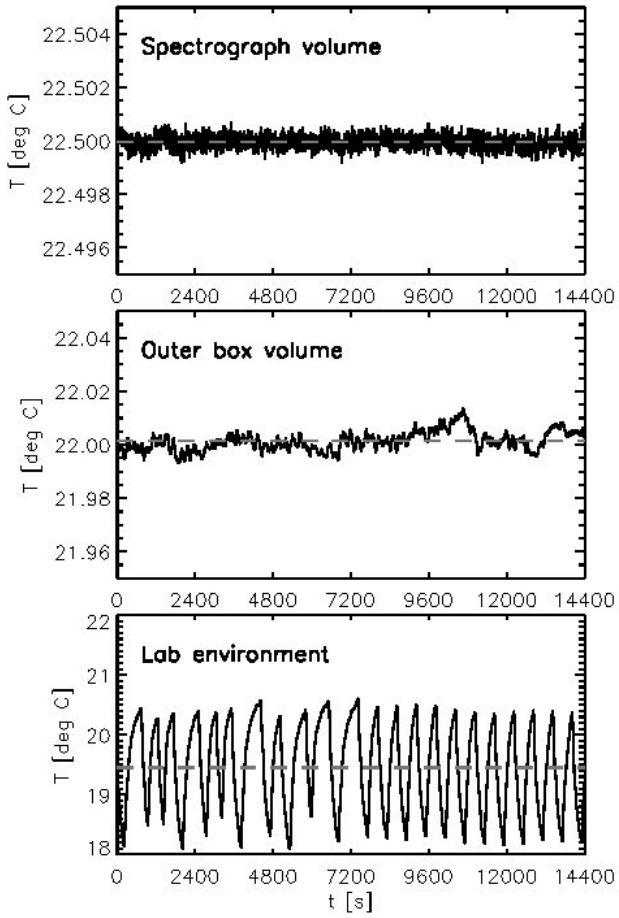

Figure 3.5: Temperature fluctuations in the inner spectrograph volume as well as in the outer box and in the laboratory room measured for four hours.

3.2 FOCES Inner and Outer Box Test

The entire "box in box" system has been used for these measurements, with the two heating layers working to stabilize actively the temperature [1].
As stated in the previous chapter, the inner box consists of 11 heating mats with a total power of 50W, and the outer larger box, that also provides for pressure stabilization, holds 36 heating foils with a total heating power of 900W. The nominal set-points for the temperature was of 22.5° C in the inner volume, of 22.0° C in the outer volume, and of 20° C for the room (always controlled by the standard lab air-conditioning system).
Fig. 3.5 shows the system behavior in a typical 4 hours test at stable weather conditions. The effect of harsher weather conditions, with room pressure fluctuations, will be shown below. The data have been acquired with pressure control running and after about 12 hours of stabilization and thermalization of the metal and glass load inside FOCES. There

[1]Based on *Grupp F.,* ***Brucalassi A.****, Lang-Bardl et al., 2011* (Grupp et al., 2011)

is no reason to believe that there are timescales longer than that affecting the system, provided the room temperature control works within $\pm 2^\circ$ C.

The achieved temperature stability is:

- σ=0.0002 K, ΔT(peak-to-valley)=0.0016 K in the inner control volume.
- σ=0.0036 K, ΔT(peak-to-valley)=0.0207 K in the outer control volume.
- σ=0.73 K, ΔT(peak-to-valley)=2.52 K in the spectrograph room.

Different test campaigns have been done to verify and confirm this behavior.
Pressure is also actively controlled and measured by two precision barometers as explained in sec. 2.5.2. The laboratory pressure instead is recorded by a simple IP weather station.

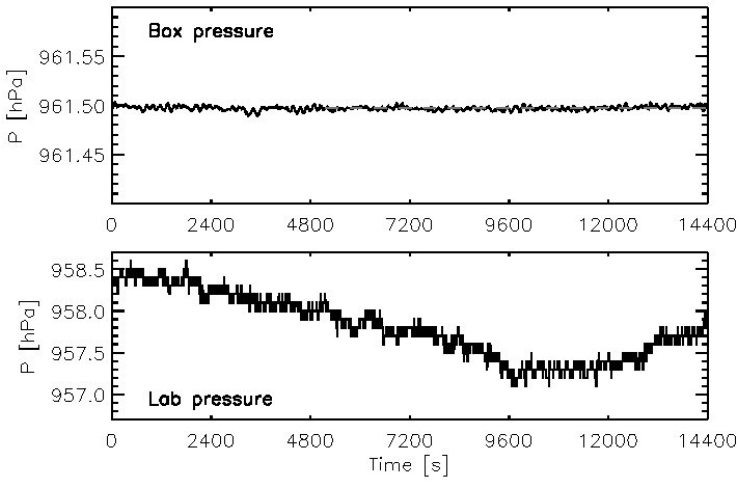

Figure 3.6: Pressure fluctuations inside the pressure box as well as in the laboratory room recorded over four hours of calm to moderate weather.

Fig. 3.6 shows the conditions reached with temperature control working and after 4 hours of stabilization.
During a test, a strong thunderstorm has been encountered. Before the systems were switched off in order to protect the CCD cameras, the influence of strong wind around the building - and thus pressure fluctuations in the lab - was recorded. Strong wind affected the room pressure stability notably, with peak-to-valley fluctuations higher than three orders of magnitude, but still the control systems reacted against fast room pressure changes (see Fig. 3.7) . It has to be noted, that under such extreme conditions normal observation runs will be stopped. Anyway, moderate to strong wind will occur at the observatory site and an accurate monitoring of the weather conditions will be needed to check fast fluctuations in the spectrograph room.

The obtained pressure stability is:

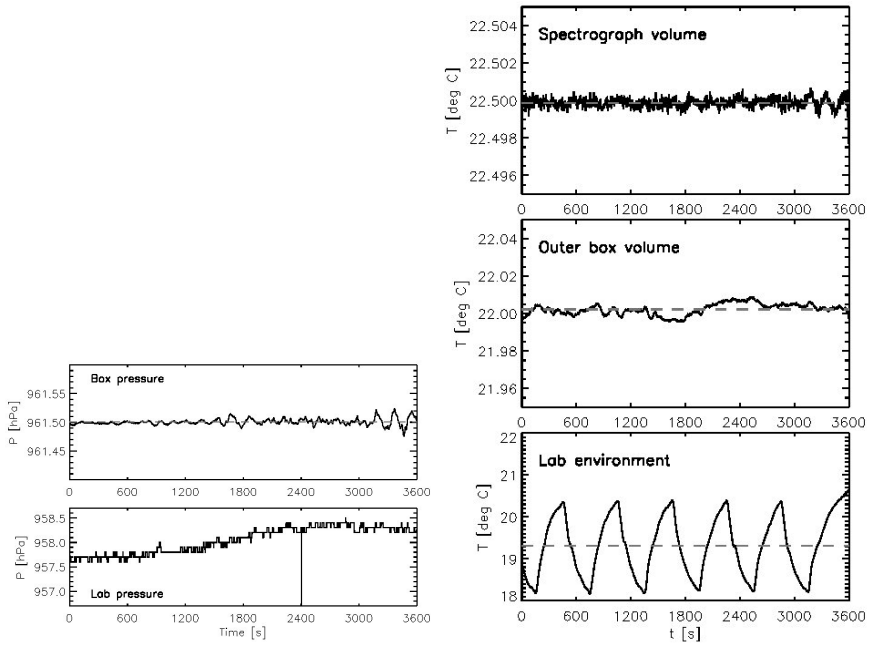

Figure 3.7: Pressure (left) and temperature (right) fluctuations inside the FOCES box as well as in the laboratory during a thunderstorm with strong wind affecting the lab environmental pressure.

- σ=0.002 hPa, ΔP(peak-to-valley)=0.014 hPa in the pressure controlled volume under nice weather conditions.
- σ=0.005 hPa, ΔP(peak-to-valley)=0.047 hPa in the pressure controlled volume under harsh weather conditions.

With peak-to-valley stabilities of <0.005 K and <0.05 hPa, the stability goal of 0.1K and 0.8 hPa has been over reached by more than an order of magnitude. Looking at the model set up in sec. 2.5.1 this corresponds to a dispersion direction spot movement due to temperature fluctuations of <1/40000 of a pixel and due to pressure fluctuations of 1/33000 of a pixel. In cross order direction the expected pixel shifts are 1/1000 for temperature and 1/1100 for pressure fluctuations.

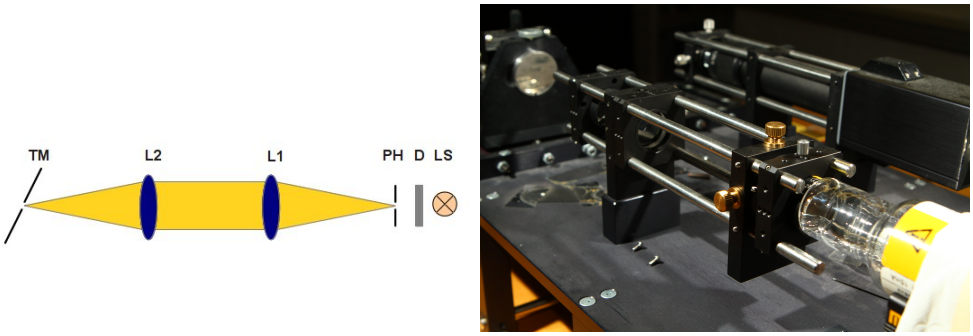

Figure 3.8: Experimental set-up for the illumination system.

3.3 Optical stability verification

In this section the results obtained by the analysis of different images taken with the system working under pressure and temperature stabilized conditions will be presented [2].
Multiple series of ThAr spectra have been acquired at regular intervals (∼15 min) using the Andor System 2K×2K camera and then analyzed by a series of IRAF packages and a dedicated IDL routine. Several measurements have been repeated also with different exposure time for the ThAr acquisitions.
This test gave us the possibility to investigate the mid term stability of the spectrograph with respect to simulations requirements previously discussed (see sec. 2.5.1). Initially, a 2D analysis has been applied to verify the stability of the spot positions in the controlled system, and to check the movement of the image on the CCD with changes of environment pressure and temperature. Subsequently, a 1D spectra analysis has been used to control directly the movement of the spectra with fluctuations of temperature and pressure.

3.3.1 Experimental setup

Fig. 3.8 shows the experimental setup used as illumination system for the measurements to simulate the telescope beam. It consists of a light source (LS), a frosted glass plate diffuser (D) and two doublets (L) with focal length of f=100 mm, that image the de-magnified pinhole (PH) on the central aperture of the small tilted mirror (TM) at the input fiber system (see sec. 2.3.1). The resulting input beam had a focal ratio of $f_{\#}$ ≈5.5 and overfilled the entrance aperture. The source used are a ThAr gas discharge working at 10-12 mA power range and a normal halogen lamp for Flat-Field exposures. In the case of the ThAr lamp, another doublet with short focal length (16 mm) was necessary just after the lamp to increase the amount of light on the diffuser plate.

[2]Based on Brucalassi et al. (2012), Brucalassi et al. (2013)

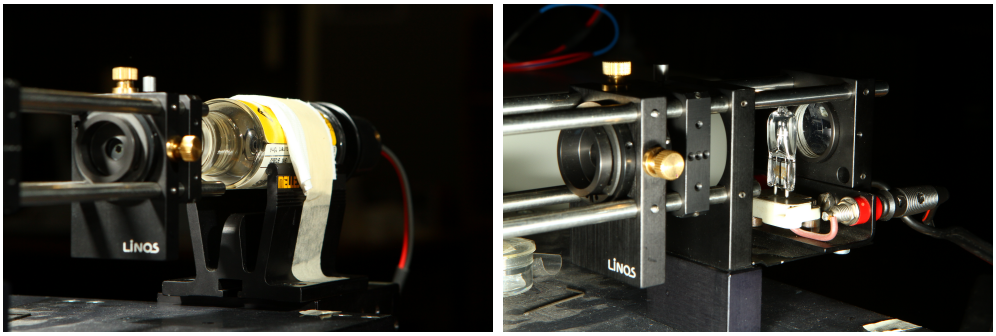

Figure 3.9: ThAr lamp (left) and Flat-Field lamp (right) in the illumination system. The diffuser and the pinhole are also visible.

3.3.2 2D Analysis

For this part of the test, all the acquisitions have been recorded with a system temperature set point of 23.0° C in the inner volume. The over-pressure inside the outer box was chosen in a range of 5.0-8.0 hPa more than the normal room pressure. Unfortunately, part of the measurements have been carried out without external room temperature control due to a problem to the lab air conditioner. It was therefore decided to acquire ThAr spectra only during cold days in such a way that the heating systems of the internal boxes could still work and thermalize the environment.

The process of analysis was done by considering 9 (3×3) sub-frames boxes (650 × 650 pixels) from each ThAr image (see fig. 3.10). Three of these sub-frames, corresponding to three different regions of the ThAr spectra, were selected: in our case the left-middle, the central and the right-middle sub-frames. Selecting the first sub-frames of each series as a reference, a 2D cross-correlation was calculated using all the remaining sub-frames in the series. Therefore, a 2D fitting algorithm was applied to the Cross-Correlation function (CCF) and the position of the centroid in x and y direction was calculated (see Fig. 3.11). The difference between the latter centroid coordinates and the centroid position of the auto-correlation function of the reference spectrum gave us an estimation of the shift between the images considered. Furthermore, the analysis of different sub-frames boxes of the ThAr images allowed to investigate the behavior of the spectra movement amplitude across the detector surface and also to check if strange edge effects or over-exposed parts of the spectra could affect the computation of the cross-correlation. The resulting centroid movement for 3 different spectra series considering the 3 different regions of each frames is shown in Fig. 3.12. As first result it can be noted that the shift in x and y with respect to the reference is <1/10000 pixels for each region, but in the central one the measurements are less homogeneous. No evidence of a preferred centroid movement along the main dispersion direction (x-axis) or the cross order direction (y-axis), was recorded. Fig. 3.13 shows the x and y shift vs. time for the same ThAr sub-frames considered in Fig. 3.12. Only in the central sub-frame a small drift as a function of the time is present for both x and y axes. Fig. 3.14 shows temperature fluctuations inside the FOCES box and in the laboratory

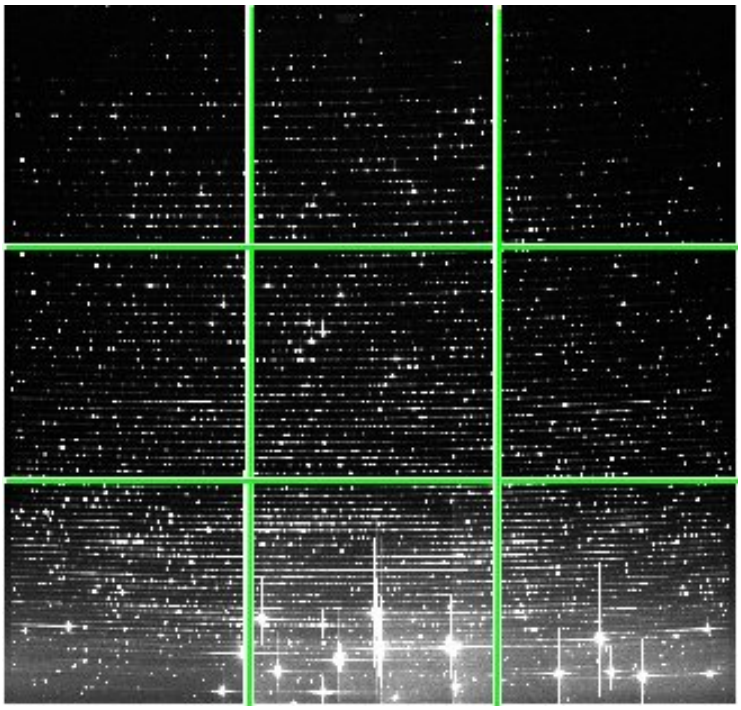

Figure 3.10: A ThAr spectra with overimposed in green the sub-frames boxes considered for the analysis.

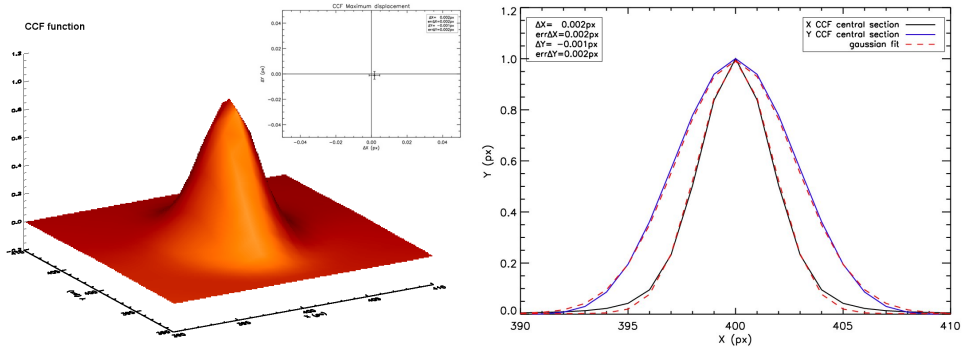

Figure 3.11: Left: 3D-Plot of the CCF with the displacement of the centroid position. Right: Central cross profile in x (black line) and y (blue line) directions of the CCF. The dashed red line corresponds the the Gaussian fit.

during the test.

3.3.3 Pressure changes

We present here the analysis of 2 other series of ThAr spectra acquired at an environment over-pressuring of +5.0 hPa and afterwards increasing the pressure at +8.0 hPa with respect to the lab pressure (see Fig. 3.15). The method utilized for the analysis is the

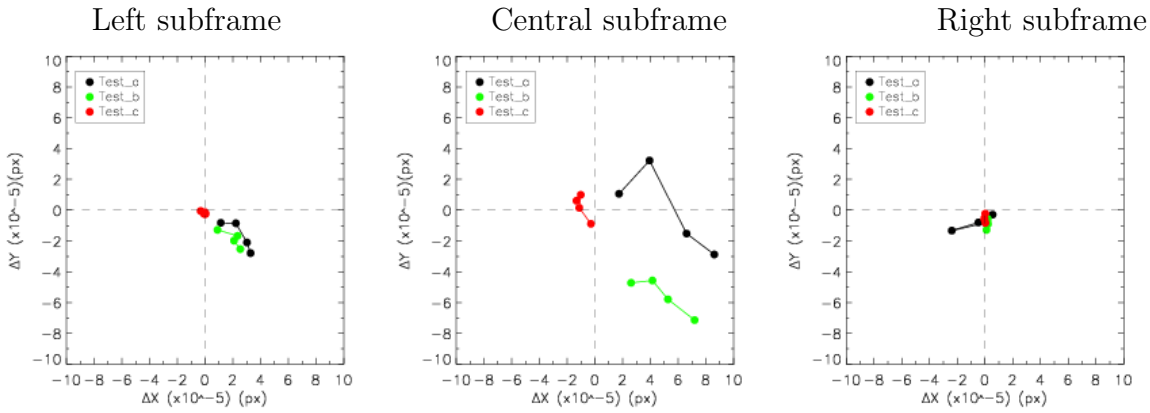

Figure 3.12: Centroid shift for three different subframes selected respectively in the left, in the center and in the right region of the original spectra. The colors correspond to different spectra series acquired after several hours.

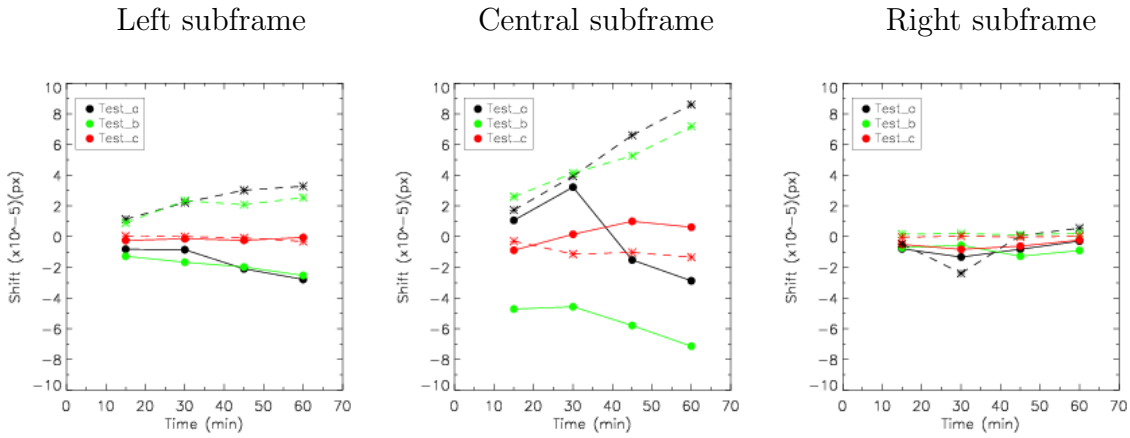

Figure 3.13: Centroid shift in x (dashed line) and y (continuous line) directions vs time calculated for the same ThAr subframes of Fig. 3.12 in the same 3 spectra regions.

same described above. According with the results presented in sec. 2.5.1, the pressure changes produce effects mostly in cross order direction. This is due to the fact that the most influenced glass-air transitions occur at the cross disperser double prism. As results, movements in x-axis - along the main dispersion direction - are found comparatively smaller than in cross order direction for pressure changes. The Y-axis movement is around $\sim$1/4000 pixels for a change of $\pm$3hPa. Furthermore, the general behavior of the centroid shift for the left and right sub-frames follows the simulation results reported in Grupp et al. (2010).

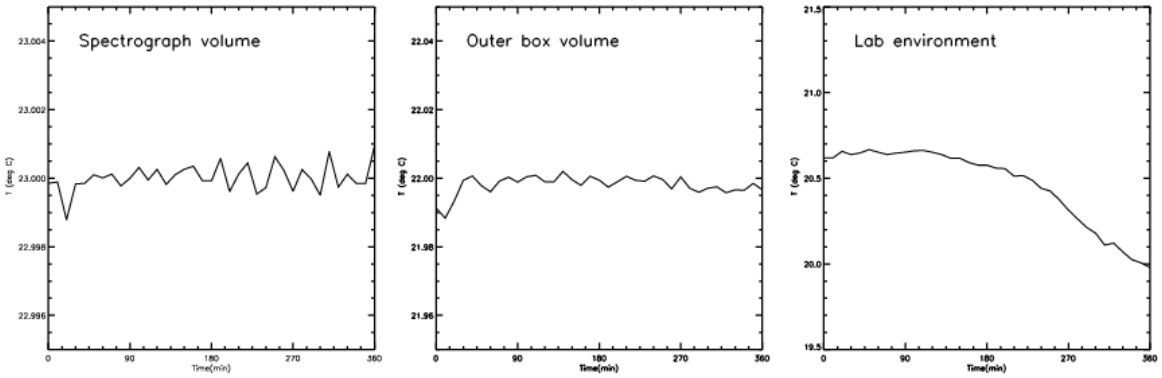

Figure 3.14: Temperature fluctuations inside the FOCES box and in the laboratory during the test.

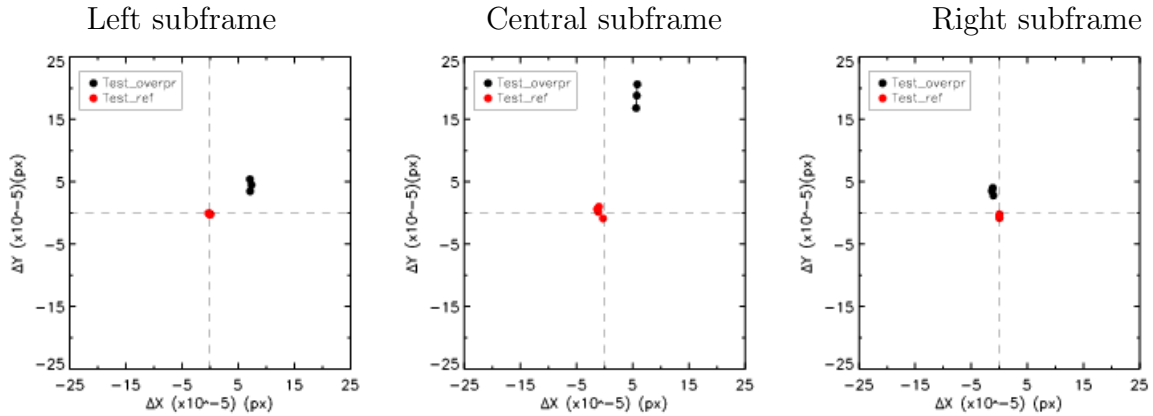

Figure 3.15: Centroid shift for different subframes selected respectively in the left, in the center and in the right region of the original spectra. Red: Spectra obtained with a system over-pressuring of $+5hPa$. Black: Spectra obtained with a system over-pressuring of $+8hPa$

3.3.4 First conclusions

One of the goal of this analysis was to estimate the movement of the image on the CCD with changes of pressure and temperature and the stability of the spot positions in the stabilized system. Working at pressure and temperature system conditions presented in sect. 3.3.2, it has been possible to measure along the main dispersion direction a movement of the ThAr images, averaged over subframes of 650×650 pixels, of ∼1/10000 pixels in a time-scale of some hours. This was a very promising result considering that, as described on sect. 2.1.2, a signal of 1 m/s corresponds to a pixel movement per resolution element of ∼1/4300 (∼1/3000 of a single pixel) at the Sodium D wavelength. Therefore, the test was

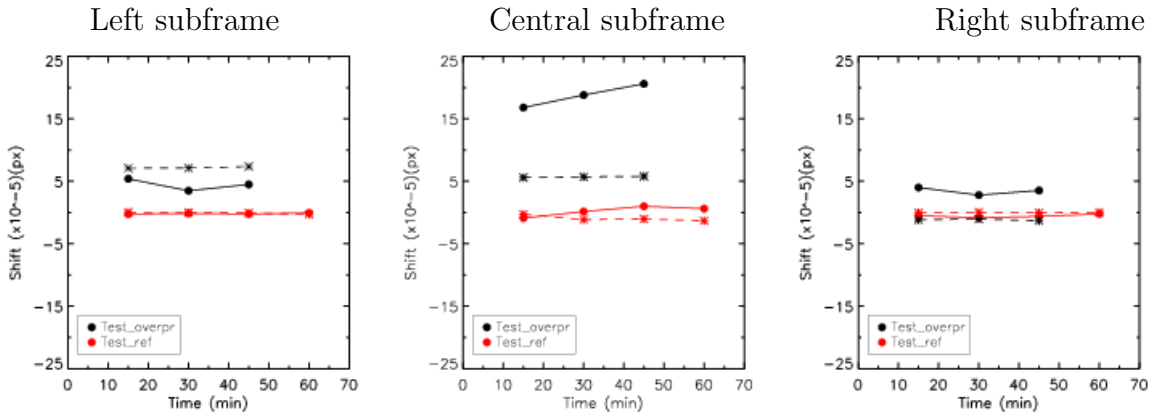

Figure 3.16: Centroid shift in x (dashed line) and y (continuous line) directions vs time calculated for the same ThAr subframes of Fig. 3.15 in the same 3 spectra regions.

repeated using spectra with better S/N and applying the 2D cross-correlation analysis to the total ThAr frames. The values obtained in the different measurements (see fig. 3.17)

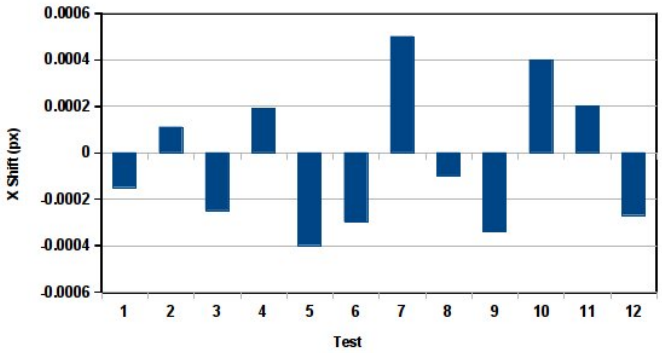

Figure 3.17: 2D CCF shift in x direction for all the tests acquired.

leaded to the conclusion that in this regime of environment stability and also considering all the spectra frames for the 2D analysis, it is possible to do RV spectroscopy in the m/s region. However, it has been decided to verify these first results by the direct analysis on the extracted spectra presented in the next section.

3.3.5 1D Analysis

As final phase of our test, the mid term stability of the spectrograph was investigated by the direct 1D analysis of ThAr spectra carried out with the system working under pressure and temperature stabilized conditions. Following the same working approach presented in the previous section, multiple series of ThAr spectra have been acquired at regular intervals

(∼15 min) using the 2K×2K Andor camera and then analyzed by a series of dedicated IDL routines. Our purpose was to control the movement of the image on the CCD and the stability of the spot positions using a correlation method that could work at the level of the individual spectral orders.

All the acquisitions have been recorded with a system temperature set point of 23.0° C or 23.2° C in the inner volume, and respectively of 22.0° C or 22.2° C in the outer volume. The over-pressure inside the outer box was set to +5.0 hPa more than the normal room pressure. The light source used was the same ThAr gas discharge introduced before. Normal exposure time for each ThAr acquisition was of 100 sec.

For the first step of the analysis process three different regions of ThAr images were considered. In our case left, central and right subframes of 400 pixels in x-direction have been chosen, to check, also in this test, if strange edge effects or over-exposed parts of the spectra could affect our analysis.

A pre-existent semi-automatic pipeline provides the extraction and the wavelength calibration of science spectra under study. This pipeline was developed when FOCES was still operating at the 2.2m Telescope of the Calar Alto Observatory (see for details Pfeiffer et al., 1998). In our case, the ThAr spectra from the whole detector images and from its subframes were considered 'science objects' and analyzed using the mentioned pipeline. A dedicated 1D algorithm was subsequently added by us to calculate a 1D cross-correlation (CC) between the spectra from the first ThAr acquisition of each series, considered as reference, and all the other spectra of the same series. The CCF analysis was repeated two times: the first time using only the central part of the extracted spectral orders, the second one with the total number of the orders. The shift in the main spectral direction was derived by fitting order by order each resulting cross-correlation function with a Gaussian to estimate the centroid position, and then averaging over all the orders. The difference between the latter coordinates and the centroid position of the auto-correlation function of the reference spectrum gave us an estimation of the shift between the spectra. An example of the resulting CCF centroid movement along all the orders for 2 different spectra in 3 different regions of each frames is shown in Fig. 3.18.

Repeating the test a second time, it was noted in both cases a small edge effect in the left and right subframes: the dispersion of the CCF shifts along all orders was higher with respect to the central subframe. It was decided therefore to eliminate 100 pixels from the edges of the original frames and to consider for our analysis only the central part with all the orders. Fig. 3.19 shows the shift in x-axis - along the main dispersion direction - with respect to the reference for all the spectral orders obtained by the analysis of the central region of 2 ThAr spectra acquired with a time interval of 30 minutes. The test was repeated several times in different days with the same set-up and a summary of the results are shown in fig. 3.20. For 11 cases, it has been obtained a CCF mean shift along the main dispersion direction of $\leq 1/1000$ pixels, that corresponds to a RV shift of less than $\sim$3 m s^{-1}. For 7 tests the RV shift was higher, remaining anyway below $\sim$4.5 m s^{-1}. This was already a quite nice result, if we consider that the different measurements were done in a time-scale of some hours with no possibility of a long temperature and pressure stabilization for the system: at the beginning of the test phase indeed, for security reasons,

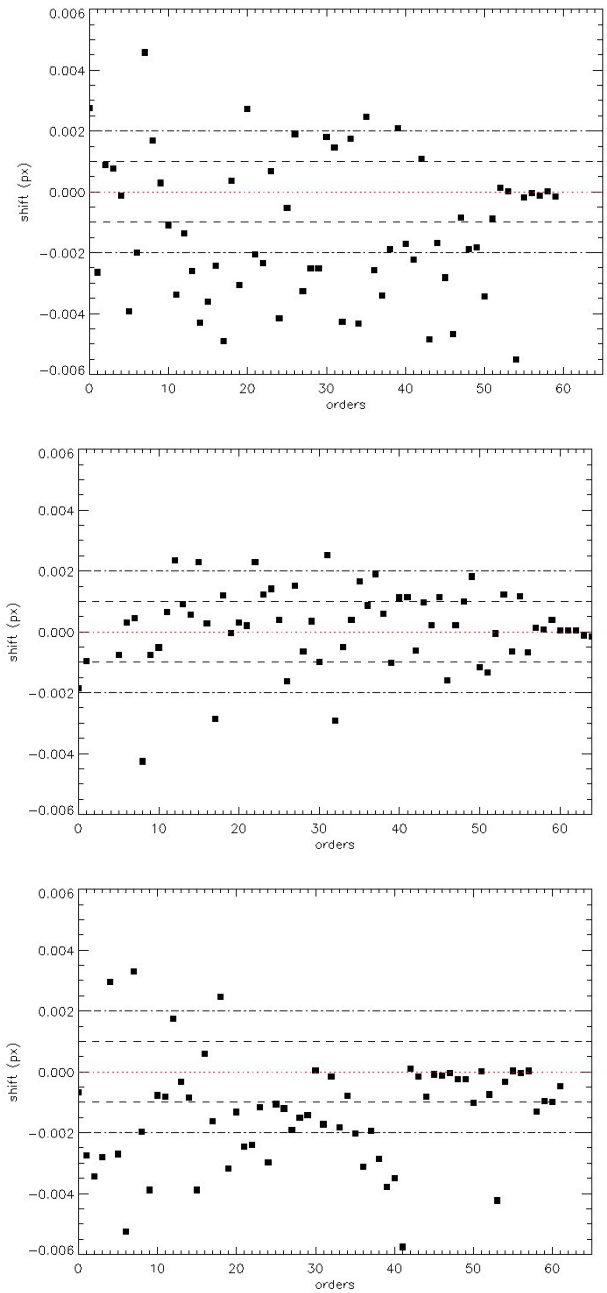

Figure 3.18: CCF centroid shift along the spectral orders for three different subframes of ThAr images: from top to the bottom in the picture, left, central and right region of the original spectra are shown. The dashed lines at a shift of ±0.002 px and ±0.001 px correspond to a displacement in RV of ±6m $s^{-1}$and ±3m s^{-1}respectively.

it was not allowed to leave the system running during the night and all the tests were done in a range of time of ∼24 hours considering also the pressuring of the FOCES boxes. Furthermore, not having implemented at that time a proper calibration unit, the extrac-

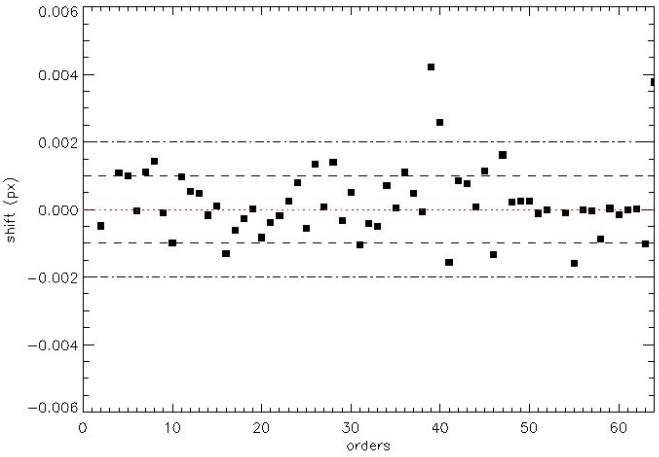

Figure 3.19: CCF centroid shift along the spectral orders obtained by the analysis of 2 subframes in the center region of the original spectra.

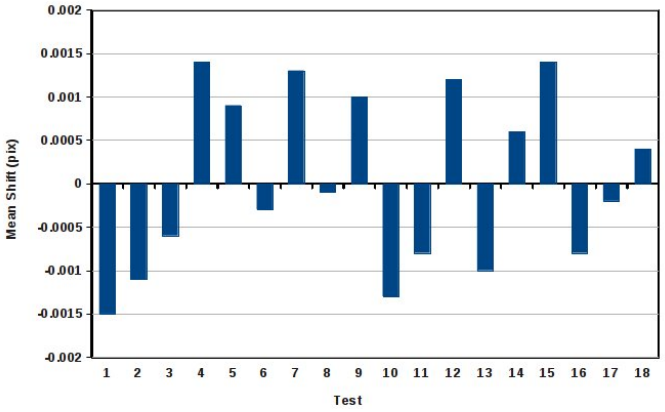

Figure 3.20: CCF mean shift in x direction for all the tests acquired in a range of time of ∼24 hours considering also the pressuring of the FOCES boxes.

tion and the wavelength calibration steps in the spectral analysis were estimated using the same calibration files (Bias, Flat-Field frames) and ThAr spectra for all the tests. Once we were allowed to work during the night, the FOCES heating and pressure systems, together with the CCD camera, were left running for more than one day, and other series of ThAr spectra were acquired with proper calibration spectra for the spectral analysis. The results are shown in fig. 3.22 for 4 tests done in the same conditions of the previous. In all the cases the corresponding RV shift of the CCF centroid along the main dispersion direction was in the region of ∼1 m s^{-1}. Fig. 3.23 shows the CCF centroid x-shift vs. time for ThAr subframes series obtained at regular intervals (∼15 min). A slight drift in function

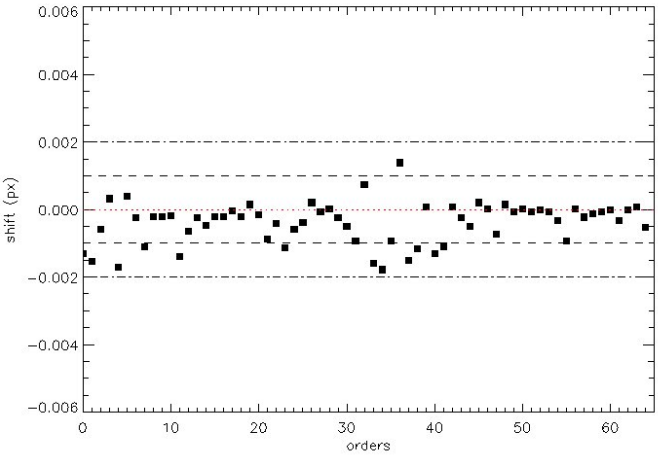

Figure 3.21: CCF centroid shift along the spectral orders obtained by the analysis of 2 subframes in the center region of the original spectra. The total system was running for more than one day.

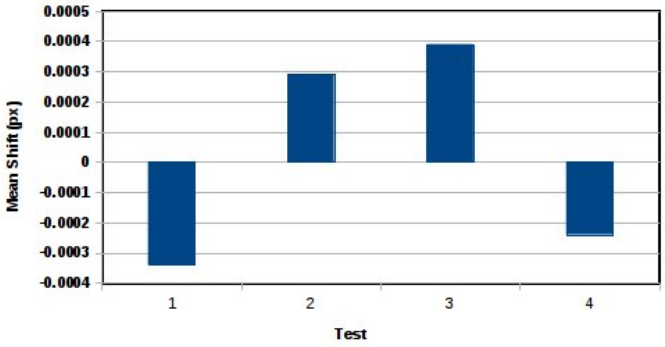

Figure 3.22: CCF mean shift in x direction for all the tests acquired with the FOCES heating and pressure systems, together with the CCD camera, running for more than one day.

of the time is present probably induced by optical bench relaxation after the environment pressuring.

3.3.6 CCD Temperature changes

Here we present the analysis of other series of ThAr spectra acquired at a CCD temperature (T) of $-80°$ C and afterwards changing the CCD T of $\pm 1.0°$ C, $\pm 5.0°$ C, $\pm 10.0°$ C, $\pm 20.0°$ C. The environment over-pressuring was set to +5.0 hPa with respect to the lab

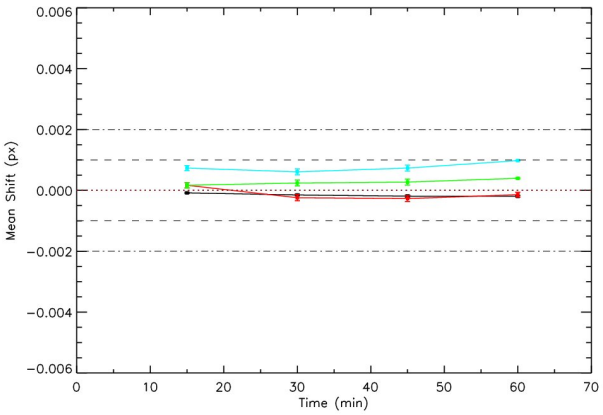

Figure 3.23: CCF mean shift along time for ThAr subframes series obtained at regular intervals of ∼15 min.

pressure for all the measurements. All the measurements were done in a time-scale of ∼24 hours, including the over-pressuring of the box. The method utilized for the 1D analysis is the same described above.

Fig. 3.24 shows the CCF centroid mean x-shift vs. time for ThAr subframes taken just

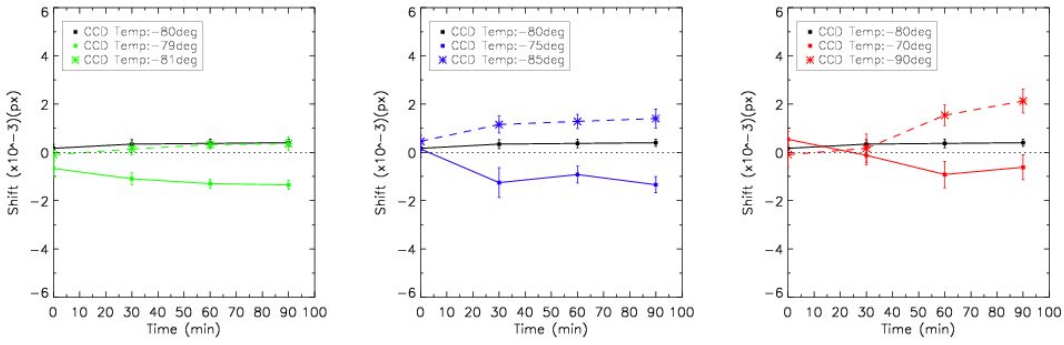

Figure 3.24: CCF centroid mean shift in x-direction along the time for ThAr subframes taken just before (t=0 with T=−80° C) and after changes of the CCD temperature.

before the change of the CCD T (corresponding in the plot to time=0.0 min with a CCD T of −80.0° C) and after a change of the CCD T of ±1.0° C (green line), ±5.0° C (blue line), ±10.0° C (red line). For comparison a serie at constant CCD temperature of −80° C (black line) is also shown.

Until the CCD temperature changes have remained below 10.0° C, the system did not seem to react in T (see Fig. 3.25) and there was not substantial effect on the CCF centroid spectral shift along the main dispersion direction: only a slightly increasing of the dispersion along the spectral orders was recorded. In contrast, it was possible to note a significant

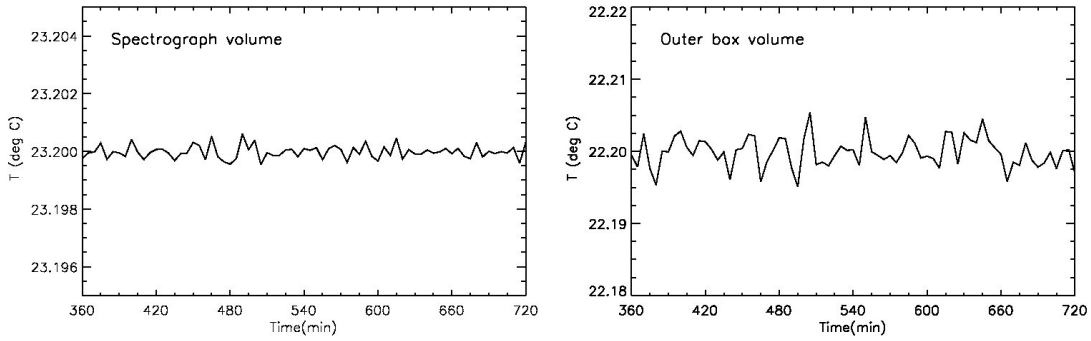

Figure 3.25: Temperature fluctuations inside the inner pressure box and in the outer box during the change of -10° C in the CCD temperature.

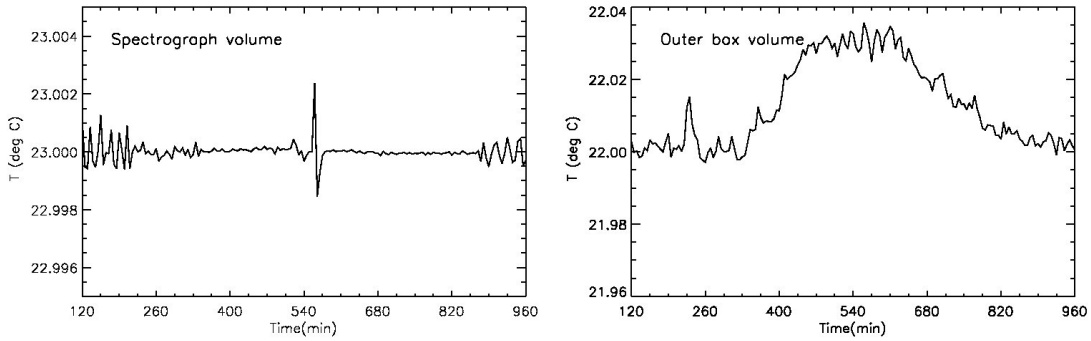

Figure 3.26: Temperature fluctuations inside the inner pressure box and the outer box during the change of -20° C in the CCD temperature.

effect on T when we varied the CCD temperature by ∼20.0° C, especially if the change occurred from the higher temperature (−60.0° C) to lower temperature (−80.0° C)(see fig. 3.26). We acquired series of ThAr spectra at regular time intervals (∼15.0 min) just before the CCD temperature shift, during the temperature changing-phase and after several hours. An example of the CCF analysis results is shown in fig. 3.27: a clear increase of the dispersion of the CCF shifts along all orders can be seen in the central plot corresponding to the period after the CCD temperature change. In addition, the shift along the dispersion direction goes from a mean value of -0.0008 px at −80.0° C (plot on the left) to a mean value of 0.002 px at −60° C (plot on the center). It is necessary to wait several hours to restore a normal behavior with a mean value of -0.0006 px (plot on the right). We repeated the test several times and we obtained in the worst case a mean shift along the main dispersion direction of ∼0.0035 pixels after the CCD temperature change. This corresponds in our system to a RV shift of ∼10 m s^{-1}.

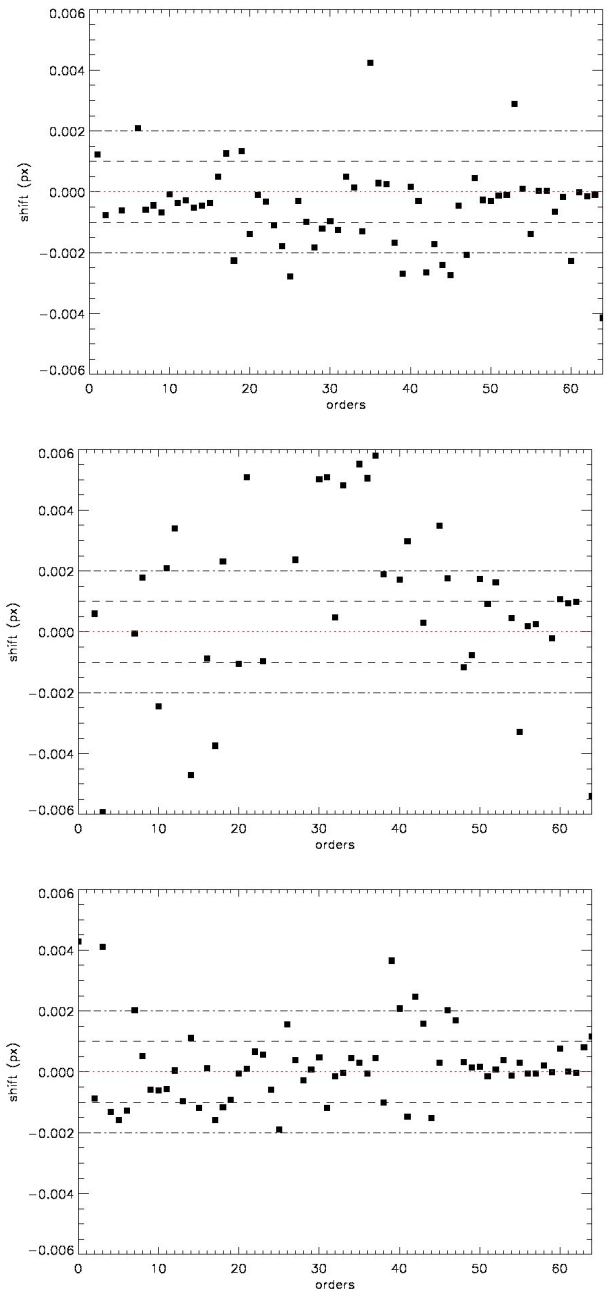

Figure 3.27: CCF centroid x-shift along the spectral orders for ThAr spectra acquired before, during and after the CCD temperature change of -20° C.

3.3.7 Final conclusions

One of the goals of this analysis is to estimate the stability of our system using a new 1D algorithm to investigate directly the movement of ThAr spectra in the stabilized system. In addition, a dedicated test is considered to evaluate the effect of CCD temperature

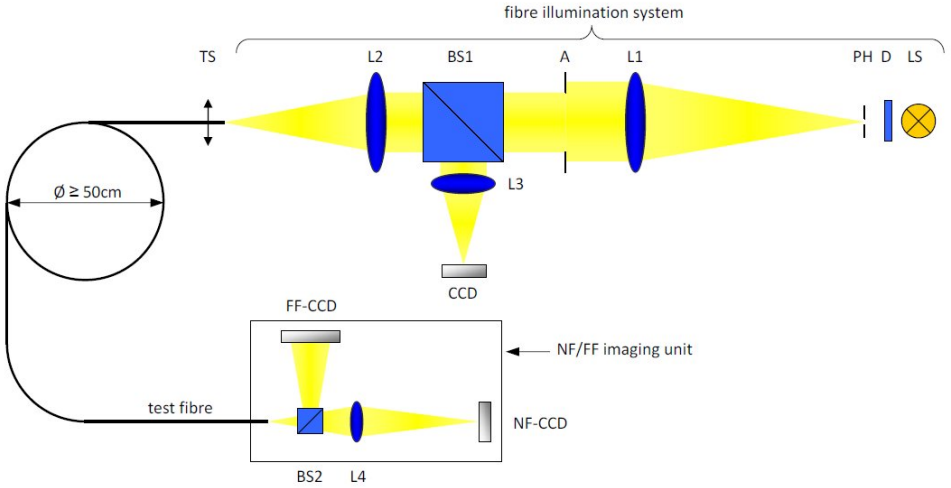

Figure 3.28: Experimental set-up to measure fiber scrambling properties.

changes on this stability. Working with the system running for more than one day at the same pressure and temperature conditions of the previous test, we see that it possible to measure along the main dispersion direction a movement of the ThAr spectra $< 1/2500$ pixels in a time-scale of some hours. With reference to sect.2.1.2, also the 1D direct spectra analysis can confirm that in this regime of environment stability it is possible to obtain RV spectroscopy in ~ 1 m s^{-1}region. The influence of the CCD temperature changes up to $\pm 10^{\circ}$ C is negligible. The mean shift along the main dispersion direction of ThAr spectra remains in fact below 0.002 px ($\sim$5 m/s). A relevant impact instead is present if the CCD temperature changes of $\pm 20^{\circ}$ C (with a peak in RV shift of $\sim$10 m/s) and several hours are necessary to wait before the system could come back to the set-point regime. Anyway the possibility that CCD temperature fluctuations of $\pm 20^{\circ}$ C could occur is quite remote and probably due only to accidental factors. In normal working conditions indeed, it is not expected a change of CCD temperature more than $\pm 1^{\circ}$ C and it is possible to deduce from our test that the purpose to reach an RV accuracy below 5 m s^{-1} in our stabilized system should be ensured.

3.4 Fiber scrambling Test

A variety of measurements have been carried out with a selection of fibers from different vendors, including state-of-the-art octagonal and hexagonal fibers [3].
After characterization of the test bench with respect to stability and resolution, scrambling measurements have been conducted using LEDs with central wavelengths ranging between 465-635 nm. The dependence on wavelength regarding to photometrical scrambling has been initially demonstrated. Moreover, two mechanical combined fiber cables

[3]Based on *Feger T.,**Brucalassi A.**, Grupp F. et al. 2012*

have been analyzed that were made from octagonal-circular and hexagonal-octagonal fiber sections. In this context an apparatus for focal ratio degradation (FRD) measurements was assembled to compare different shaped fibers and fiber combinations.

3.4.1 Scrambling Test bench

Figure 3.28 shows the experimental apparatus used to investigate photometrical scrambling properties of single and combined fibers in near-field and far-field. The setup is built out of two individual subsystems that may be called illumination system and NF/FF imaging unit. The NF/FF imaging unit allows to measure fiber near-field and far-field simultaneously. The illumination system is used to simulate a telescope beam and consists of a light source (LS), a frosted glass plate diffuser (D) and two doublets that image the de-magnified pinhole (P) onto the test fiber. The optical diffuser has been used to provide a homogeneous illumination across the pinhole. According to previous measurements performed by other groups the spot diameter was in the order of half fiber core diameter which corresponds to a filling factor of 25%. This provides enough space to move the entrance spot over the fiber core without crossing the core-cladding boundary. An aperture stop (A) placed between both doublets limits the beam speed to f/3.5, a typical focal ratio used to keep FRD as small as possible. The test fibers were gently clamped within custom made fiber ferrules and mounted on a five axis adjustment holder with three lateral and two rotational degrees of freedom. This guarantees a good alignment with respect to the illumination system. A HPS-170 high precision translation stage (TS) from miCosy was used to scan the fiber across the focal spot with directional resolution of 1.25 micron. The scan range was ±70 micron for 200 micron fibers and ±35 micron for 100 micron fibers. The step size was in the order of 5-10 micron, depending of the core size. The bench for simultaneously near-field and far-field measurements was mounted on a separate plate made from aluminum (see Fig. 3.29). This enables to fix all important components properly with respect to each other. The fiber ferrule was mounted onto a translation stage with two lateral degrees of freedom. A 50:50 non-polarizing beam splitter (BS2) placed behind the fiber exit takes a portion of the light leaving the fiber. One part of the beam is caught by a 10x corrected M-PLAN objective (L4) with long working distance and imaged onto a CCD-detector (Apogee Ascent 340) with 640×480 pixels. The other portion of the light is deflected inside the beam splitter towards the far-field CCD-detector (Apogee Ascent 16000). The FF-CCD is located close to the fiber exit (within the Rayleigh distance) to keep the exposure time as short as possible. Finally, it was required to protect the scrambling bench from scattered light that was continuously present within the lab environment. Most of these sources where buffered and screened using simple black cardboard or tape.

3.4.2 The fiber specifications

Test fibers were obtained from Polymicro Technologies, CeramOptec respectively j-fiber and specified as listed in Table 1. All fibers are step-index multi-mode and built out of a fused silica core, a fluorine doped silica cladding and a buffer material that is either made

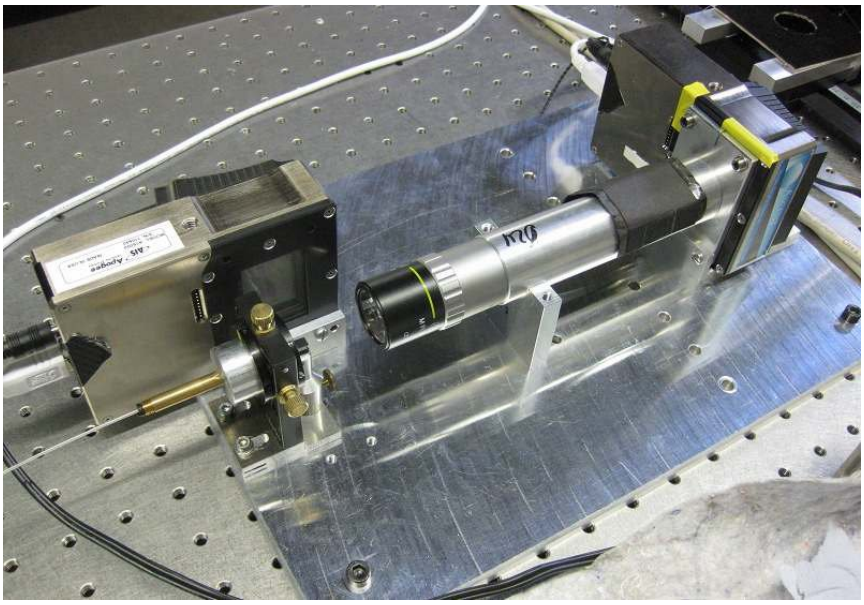

Figure 3.29: Near-Filed and Far-Field Imaging Unit with the NF-CCD and FF-CCD, the beam splitter and the microscope objective.

Table 3.1: Technical specifications for the test fibers.

Product code	shape	core $[\mu m]$	cladding $[\mu m]$	buffer $[\mu m]$	NA	Vendor
FBP100140170	circ	100	140	170	0.22	Polymicro Technologies
FBP200240270	circ	200	240	275	0.22	Polymicro Technologies
OCT-WF200/660N	oct	200	672	780/1100	0.22	CeramOptec
OCT-WF100/660N	oct	100	–	–	0.22	CeramOptec
OCT-WF67/660N	oct	67	–	–	0.22	CeramOptec
AK482738BA	hex	190.2	200.2	392	0.20	j-fiber

from nylon or polyimide. The Polymicro FBP specification designates a fiber which has a high UV transmission, comparable to a low-OH material but with water absorption peaks at about 950 nm, 1240nm and 1380 nm. FBP fibers are furthermore solarization resistant and operate over a broad spectral range reaching from 275nm to 2100 nm. CeramOptec polygonal fibers are made from Optran NCC WF silica glass that exhibits a similar performance and transmission over a huge spectral coverage from 300nm to 2400 nm. The spectral characteristics of the hexagonal fiber are not known. Images from polished circular and non-circular fiber ends are shown in Figure 3.30.

3.4.3 Data processing and reduction

Near-field image processing was done in IDL. A typical near-field measurement obtained with the test bench consists of 15 individual sample sets where for each displacement step a sequence of 10 raw images have been recorded. Following the principle of first order data reduction a masterdark with equivalent exposure time was then removed from all 150 light images. Within the next step, the barycenter of the nominal near-field light distribution was obtained from the center image. The coordinates were required to define the location of a new coordinate system with origin referring to the nominal position. Around the computed barycenter a square box was equally applied to all calibrated near-field patterns. The box side length was set to 320 respective 160 pixels, depending on the diameter of the near-field pattern. Pixel values beyond the box boundary were just ignored. Finally, from all subframes the intensity barycenter was computed in x and y direction using the following well-known expressions:

$$X_{CM} = \frac{\Sigma I_i \cdot x_i}{\Sigma I_i}, \qquad Y_{CM} = \frac{\Sigma I_i \cdot y_i}{\Sigma I_i} \tag{3.1}$$

where x_i is the pixel position in x-direction (row), y_i the pixel position in y-direction (column) and I_i corresponds to the intensity value of each single pixel element. For each step of the scan, 10 frames have been acquired and the mean values of the barycenter coordinates have been derived. The standard deviation divided by the square root of the number of frames for each step has been attributed as error on the mean values. Therefore, using the eq. 2.18, it was possible to obtain the scrambling gain for the tested fibers. The scrambling gain is typically calculated for spot displacements in the order of ± 0.5 times the fiber diameter. Assuming a 200 μm fiber with entrance spot size of half the fiber diameter, or in other words 25% core filling, the displacement corresponds then to ± 100 μm. However, non-circular fibers with external cladding only allow entrance spot displacements slightly beyond the core-cladding boundary without showing secondary patterns. Light guiding becomes possible when crossing the internal cladding structure. The resulting ring shaped pattern may correlate with the light distribution at the fiber output and eventually influence the whole measurement. Thus the largest displacement was limited by ± 0.35 of the fiber diameter in order to avoid secondary patterns.

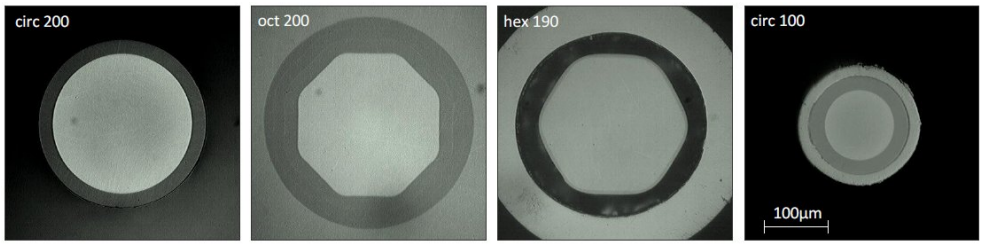

Figure 3.30: Polished fiber ends imaged through a microscope at 400x magnification.

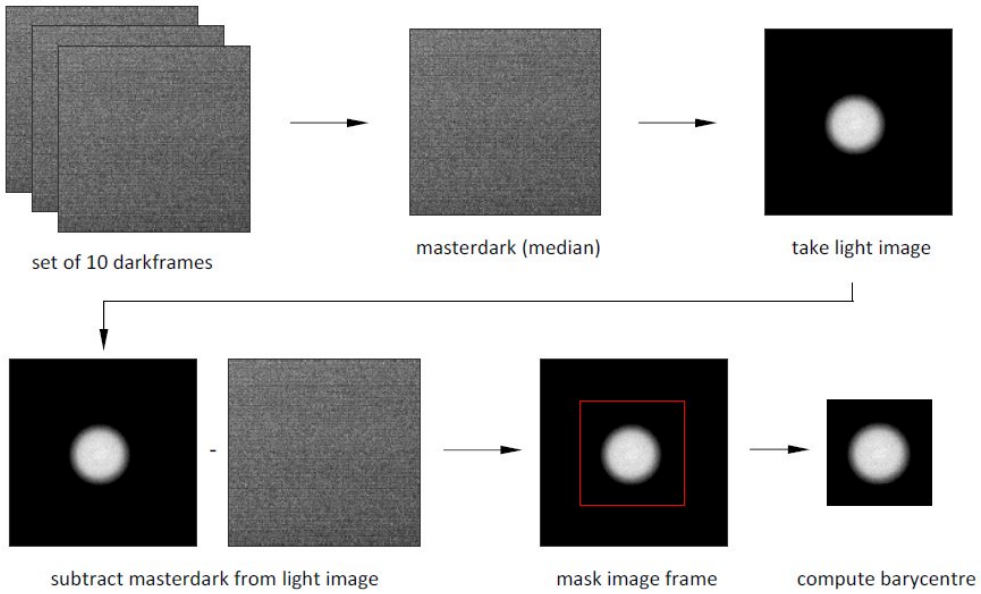

Figure 3.31: Schematic overview of the data reduction steps.

According to Grupp et al. (2010), the FOCES stability goal was assumed to recover a radial velocity signal of 1 m s^{-1}. Equipped with the new Andor CCD-detector (13.5 μm) FOCES will provide a resolving power of R=70000 within a sampling of roughly two pixels per resolution element. Referring to the given spectral line shift, the intensity barycenter of the fiber near-field would experience a geometrical shift of 23.3 nm (100 μm fiber assumed). On the other hand this will correspond to a scrambling gain of G=1500 what the potential fiber-link must provide.

3.4.4 Characterization of the test bench stability

Stability measurements of the test bench were conducted in order to verify the current bench limitation. The measurement was done in a time scale of a few minutes corresponding to the period that was required to obtain a whole near-field measurement. The fiber surface was centered with respect to the entrance spot in order to achieve the maximum throughput. Then a large number of images (typically 200) were recorded. Finally, the barycenter was computed from all images in x and y direction. The stability measurement was performed for 100 micron and 200 micron circular fibers likewise and the outcome is shown in Fig. 3.32. According to the obtained results the bench stability is limited by ∼0.126 (d/1000) for 200 micron fibers. Smaller geometrical shifts of the barycenter might not be resolvable anymore. This also holds for 100 micron fibers. Here is the variation of bench stability roughly two times higher and limited to ∼0.211 (d/1000). This eventually results from smaller intensity coverage which was only 0.25 times the area of a 200 micron pattern.

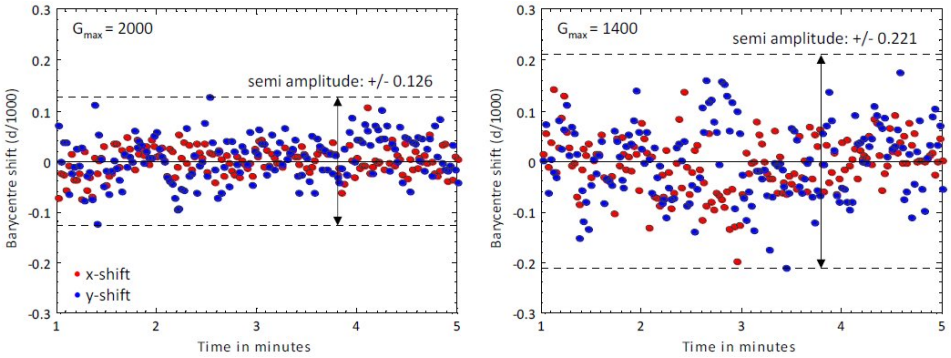

Figure 3.32: Measurement of bench stability obtained form 100 μm and 200 μm fibers (1 d/1000 $\simeq$ 0.2 pixel). G_{max} indicates the scrambling gain limit that can be obtained with these fibers. The red and blue points represent barycenter movements in x-direction and y-direction. An error of $\sim 0.003(d/1000)$ (not shown in figure) corresponding to the standard deviation of the data values divided by the square root of the total number of the measurements has been attributed to all the measurements.

3.4.5 Near-Field measurements

From eq. 2.17 it can be deduced that the number of modes strongly depends on wavelength. However, this equation only holds for strictly monochromatic light and gives just a very rough approximation when using broad band sources such as LEDs or tungsten light bulbs. Nevertheless, it was interesting to prove any evidence of wavelength dependence. The measurements have been carried out using LEDs with four different wavelengths ranging from 465nm to 635nm in order to cover the visible spectrum. We have used a standard 200 μm circular fiber from Polymicro to better visualize geometrical barycenter shifts. The near-field is scanned at least three times over the full span width in order to achieve reliable geometrical shifts. The results of this measurement are shown in Fig. 3.33. Even for broad band sources with more than 100 nm coverage such as the LEDs used, the barycenter shift depends clearly on wavelength. The geometrical displacement was for blue light (465 nm) two time better than for the red light (635 nm).

Octagonal and hexagonal fibers have been purchased in order to compare their performance with previous results obtained from circular fibers. Fig. 3.34 shows the near-field scrambling obtained from a 200 μm octagonal and a 190 μm hexagonal fiber. The circle in the left graphs indicates the current bench limit (G=2000). The measurements clearly show that a 200 μm octagonal fiber performs 5-6 times better than its circular counterpart. A focal spot displacement of $\pm$70 μm would correspond to a scrambling gain of G=650. All the test have confirmed the outstanding performance of the octagonal fibers, especially regarding to better radial scrambling. The resulting near-field light distribution has a top-hat intensity profile for all spot positions within the core region. A comparison between intensity profiles of the octagonal and circular fibers is shown in fig. 3.35. For all positions inside the core region the top-hat light distribution does not change its shape. Even with

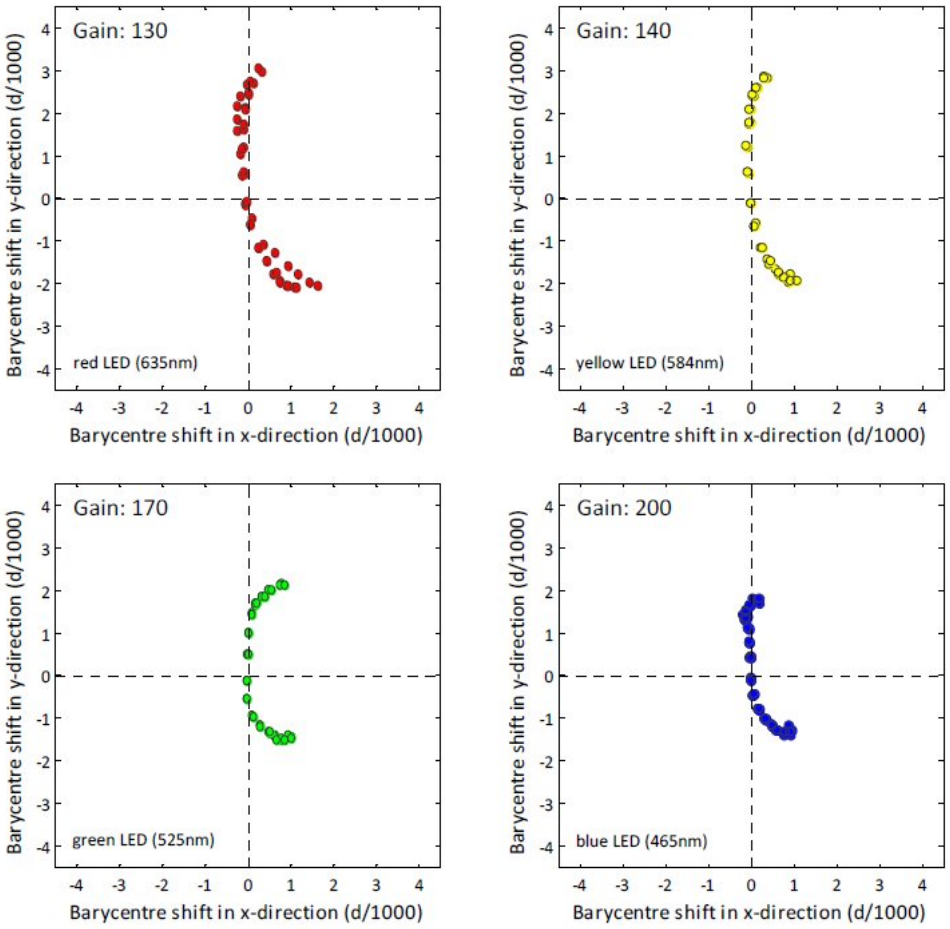

Figure 3.33: Geometrical barycenter shifts obtained from a 200 μm circular fiber using different LEDs.

crossing the core-cladding boundary only the throughput drops slightly. Circular fiber however do not preserve their light distribution. By moving the entrance spot slightly out of its nominal central position the intensity profile gets immediately radially re-distributed to outer core regions. However, this is still not good enough to fulfill the FOCES stability requirement (i.e. G$\geqslant$1500) but far better than first expected. Since the octagonal fiber was very short (less than 3m) their scrambling performance eventually was not fully developed. However, it was shown by other groups that radial scrambling strongly depend on fiber length (Spronck et al., 2012). Thus, slightly improved results will be expected using longer fiber sections in the order of 20m or even longer. Shaking the fiber with any kind of vibrating device may also enhance the amount of radial scrambling.
Hexagonal fibers are quite new and they have been never investigated on fiber scrambling. Since polygonal fibers in general demonstrated their capability as potential candidates for scrambling applications it was obvious to test also the performance of an hexagonal shaped fiber as a reference measurement for prospective projects. The purchased test fiber was

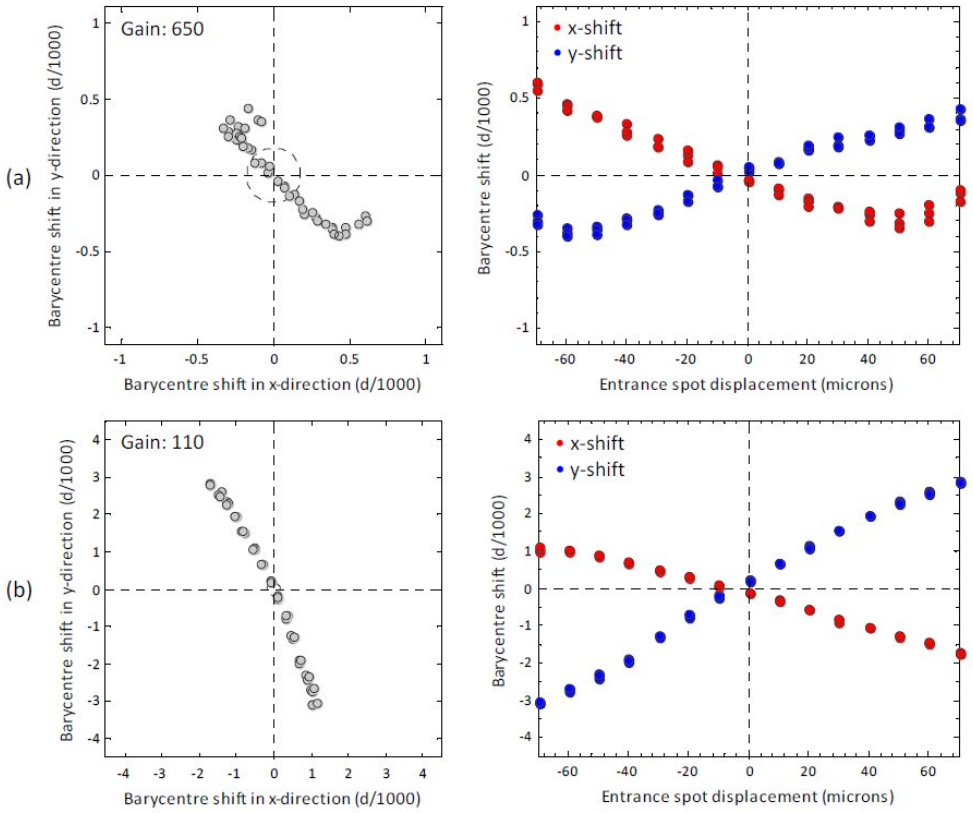

Figure 3.34: Near-field scrambling obtained from a 200 μm octagonal (a) and a 190 μm hexagonal (b) fiber. The red and blue points represent barycenter movements in x-direction and y-direction. The circle (left graphs) denotes the current bench resolution which is limited to G=2000.

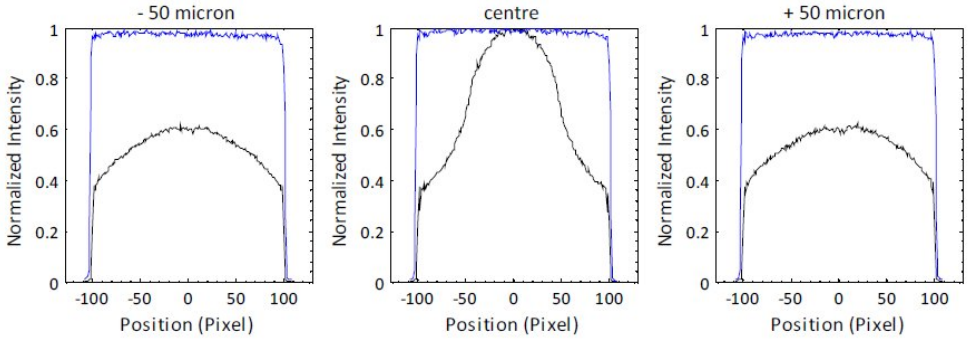

Figure 3.35: Near-field cross-section a 200 μm circular (black) and octagonal (blue) fibers.

2m long and regarding to its properties nearly comparable to the short piece of octagonal fiber. Unlike state-of-the-art octagonal fibers from CeramOptec, the hexagonal fiber is not directly equipped with any glass layer that protects the cladding against mechanical stress. However, it seems that the fiber is embedded within a soft layer and surrounded by a solid

shell made from any hard plastic buffer. Against all expectations, the scrambling capability was very low (G=110) what might be a reason of short fiber length and thin cladding.

3.4.6 Far-Field measurements

Selected Far-Field patterns were analyzed according to the principle applied to investigate barycenter shifts in near-field images. The presented profiles are cross-sections from far-field patterns of circular, octagonal and hexagonal fibers. Vertical and horizontal cross-sections including a detailed view of inverted and overlapped central structures obtained from all three test fibers are shown in Figure 3.36. We observed that far-field patterns have

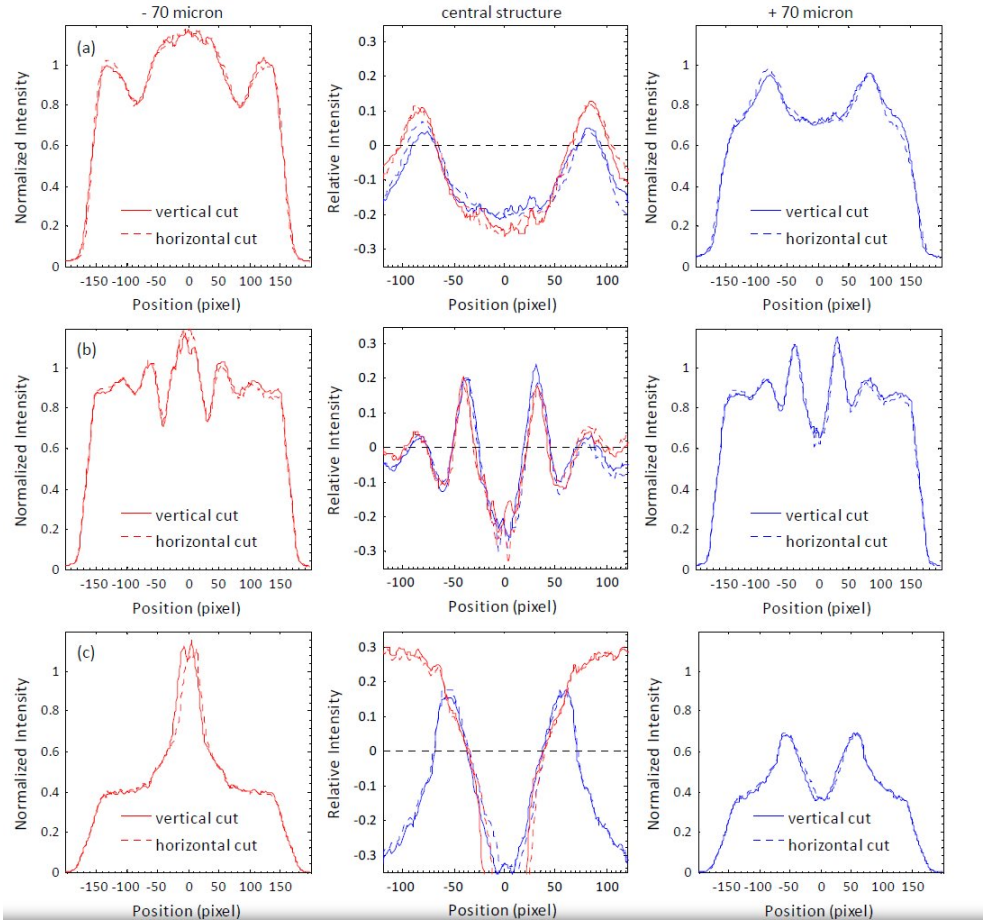

Figure 3.36: Far-field cross-section of 200 μm circular (a), 200 μm octagonal (b), 190 μm hexagonal fibers for two entrance spot positions ($\pm$70 μm). The middle plots show overlapped central structures.

symmetric shapes, even for large displacements when crossing the core-cladding boundary. No significant difference is visible between horizontal and vertical structures. Their central

structures are radial symmetric, too. However, the evolution of such patterns is quite different. Where the central images (i.e. nominal spot position) only show little structures, displaced spots excite highly developed sine-shaped patterns following an inverse relationship between negative and positive displacements. By flipping and aligning the middle parts one may clearly see that the central patterns surprisingly well match together. This leads to the conclusion that intensity re-distribution happens within the central region of far-field patterns. However, their influence on the instrument profile is not fully clear and needs further investigations.

3.4.7 An improved fiber-link

To date optical and mechanical scramblers have been successfully applied to enhance the radial scrambling performance of existing fiber-links. However, these devices have two major drawbacks. Optical scramblers often show high transmission losses, whereas mechanical scramblers usually downgrade the FRD performance. Patchwork fiber cables made from circular and octagonal sections have been initially developed and successfully implemented into the fiber-link of the SOPHIE spectrograph (Perruchot et al., 2011). The combined cable showed surprisingly good performance with scrambling gains greater than G=2200. The SOPHIE fiber-links were built from terminated fiber pieces with Ferrule Connectors (FC-FC). To prove the suitability of combined fibers for the next generation fiber-link of FOCES a mechanical apparatus was developed to combine different sections. Fiber cables

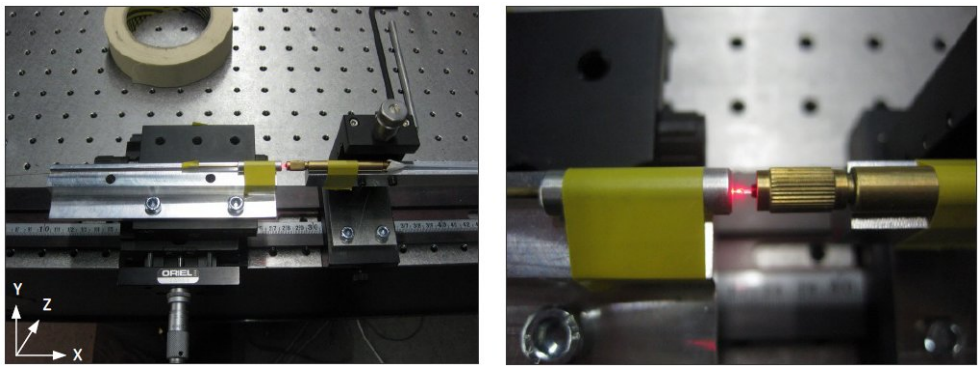

Figure 3.37: Mechanical fiber matcher.

that were built of FC-FC connections provide already good performance. However, there might still be the evidence of core misalignment due to high tolerances in fiber terminations. Light loss at the junction point (splice) is only considerable low if both cores are perfectly aligned. Therefore, adjustable position stages are indispensable when matching different shaped fibers efficiently together and align them with high accuracy. Back reflection losses at glass-air boundaries may be considerably reduced by using a drop of index matching gel with similar refractive index as those of both cores. Figure 3.37 shows a simple mechanical fiber matcher where the left fiber can be aligned in z and x and the right fiber in y direction. Altogether, two different fiber cables have been analyzed with

Table 3.2: Technical specifications of both combined fibers.

	Product core	core $[\mu m]$	length $[m]$	Product core	core $[\mu m]$	length $[m]$
slice 1	OCT-WF200/660N	190.2	2.8	FPB200240280	200	2.8
splice 2	AK482738BA	190.2	2	OCT-WF200/660N	200	2.8

octagonal-circular and hexagonal-octagonal sections (hereafter indicated as splice 1 and splice 2) whose technical specifications are presented in Table 3.2. The results obtained in near-field scrambling are shown Figure 3.38. Compared to single fiber sections both fiber cables showed an outstanding scrambling performance. However, the current bench stabil-

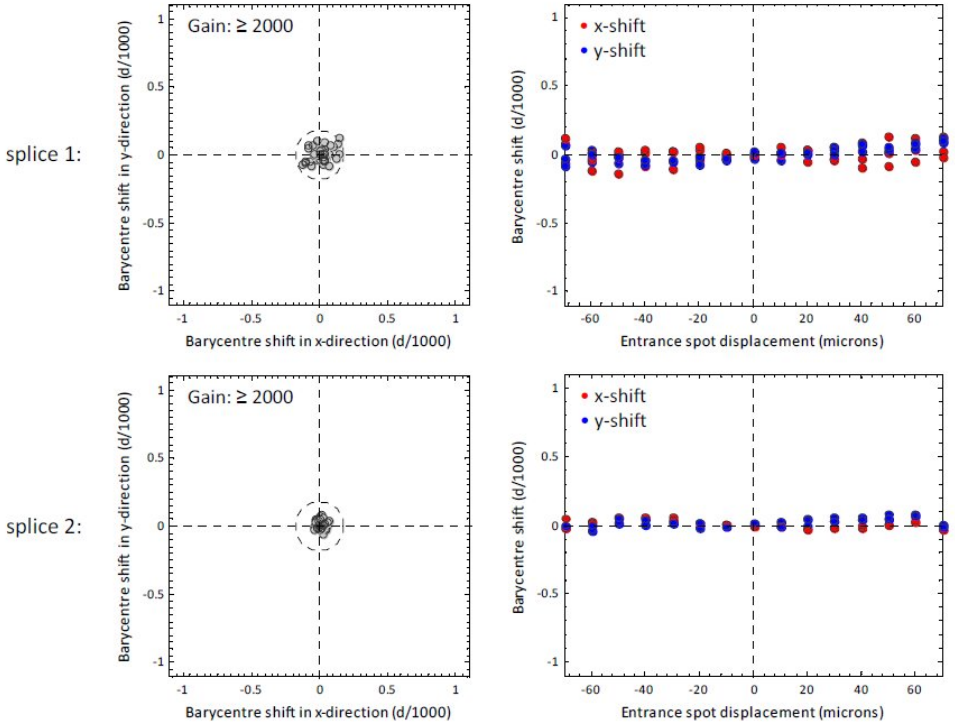

Figure 3.38: Near-field scrambling obtained from octagonal-circular (splice 1) and hexagonal-octagonal (splice 2) fiber cables. The dashed circle on the left graphs denotes the current resolution limit of the scrambling bench (G=2000).

ity is limited by a scrambling gain of G=2000 and the measured geometrical shift already exceeds the bench limit. Thus, the obtained results can not be more clearly distinguished from barycenter fluctuations that are governed by the presence of several sources of noise (e.g. shot noise and thermal noise), i.e. ± 0.058 (d/1000) for 200μm and ± 0.052 (d/1000) for 100 μm fibers. Also differences in scrambling among widely separated central wavelengths are not visible anymore. Considering the maximal amplitudes in x and y directions scrambling gains may be achieved that stay already within the current bench limitation!

The obtained results fit greatly to the stability requirement that shall be fulfilled to reach a spectral stability of 1 m/s. Figure 3.39 shows three cross-sections through near-field

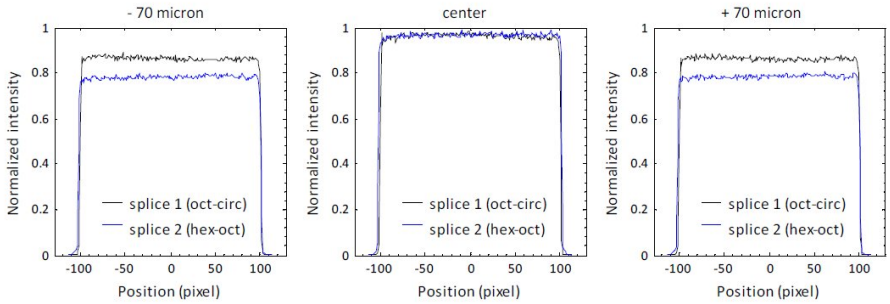

Figure 3.39: Near-field cross-sections of both fiber cables for three entrance spot positions (center, ± 70 μm).

patterns obtained from both fiber combinations. One may clearly see that even for off-centered focal spots the fibers still show top-hat shaped illumination profiles. According

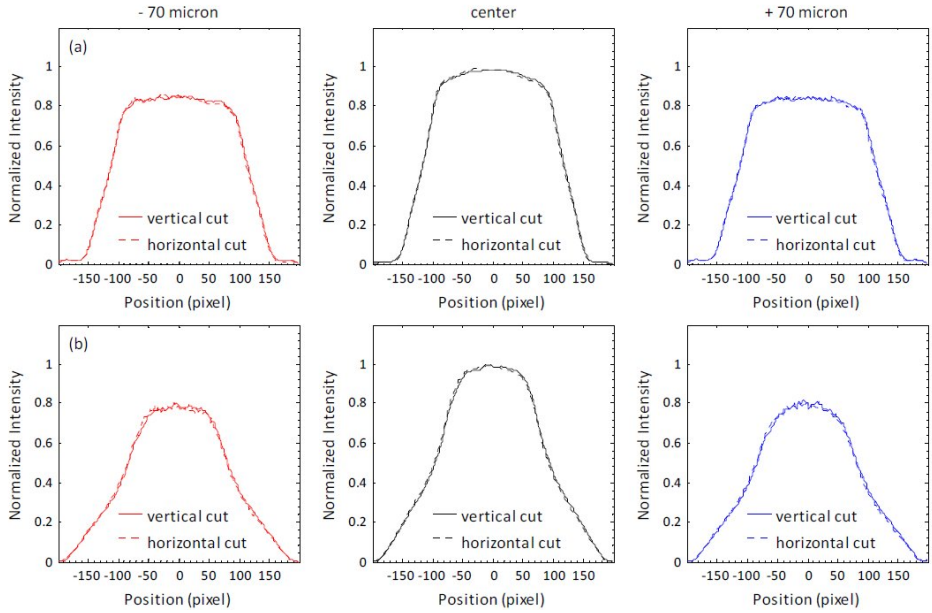

Figure 3.40: Vertical and horizontal cross-sections through far-field patterns obtained from octagonal-circular (a) and hexagonal-octagonal (b) fiber cables for three selected entrance spot positions (center, ± 70 μm).

to previous measurements non-circular fibers deliver typically well defined top-hat shaped near-field profiles even if they were illuminated by an off-centered light cone. However, their far-field patterns do not preserve smooth intensity distributions and typically show diffraction patterns within the central region that gain on visibility for large entrance spot displacements (see Fig. 3.36). Tests performed with mechanically combined fiber cables

have demonstrated that uniformly distributed illumination profiles obviously do not excite any kind of unwanted central structures. The obtained far-field patterns were symmetric over the full scan range. A combination of two different shaped fibers might be a clever strategy to get rid of the highly developed far-field structures. Three selected far-field cross-sections of each fiber cable are shown in Figure 3.40.

As first impression the far-field profiles looked surprisingly good. It can be seen that vertical and horizontal cross-sections are nearly identical without showing central patterns. Only the throughput drops slightly after the entrance spot exceeds the core-cladding boundary. However, apart from their scrambling performance all far-field cross-sections show distinctive broad wings which typically indicate high FRD. This eventually results from insufficient power exchange between guided modes and lossy modes in circular fibers.

3.4.8 Focal Ratio Degradation Test

Focal ratio degradation (FRD) describes the change of input/output focal ratio due to imperfections in optical fibers. This can be a significant parameter when matching telescope-spectrograph systems such as used in astronomy. The figure 3.41 illustrates the problem

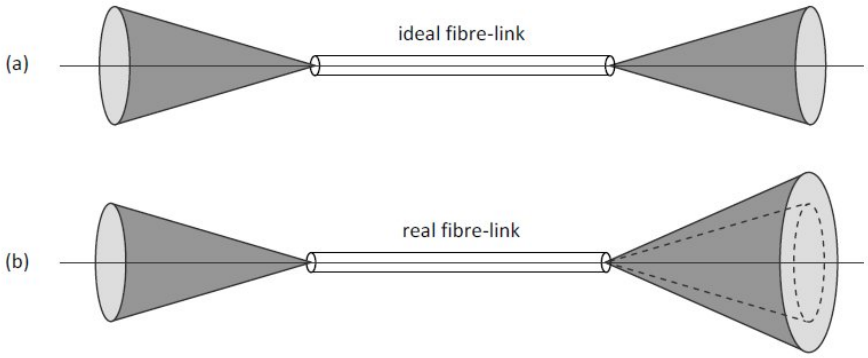

Figure 3.41: Schematic illustration of focal ratio degradation. The top (a) figure shows an ideal fiber with no FRD losses. whereas figure (b) represents a real fiber with a wider output cone than the its respective input cone.

of beam spreading due to FRD in optical fiber. FDR is manly a mode-dependent loss and can be divided in two domains, waveguide scattering and mechanical deformation. Any applied macroscopic bending to a dielectric waveguide causes light losses, on the other hand, tiny microscopic deformations of the core shape are the main cause of the FRD. We performed focal ratio degradation measurements of all test fibers for different input focal ratios ranging from f/2.4 to f/10.3. The apparatus that measures the beam speed exiting a fiber using the light cone technique was in principle similar to the setup presented in Figure 3.28. The following graph shows the results of all FRD measurements as a function of encircled energy and equal input/output focal ratio. The obtained results were compared with a previous measurement conducted with a 100 μm octagonal fiber from CeramOptec. This fiber comes from the first batch of non-circular fibers and was thus not equipped with

a massive protective layer. As it can be seen in Figure 3.42 the circular and octagonal

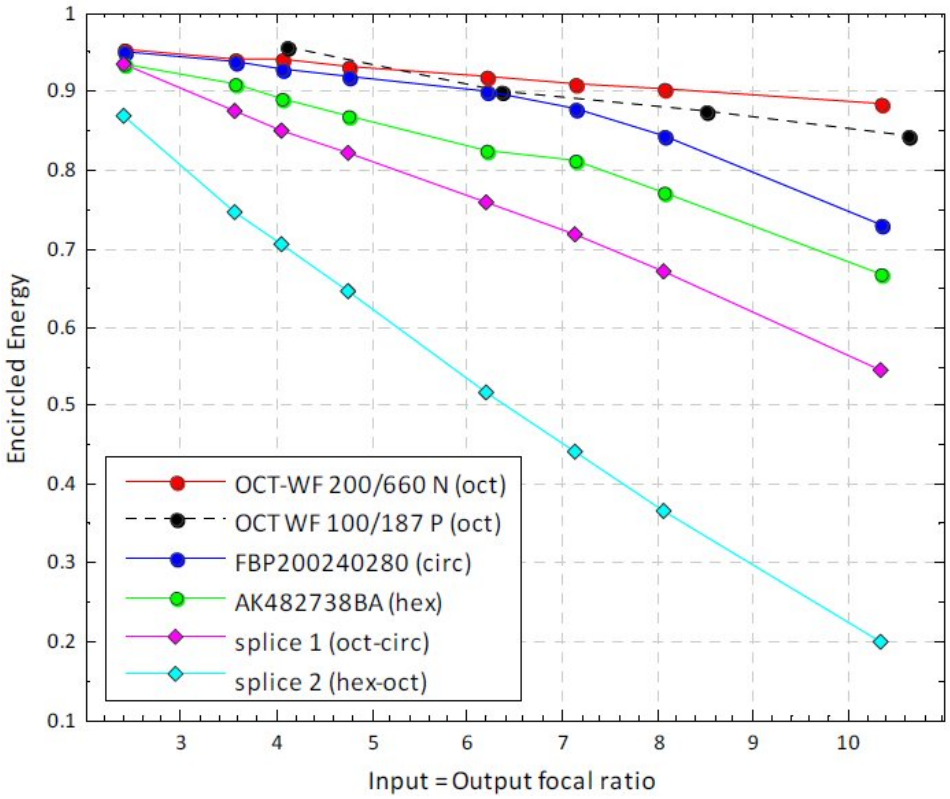

Figure 3.42: Encircled energy as a function of input/output focal ratio.

fiber deliver remarkable results until f/8. Numerically expressed, this means that the circular fiber for example provides 84 percent of the entire energy encircled within an f/8 output beam. The octagonal fiber showed a slightly better result even compared to a 100 μm octagonal fiber, which was previously tested. This eventually implies the evidence of higher beam spreading for small core fibers. Further tests were conducted with combined fiber cables made from octagonal-circular and hexagonal-octagonal sections. Both fibers showed considerably broadened far-field patterns which indicates high FRD. Especially the hexagonal-octagonal fiber cable (splice 2) delivers an unsatisfactory performance. As previously discussed, this could be a serious problem of the stress sensitive hexagonal fiber. However, all far-field patterns obtained from both cables were completely free from any artificial structures. This enables the possibility of testing more unusual combinations in order to find the best performing fiber-link. Of course, coupling fast beams into fibers already lowers the impact of FRD.

3.4.9 Summary

The main features of a scrambling test bed, that enables simultaneous measurement of fiber near-field and far-field, were presented. The setup was subsequently characterized with

respect to long-term stability and resolution. Scrambling properties are being measured from circular and polygonal fibers and first results of a sample fiber system are presented. Moreover, an apparatus for focal ratio degradation (FRD) measurements was assembled in order to compare circular fibers, polygonal fibers and combined fiber cables regarding to beam spreading. The test results from all measurements are summarized in Table 3.3.

Table 3.3: Summary of results obtained from scrambling and FRD measurements. The different columns represent: the product code, the fiber shape, the fiber length, the mean barycenter displacement (scrambling), the scrambling gain calculated from entrance spot displacement of $\pm 35\mu$m, the encircled energy (EE) at f/3.5 and f/8 focal ratio.

Product code	shape	length $[m]$	scrambling $[d/1000]$	Gain $[at 35\mu m]$	EE $[f/3.5]$	EE $[f/8]$
FBP100140170	circ	–	2.3	140	–	–
FBP200240270	circ	4.8	$5.8 - 1.8$	$60 - 200$	0.94	0.84
OCT-WF200/660N	oct	2.8	0.5	650	0.94	0.9
AK482738BA	hex	2	3.4	110	0.91	0.77
splice 1	–	7.6	≥ 0.18	≥ 2000	0.87	0.67
splice 2	–	4.3	≥ 0.18	≥ 2000	0.76	0.36

3.5 Future prospects: FOCES at Wendelstein

In this section a summary of the preliminary study for the new FOCES configuration at the Wendelstein Observatory is given. The transfer of the instrument to the observatory, installation and on site commissioning is foreseen to take place between the end of 2014 and early 2015. FOCES will be placed in the Coude Laboratory at the Wendelstein Observatory and the telescope light will be fed to the instrument via optical fibers along a path of ∼20-30 m. An overview of the new room intended to accommodate FOCES is shown in Fig. 3.43. This is located in the basement of the building under the telescope with dimensions of 3.08×2.30×5.84 m. The spectrograph will be placed on solid rock and surrounded by 20cm-thick concrete walls, two of them in contact to the mountain rock, one close to a building room, the last one facing outside. The ceiling is directly connected with the outside terrace and is removable in case a crane will have to operate at the telescope in the future. The four anchorage bases for the crane are fixed in the mountain rock and protrude from the floor of the Coudé room of ∼20cm.

After the last evaluation phase, it has been decided that the room will host the FOCES spectrograph with all the pressure and temperature control units, a Frequency Comb system (FC) with all the electronics and a calibration unit with a ThAr source and Flat-Field lamp. The other spectrograph VIRUS-W (see sec. 2), originally expected in this room too, will be located in a different ambient. The environment control for FOCES inside the Coude room in Wendelstein will follow substantially the same configuration used for the laboratory test in Munich and presented in the sec. 2, but with some fundamental improvements and modifications.

Important suggestions for the project and the construction of the new environment control system have been obtained from some members of the PEPSI team (Strassmeier et al., 2008) and a first initial study has been subsequently prepared.

The spectrograph will be set up in two shells of thermal and pressure stabilized "boxes", still probably reinforced by an aluminum exo-skeleton. No wood material will be used for the external chamber but likely inner and outer sandwiches of Jackodur panels with rubber sealing profiles fixed to a frame of square steel tubes. Furthermore, a different mechanical design for a new reinforced access to the external box is under development. The total size of the current FOCES thermal system, used for the test at the Munich laboratory, exceeds the dimensions allowed inside the observatory room and thus a new design for the external FOCES box has to be evaluated. As first analysis, the maximum available dimensions for the new FOCES box are 3.08×2.30×5.84 m including an eventually exoskeleton (see Fig. 3.44).

Another important point to consider, concerns the ambient conditions at this location in the building. Here a pressure and temperature monitoring has been carried out in different moments during the last year using 4 temperature sensors and a IP weather station for the pressure. In general, temperature conditions are quite stable inside the room thanks to the good isolation and the use of an air conditioning system (see fig. 3.45). Although in fact a temperature gradient is present inside the room, this is not a prob-

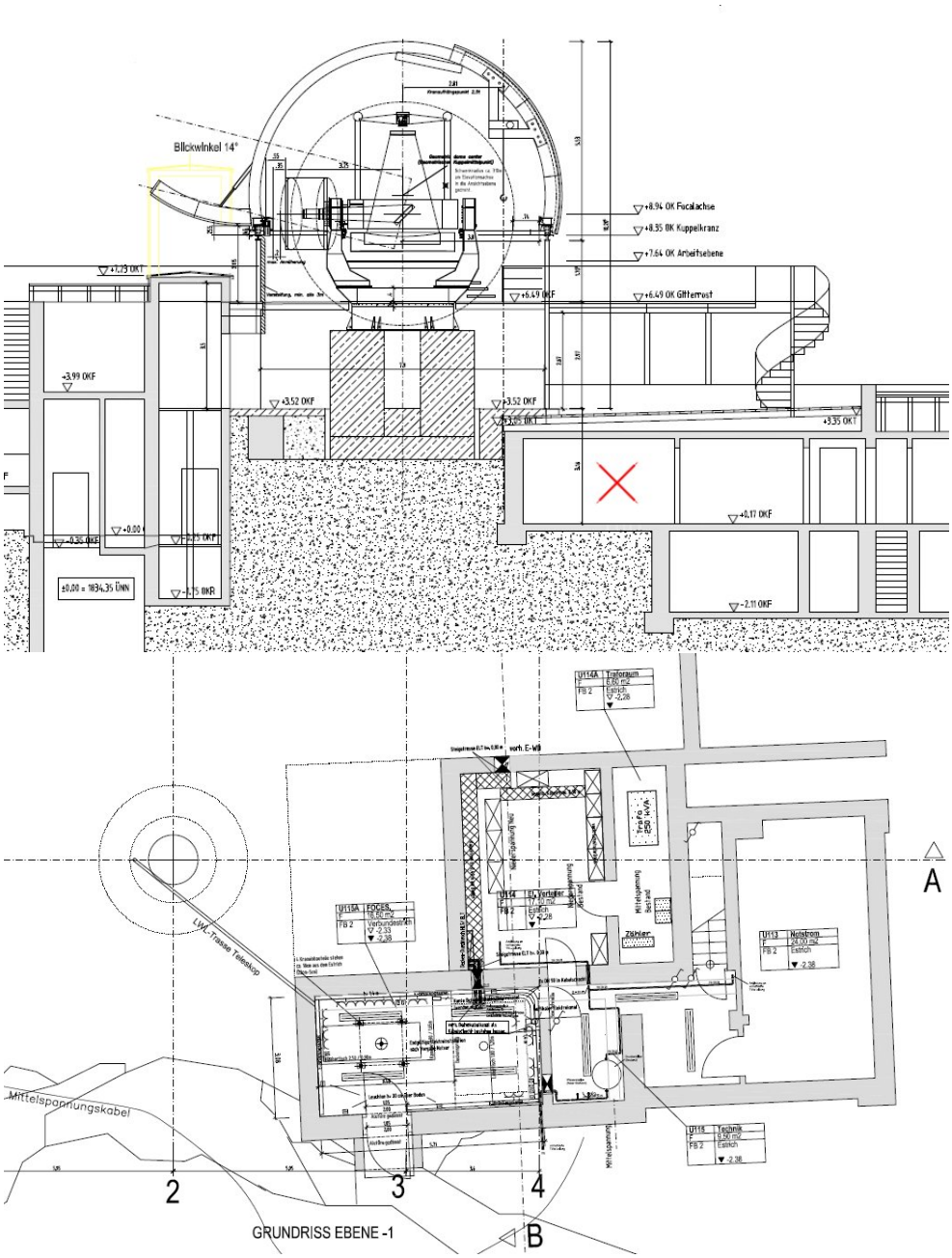

Figure 3.43: Section and blueprint of a portion of the Wendelstein Observatory. The room where FOCES will be placed, is marked with red cross in the vertical view. The channel for the new fiber link between the telescope and the room is also visible in the blueprint below.

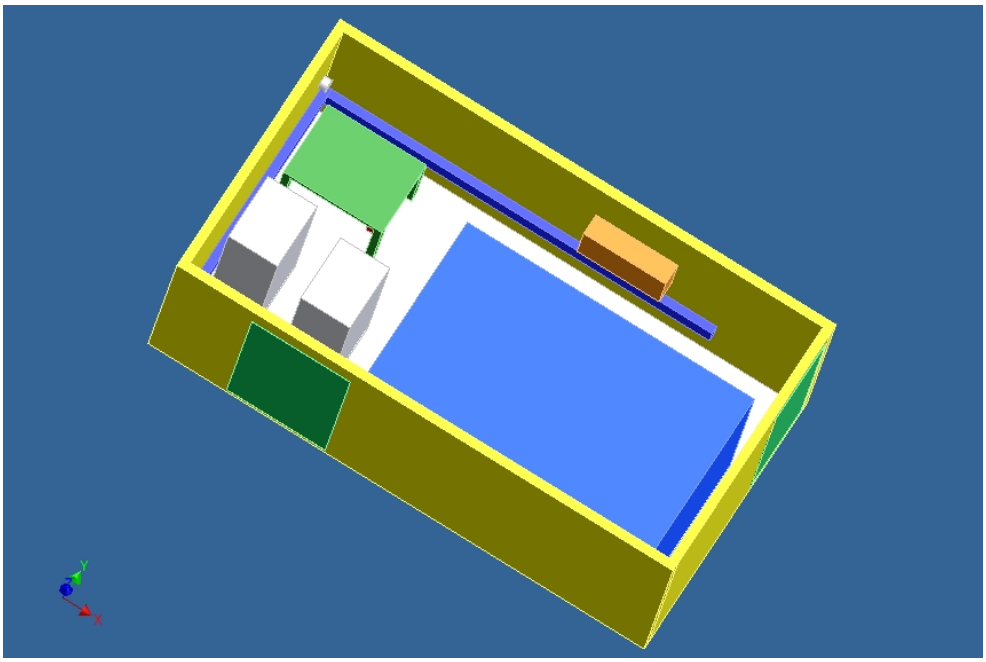

Figure 3.44: Preliminary study for the arrangement of the different instruments in the room. The blue box corresponds to the maximum space available for the FOCES thermal box. The white racks are for the electronics The green table, that probably will have two layers, will host the Astro-Comb system.

lem for our goals, since the temperature behavior is substantially constant in time with variations (peak-valley) of $\sim 2^{\circ}$ C. Barometric pressure instead is quite instable for the not so high altitude of the observatory and thus can vary systematically with the day/night and summer/winter cycle reaching extreme values up to $\sim$40hPa (peak-valley) between summer and winter (see fig. 3.46). However, the proposed project for the FOCES chamber can only support a difference in the outside-inside air pressuring up to $\sim$30 hPa. To answer this problem, the proposed solution consists in develop a new control system that can change the FOCES box pressure and slowly follow the atmospheric behavior until a working regime is obtained. This solution can be justified also by the fact that such days with huge pressure difference correspond most likely to bad weather conditions, when the observations will not be possible.

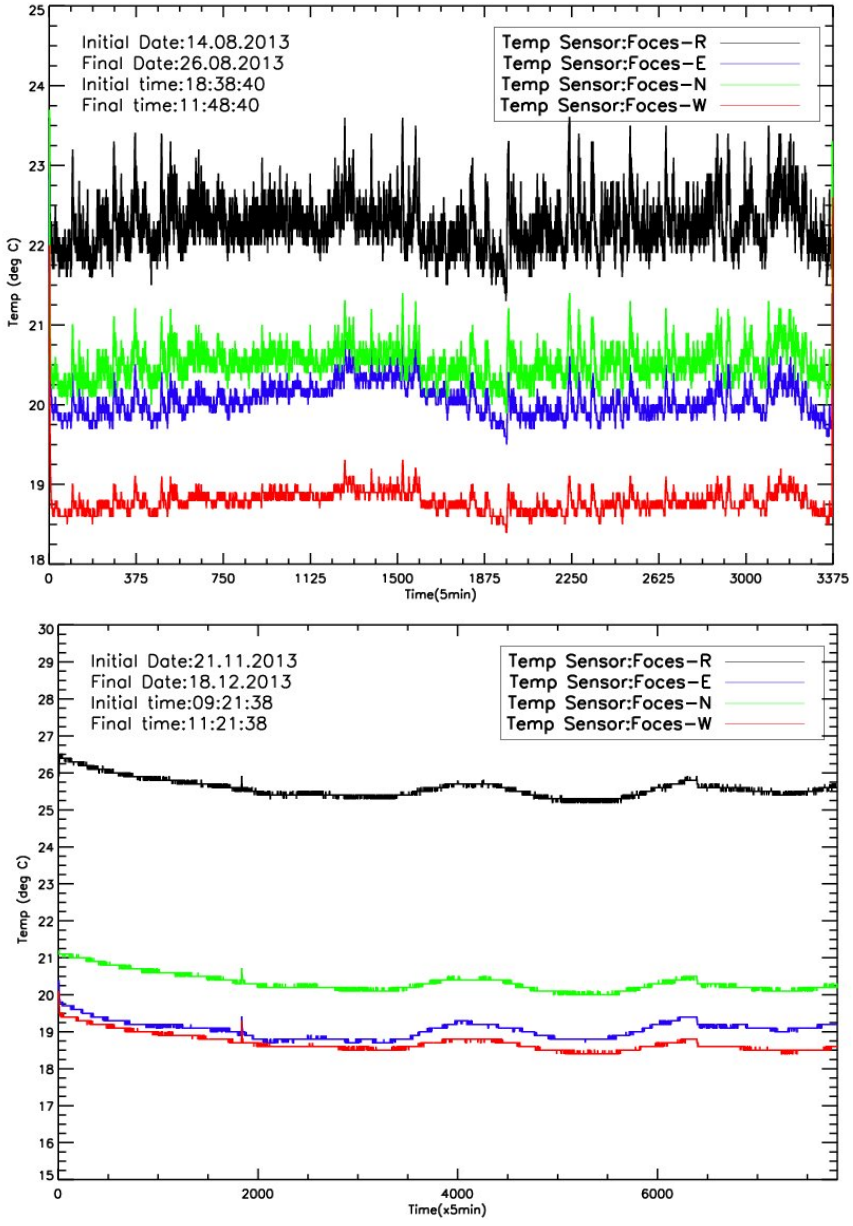

Figure 3.45: Temperature variations acquired in two different moments of the year with the air conditioning system working. The different colors correspond to the temperature behavior at the roof (black) and at three walls of the room.

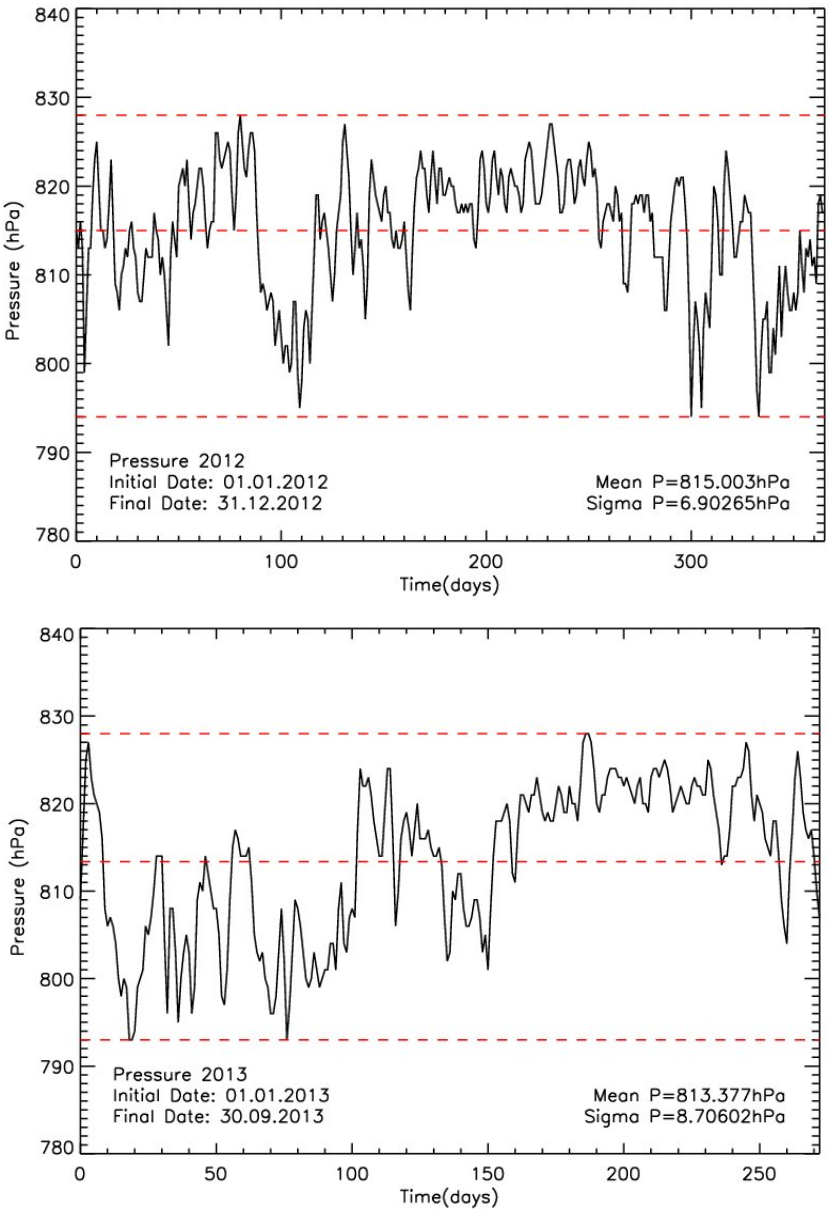

Figure 3.46: Pressure variations at the Wendelstein Observatory acquired in 2012 (top) and 2013 (bottom). The dashed lines indicate the minimum, the maximum and the average pressure values reached.

Chapter 4

Search for giant planets in M67

Figure 4.1: The M67 Open Cluster. Donald P. Waid©

4.1 Introduction

THIS CHAPTER INTRODUCES the second main part of this Phd project, dedicated to the search for giant planets around a sample of main sequence and evolved stars in the open cluster (OC) M67 using radial velocity (RV) measurements. I focused on the acquisition and the analysis of RV data obtained with HARPS (Mayor et al., 2003) at the ESO 3.6-m telescope (La Silla), SOPHIE (Bouchy & Sophie Team, 2006) at the 1.93-m telescope of the Observatoire de Haute-Provence (OHP) and HRS Tull et al. (1998) at the 9.2-m Hobby-Eberly Telescope (HET), to detect signatures of giant planets around their parent stars. Additional RV data came from CORALIE (Baranne et al., 1996) at the Euler Swiss Telescope (La Silla). The goal of this campaign, originally started in 2008, is to study the formation of giant planets in OCs to understand whether a different environment, such as a rich cluster like M67, might affect the planet formation process, the frequency, and the evolution of planetary systems with respect to field stars. In addition, searching for planets in OCs enables us to study the dependence of planet formation on stellar mass and to compare in detail the chemical composition of stars with and without planets. Also this part of the work has been an exciting one. I had the possibility to understand what does it mean to observe with important facilities and to learn several new techniques for high resolution analysis that hopefully I will apply when the FOCES spectrograph will be moved at the Wendelstein Observatory. The following sections present the stars sample and the observations, describe the cluster characteristics, the radial velocity (RV) distribution of the stars, and how the most likely planetary host candidates have been individuated [1].

4.1.1 Why a search in M67?

M67 is one of the most well-studied open clusters. It has been comprehensively observed to establish astrometric membership (Sanders, 1977; Girard et al., 1989; Yadav et al., 2008), precise photometry (Montgomery et al., 1993; Sandquist, 2004), and a rather precise RV and binary search (Mathieu et al., 1986; Melo et al., 2001; Pasquini et al., 2011). X-ray sources have been identified (Pasquini & Belloni, 1998; van den Berg et al., 2004), and it was one of the first clusters for which observations of stellar oscillations were attempted (Gilliland et al., 1991). Its chemical composition and age are very close to solar values (Randich et al., 2006; Pace et al., 2008; Önehag et al., 2011) and it hosts very good candidates for solar twins (Pasquini et al., 2008; Önehag et al., 2011, 2014).

For an open cluster, M67 is quite rich in stars, and its color magnitude diagram (CMD) is well populated in the main sequence, in the subgiant and red giant branches (RGB). With a distance modulus of 9.63 (Pasquini et al., 2008) and a low reddening (Taylor, 2007, E(B-V)=0.041), the solar stars have an apparent magnitude of V=14.58 and a (B-V) of 0.69 (Pasquini et al., 2008), and the cluster contains more than 100 stars brighter than this magnitude, suitable for a RV planet search.

[1] Based on Pasquini L., **Brucalassi A.**, Ruiz M.T. et al. 2012

4.2 M67 stars sample and observations

The M67 sample includes a total of 88 stars with V mag. between 9 and 15, and a mass range between 0.9-1.4 $M_{\odot}$.

We selected main-sequence stars with a membership probability higher than 60% and a proper motion shorter than 6 mas/yr with respect to the average according to Yadav et al. (2008). For the giants we refer to Sanders (1977). The RV membership was established for the latter following the work of Mermilliod & Mayor (2007), who studied the membership and binarity of 123 red giants in six old open clusters, and of Mathieu et al. (1986), who made a very complete RV survey of the evolved stars of M67 with a precision of a few hundreds of m s^{-1}. The majority of the other stars were selected according to Pasquini et al. (2008), who used several VLT-FLAMES exposures for each star to classify suspected binaries.

The bulk of the observations were carried out with HARPS at the ESO 3.6m telescope (Mayor et al., 2003), and this instrument has been our reference for all the observations. After the project started, it was clear that one limitation of our program was the sparse sampling frequency of the observations: typically a few nights/yr awarded in the period January-April, and large gaps, longer than six months, present between one season of

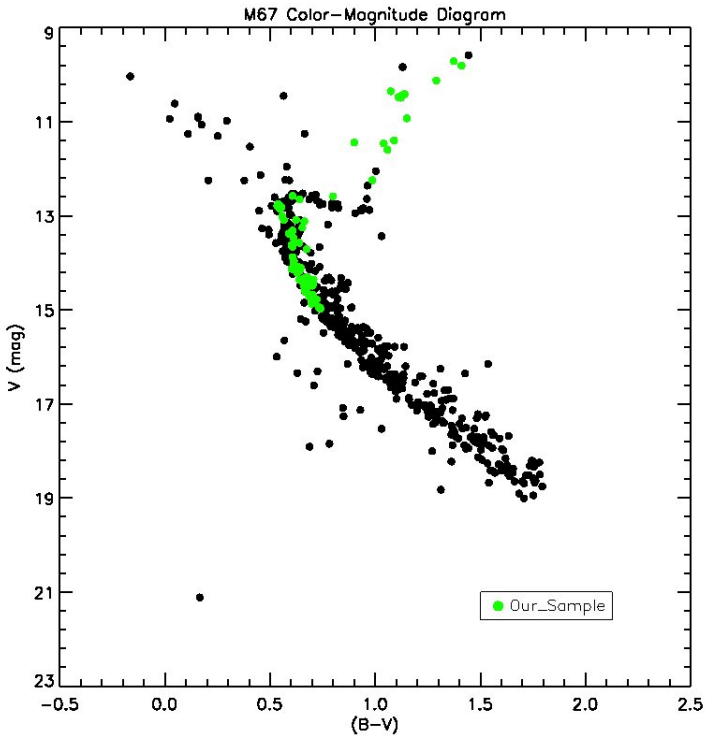

Figure 4.2: Color-magnitude diagram (CMD) of M67. The photometry is from Yadav et al. (2008). Only stars with a high membership probability (≥60%) are shown. The stars observed in this survey are marked in green.

Instrument	HARPS	SOPHIE	HET	CORALIE
N obs.Stars	88	71	26	17
Observations	642	150	134	123
MS stars	58	44	11	
TO stars	7	6	4	
G stars	23	21	11	17
Period	2008-2013	2008-2013	2010-2013	2003-2005

Table 4.1: Table presenting the number of observed stars, the total number of observations, the number of main-sequence (MS), turn-off (TO), giant stars (G) observed for each instrument.

observations and the next. We applied to other facilities for observation time and we could obtain RV data from the spectrograph SOPHIE at OHP and HRS at HET. In parallel, we tried to gather HARPS observations for stars all over the CMD, to have enough points to derive proper zero-point offsets for the other instruments. Table 4.1 summarizes the number of the observed stars and the total number of observations for each instrument updated to the cut-off date of December 31^{st}, 2013.

Given the superior performances of HARPS, we concentrated mostly on the faintest objects with this facility. We added also the sample of evolved stars observed by CORALIE in the years 2003-2005, as part of a program of planet search of giants in open clusters (cfr. Lovis & Mayor, 2007).
Figure 4.2 presents the CMD of M67, using the photometry of Yadav et al. (2008). Stars with at least 60 % membership probability from proper motions are shown. The sample of stars observed in this survey are marked in green.

4.2.1 HARPS observations

HARPS (Mayor et al., 2003) is the planet hunter at the ESO 3.6m telescope. In high accuracy mode (HAM) it has an aperture on the sky of one arcsecond, and a resolving power of 115000. The spectral range covered is 380-680 nm. In addition, to be exceptionally stable, HARPS achieves the highest precision using the simultaneous calibration principle: the spectrum of a calibration (ThAr) source is recorded simultaneously with the stellar spectrum, with a second optical fiber. Since the M67 stars are quite faint for this instrument, we opted to use HARPS in the high efficiency mode (EGGS): the fiber has a larger aperture on the sky (1.2 arcseconds, corresponding to R=90000) and is not equipped with an optical scrambler. This mode is limited to a precision of a few (5-7) m s^{-1}, but it is 30-40 % more efficient than the HAM mode. For our purposes this precision was sufficient, and the improved efficiency ensures that a high enough signal-to-noise (S/N) ratio can be obtained even for the faintest stars. As a rule of thumb we can consider that the precision of HARPS scales as $\epsilon_{RV} \propto 1/(S/N)$ (see below). Since the aim of this giant planet survey was a precision of the single measurement of $\sim$ 10 m s^{-1}, it was possible to reach our goal with limited S/N observations, of on the order of S/N=10 at the peak of the signal. As a

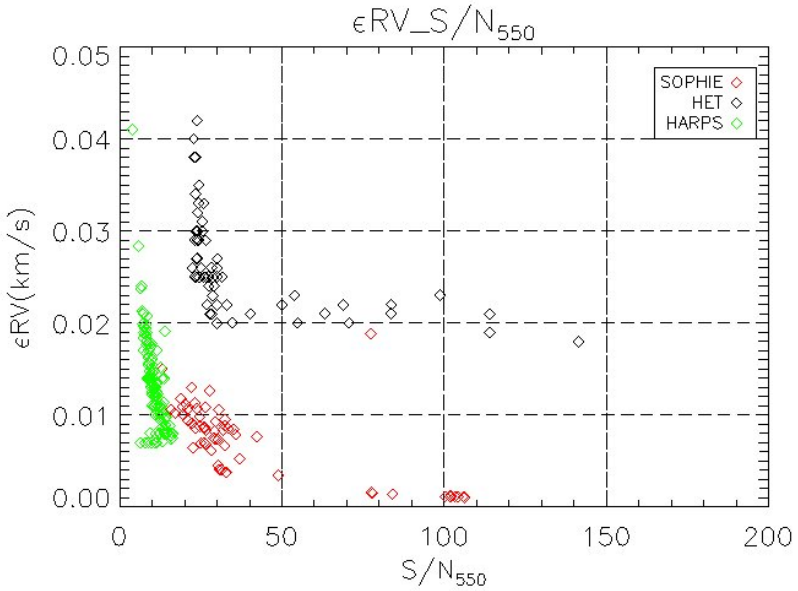

Figure 4.3: Errors in the RV measurement of single observations vs. S/N at 550 nm for HARPS (green points, only observations of MS faint stars), SOPHIE (red points, all measurements, typically TO and evolved stars) and HET HRS (black points, all measurements,mostly TO and evolved stars) are presented. The precision of the majority of the measurements for the faint stars is between 10 and 20 m s^{-1}. For HARPS, systematic dominates the uncertainty at 8m $s^{-1}$for S/N's above ∼13 in EGGS mode. For our SOPHIE observations we estimate that systematic effects (not included in the figure) dominate the error below ∼12 m s^{-1}. The V mag range of the star sample for SOPHIE and HET HRS is brighter than HARPS.

consequence, we could limit the integration time to less than one hour even for the faintest stars. Our HARPS spectra have typically a peak S/N of 15 for the faintest stars.

HARPS is equipped with a very powerful pipeline that provides on-line RV measurements with associated RV errors. After several steps including standard calibration, cleaning of cosmic rays and wavelength calibration using a 'Thorium-Argon lamp' (ThAr) as source, the radial velocities are computed by cross correlating the stellar spectrum with a numerical template mask and then by fitting each resulting cross-correlation function (CCF) with a Gaussian (Baranne et al., 1996; Pepe et al., 2002). For all of our stars, irrespective of the spectral type and luminosity, we used the solar template (G2V) mask obtained from the Sun spectra.

Figure 4.3 shows the error associated with the HARPS RV measurements versus (vs.) the S/N of the observations computed at the middle of echelle order 50 (555 nm) for the faintest stars of the sample (Vmag >14). The RV precision scales approximately as $\epsilon_{RV} \sim 100/(S/N)$ when expressed in m $s^{-1}$and it levels off, as expected, at 8 m $s^{-1}$for S/N above 13 for this order. In the figure, the uncertainty associated with each RV measurement is also given for SOPHIE (red) and HET HRS (black). The magnitude range of the

star sample is between 10.0-14.5 for SOPHIE and 9.8-14.0 for HET HRS.
Between January 2008 and December 2013 we gathered 642 observations of 88 stars with HARPS.

4.2.2 SOPHIE observations

SOPHIE is the planet hunter at the 1.93-m OHP telescope (Bouchy & Sophie Team, 2006). The instrument concept and data reduction is similar to that of HARPS; in high efficiency mode it has an aperture on the sky of three arcseconds with which a resolution of 40000 is obtained. In our first observing runs we observed all M67 stars with SOPHIE, including solar twins, but the smaller telescope diameter and the somewhat more critical weather conditions in winter at OHP than at La Silla, prompted our decision not to use this instrument further for the faintest objects.

We considered 34 M67 stars in common between our targets observed with SOPHIE and HARPS to compute the zero point between the two instruments. For each stars, the average value of the RVs related to the SOPHIE spectra was calculated. The associated error was the standard deviation of the RV values divided by the square root of the number of data points related to a single star. The same was performed for the HARPS RVs related to the single stars. The difference between the mean values of the two telescopes are evaluated and the related uncertainties are computed summing in quadrature the mean value errors. The average of the differences gives the estimate of the offset correction to be applied to the SOPHIE measurements. The uncertainty on the zero-point correction was computed as before, accordingly to the formula for the estimation of the mean value uncertainty.

The comparison gives RV (SOPHIE)= RV HARPS -12.34±8.0 m s^{-1}, with no dependence on the spectral type. This value is confirmed by the observations of the star 104Tau (HD32923), for which a difference of -11.40±7.0 m s^{-1}between the two instruments is found (for a sample of 11 observations with HARPS and 5 with SOPHIE). We finally adopt a zero-point offset of -11.40 m s^{-1}between SOPHIE and HARPS.

We analyzed 150 SOPHIE observations of M67 stars with an associated precision of $\simeq$12 m s^{-1}. Since the observations with HARPS and the other instruments were not simultaneously acquired, we assumed that the precision with which the offsets are computed also includes the contribution from the intrinsic variability of the stars (and of course the photon and the instrumental noise).

4.2.3 CORALIE observations

CORALIE is located at the 1.2m Euler Swiss telescope at La Silla (Baranne et al., 1996). The M67 stars were observed between 2003 and 2005 in the framework of a larger program of search for planets around giants in open clusters (Lovis & Mayor, 2007). The technique used to measure the RV in CORALIE observations is again the same as described for HARPS. As for the other instruments, the zero-point shift to HARPS was computed by using observations of stars in common to both instruments. Since the stars in common are only giants, it is expected that the intrinsic RV variability of these stars is larger than

for main-sequence objects (Setiawan et al., 2004), and not negligible. We used 10 stars in common between HARPS and CORALIE to evaluate the offset, obtaining RV(Coralie)= RV HARPS + 26.8 ± 5.0 m s^{-1}. We have so far gathered 123 observations for 17 giants with CORALIE with a precision associated with these observations of ≃20 m s^{-1}.

4.2.4 HET observations

The HRS, mounted on the 10 m HET telescope Tull et al. (1998), was the last instrument used in our survey. We were granted 134 observing runs in service mode between November 2010-April 2013. The spectrograph is a single channel adaptation of the European Southern Observatory (ESO) Ultraviolet and Visual Echelle Spectrograph (UVES) with four effective interchangeable slit widths and corresponding resolving powers of R∼15 000, 30 000, 60 000 and 120 000.

The configuration was set to a wavelength range between 407.6 nm and 787.5 nm with a central wavelength at 593.6 nm and a resolving power of R=60000. We were able to observe 26 objects selected from our sample with 9.0≤Vmag≤14.6. The S/N for the faintest stars is ∼10.

The spectral orders are defined using an R-4 échelle mosaic with cross-dispersing gratings. Two Charge Coupled Devices (CCD) with 2048×4100 pixels of 15 μm size image the spectrum through an all-refracting camera. A dead space parallel to the spectral orders of ∼ 72 pixel is present between the CCDs, thus one échelle spectral order is lost during the exposure. The two frames coming from the two CCDs composing the detector are saved in two distinct components: red and blue components or components [1] and [2], respectively.

Each run consisted of two exposures: a ThAr calibration frame, is acquired immediately before and after two science exposures of 1320 s (ThAr1, science1, science2, ThAr2). This strategy allows to keep under control any systematic effect which can occurs during the visit and is recommended especially for science exposures longer than 30 minutes in order to reduce the cosmic-rays (CR) hits in each frame.

The HRS is not equipped by an online pipeline and the radial velocities had to be computed using a series of dedicated routines based on IRAF and MATLAB. For a more detailed description of these tools, we refer to Cappetta et al. (2012) and his Phd thesis, as they have been developed as part of his Phd work. Here only a summary of the different steps followed for the reduction and the analysis of the data is given.

Several calibration frames are required in addition to the proper science files in order to correctly reduce the data. These files are the bias, the flat-fields and exposures with the ThAr lamp. Examples of such calibration frames are reported in Figure 4.4. A bias frame is essentially a zero-length exposure obtained with the shutter closed. For a unexposed pixel, the value of zero collected photoelectrons will translate, during the process of reading the image from the CCDs and converting it into a digital image file, in a mean value with a distribution around zero. A pre-defined constant voltage is applied in order to introduce an off-set in the number of counts to avoid null or negative values of the final measured signal. This bias level is removed from all the science and ThAr frames during the calibration phase.

The flat-field is the second kind of frames involved in the calibration. Each pixel has its own read out electronic noise and a different sensitivity to the photons reaching the detector. Furthermore, the optical system is characterized by a given efficiency profile, the intra-order blaze function, which depends mainly on the configuration of the spectrograph. The effects of all these systematics can be detected and removed from the scientific frames uniformly illuminating the detector. A 'Flat-field calibration lamp' is used in order to provided a flat illumination of all the pixels. A dedicated fiber connects the white lamp to the HRS. The exposure time of a flat-field frame is usually as long as 6 sec.

The ThAr frames are essential for the wavelength calibration of the science extracted spectra. The spectrum of such a lamp shows a great number of sharp emission lines which rise over a practically null continuum, although the lines are not evenly distributed over the spectral coverage and their intensities can vary widely: some of them saturate the pixels of the CCDs (see Figure 4.4). The exposure time of a ThAr frame is usually 20 sec.

The pipeline consists in two main parts that in this context are referred as data reduction (DR) and data analysis (DA). The first part individuates the position of all the absorption lines present in the spectra due to the stellar atmosphere and it includes the following steps [2]:

- **Cosmic-rays filtering**: The first step in the reduction of the data is the filtering of the science frame in order to remove the CR hits. In case the exposure time of the science frame is longer than ∼10 minutes, the presence of the CRs becomes significant and can affect the other steps of the DR and, as a consequence, the final quality of the observed spectra.

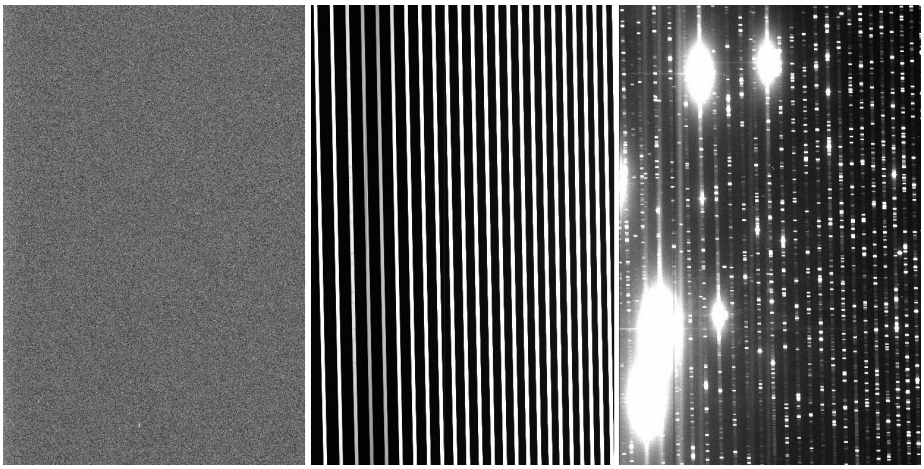

Figure 4.4: Example of the three calibration frames taken with the HRS. From left to right: bias, flat-field and ThAr frames. Saturated lines are clearly visible in the ThAr frame as white ellipses.

[2]Based on Cappetta M., *WTS-1b: the first extrasolar planet detected in the WFCAM Transit Survey*, 2012

- **Frame calibration**: This is the standard procedure that removes the bias applied during the read-out of the data from the detector, as well as corrects systematics of the camera and of the optical system. A set of 5 bias and 12 flat-field frames is generally acquired at the begin and/or at the end of an observing night with the same instrumental setting used for the science and ThAr exposures. The master bias and the flat-field frames (both the red and the blue components) are obtained stacking the respective sets of the single bias and flat-field frames in order to reduce the read-out noise related to each single pixel of the master frames by a factor $\sqrt{5}$ and $\sqrt{12}$ respectively. The bias level introduced during the read-out is removed subtracting from all the frames the master bias. The flat-fielding correction eliminates the noise introduced by the different sensitivity to the photons of each pixel and corrects also for the intra-order blaze function (the smooth efficiency profile variation along each order). This operation consists in the pixel-by-pixel division of the image to be calibrated by the master flat-field frame. The S/N ratio of a spectrum extracted from a calibrated frame results higher by $\sim$10% with respect to that extracted from a non-calibrated one.

- **Apertures definition and tracing**: An observed spectrum results in a series of the stripes visible in the frames, called generally 'orders' or 'apertures', each of them uniquely related to a diffraction order.

  The master flat-field frame is employed for the definition of the position, thickness and inclination of each aperture detected by the CCDs. This operation is fundamental for the correct extraction of the spectra from the science and ThAr frames. The estimation of the spectral flux must be obtained only from the values of the pixels receiving the light coming from the observed target or the calibration lamp.

  In the configuration adopted (standard configuration) the apertures to be defined are 24 in the red component of the detector and 40 in the blue component, corresponding diffraction orders are 78th to 101st and 103rd to 142nd for the red and blue components respectively. The whole set of quantities estimated during the definition of the apertures allows to know uniquely which pixels contribute to the computation of the flux for the extraction of the spectra from the scientific and ThAr frames.

- **Spectral extraction**: The following step of the DR consists in the extraction of the spectra from the calibrated scientific and ThAr frames. The flux value of the spectrum in a particular position along the order is defined by the sum of the contributions of the pixels within the width of the aperture (across the dispersion axis) This operation is repeated for each position along the dispersion axis, i.e. for each line of the frame. Each single spectral order is individually extracted. The final spectrum consists in a sequence of flux values (expressed in ADU) as a function of the position along the order (expressed in 'pixels').

- **Wavelength calibration**: The wavelength calibration of the extracted science spectra is the most critical phase of the DR. In this phase the ThAr spectra are used for

the definition, through polynomial best fitting, of the dispersion function (DF), which allows to assign a wavelength value to each pixel of the extracted science spectra.

In case of 'standard visit', the ThAr calibration exposures are two (ThAr1 and ThAr2). For both, the DF is computed and consequently applied. This leads to two different sets of wavelength calibrated spectra starting from the only set of science extracted spectra. All the steps in the following DA are performed for both these two sets of wavelength calibrated science spectra. The final RV values related to the two different wavelength calibrations, if no unexpected systematics occurred during the observations, are consistent within the uncertainties.

The extracted and wavelength calibrated spectra represent the input of the second part of the whole pipeline: the data analysis (DA). The goal of the DA is to prepare the stellar spectra for the measure of the position of the stellar lines, *i. e.* for the estimation of the RV values of the observed star. It results in:

- **Crop of the spectra**: The initial and/or the final portions of the spectra are removed as the quality of the spectra drops at the extremes and the S/N ratio is too low (S/N$\leq$4). Such portions of spectrum, where the noise (both statistical and/or systematic) dominates over the signal, can critically contaminate the RV measurements.

- **Spectra normalization**: In this step the continuum of the spectra is estimated in order to normalize the stellar spectra. This allows to apply the following steps of the DA (mainly the telluric lines masking and the CR peaks filtering) in a much easier way. The continuum can be removed from a spectrum simply dividing the spectrum by an estimation of the continuum itself. However, the computation of a function that estimates the continuum is quite difficult due to the presence of the absorption lines. These lines are due to the outer layers of gas of the star and the different chemical species present in the Earth atmosphere (in particular water vapor).

- **Telluric lines masking**: In this steps the atmospheric absorption lines, referred usually as telluric features and generated in the Earth atmosphere, are removed from the observed spectra, before being cross-correlated, in order to avoid systematics contamination on the final RV measurements. Such features are significant in the red end of the visible window and in the infrared domain.

- **Cosmic-rays peaks removal**: The preliminary CRs filtering performed on the raw science frame can result insufficient to remove the CR hits that fall on the echelle orders, especially if the observed star is particularly faint ($m_V > 13$) and the exposure time required for an acceptable S/N ($\gtrsim 10$) increases up to 30 minutes. Such hits appear as sharp peaks in the observed spectra. As in the case of the telluric lines, they can introduce systematic uncertainties on the final RV measurements. Thanks to the multiple observations of the same target, the spectra taken at different epochs are compared and the CR peaks, being randomly distributed over the spectral coverage

and not falling at the same wavelength in all the spectra, are detected and removed by a σ-clipping algorithm.

- **Spectra resampling**: The last step of the DA, before the cross-correlation (CC) phase, is represented by the resampling of the wavelengths of both the observed spectra and the template spectrum to a common wavelength binning.

- **Cross-correlation**: The observed stellar spectra are now ready to be cross-correlated with the template synthetic stellar spectra (see sec. 1.7).

  A specific IRAF task performs directly the CC using the input object spectrum and the template spectrum. The peak of the cross-correlation function CCF is fitted with a Gaussian profile considering the 13 points closer to the absolute maximum of the CCF. The Gaussian fit allows to accurately measure the position of the center of the peak, expressed in pixel, and therefore to obtain a RV measure accordingly to the value of the dispersion (km s^{-1} per pixel[3]). Analogously, the full width half maximum (FWHM) of the Gaussian fits determines the uncertainty associated to the RV measure.

  The synthetic spectrum of a G2 main sequence star was employed as template for the CC. It was generated using the MAFAGS code (Grupp, 2004) and normalized with an IRAF task. Each single observed spectral order is cross-correlated with the related template spectrum in order to provide one RV measurement. This and the other sets of RVs related to all the epochs are the output of the CC phase. How the final RV values are computed is described in the following section.

- **Final RV values**: The last step of the DA consists in the computation of the RV mean value and its uncertainty for all the epochs in which the stellar target was observed. For a single epoch, 64 RVs are provided: 24 related to the red spectral orders and 40 to the blue ones. As discussed previously, the presence of strong telluric absorption lines affects significantly several red orders. For these orders, the RVs obtained significantly deviate from the average value of the RVs over the bluer orders. However they can be easily detected. Focusing on the set of RVs for each epoch, the outliers are firstly rejected performing a σ-clipping algorithm. Then, the mean value is estimated by computing the average value over the orders that passed the σ-clipping selection. The average is weighted with the inverse of the uncertainty square of each single RV value. Finally, the uncertainty on the mean value is obtained computing the standard deviation of the RVs, via bootstrap of the sample, and dividing it by the square root of the number of the orders.
  The RV values computed from the raw data represent the measures of two distinct movements projected along the line of sight: the movement of the observed star and the displacement of the observatory within the heliocentric rest frame as a function of the time. The latter is the result of the sum of three different movements: the

[3]For $R = 60\,000$ and 4 pixels per resolution element, the dispersion is 1.25 km s^{-1}/pxl

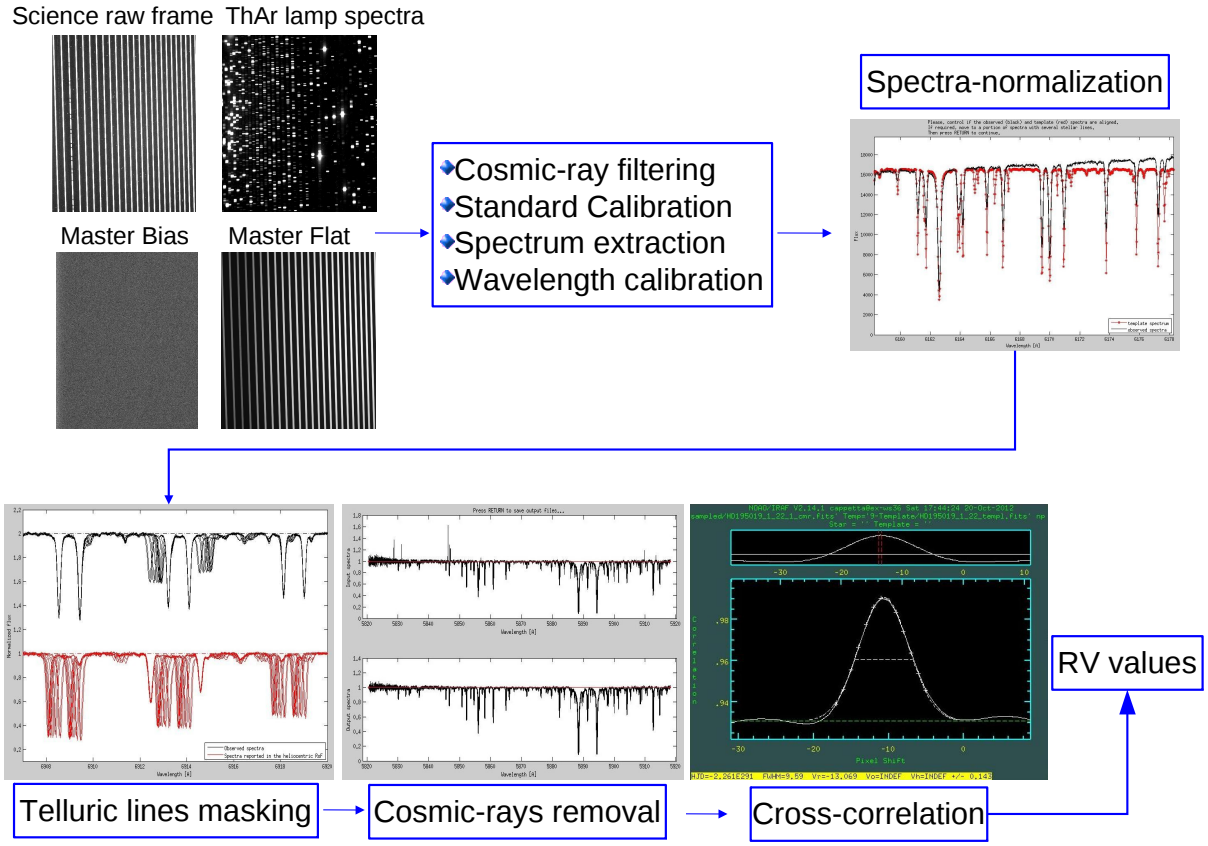

Figure 4.5: Main steps of the HRS HET pipeline to obtain RV measurements.

revolution of the Earth around the Sun, the rotation of the Earth around its proper axis and the rotation of the Earth around the Earth-Moon center of mass. The overall displacement introduces a Doppler shift in the observed spectra of the order of few tens of km s^{-1}(up to ∼60km s^{-1}) which varies on time-scales of ∼6 months. In order to obtain the true RV variation of the star only, the heliocentric velocities of the observatory must hence be subtracted. The final uncertainties on the single RV measures were $20 - 40$ m $s^{-1}$with a S/N of the spectra related to the faintest stars of ∼10.

Fig. 4.5 schematically summarizes the main steps of the HRS HET pipeline (Cappetta et al., 2012). Six stars in common showing a flat trend of the RVs measured with both HRS HET and HARPS, were used for the comparison of the two instruments. When considering the different analysis used for the HRS HET data with respect to the other instruments, it is unsurprising to find a larger offset with respect to HARPS for HRS HET than for the other instruments: RV (HRS)= RV(HARPS)+ 242.0 ± 12m s^{-1}. The mean values of the HRS HET and HARPS RVs are shown in Figure 4.6. In the lower panel of the

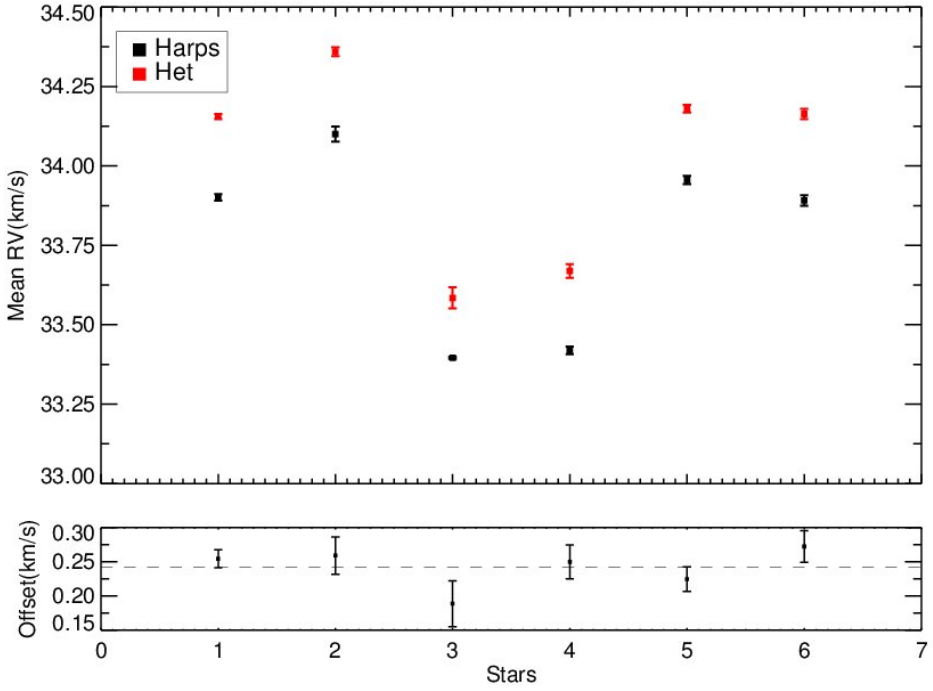

Figure 4.6: *Upper panel*: HARPS (black) and HRS HET (red) RVs mean values for 6 stars of the `M 67` sample observed in common and showing a flat trend of the RVs. *Lower panel*: offsets between the HARPS and HRS HET mean RV values. The zero-point mean value weighted on the squares of the single offset uncertainties is shown by a dashed line.

figure, the difference between the two mean values are plotted. The HRS HET RVs are systematically higher than the HARPS ones, with an offset between the two data series likely given by a combination of more factors. First, the observations with HARPS and HRS HET are obtained with a different spectrograph resolution, R=90000 and R=60000 respectively. Then, unlike HRS HET, HARPS is provided with optical scrambling (Avila & Singh, 2008) for the optical fibers connection between the telescope focus and the entrance of the spectrograph. Finally, the pipeline for the data reduction and analysis are different. In particular, a synthetic stellar spectrum is employed with HRS for the CC of the spectra observed instead of a binary mask used with HARPS. Furthermore it has to be noted that in the case of HRS HET a check of the absolute wavelength calibration of the scientific spectra has been performed using the brightest sky emission lines in a stellar spectrum, primarily due to neutral Oxygen O I in the Earth atmosphere. These sky lines can be identified and fitted with a Voigt profile. Comparing the measured central wavelength of each line with the expected values (Hanuschik, 2003) a shift of $\Delta v \sim 250 \pm 50\,\mathrm{m\ s^{-1}}$ was found with a flat behavior over the whole spectral coverage. This is quite in agreement with previous result.

Table 4.2: The binary candidates of our sample

Object	V	B-V	RV(km/s)	σRV(km/s)
Y288	13.9	0.637	37.691	1.299
Y769	13.5	0.641	$CCF double-peaked$	
Y851	14.1	0.617	34.759	1.417
Y911	14.6	0.673	33.738	0.703
Y1090	13.8	0.650	35.186	1.265
Y1304	14.7	0.723	32.512	2.670
Y1758	13.2	0.653	29.653	1.521
Y1315	14.3	0.693	34.885	0.801
Y1716	13.3	0.619	36.205	0.651
Y1067	14.6	0.642	33.667	1.030
S1583	$B = 13.1$		$CCF double-peaked$	

4.3 Binaries

Once corrected to the zero points of HARPS, all the observations for each star were collected and analyzed together. One of the first findings of our survey is that, despite all the stars having been previously observed and found to have no evidence of companions, 11 stars in the original sample of 88 (13%) show RV variations that are too large to be produced by an exoplanet, or by a non-stellar object (cfr. Table 4.2). We considered as binary candidates all the stars displaying a peak-to-peak RV amplitude of at least 1.7 km s^{-1}. Considering half of the difference as a lower limit to the orbital semi-amplitude, this amplitude corresponds to a companion of 15 Jupiter masses on a 30 day period for a circular orbit around a star of $1.2M_{\odot}$.

The RV range spanned by these stars is so large that planetary companions can be excluded, as can be seen from Figure 4.7, where the RV measurements for 9 of the binary candidates are shown. The binary/long-term RV variable nature of 7 of them was confirmed by D. Latham (private communication), who is performing a long-term RV monitoring of more than 400 M67 stars (Latham, 2006). These stars are binary candidates, and were not observed after a large variation of their RV was measured. Given that these stars are high-probability M67 proper-motion members, and that their RV is close to that of the cluster, it is very likely that they are spectroscopic binaries belonging to the cluster.

Two stars (S815 and S1197) show peak to peak RV variations of the order of 700m s^{-1}; they are retained in the single star sample, although the amplitude of the RV variation is possibly too high to host a planet.

In the process of evaluating the effects of binaries in M67 CMD, we found that binaries are identified in many works in the literature and sometimes different names are used; in addition several works have been published after the compilation of Sandquist (2004). We therefore opted to create a new catalog of binaries in M67 that includes our candidates, binaries from the literature, as well as binary candidates from X-ray observations. The catalog is given in Table 4.4, with reference to the original studies.

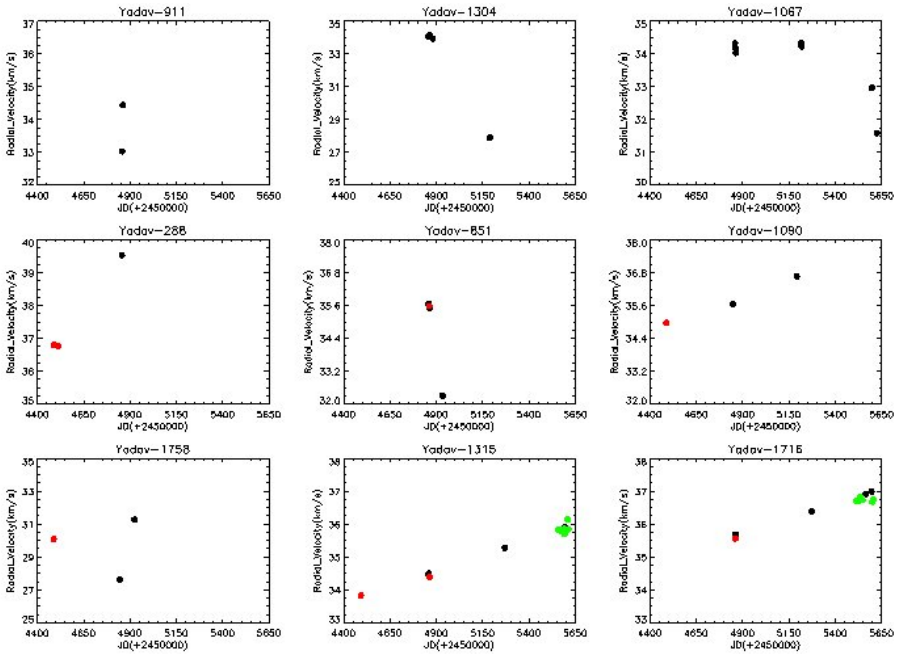

Figure 4.7: Radial velocity measurements of 9 binary candidates. The minimum span in RV is about 1.7 km s^{-1}. The error bars are not shown. Different colors refer to HARPS (black), SOPHIE (red), and HRS HET (green) observations. The other two binary stars not shown have double-line CCF, so are double-line spectroscopic binaries.

The binary stars from Table 4.4 are plotted in Figure 4.8. The high percentage of binaries in M67 is unsurprising, given that to retain the stars for such a long time, M67 has the most massive stars in the core, and some mass segregation has occurred.

A complete census of the binaries in M67 is helpful because this cluster can be used to test the effects of several mechanisms debated in stellar evolution, such as diffusion and overshooting (Magic et al., 2010, see e.g. the discussion in). Cleaning of the CMD is especially important in the region of the turn-off, because, as is clear in Figure 4.9, in that region binaries cannot be photometrically distinguished from single main-sequence stars. They separate more clearly along the main sequence, where a detached binary sequence is present, although several fainter binaries lie on the main sequence and are photometrically indistinguishable from single stars in the CMD.

In his extensive study of M67, Sandquist (2004) created one table containing the fiducial sample of single stars and a second table with a list of interesting or peculiar stars. In the first list, 11 stars are indicated as possible binaries according to our catalog (S1305, 1458, 990, 1300, 1075, 1201, 982, 1102, 1452, 951, 820), and one star (S1197) has large RV variations. Among these 11 binary candidates, some have weak evidence coming from a few FEROS or FLAMES multiple spectra, which had a limited precision. For instance star S1305, a low-RGB star, is indicated as a suspected binary in Pasquini et al. (2011), but is not confirmed by our higher precision measurements. Other Sandquist' single-star

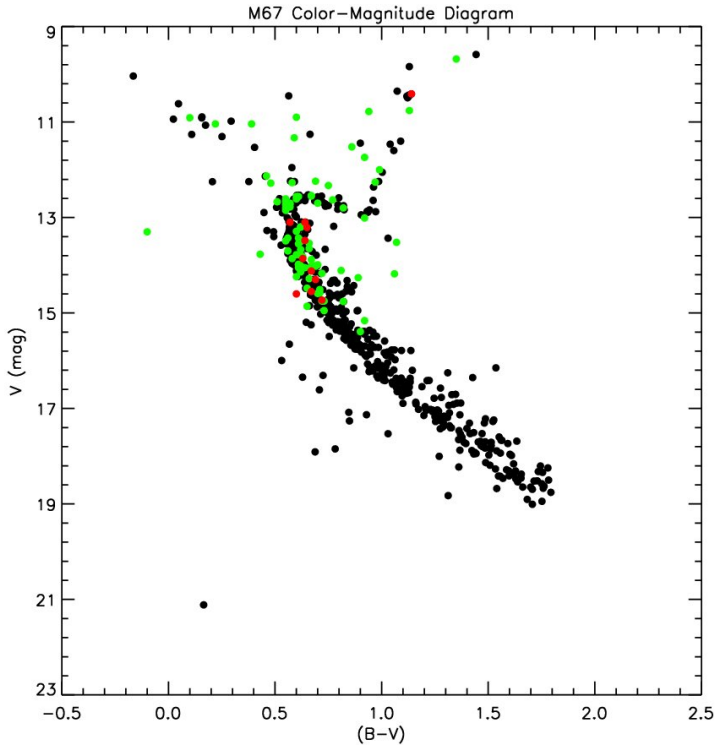

Figure 4.8: Color-magnitude diagram (CMD) of M67. Only stars with a high membership probability ($\geq$60%) are shown (Yadav et al., 2008). The binary stars from Table 4.4 are plotted as green points, with over imposed in red the binaries candidates detected with our observations.

sequence fiducial stars (e.g. S982, 1201, 1452) are, on the other hand, confirmed to be binaries by our high-precision RV measurements.

Three stars of the Sandquist 'unusual stars' table are confirmed to be RV multiple candidates according to Table 4.4 (S1292, S816, S1011).

The above results show that, in spite of the large efforts to clean the CMD of M67, a number of unknown binaries are still present and the detailed comparisons required to distinguish between different potential mechanisms (Magic et al., 2010) could strongly benefit from additional cleaning, in particular around the turn-off.

4.4 Color-magnitude diagram

In Figure 4.9, we report the observed region of the color-magnitude diagram CMD, indicating in different colors the the position of the stars of our sample (green), including the three planets hosts (red) presented in the next Chapter and the solar analog, as determined in Pasquini et al. (2008).

We superimposed the isochrones from Pietrinferni et al. (2004) with solar metallicity, moderate overshooting and age corresponding to 3.5 Gyr (black curve), 4.0 Gyr (dark-blue

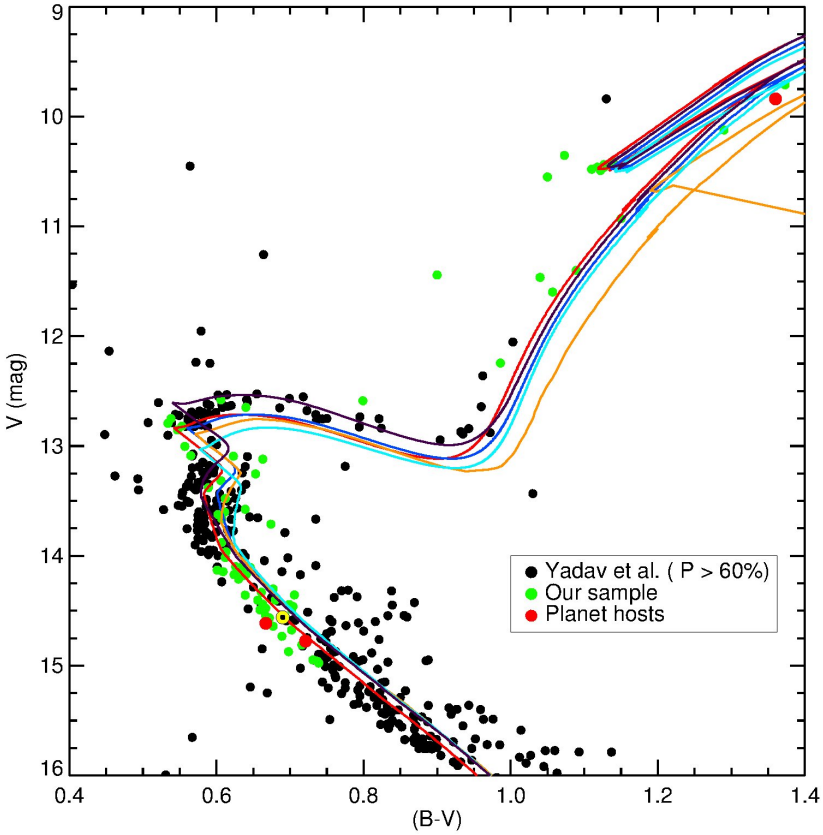

Figure 4.9: CMD of M67 (photometry from Yadav et al., 2008) for probable members ($P_\mu > 60\%$). The isochrones are taken from the BaSTI library (Pietrinferni et al., 2004). The isochrones in black, dark blue, and light blue correspond to 3.5 Gyr, 4.0 Gyr, and 4.5 Gyr with a reddening E(B-V)=0.041±0.004 (Taylor, 2007). The isochrone in red is a 4.0 Gyr with a lower reddening (E(B-V)=0.02). The isochrone in gold is a 4.47 Gyr from Girardi et al. (2000) with E(B-V)=0.041±0.004. The location of the Sun, if it were within M67, is marked with a ⊙ in yellow.

curve) and 4.5 Gyr (light-blue curve). We also included the 4.0 Gyr isochrone (red curve) with a slightly lower reddening (E(B-V)=0.02 instead of 0.041 (Taylor, 2007)). This curve seems to match better the colors of the turnoff (see also the discussion in Pasquini et al., 2012). In the same figure, we report the Padova isochrone using E(B-V)=0.041±0.004, with solar metallicity, age 4.47 Gyr, and Y=0.26 (Girardi et al., 2000).
The isochrone fits the turnoff very well, but produces a RGB and clump that are too red. The mismatch is not dramatic and may indicate some problem in either the bolometric correction used or some of the free parameters adopted (e.g. mixing length). We also note that there are a number of stars, apparently with constant RVs, and a high probability of proper motion membership, that are above the main sequence. This analysis confirms that, in addition to its extraordinarily similar abundance pattern, M67 has an age compatible with that of the Sun.

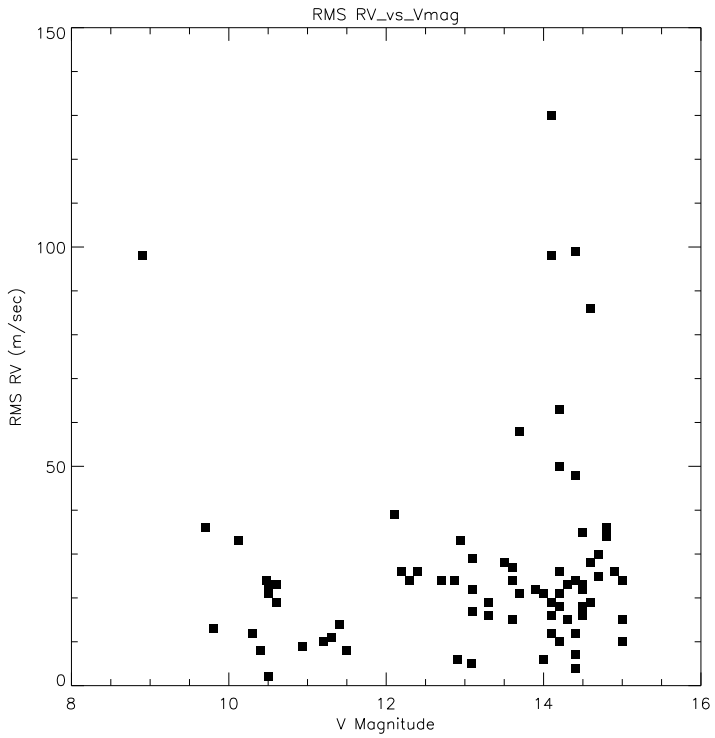

Figure 4.10: Radial velocity (RV) variability of the observed stars vs. V magnitude. The bulk of the stars show a flat behavior. This is likely a combination of larger intrinsic variability for the more luminous stars and larger measurement uncertainty for the faintest ones. The excess of variability seems real, and may indicate that more stars have low mass companions.

4.5 Radial velocity variability

As first step to individuate our planet host candidates we investigated the observed variability of the RV measurements for each star. Since all the stars belong to the cluster with high probability, we had the unique opportunity to study how RV variability changes along the CMD diagram, for a given chemical composition and age.

Setiawan et al. (2004) and Hekker & Meléndez (2007) showed that the intrinsic RV variability of giants increases with stellar luminosity and becomes large for bright, low-gravity giants. Since we cover a six magnitude interval, it could be useful to determine for each magnitude or evolutionary status a typical average RV variability. This quantity should depend solely on both, the intrinsic stellar RV variability and the RV measurement error (typical photon errors associated with the bright stars are smaller because faint star observations are limited by photon noise).

Figure 4.10 shows the rms RV vs. V diagram for 75 single stars. Binary candidates have been excluded, and the two stars (S815 and S1197) with high RV variability are not shown.

Some of the stars with very little or no RV variability have very few observational points,

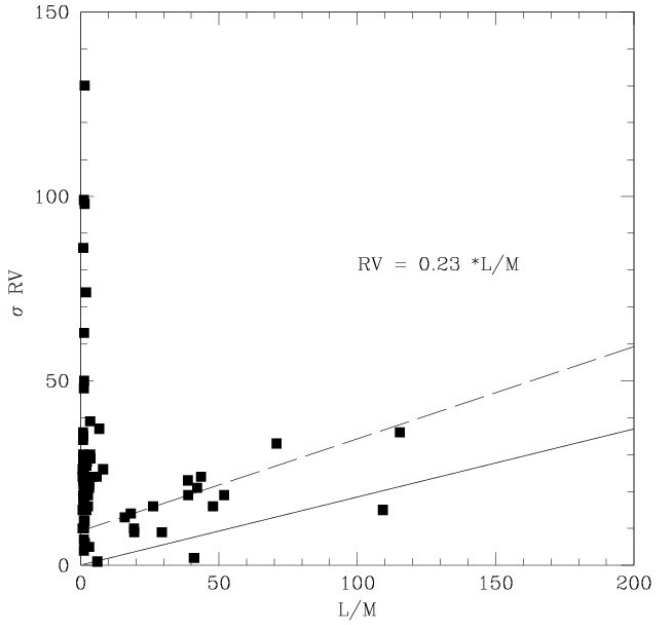

Figure 4.11: Radial velocity variability σ RV of the observed stars vs. the luminosity/mass ratio. The solid line represents the scaling law proposed by Kjeldsen & Bedding (1995) to extrapolate solar type oscillations to other stars. To plot the scaling law a fixed value (1.2 $M_{\odot}$) for the mass has been assumed. To first approximation all M67 evolved stars have the same mass. The continuous line is the scaling law, the dashed line is the best fit to the evolved stars data, which is perfectly consistent with the scaling law, when measurement uncertainties are taken into consideration.

and their small scatter is very likely the result of our low data statistics. The increase in RV scatter with stellar luminosity observed in field stars (Setiawan et al., 2004) is not evident in our sample. There is a possible hint of an increase in the range of magnitudes 12<V<14, but the RV variability does not increase further for the more luminous stars.

As a general conclusion, we can say that the RV variability shown in Figure 4.10 is basically constant at 20 m $s^{-1}(\sigma)$, independent of the stellar magnitude. The bulk of our observations have a RV variability that is well represented by a Gaussian distribution centered at 20 m $s^{-1}$of width σ = 10 m s^{-1}.

The unexpected flatness of the RV variability with magnitude is most likely due to the combination of two effects. In the evolved stars, some measurable stellar RV variability is present, while for the faint main-sequence stars the uncertainty in the measurements increases because of the limited S/N. To investigate these points, in Figure 4.11 we plot the RV variability as a function of the stellar luminosity to mass ratio (L/M). According to Kjeldsen & Bedding (1995) the RV jitter induced by solar oscillations is expected to grow according to the law RV $\propto$ 0.23*L/M (with RV expressed in m s^{-1}). This law is represented by the continuous line. Figure 4.11 illustrates the very good agreement between this scaling law and the RV variability of evolved stars in M67. The continuous line remains

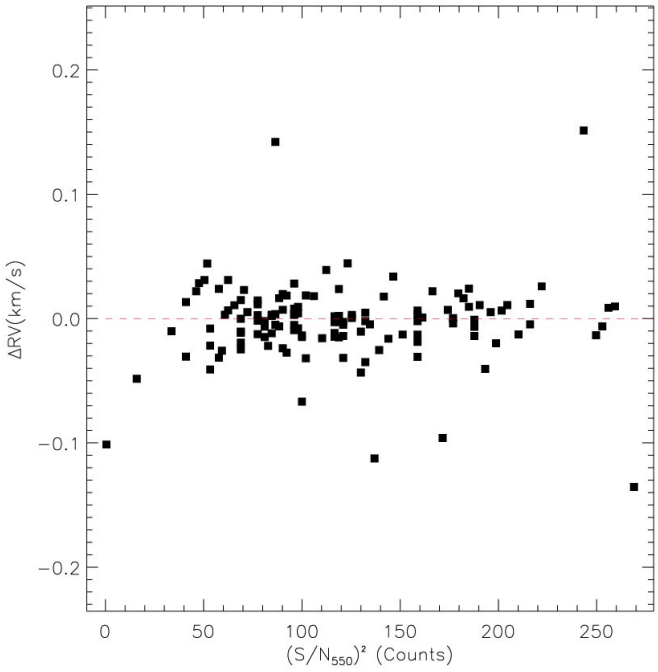

Figure 4.12: Difference in RV measurement from the average for faint stars in the sample vs. the square of the S/N at 550 nm, a quantity that is roughly proportional to the flux recorded in the spectra. No trend is visible, and this indicates that if detector charge transfer inefficiency is present, it does not affect our measurements in a detectable way.

just below the measurements, but this does not take into account that the measurements, in addition to the stellar intrinsic variability, include measurement uncertainties that are not negligible. A fit to the evolved star data (L/M > 5) gives $\sigma_{RV} = 0.25$ L/M + 9.3 (m s^{-1}), which is shown by the dashed line in Figure 4.11. The observations and the predictions therefore match quite well, when the measurement errors are considered. We note that this comparison implies that the oscillation RV amplitude and its variations are of comparable size. More precise RV measurements would allow us to quantitatively investigate this point in more detail. We conclude that the M67 evolved stars show signs of intrinsic RV variability and that for most of the evolved stars the observed RV variability is consistent with that expected from the Kjeldsen & Bedding (1995) scaling law for solar-type oscillations.

As far as the lower main sequence is concerned, the behavior of the faint stars in our sample (which are also the least massive ones) is quite interesting, because if the RV variability observed were induced by substellar companions, this would already indicate a correlation between planet frequency and mass in M67. There are good arguments to believe that an RV variability as large as 20 m s^{-1}cannot be caused by intrinsic stellar noise, because stellar noise for solar stars scales with activity and therefore age, and M67 is almost as old as the Sun (see e.g. Saar et al., 1998; Dumusque et al., 2011). On the other hand we have seen that the uncertainties in the RV measurements of faint stars is

Table 4.3: Stars with the largest RV variability, which are candidates to host substellar companions.

Object	V	B-V	RV(km/s)	σRV(km/s)
Y401	13.7	0.566	33.203	0.058
Y673	14.4	0.665	33.766	0.099
Y1051	14.1	0.595	33.290	0.130
Y1587	14.2	0.600	33.434	0.063
Y1722	14.2	0.560	34.460	0.098
Y1788	14.4	0.622	34.150	0.048
Y1955	14.2	0.589	33.192	0.050
Y2018	14.6	0.631	31.953	0.086
S488	8.9	1.550	32.910	0.089
S815	12.9	0.497	33.326	0.378

above 10 m s^{-1}(cfr. Figure 4.3) but well below 20 m s^{-1}. We investigated whether other instrumental effects, not included in the data analysis, could affect the RV measurement precision at low count levels. At least two effects could influence the observations, and we investigated whether our measurements depend on observational parameters, such as the observed flux or airmass. A dependence on flux could be induced, for instance, by CCD transfer inefficiency, which has been reported to be high in SOPHIE (Bouchy et al., 2009). A dependence of RV on airmass could instead indicate that some systematic effects are induced by the HARPS atmospheric dispersion compensator at high airmass or by the guiding system of the telescope. For every solar star, we therefore computed the ΔRV of each observation with respect to the average stellar radial velocity, and analyzed all the measurements of all stars together, as functions of counts and airmass. No trend is present, as is clear from Figure 4.12, where the ΔRV is plotted vs. the square of the S/N at 550 nm. We conclude therefore that these two quantities do not affect our measurements in an appreciable way. We note that in these comparisons only the HARPS data have been used, because they by far dominate the faint star statistics. With a RV variability for the whole sample centered at 20 m $s^{-1}$and a width σ of 10 m s^{-1}, we could safely assume that stars with a RV variability at or above 50 m s^{-1}were very good candidates for low mass companion hosts.

A number of stars (9) stand out clearly from the general constant trend of Figure 4.10, showing a σ RV variability of 50 m s^{-1}or larger. These stars (plus S815, and S1197, which are not included in the figure) were considered as candidates to host giant planets or substellar objects and deserved to be investigated further. The list of the most likely 11 candidates is given in Table 4.3. In parallel, we decided to follow also another 6 candidates with smaller ($\sim 30 - 40$ m s^{-1}), but still interestingly RV variability. In fact the large scatter in the radial velocities, in excess of the measurement errors, could indicate that more stars, in addition to those indicated in Table 4.3 were suitable candidates for hosting planets.

Table 4.4: Binary candidates in M67. Stars $B-V$ colors, apparent V magnitudes. For object identifications, 'S' are from Sanders (1977);'YBP' from Yadav et al. (2008). References to original papers: I) Pasquini et al. (2011); II) Pasquini et al. (2008); III) Pasquini et al. (1997); IV) Mathieu et al. (1990); V) Latham et al. (1992); VI) Mathieu et al. (1986); *VII)* New binary from our sample; VIII) Pasquini & Belloni (1998); IX) van den Berg et al. (2004); X) Sandquist & Shetrone (2003); XI) Belloni et al. (1998); XII) Sandquist et al. (2003).

Object	$B-V$	V	Reference
S251	0.67	12.55	IV,V,IV,VI
S440	2.05	08.15	IV
S1000	0.39	12.80	V,IV
S1011	0.63	13.82	I,VII
S1040	0.49	11.52	V,IV,VI,VIII,IX
S1072	0.62	11.33	V,IV,IX
S1182	0.99	12.00	IV,VI
S1216	0.57	12.73	V,IV,VI
S1221	1.13	10.76	I,V,IV
S1234	0.55	12.66	V,IV,VI,IX
S1237	0.94	10.78	V,IV,VI,IX
S1242	0.70	12.70	V,IV,VI,IX
S1250	1.35	9.68	I,V,IV
S1264	0.92	11.74	V,IV,VI
S1272	0.60	12.56	V,IV,VI
S1285	0.67	12.54	V,IV,VI
S1508	0.57	12.78	V,IV
S2206	0.75	12.33	V,IV
S999	0.77	12.63	V,IV,VI,VIII,IX
S1024	0.57	12.70	V,IV,VI,IX
S1045	0.55	12.61	V,IV,VI,IX
S1053	0.69	12.24	V,IV,VI
S963	0.71	14.51	III
S982	0.67	14.12	III,VII
S1292	0.62	13.20	V,III
S990	0.56	13.43	V,III
S986	0.55	12.73	V,III,IV,V
S1284	0.22	11.04	V
S821	0.55	12.85	V,VI
S973	0.56	13.49	V
S1063	1.07	13.52	V,VIII,IX
S1009	0.56	13.70	V,IX
S1224W		13.70	V,VII
S1070	0.61	13.98	V,IX

Table 4.5: Continued.

Object	$B-V$	V	Reference
S1247	0.61	14.05	V
S1014	0.81	14.11	II,V
S981	0.62	14.14	V
S2222	0.82	14.76	V
S810	0.92	15.16	V
S948	0.57	13.50	II
S951	0.66	14.58	II
S956	0.56	13.99	II
S1458	0.88	13.01	II
S1211	0.62	14.02	II
S1431	0.62	13.65	II
S747	0.66	14.02	II
S969	0.67	14.17	II
S1222	0.66	14.69	II
S757	0.62	13.54	II, IX
S758	0.56	13.43	II,III
S1442	0.70	14.75	II
S1246	0.65	14.59	II
S1247	0.64	14.01	II
S2209	0.59	13.48	II
S1012	0.66	14.18	II
S1457	0.63	13.88	II
S1022	0.64	13.99	II
S1050	0.61	14.28	II
S1287	0.58	14.01	II
YBP1424	0.58	13.20	II
S1300	0.55	13.78	II
S1481	0.69	14.75	II
S820	0.69	14.95	II
S1102	0.58	14.24	II
YBP1862	0.60	14.48	II
S1331	0.58	13.79	II
S1333	0.61	14.86	II
S1334	0.61	14.86	II
S1064	0.64	14.05	I
S1314	0.65	13.67	I
S1016	1.26	10.31	I not confirmed
S1075	0.58	13.86	I
S1305	1.00	12.27	I not confirmed
S1197	0.57	13.10	VII

Table 4.6: Continued.

Object	$B-V$	V	Reference
S1201	0.59	13.86	VII
S991	0.63	14.55	VII
S1041	0.68	14.73	VII
S816	0.61	13.21	VII
S1583	0.60	13.10	VII
S984	0.58	12.27	VI
S1005	0.51	12.67	VI
S1077	0.61	12.61	VI,VIII,IX
S2015	0.61	12.56	VI
S1452	0.64	14.6	VII
S1462	0.69	14.3	VII
S1092	0.62	13.3	VII
S1082	0.42	11.25	VIII,IX
S1019	0.71	14.32	VIII,IX
S972	0.84	15.49	VIII,IX
S1013	0.41	11.55	IX
S1282	0.56	13.33	IX
S1036	0.49	12.78	IX
S773	0.59	13.31	IX
S1042	0.86	15.68	IX
S996	0.83	15.05	IX
S1466	0.34	10.60	IX
S1281	0.55	13.72	IX
S997	0.46	12.13	IX
S986	0.55	12.73	IX
S2214	0.72	14.82	IX
S1601	0.80	14.44	IX
S1036	0.55	12.80	X
S1082	0.45	11.19	IX
S972	0.90	15.39	XI
S1019	0.83	14.26	IX
S1113	0.43	13.77	IV
S1267		10.91	XII
S760	0.60	13.29	IX
S752	0.60	11.32	XII
S1195	0.42	12.28	XII
S975	0.39	11.04	XII
S997	0.45	12.13	XII

Chapter 5

Three planetary companions around M67 stars

Figure 5.1: Johannes Kepler Uphill Battle. Astron52©

5.1 Introduction

In this chapter we present the study of the RV data obtained for the two G dwarfs YBP1194, YBP1514, and the evolved star S364 that reveal the presence of Jovian-mass companions. The orbital solution for YBP1194 yields a period of 6.9 days, an eccentricity of 0.24, and a minimum mass of 0.34 M_J. YBP1514 shows periodic RV variations of 5.1 days, a minimum mass of 0.40 M_J, and an eccentricity of 0.39. The best Keplerian solution for S364 yields a period of 121.7 days, an eccentricity of 0.35 and a minimum mass of 1.54 M_J. The results from simulations based on a Monte Carlo approach devoted to analyze the detectability and the occurrence of giants planets in our Radial Velocity Survey are also shown. Finally the status of the observation campaign on the M67 stars sample and the future prospects are discussed [1].

5.2 Stellar characteristics

The three stars belong to the M67 sample presented in the previous chapter (see also Pasquini et al., 2012), with a proper motion membership probability higher than 60% according to Yadav et al. (2008) and Sanders (1977). We found that YBP1194, YBP1514, and S364 are probable RV members with a mean radial velocity within one-sigma from the average cluster RV. For the latter, we adopted the value of $\langle RV_{M67} \rangle = 33.724$ km s^{-1}and the dispersion of $\sigma = \pm 0.646$ km s^{-1}estimated in Pasquini et al. (2012).
Table 5.1 shows proper motions and membership probability for the three stars discussed.

Table 5.1: Object ID, proper motions, membership probability of the targets and reference.

Object	$\mu_x \pm \Delta\mu_x$	$\mu_y \pm \Delta\mu_y$	Prob%	Reference
YBP1194	0.30±1.01	-0.42±0.65	99	Yadav et al. (2008)
YBP1514	-0.12±1.13	1.73±1.37	98	Yadav et al. (2008)
S364	-0.088	0.164	82	Sanders (1977)

Details about selection criteria and motion errors can be found in the original Yadav et al. (2008) and Sanders (1977) works.
Figure 4.9 reports in red the position of the three stars over the observed region of the color-magnitude diagram (CMD). The three stars analyzed in this section lie quite well on the cluster sequence in the CMD.

The basic stellar parameters (V, B-V, $T_{\rm eff}$, log $g$and [Fe/H]) with their uncertainties were adopted from the literature. Considering a distance modulus of 9.63 ± 0.05 (Pasquini et al., 2008) and a reddening of E(B-V)=0.041±0.004 (Taylor, 2007), stellar masses and radii were estimated using the 4 Gyr theoretical isochrones from Pietrinferni et al. (2004) and Girardi et al. (2000). The parameters derived from isochrone fitting are comparable, within the errors, with the values adopted from the literature. The main characteristics of the three host stars are listed in Table 5.2. We note that the errors on these values

[1]Based on Brucalassi et al. (2014)

Table 5.2: Stellar parameters of the three M67 stars hosting planets

Parameters	YBP1194	YBP1514	SAND364
α (J2000)	08:51:00.81	08:51:00.77	08:49:56.82
δ (J2000)	+11:48:52.76	+11:53:11.51	+11:41:33.00
Spec.type	G5V	G5V	K3III
$m_{\rm V}$ [mag]	14.6[a]	14.77[a]	9.8[b]
$B-V$ [mag]	0.626[a]	0.680[a]	1.360[b]
$M\star$ [$M_\odot$]	1.01±0.02[c]	0.96±0.01[d]	1.35±0.05[d]
$R\star$ [$R_\odot$]	0.99±0.02[d]	0.89±0.02[d]	21.8±0.7[d]
log g[cgs]	4.44±0.035[c]	4.57±0.05[e]	2.20±0.06[f]
$T_{\rm eff}$[K]	5780±27[c]	5725±45[e]	4284±9[f]
[Fe/H][dex]	0.023±0.015[c]	0.03±0.05[e]	−0.02±0.04[f]

[a] Yadav et al. (2008).
[b] Montgomery et al. (1993).
[c] Önehag et al. (2011).
[d] Pietrinferni et al. (2004) and Girardi et al. (2000).
[e] Smolinski et al. (2011) and Lee et al. (2008).
[f] Wu et al. (2011).

do not include all potential systematics. Given that the values of stellar parameters have influence on the estimation of the planet masses, we evaluated the effects on the host star masses and radii of using isochrones with different ages and slightly lower reddening (see discussion in sec. 4.4). While for the two main-sequence stars YBP1194 and YBP1514 we found no significant incidence, for the giant S364, an age uncertainty of ±0.5 Gyr and a lower reddening would induce an error on the star mass of 4% and on its radii of 3%. Therefore, we decided to include this effect in the uncertainties of S364 listed in Table 5.2 and in the error of the planet mass.

YBP1194 is a G5V star, described by Pasquini et al. (2008) as one of the five best solar analogs in their sample. A detailed spectroscopic analysis (Önehag et al., 2011) has confirmed the star as one of the best-known solar-twins.

YBP1514 also is a G5 main sequence star. We adopted the atmospheric parameters obtained by Smolinski et al. (2011), who used spectroscopic and photometric data from the original Sloan Digital Sky Survey (SDSS-I) and its first extension (SDSS-II/SEGUE). These values are consistent, within the errors, with what has been found in previous work on the same data by Lee et al. (2008) and in the study of Pasquini et al. (2008).

S364 (MMJ6470) is an evolved K3 giant star. The stellar parameters, summarized in Table 5.2, are taken from Wu et al. (2011) . We derived its mass and radius by isochrone fitting (Pietrinferni et al., 2004).

Table 5.3: Orbital parameters of the planetary companions. P: period, T: time at periastron passage, e: eccentricity, ω: argument of periastron, K: semi-amplitude of RV curve, $m \sin i$: planetary minimum mass, γ: average radial velocity, σ(O-C): dispersion of Keplerian fit residuals.

Parameters	YBP1194	YBP1514	SAND364
P [days]	6.958±0.001	5.118±0.001	121.710±0.305
T [JD]	2455978.8±0.5	2455986.3±0.3	2456240.9±3.7
e	0.24±0.08	0.39±0.17	0.35±0.08
ω [deg]	98.62±25.68	327.49±16.05	273.51±12.81
K [m s^{-1}]	37.72±4.27	52.29 ±10.39	67.42±5.85
$m \sin i$ [M_J]	0.34±0.05	0.40±0.11	1.54±0.24
γ [km s^{-1}]	34.184±0.006	34.057±0.017	33.217±0.018
σ(O-C) [m s^{-1}]	11.55	14.6	15.0

5.3 Radial velocities and orbital solutions

The RV measurements were obtained using the HARPS spectrograph (Mayor et al., 2003) at the ESO 3.6m telescope in high-efficiency mode; the SOPHIE spectrograph (Bouchy & Sophie Team, 2006) at the OHP 1.93 m telescope in high-efficiency mode, and the HRS spectrograph (Tull et al., 1998) at the Hobby Eberly Telescope. In addition, we gathered RV data points for giant stars observed between 2003 and 2005 (Lovis & Mayor, 2007) with the CORALIE spectrograph at the 1.2 m Euler Swiss telescope (see sec. 4.2 for a more detailed description of the acquisition setting for the instruments). All the observations for each star were corrected to the zero point of HARPS, as explained in the previous chapter (see also Pasquini et al., 2012), and were analyzed together. Two additional corrections were applied to the SOPHIE data, to take into account the modification of the fiber link in June 2011 (Perruchot et al., 2011) and the low S/N ratio of the observations. For the first, we calculated the offset between RV values of our stellar standard (HD32923) before and after the change of the optical setup. For the second, we corrected our spectra using eq.(1) in Santerne et al. (2012). We studied the RV variations of our target stars by computing the Lomb-Scargle periodogram (Scargle, 1982; Horne & Baliunas, 1986) and by using a Levenberg-Marquardt analysis (Wright & Howard, 2009, RVLIN) to fit Keplerian orbits to the radial velocity data (see Appendix B.1 and B.2). The orbital solutions were independently checked using the Yorbit program (Segransan et al. 2013 in prep.).

YBP1194

We have acquired 23 RV measurements since 2008. Fifteen were obtained with HARPS with a typical S/N of 10 (per pixel at 550 nm), leading to a mean measurement uncertainty of 13 m s^{-1}including calibration errors. Eight additional RV measurements were obtained with SOPHIE and HRS HET with mean measurement uncertainties of 9.0 m s^{-1}and 26.0 m s^{-1}. A clear 6.9-day periodic signal can be seen in the periodogram (see fig. 5.2 top) with its one-year and two-year aliases on both sides (at 6.7 d and 7.03 d). A single-

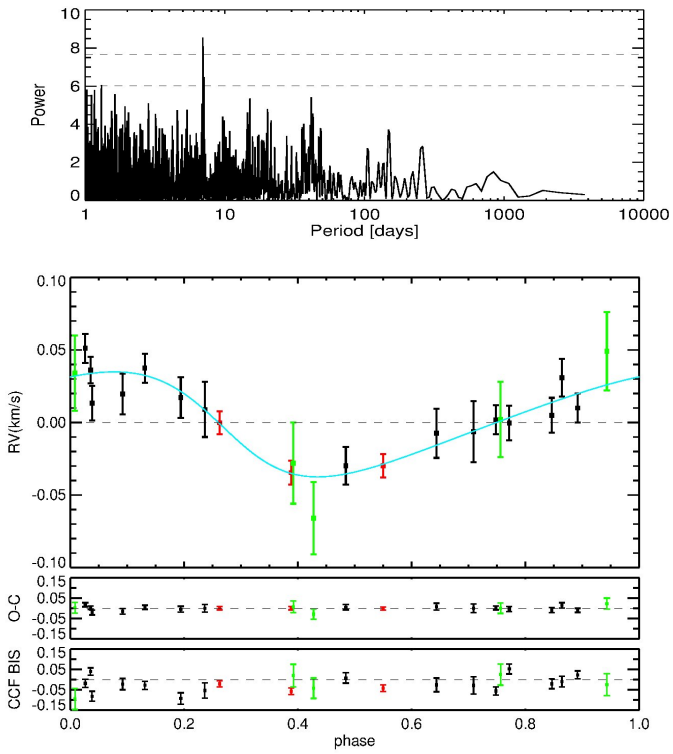

Figure 5.2: Top: Lomb-Scargle periodogram for YBP1194. The dashed lines correspond to 5% and 1% false-alarm probabilities, calculated according to Horne & Baliunas (1986) and white noise simulations. Bottom: phased RV measurements and Keplerian best fit, best-fit residuals, and bisector variation for YBP1194. Black dots: HARPS measurements, red dots: SOPHIE measurements, green dots: HRS HET measurements.

Keplerian model was adjusted to the data (fig. 5.2 bottom). The resulting orbital parameters for the planet candidate are reported in Table 5.3. The residuals' dispersion is σ(O-C)= 11.55 m s^{-1}, comparable with the mean measurement accuracy ($\sim$15 m s^{-1}), and the periodogram of the residuals does not show significant power excess, although structures are present (see fig. 5.8).

YBP1514

Twenty-five RV measurements have been obtained for YBP1514 since 2009: 19 with HARPS, the others with HRS HET and SOPHIE. The typical S/N is $\sim$10 and the measurement uncertainty is $\sim$15 m s^{-1}for HARPS, $\sim$25 m s^{-1}for HRS, and $\sim$10 m s^{-1}for SOPHIE. A significant peak is present in the periodogram at 5.11 days (fig. 5.3 top), together with its one-year alias at 5.04 days. We fitted a single-planet Keplerian orbit corresponding to the period P= 5.11 days (fig. 5.3 bottom). The orbital parameters resulting from this fit are listed in Table 5.3. Assuming a mass of 0.96 M$_\odot$ for the host star, we computed a minimum mass for the companion of 0.40$\pm$0.11 M_J. The residuals to the fitted orbit have

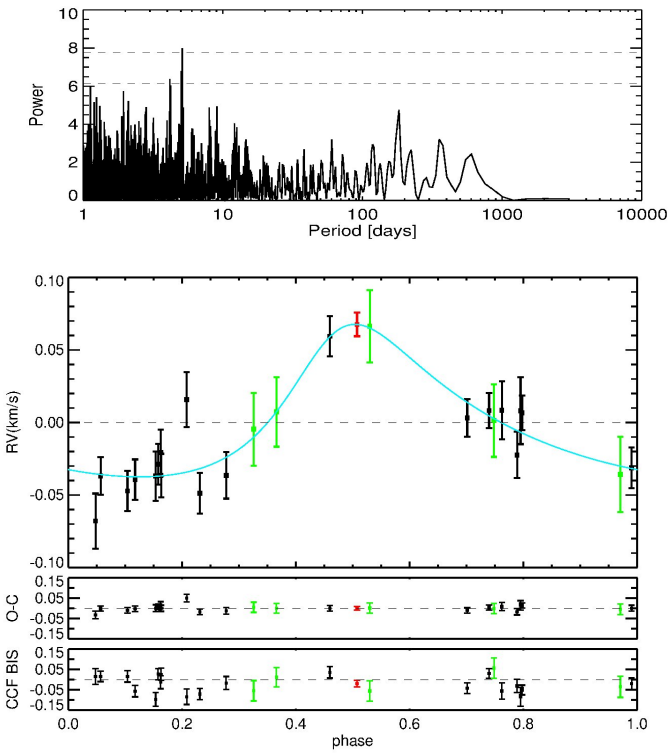

Figure 5.3: Top: Lomb-Scargle periodogram for YBP1514. Bottom: phased RV measurements and Keplerian best fit, best-fit residuals, and bisector variation for YBP1514. Same symbols as in Fig. 5.2.

a dispersion of σ(O-C)= 14.6 m s^{-1}, within the mean measurement uncertainty, and show no significant periodicity (see fig. 5.8).

S364

We collected 20 radial velocity measurements of S364 in about four years with HARPS, HRS HET, and SOPHIE. The average RV uncertainty is ∼3.0 m s^{-1}for HARPS, ∼7.0 m s^{-1}for SOPHIE and ∼20 m s^{-1}for HRS HET. Seven additional RV measurements were obtained with CORALIE between 2003 and 2005, with a mean measurement uncertainty of ∼12 m s^{-1}. The periodogram of the observed data is shown in fig. 5.4 (top) and indicates an excess of power at ≈121.7 days. The other clearly visible peak at 182 days is the one-year alias of the planetary signal at P=121.7 days. It disappears in the periodogram of residuals, which no longer shows any signal. We fitted a single-planet Keplerian orbit to this signal (fig. 5.4 bottom) and found an orbital solution whose parameters are reported in Table 5.3. The residuals to the fitted orbit show a level of variation of σ =16.0 m s^{-1}, higher than the estimated accuracy, but the periodogram of the residuals does not reveal significant peaks (see fig. 5.8).

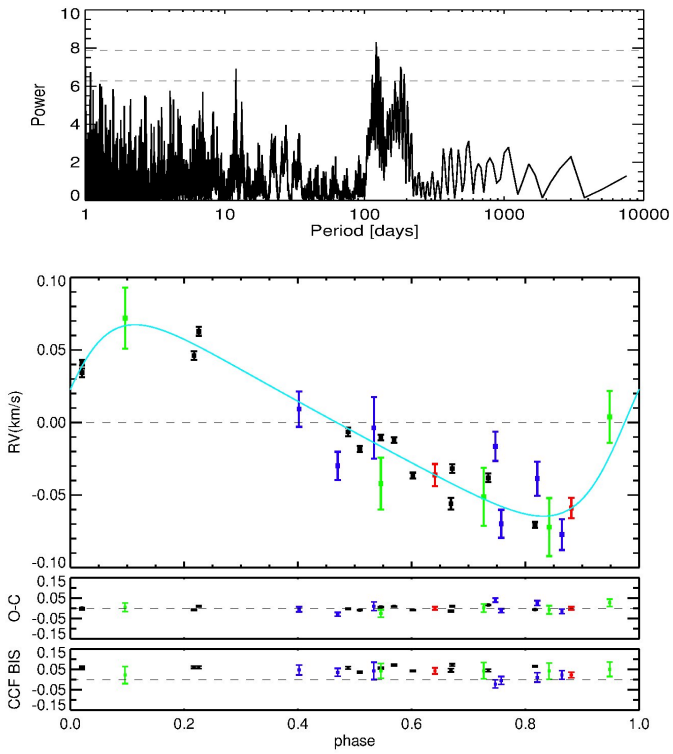

Figure 5.4: Top: Lomb-Scargle periodogram for S364. Bottom: phased RV measurements and Keplerian best fit, best-fit residuals, and bisector variation for S364. Same symbols as in Fig. 5.2. blue dots: CORALIE measurements.

5.4 Discussion

One problem of the Radial Velocity technique is stellar jitter due, in part, to flows and inhomogeneities on the stellar surface that can produce variations in the measured radial velocity of a star, and can even mimic or mask out a planet signature. (Queloz et al., 2001; Henry & Fekel, 2002; Santos et al., 2003). There have been several instances in the past when stars have shown periodic RV variations which are firstly attributed to a planet and later found to be due to stellar spots, e.g. BD+20 1790 (Figueira et al., 2010).

To rule out activity-related rotational modulation as the cause of the RV variations in our object data, we investigated chromospheric activity in these stars by measuring the variations of the core of Hα with respect to the continuum. The low S/N ratio of our observations does not provide sufficient signal in the region of the more sensitive Ca II H and K lines. We followed a method similar to the one described in Pasquini & Pallavicini (1991). It has been widely demonstrated that the Hα line can be used as a good activity indicator of chromospheric emission (Herbig, 1985; Pasquini & Pallavicini, 1991; Freire Ferrero et al., 2004). The central core of Hα indeed forms in the chromosphere and consequently stars of different chromospheric activity show a different shape (depth and breadth) of the Hα core (Pasquini & Pallavicini, 1991). The normal procedure adopted was to restrict our Hα measurements to the region within $\pm$0.4Å of the line center. Two additional spectral

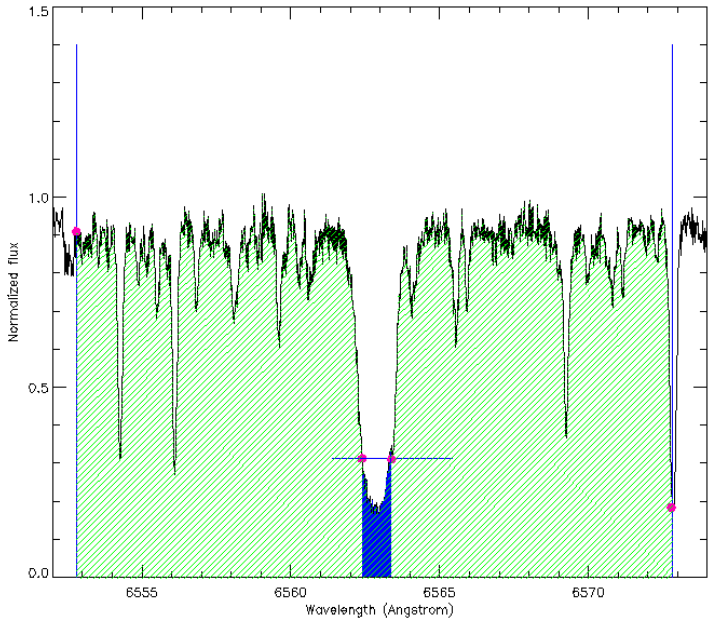

Figure 5.5: Example of the method used to investigate the presence and variability of chromospheric active regions in the stars by measuring the variations of the core of Hα. The flux ratio is calculated by the ratio of the blue area ($\pm$0.4Å of the Hα line center) over the green area ($\pm$10Å).

regions located at $\pm$10Å provided the *continuum* measurement (see fig. 5.5). All of these regions were free of telluric contamination. The Hα core measurement was done using a program that shifts the available spectra of each star to a common rest wavelength and measures the flux ratio of the defined areas (Biazzo 2007, private communication). All the targets exhibit a very low level of activity: S364 shows a variability in Hα of 2%, YBP1514 and YBP1194 of 3% without significant periodicity. Furthermore, the correlation between the RVs and the flux ratio has been inspected with negative results (see fig. 5.6).

In general, the M67 stars have a very low level of chromospheric activity (Pace & Pasquini, 2004), which is not compatible with the high RV variations we observe. Therefore, rotationally modulated RV variations for the dwarfs in M67 are certainly not a concern. The remote possibility that these stars are short-period binaries seen pole-on can also be excluded, because they are very active, and will show enhanced Hα cores and strong X-ray emission, which has not been observed for these stars (van den Berg et al., 2004). The fact that these stars are of solar age and that our research is focused on finding giant planets with an expected RV variability of tens of m s^{-1}makes the contamination by activity irrelevant.

In addition, for each stars we verified that the RVs did not correlate with the bisector span of the CCF (calculated following Queloz et al. (2001)) or with the FWHM of the CCF. The CCF bisector is the locus of median points between equal intensities on either side of the cross-correlation function, and is frequently used in distinguishing planetary signatures from other types of radial velocity modulation (Povich et al., 2001; Martínez Fiorenzano

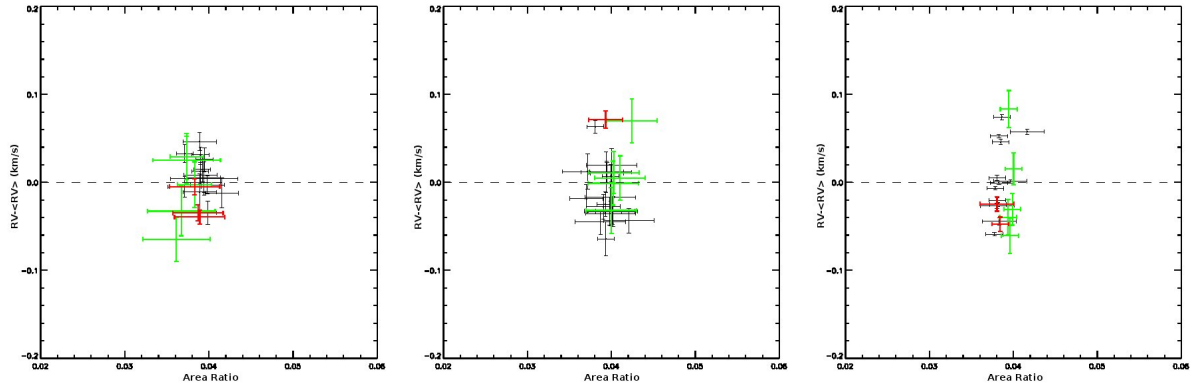

Figure 5.6: RV measurements related to the RV mean as a function of the Hα flux ratio for YBP1194 (left), YBP1514 (center), S364 (right) respectively. Black dots: HARPS measurements, red dots: SOPHIE measurements, green dots: HRS HET measurements. No correlation is evident.

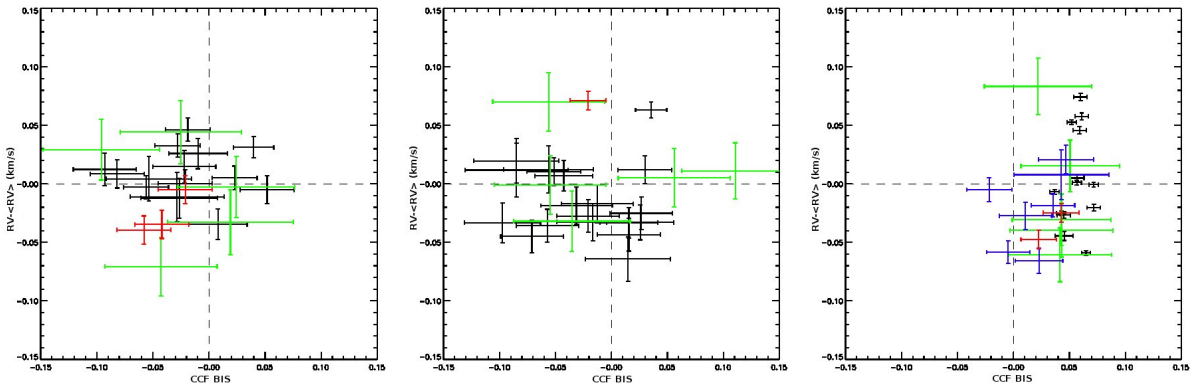

Figure 5.7: RV measurements related to the RV mean as a function of the bisector span (BIS) for YBP1194 (left), YBP1514 (center), S364 (right) respectively. Black dots: HARPS measurements, red dots: SOPHIE measurements, green dots: HRS HET measurements, blue dots: CORALIE measurements. No correlation is evident.

et al., 2005). For a planetary signal the bisector span is expected to be independent of radial velocity, whereas a distinct correlation results for blended systems (see Santos et al., 2002), or for periodic variations due to star spots (Queloz et al., 2001). We quantified the shape of the CCF line bisector using the *bisector inverse slope* (Queloz et al., 2001), defined as $v_t - v_b$ where v_t is the mean bisector velocity between 30-40% of the CCF depth (top) and v_b is that between 55-90% (bottom).

Figure 5.7 represents the ΔRV as a function of the bisector span (BIS). Uncertainties in the BIS are assumed to be twice the RV ones. No correlation is seen between BIS and the RV values and the extra variability is unlikely to be caused by stellar activity (see also the bottom panels of the RV fit in fig. 5.2, 5.3 and 5.4).

Moreover, the periodograms of the RV residuals, shown for the three stars in fig. 5.8, do not reveal any significant peak, although some structures are present.

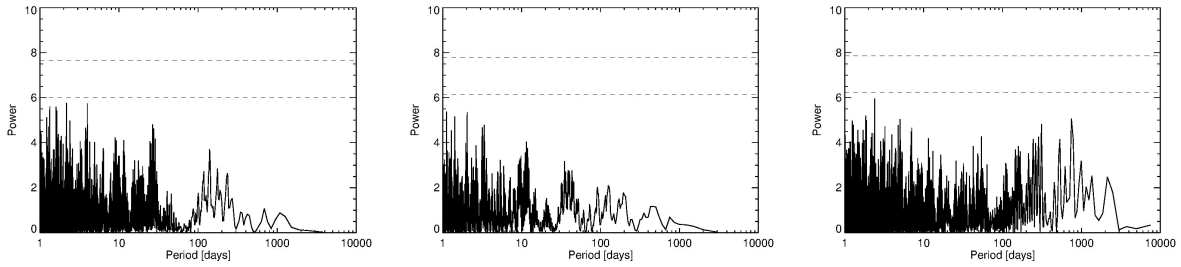

Figure 5.8: Lomb-Scargle periodogram of the RV residuals for YBP1194, YBP1514, S364 respectively. No significant peaks are detected.

Finally, it has to be noted that all the orbital solutions show nonzero eccentricity, but this is also common among planets found around field stars. Quinn et al. (2013) explained that hot-Jupiters in OCs with nonzero eccentric orbits and circularization time-scales t_{circ} longer than the system age, might provide an observational signature of the hot-Jupiter migration process via planet-planet scattering. We evaluated t_{circ} for the eccentric orbits of YBP1194 and YBP1514. Assuming a tidal quality factor $6 \times 10^4 < Q_p < 2 \times 10^6$, we calculated $409Myr < t_{circ} < 13.6Gyr$ for YBP1194 and $220Myr < t_{circ} < 6.9Gyr$ for YBP1514 (see Quinn et al. (2013) for details). Given the solar age of M67 and the wide range of possible t_{circ}, reflecting the choice of the Q_p and the estimation of the planetary radius, no firm conclusion can be drawn for the origin of the eccentric short-period orbits of these stars. Moreover, further investigations and more RV data are needed to better constrain the eccentricities of these objects (see Pont et al., 2011).

5.5 Monte Carlo simulations

In the last section of this chapter we present the results of a series of Monte Carlo simulations performed using the RV signals. Two main goals motivated this part.
First, we needed a tool to estimate the minimum number of the RV observations to be able to assess the possible presence of a planet at high confidence. This study was justified by the sparse sampling frequency of the observations and the few RV points for stars we gathered during the initial phase of our campaign. After the first observation runs indeed, we obtained on average 7 observations per star, but in a range from a minimum of 2 to more than 20. Furthermore, the runs were only based on a few nights and assembled in the period of January-April with large gaps.
Second, we wanted to evaluate the detectability and the occurrence of giants planets in our Radial Velocity Survey.

5.5.1 Methodology

We generated a large number of data pairs ($\sim 10^5$) corresponding to planet mass and period of our 'potential planets', uniformly distributed in a mass range of 0.01-10.0$M_J$in log10 scale, and in a period range of 1.0-100 days in linear scale. For each star we considered the real number of the observation nights, expressed in Barycentric Julian Date (BJD), and in addition we generated virtual time observation dates following the usual schedule for the observation runs previously awarded: on average 2 observation nights every 2-3 months during the winter season. We assumed circular orbits and for random choices of the mass-period pairs, we calculated the contribution to the radial velocity amplitude K from a giant planet using the relation:

$$K = \left(\frac{2\pi G}{P}\right)^{1/3} \left(\frac{m_p sin(i)}{M_J}\right) \left(\frac{M_\star}{M_\odot}\right)^{-2/3} \tag{5.1}$$

where $M_\star$ is the mass of the host star that we obtained from isochrones fitting (see sec. 5.2). A random distribution of the orbit inclination was also considered. Then, we derived RV values following the eq. for circular orbit:

$$V_r(t) = K sin\left(\frac{2\pi}{P}(t - t_0)\right) + c \tag{5.2}$$

where t_0 was selected randomly in the time span of the observations and c, the systemic velocity of the system, was allowed to vary around the RV value of M67 obtained in Pasquini et al. (2012). We added to the RV values also noise, estimated by randomly varying the mean measurements errors of the real observations. We fitted the RV points with a sinusoid curve (assuming circular orbit) using a least-squares fitting procedure that minimized the χ^2. The fit was repeated for 10.000 trials.

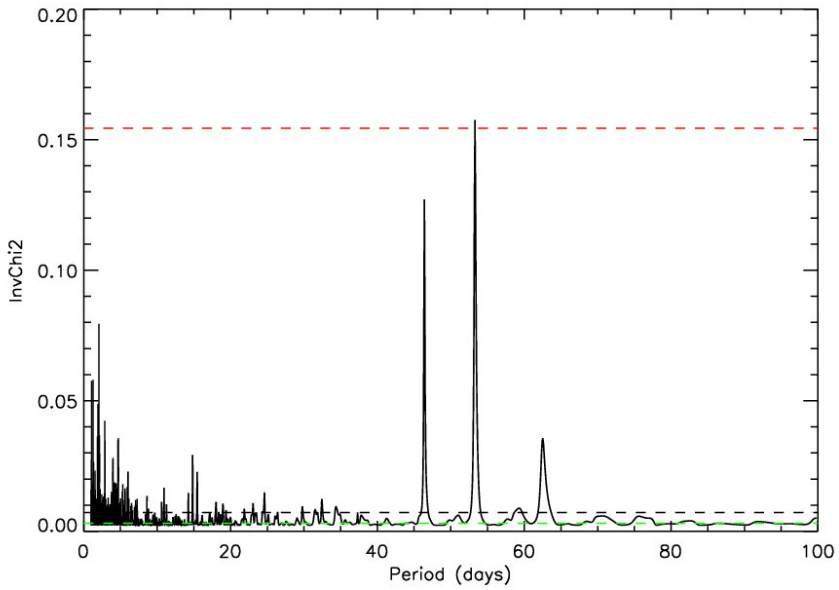

Figure 5.9: Example for the star YBP266 showing $1/\chi^2$ values as function of period for 10.000 trials of the sinusoid curve fit. The mean and the standard deviation σ_r of the $1/\chi^2$ values that passed a 3σ-clipping selection are calculated. The red dashed line represents the difference between the maximum peak of $1/\chi^2$ values and the $1/\chi^2$ mean. The black dashed line corresponds to $10\sigma_r$, where σ_r is the standard deviation of $1/\chi^2$ values. The green dashed line is equivalent to the $1/\chi^2$ mean.

5.5.2 Estimation of the minimum number of observations

The following method was employed to asses a planet detected for a given mass-period pair and a number of observations. We applied a 3σ-clipping algorithm to the $1/\chi^2$ values. Then, we calculated the mean and the standard deviation σ_r of the $1/\chi^2$ values that passed the 3σ-clipping selection. We considered a planet detected for that mass-period pair if the maximum peak of the $1/\chi^2$ values with respect to the $1/\chi^2$ mean exceeded $10\sigma_r$ (see fig. 5.9). We launched the simulations first with the original number of the real observations and then adding the simulated BJD dates. For each set of observations, the simulations were repeated 3 times. In the mass-period plane we consider a grid of 20 period intervals per 20 log-spaced mass intervals and for each bin we calculated the fraction of the detected planets with respect to the total simulated planets in that bin of mass and period. The detections efficiency is shown in fig. 5.13 as orange contour from 0.0 to 1.0 over the mass-period plane with increasing number of observations. For each star then we estimated the mean detection efficiency and we analyzed how it could change as function of the number of observations. Figure 5.10 shows the mean detection efficiency as a function of the number of observations for the star YBP266. The simulation analysis, extended to all the stars of the sample, has resulted in the need to ensure at least 9-10 observations per star to have a mean detection efficiency higher than 80%.

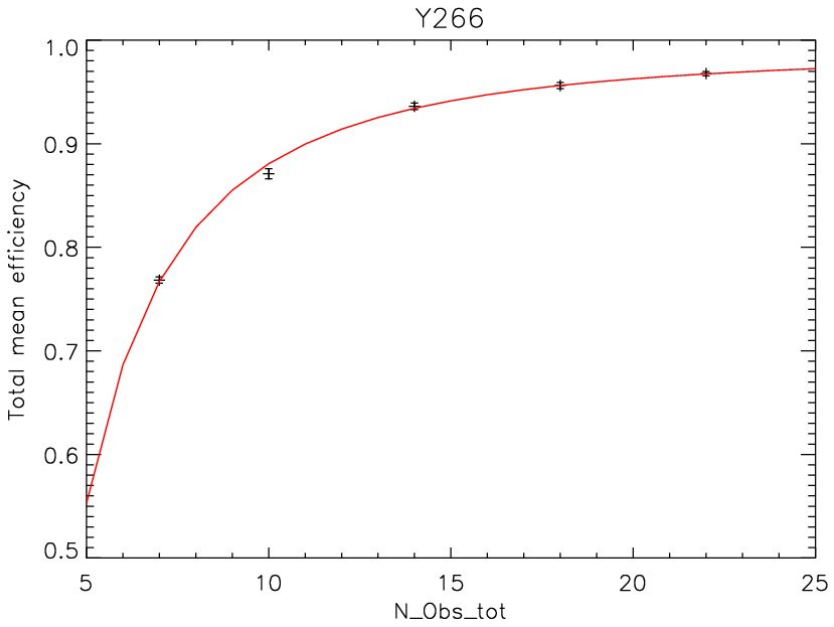

Figure 5.10: Mean detection efficiency as a function of the number of observations for the star YBP266. The red line represents the best fit to the values obtained from the simulations.

5.5.3 Planets Probability and Detection limits

A second phase of study has started considering the RV data and the results obtained up to December 31^{st}, 2013. The goal was to determine the detection limits and a trustworthy estimation of the occurrence rate of giant planets in our RV survey. We followed a similar approach to the previous analysis, generating a large number of mass and period values ($\sim 10^6$) of our 'potential planets', this time uniformly distributed in a mass range of 0.2-10.0 Mjup in log10 scale, and in a period range of 1.0-1000 days in linear scale. Using the real number of the observations (expressed in BJD) for each star, we assumed circular orbits and for randomly choices of the mass-period pairs, we calculated the RV values and the rms of the RV measurements. A new method, based on a periodogram analysis (Scargle, 1982), was applied to assert a planets detected. This new approach was chosen because we had enough measurements for a reliable periodogram analysis, furthermore it was more consistent with the method we applied for the analysis of the real RV data. The Lomb-Scargle periodogram (Scargle, 1982) is a commonly used technique for searching for periodic sinusoidal signals in unevenly-sampled data, and allows estimates of the detection threshold to be written down for periods less than the duration of the observations (Horne & Baliunas, 1986). The significance of the sinusoid best fit of our RV values was determined calculating analytically the False Alarm Probability (FAP) level (Horne & Baliunas, 1986). For a more detailed explanation of the Lomb-Scargle method and the derivation of the FAP we refer to the Appendix B.1. For a given mass and period values, we considered a planets detected if we could obtain from the frequency analysis a signal with a power higher than

the power associated to a 0.01 FAP. The simulations have been repeated considering a 0.05 FAP. In all the cases 10^6 trials have been used.

As previously done, in the mass-period plane we consider a grid of period and log-spaced mass intervals and for each bin we calculated the fraction of the detected planets with respect to the total simulated in that bin of mass and period. For the planets detected, in each bin of the mass-period grid, we evaluated the average rms of the derived RV velocities and we attributed to this mean an error of $\pm$6m s^{-1}corresponding to the mean scatter of the rms in the bins. Subsequently, we looked for the mass-period bins with mean rms consistent with the rms of our real measurements. From the real data we removed linear trends and stellar activity correlation before calculating the rms values. The detections efficiency is shown in fig. 5.14 and 5.15 (with a 0.01 FAP level used in the simulations as detection threshold) as color contours from 0.0 to 1.0 with overplotted the rms curve corresponding to the values obtained from the real RV data. Fig. 5.16, 5.17, 5.18 and 5.19 represent the detections efficiency derived from simulations where a 0.05 FAP level was used as detection threshold. In this way, we have an estimation of the fraction of the stars with sufficient measurements to rule out a planet of a given minimum mass and orbital period.

We computed the occurrence rate $\gamma(P, M)$, e.g. the fraction of stars orbited by planets, in the selected period-mass ranges, using the following formalism. For each star we weighted the detections efficiency with the mass-period distribution of planets derived from the relation of Cumming et al. (2008): $df \propto M^{-0.31\pm0.2}P^{0.26\pm0.1}dlogMdlogP$. This was estimated by

$$R_\star = c \sum_{ij}^{Nbins} E_{ij} \cdot D_{ij} \tag{5.3}$$

where the sum is evaluated over all the bins. E_{ij} corresponds to the detections efficiency for each period-mass bin, D_{ij} represents the mass-period distribution of planets per period-mass bin and is calculated by

$$D_{ij} = \int_{bin} M^\alpha P^\beta dlogMdlogP \tag{5.4}$$

where $\alpha = -0.31 \pm 0.2$ and $\beta = 0.26 \pm 0.1$. The normalization constant c is defined conveniently inside our mass-period domain by the relation

$$1 = c \int_{1.0}^{1000} \int_{0.2}^{10} M^\alpha P^\beta dlogMdlogP \tag{5.5}$$

Adding together the values obtained from the analysis of all the Main-Sequence stars (MS) and the Giants stars (G) respectively as

$$R_{MStot} = \sum_{MSstars} R_{\star i}, \quad R_{Gtot} = \sum_{Gstars} R_{\star i}, \tag{5.6}$$

we imposed the result to be proportional to the number of real detected planets in the survey (2 for the MS and 1 for the Giants):

$$2 = \gamma_{MS} R_{MStot}, \quad 1 = \gamma_G R_{Gtot}. \tag{5.7}$$

Therefore, the proportional constants γ_{MS} and γ_G represent an estimation of the occurrence rate of our survey for the MS stars and the Giants stars respectively. In the computation, Turn-Off stars with $12.5 \leq M_V \leq 13.5$ and $0.540 \leq (B-V) \leq 0.640$ were considered part of the MS sample, whereas the others with the Giants sample.

5.5.4 Discussion

In the more conservative case, where the simulations have been done using a 0.01 FAP level as detection threshold, the analysis results in the possibility to evaluate the detection limit only for 9 MS stars and 11 evolved stars. For the other stars, excluding the object with less than 6 observations on the base of the previous analysis, the detection efficiency is not sufficient to detect any planet with the available number of observations. For the 11 MS and 9 evolved stars, if a Hot Jupiter (with short period) would be present with a rms higher of the real one, our detection efficiency is high enough for the number of observations to allow the detection of the planets at a 0.01 FAP level: if the planet was there we should be able to see it. For RV values with rms smaller than ours RV measurements the detection efficiency decreases and we are not able to discover the presence of any planet at high confidence. The detection efficiency drops also with the increase of the period, likely due to the still not sufficient number of measurements for a star and to the distribution of the observations. Considering only these 20 stars, the evaluation of the planets occurrence in our survey results in quite high values ($\sim$46% for the MS and $\sim$27% for giants). However, these values should be rescaled to the total sample of MS and evolved stars previously cleaned of the binaries. In the worse case that all the stars where the detection efficiency is insufficient and we can not say anything about the presence of a planet, do not have a companions, the occurrence of planet becomes $\sim$9% for the MS stars and $\sim$13% for the giant stars. However, this seems not our situation (see below).

In the less conservative case, where the simulations have been done using a 0.05 FAP level as detection threshold, we can evaluate the detection limit for 25 MS stars and 16 evolved stars. We decided to take into account also this scenario since stars with periodogram showing an excess of power higher than 0.05 FAP level were monitored with much more attention and used for a first Keplerian fitting analysis. In this case, the periodogram analysis and the Keplerian fit revealed other 3 good planets host candidates, 2 main sequence stars and 1 giant with orbital solutions for 1 Hot Jupiter and 2 long period giant planets (see following section). Considering also these objects in the computation of the planet's frequency and rescaling our results to the total sample of MS and evolved stars as before, we can obtain a giant planet occurrence of $\sim$13% for the MS stars and $\sim$17% for the evolved stars.

As mentioned, RV surveys around FGK stars show exoplanet rates higher than 10% Jupiter-mass planets with a period of up to a few years and 1.20±0.38% at solar metallicity, for very close-in hot-Jupiters with a period shorter than ten days (Cumming et al., 2008; Mayor et al., 2011; Wright et al., 2012).

In contrast with early reports, the discovery of two hot-Jupiters in the Praesepe (Quinn et al., 2012), of two sub-Neptune planets in the cluster NGC6811 (Meibom et al., 2013), the new announcement of a hot-Jupiter in the Hyades (Quinn et al., 2013), and the detection in M67 of three Jupiter-mass planets presented in this work (Brucalassi et al., 2014), seems to confirm that massive planets around stars of open clusters are as frequent as those around field stars. Quinn et al. (2012) obtained a lower limit on the hot-Jupiter frequency in Praesepe of $3.8^{+5.0}_{-2.4}$%, which is consistent with that of field stars considering the enriched metallicity of this cluster. Meibom et al. (2013) have found the same properties and frequency of low-mass planets in open clusters as around field stars.

In our case, for short-period giant planets we derived a frequency of ∼2%, which is slightly higher than the value for field stars. Adding giant planets with long periods, our simulations give a rate of ∼9% for the whole sample, that is quite in agreement with the rate of giant planets found by Cumming et al. (2008); Mayor et al. (2011) for field stars. However, this fraction is a lower limit that has to be better constrained with the follow-up of some other candidates (see Pasquini et al., 2012), which reveal suggestive signals for additional planetary companions.

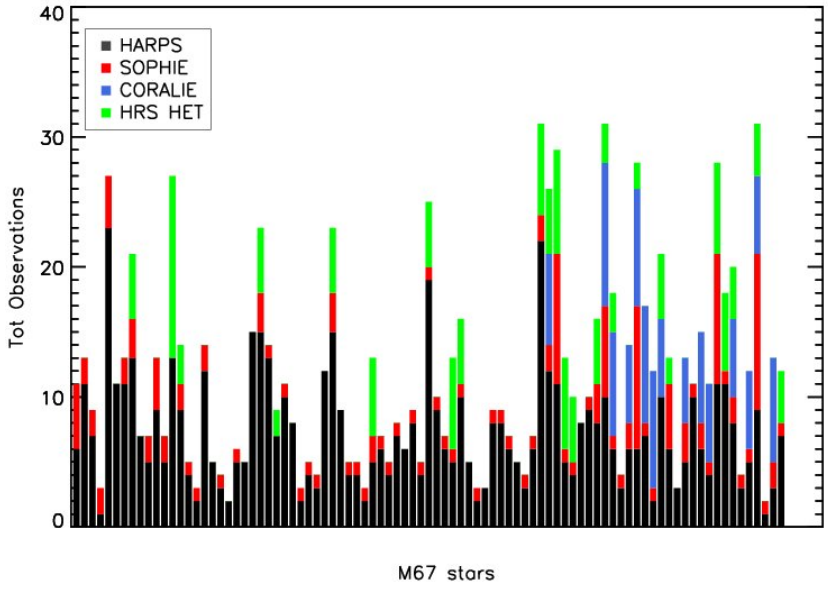

Figure 5.11: Histogram showing the number of observations per star for our total sample. All observations from HARPS, SOPHIE, CORALIE, and HET HRS are included in the plot updated to December 31st, 2013.

5.6 Status of the research campaign and prospects

In this section the status of our research campaign on the M67 star sample is given. Some considerations about the work done until now and the future prospects are discussed.

Figure 5.11 shows a histogram with the number of observations per star updated to December 31st, 2013. We have obtained, on average, 11 observations per star: 9 observations/stars for the MS stars and 15 observations/stars for the Giants and Turn-Off stars. After the last run of observations other three stars show significant hints for the presence of Jovian-mass companions. Two planets candidates are in orbit around the two G dwarfs YBP401 and YBP778, and one around the evolved star S978. Following the same method presented in sec. 5.3, we studied the RV variations of our target stars evaluating the Lomb-Scargle analysis (see Appendix B.1) and subsequently computing a Keplerian fit to the RV data (see Appendix B.2). A possible orbital solution for YBP401 yields a period of 4.1 days, an eccentricity of 0.1 and a minimum mass of $0.43 M_J$, whereas the YBP778 and S978 show Keplerian solutions for giant planets with long period of 211.6 days and 510.4 days, an eccentricity of 0.08 and 0.24, a mass of $3.0 M_J$ and $1.98 M_J$ respectively (see fig. 5.12).

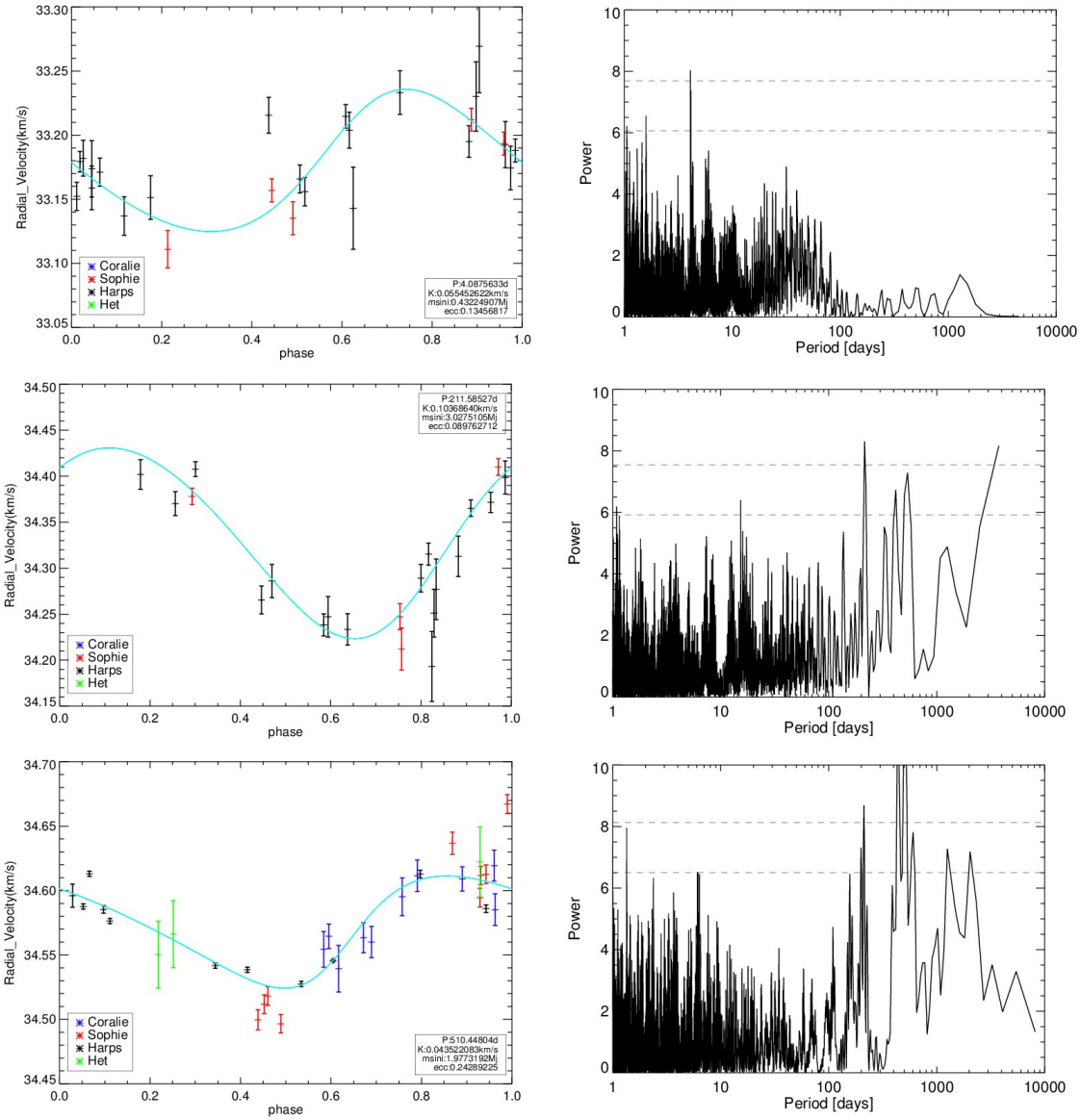

Figure 5.12: Left: Phased RV measurements and Keplerian best fit for YBP401 (top), YBP778 (center) and S978 (bottom). Black dots: HARPS measurements, red dots: SOPHIE measurements, green dots: HRS measurements, blue dots: CORALIE measurements. Right: Lomb-Scargle periodogram for YBP401 (top), YBP778 (center) and S978 (bottom). The dashed lines correspond to 5% and 1% false-alarm probabilities, calculated according to Horne & Baliunas (1986).

Three stars (YBP1051, YBP673, YBP2018) show peak to peak RV variations of the order of 700 m $s^{-1}$and therefore possibly too high to host a planet. Finally a number of additional interesting candidates are being monitored, but the baseline is not yet long enough to determine the nature of the companion and more RV points are required to lower the false alarm probability. Thus for the future, we will continue to ask for observation

time to obtain additional RV points for the most relevant targets. In parallel, YBP1194 together with Y1514, S364, and the other M67 targets will be subject of a detailed differential abundance analysis to compare the chemical composition of stars with and without giant planets.
After some experience acquired during these years of my Phd work, an important consideration maybe needs to be discussed at this point regarding a future strategy for the study of giants planets in open clusters with the RV technique. Small optical observatories equipped with competitive high-resolution spectrographs can play a major role in this kind of astronomical research besides the major, ground-based facilities with their 8-m class telescopes and besides satellite observatories. Due to their different operational approach and minor schedule pressure with respect to large facilities, they can devote major fractions of time and with more flexibility in the monitoring of planets host candidates, where large amount and dedicated observing time is essential for a scientific success. This one of the reasons to push the construction of a competitive high-resolution optical spectrograph as FOCES on the 2m-class telescope at the Wendelstain Observatory.

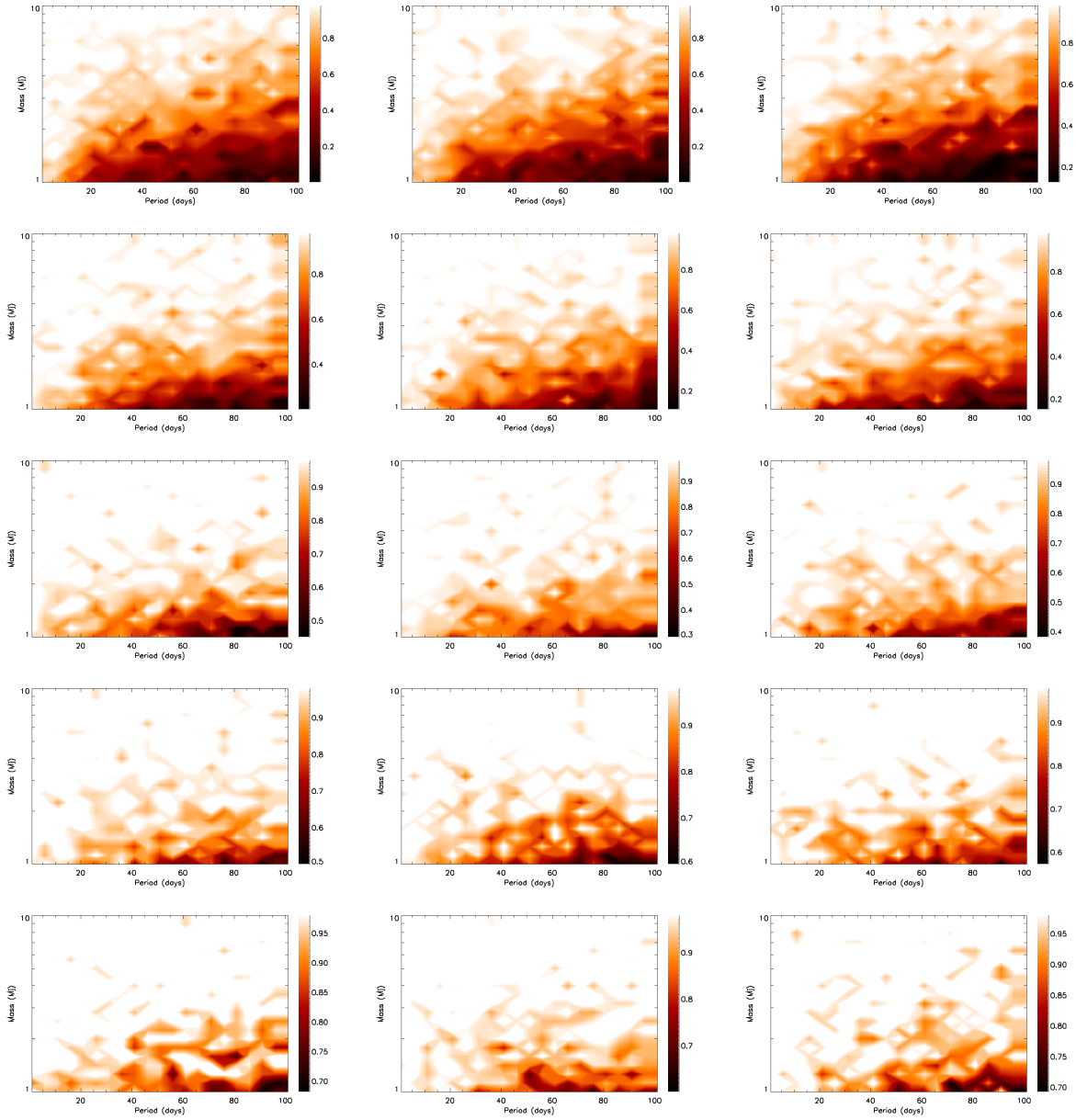

Figure 5.13: The detections efficiency of the star YBP266 is shown as example with orange contour from 0.0 to 1.0 in the period-mass domains of 1-100 days and 1-10M_J. We repeated the simulations three times (different columns) for each number of observations considered. Starting from the top with the original number of real data and moving through the bottom, the the simulations are launched again (different rows) adding +4, +8, +12,+16 simulated observations respectively. We caution the reader for the different color scale in the contours.

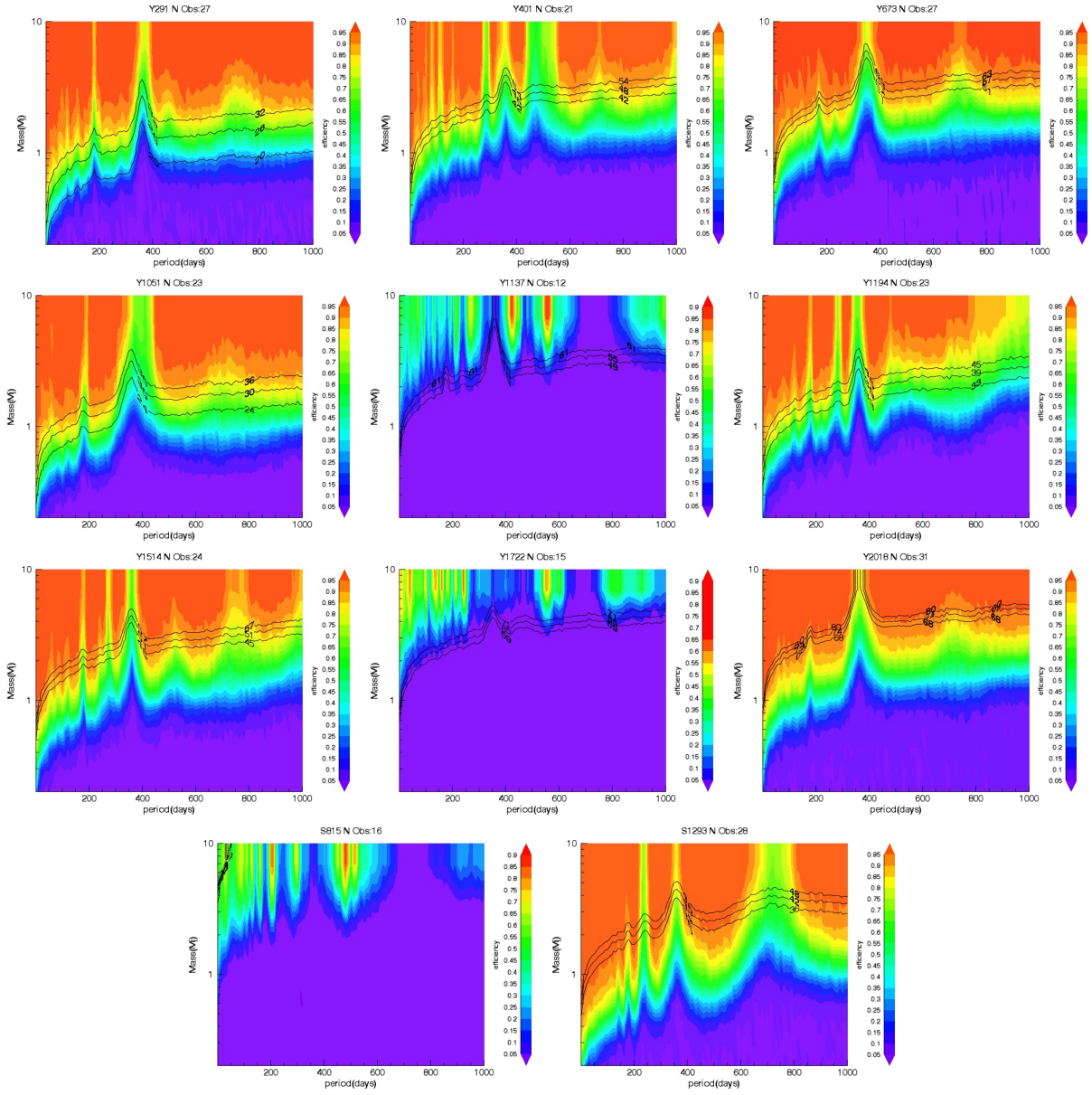

Figure 5.14: Contours of the planets detection efficiency for the MS stars in the period-mass domains of 1-1000 days and 0.2-10M_J. A 0.01 FAP level has been used as detection planets threshold. The lines related to the rms of the observed RV points with an error $\pm$6m s^{-1}error are overimposed.

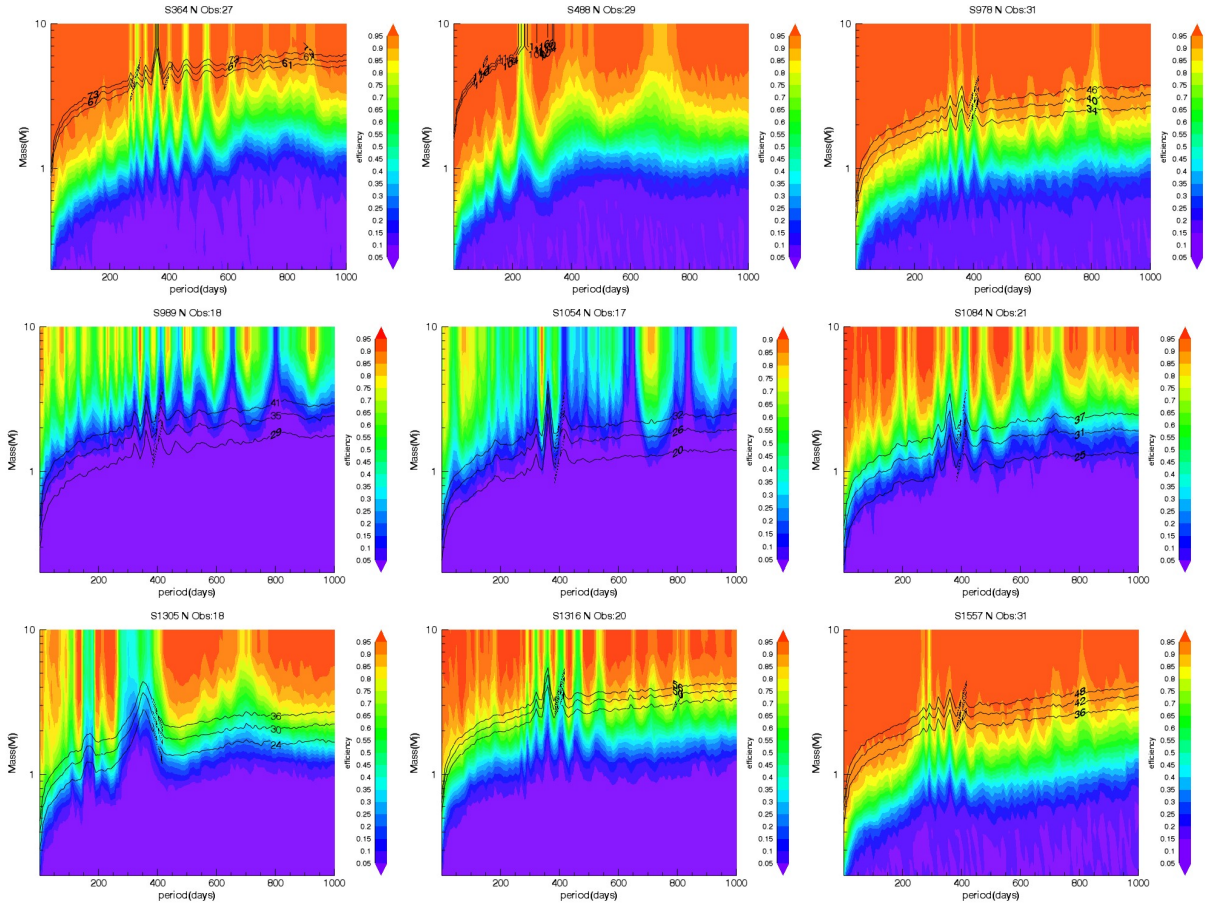

Figure 5.15: Contours of the planets detection efficiency for the Giants stars in the period-mass domains of 1-1000 days and 0.2-10M_J. A 0.01 FAP level has been used as detection planets threshold. The lines related to the rms of the observed RV points with an error $\pm$6m s^{-1}error are overimposed.

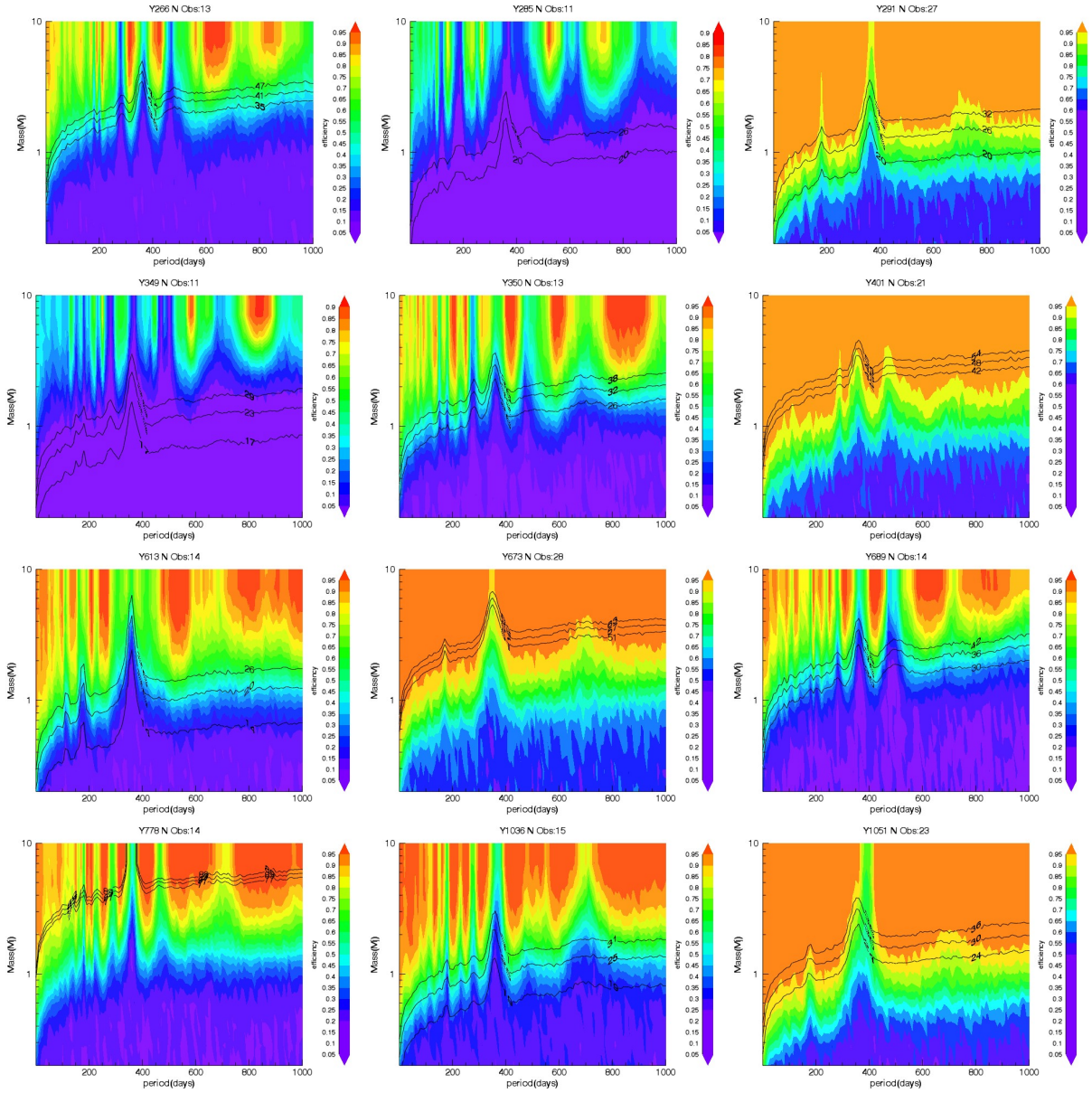

Figure 5.16: Contours of the planets detection efficiency for the MS stars in the period-mass domains of 1-1000 days and 0.2-10M_J. A 0.05 FAP level has been used as detection planets threshold. The lines related to the rms of the observed RV points with an error $\pm$6m s^{-1}error are overimposed. We caution the reader for the different color scale in the contours.

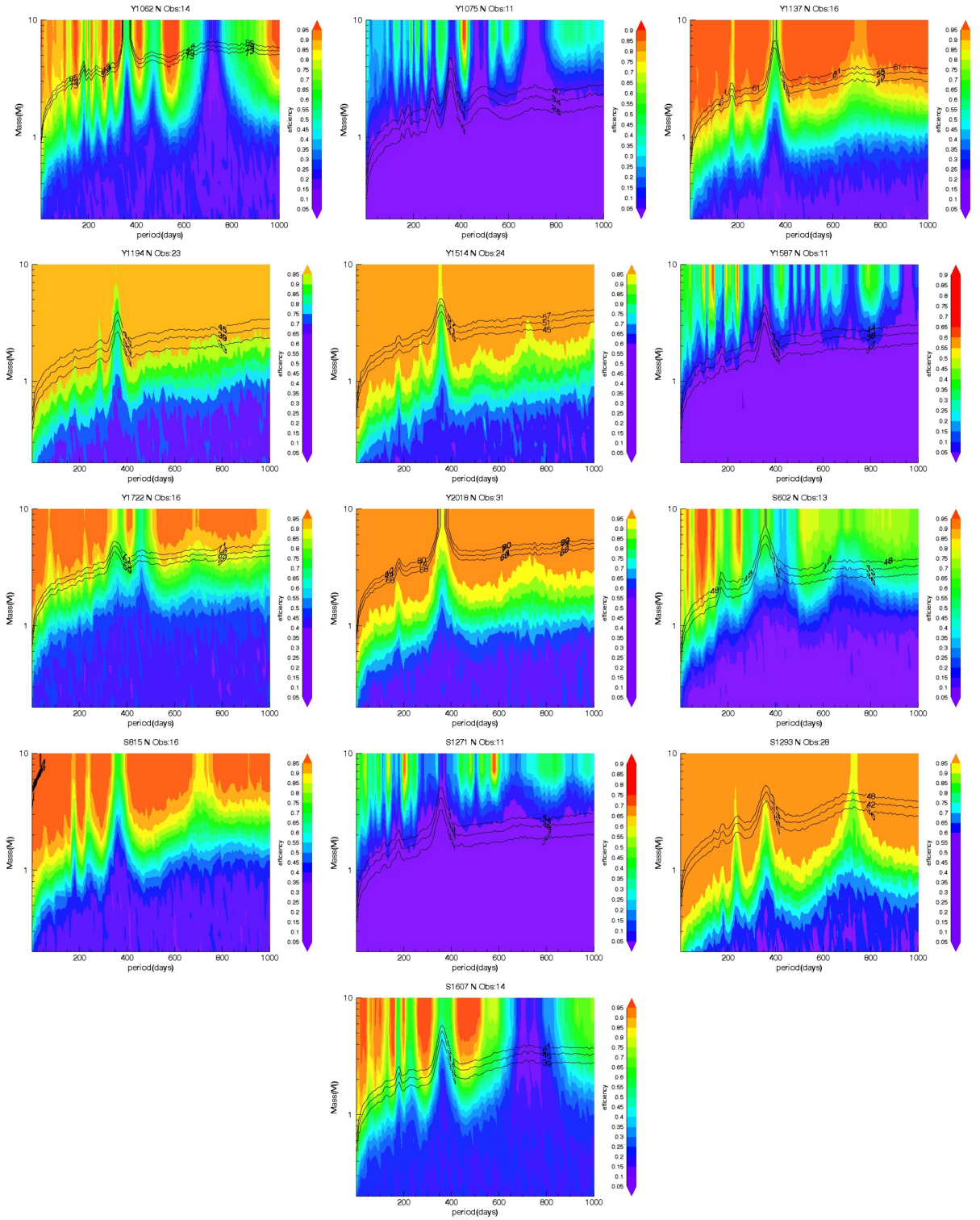

Figure 5.17: Continued as before. Contours of the planets detection efficiency for the MS stars in the period-mass domains of 1-1000 days and 0.2-10M_J. A 0.05 FAP level has been used as detection planets threshold. The lines related to the rms of the observed RV points with an error $\pm$6m s^{-1}error are overimposed. We caution the reader for the different color scale in the contours.

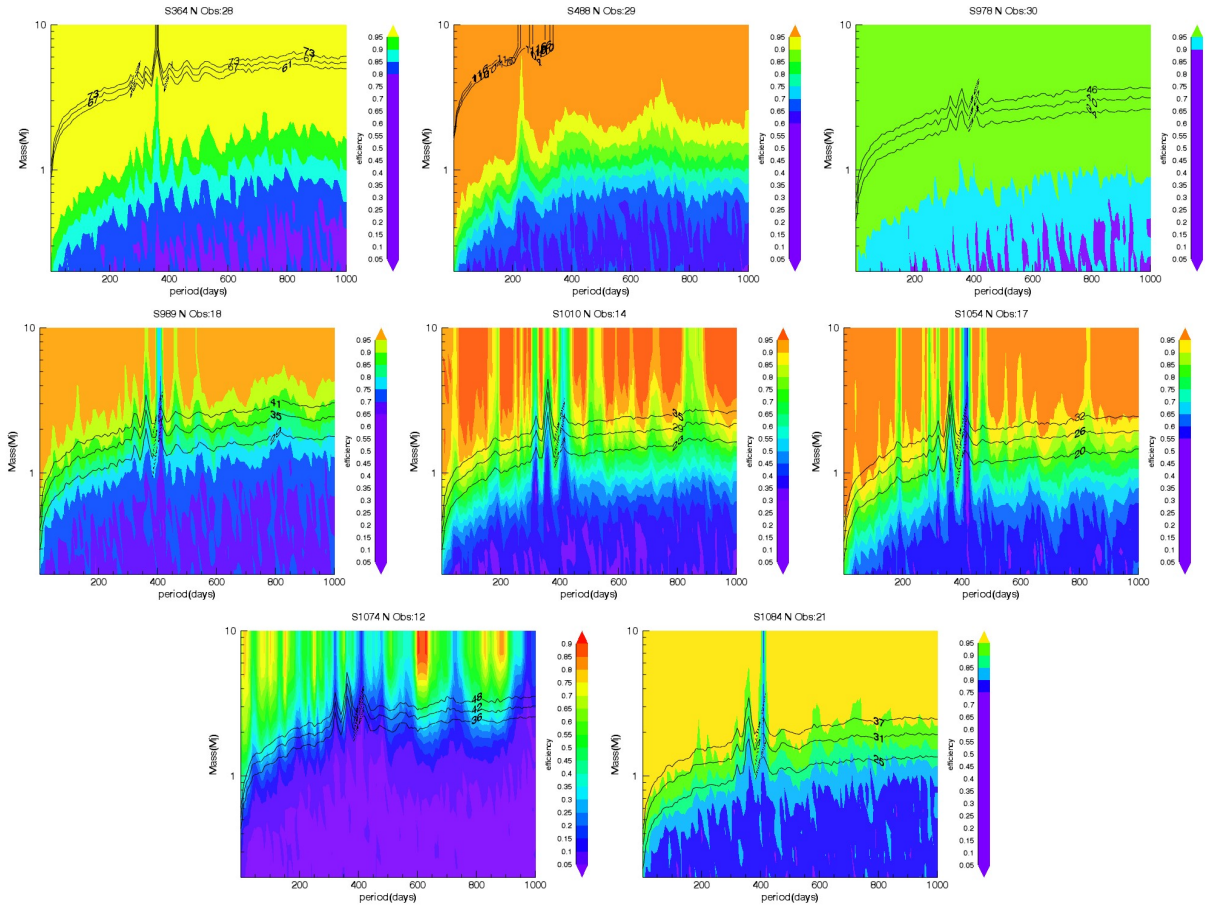

Figure 5.18: Contours of the planets detection efficiency for the Giants stars in the period-mass domains of 1-1000 days and 0.2-10M_J. A 0.05 FAP level has been used as detection planets threshold. The lines related to the rms of the observed RV points with an error $\pm$6m s^{-1}error are overimposed. We caution the reader for the different color scale in the contours.

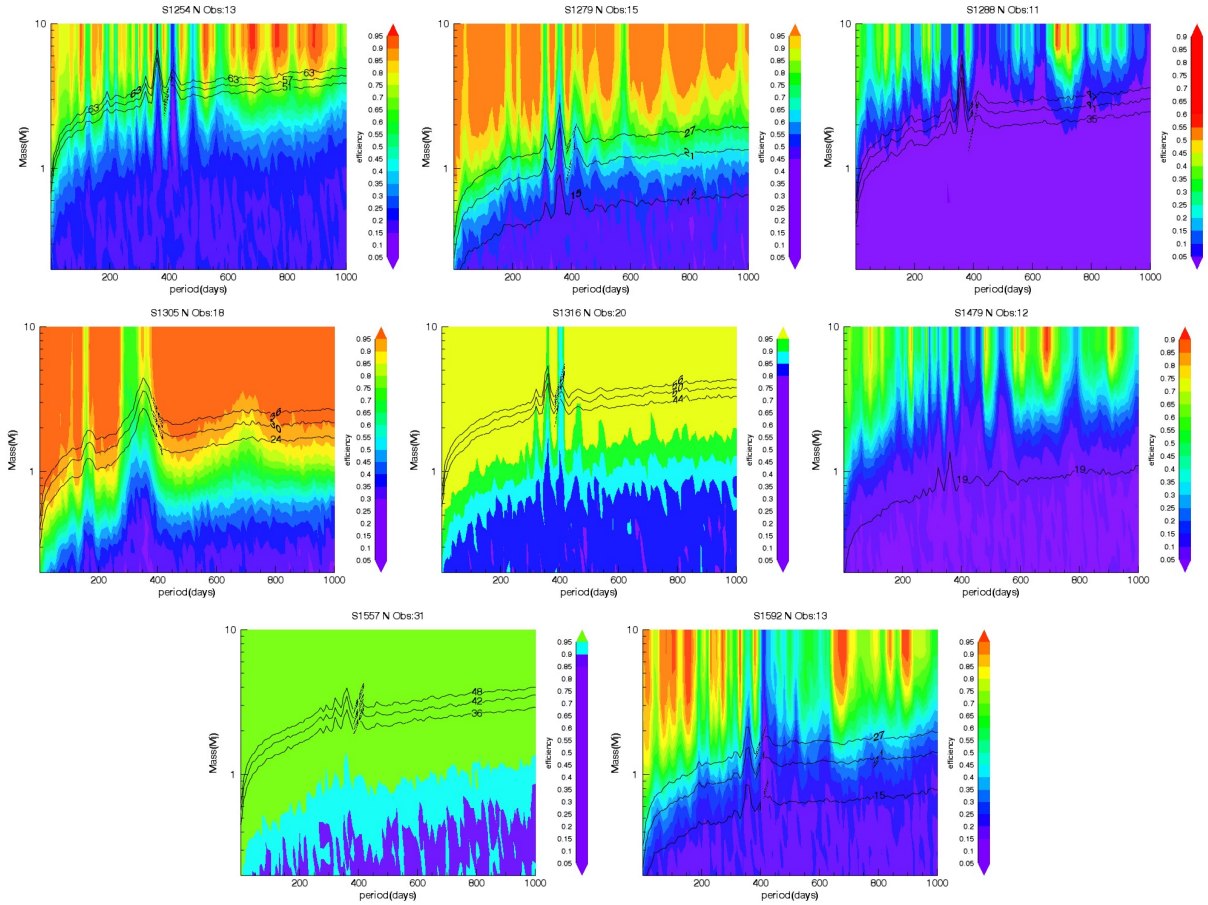

Figure 5.19: Continued as before. Contours of the planets detection efficiency for the Giants stars. A 0.05 FAP level has been used as detection planets threshold. The lines related to the rms of the observed RV points with an error $\pm$6m s^{-1}error are overimposed. We caution the reader for the different color scale in the contours.

Chapter 6

Conclusions

This Ph.D. Thesis is based on the study of extrasolar planets using Radial Velocity technique from both instrumental and observational points of view. Two main parts indeed compose this project: the upgrade of the spectrograph FOCES, an high resolution spectrograph that will be installed next year at the Wendelstein Observatory, and the search of giant planets around stars in the open cluster M67 using RV measurements acquired with different important facilities, as HARPS at ESO 3.6-m telescope, SOPHIE at 1.92-m OHP telescope, HRS at the 9.2-m Hobby-Eberly Telescope and CORALIE at the 1.50-m Eurelian Swiss Telescope.

An introduction to the extrasolar planets is given in Chapter 1. The main methods for their detection, in particular Doppler method and photometric transit are presented. The formation of both rocky and gaseous planets is discussed within the 'Solar Nebular Disk Model'. The three main hypothesis for planetary migration are described too. Gas disk interaction, planetesimal-driven migration and planet-planet scattering have been proposed in order to explain the discovery of several giant gaseous planets orbiting their parent stars in just few days. Several and controversial studies regarding the correlations between the presence of planets and different stellar properties, and a brief introduction of the status of the search for planets in clusters are also presented. A description of the tools and algorithms used for the analysis of the RV measurements concludes the chapter.

The first part of this PhD work describes the new configuration of the spectrograph FOCES setup and the realization of a complete new system for the environmental stability of this instrument. After the decommissioning in early 2010 the instrument has been returned to Munich from the Calar Alto 2.2-m telescope and located at the laboratories of the Munich University Observatory. In 2015 it will be moved to the Wendelstein Observatory, where the integration of a new 2m Fraunhofer robotic telescope and competitive astronomical instruments is on-going.

The unique opportunity to use the échelle spectrograph FOCES as test bed for more than two years in Munich has inspired the *Munich Spectrograph Stability Project* (MSSP) that focuses the efforts and expertise of people working on different fields of spectroscopy, spectrograph design and quantum optics to better understand and improve on issues related to high precision and high stability spectroscopy. Spectrograph stability, fiber and illumination stability have been the main investigation fields of this project.

After an introduction of the theory and the fundamental spectrograph components of an optical spectrograph, the new FOCES configuration later the arrive from Calar Alto Observatory and the total alignment and fine-tuning of its different optical parts, are described in Chapter 2.

Movable and remote controlled components including the adjustable slit, grating mount and prism cross disperser were either changed or fixed permanently to guarantee high mechanical stability. An old 1024×1024 Tektronix CCD-detector with 24 μm pixel size has been replaced by a new AndorSystem 2048×2048, with 13.5 μm pixel size. A initial phase of study and costs evaluation concluded to place the spectrograph in two shells of thermal and pressure stabilized "boxes", following the PEPSI spectrograph approach. The

complete construction, performance measurements and analyses of a new system for the environmental stability of the FOCES spectrograph are presented at end of Chapter 2 and in Chapter 3.

Furthermore, a variety of measurements with a selection of fibers from different vendors, including state-of-the-art octagonal and hexagonal fibers is described. According to the results presented in Table 3.3, octagonal fibers have shown their outstanding performance providing scrambling gains typically 3−5 times higher compared to their circular counterpart. In contrast to initial expectations the hexagonal fiber performed not as good as expected which may result from constraints such as short fiber length and low core protection. Finally, different fiber sections were combined and proved on their capability as the next generation of mode scramblers and eventually as a potential solution for the new FOCES fiber-link. The octagonal-circular (splice 1) fiber exhibits an excellent performance. Near-field and Far-Field tests have shown that the achieved results greatly meet the stability requirement of the FOCES spectrograph.

The values obtained in the different measurements leaded to the conclusion that with the new FOCES configuration and in this regime of environment stability, it is possible to obtained RV spectroscopy in the m/s region. All these preliminary investigations form the subject of this part of the dissertation and will help in choosing the final configuration for the échelle Spectrograph (FOCES) at the Wendelstein Observatory.

Future work includes the complete construction of the environmental stability system at the Wendelstein Observatory where harsh temperature and especially pressure conditions make the realization of this project quite demanding. A preliminary phase of study is already started.

A new optical fiber link will be implemented to transport the science light and the calibration light from the telescope and a calibration unit to the spectrograph. The use of new octagonal fibers and octagonal-circular (splice 1) fibers is planned. We also consider equipping the fiber link with a mechanical scrambler, contributing thus to improve the scrambling properties and the accuracy of radial-velocity measurements. Finally, an Astro Frequency Comb (Steinmetz et al., 2008) will be installed in few years as a new complementary calibration source. Producing calibration spectra with equidistant spectral lines at very high accuracy over the whole spectral range, this instrument will provide significant advantages with respect to a ThAr calibration source, normally used in high resolution spectroscopy.

The design, construction, integration and commissioning of an optical astronomical high resolution spectrograph is a complex and multi-disciplinary process. A wide range of competences is required, including optics, mechanics, electronics, software, astrophysics, administration, etc. Building this kind of instrument is not a one-person project and the successful realization of the project is due to the contribution and the help of many. As far I can say it was a pleasure to work in a very collaborative team, where I could learn a lot through useful discussion with very expert people. My personal contributions to the project include the new complete integration of the instrument setup after the arrive from Calar Alto Observatory, the total alignment and fine-tuning of the different optical parts, the participation to the assembly of the box system for the environmental stability, the

preparation of the pressure and temperature control system. Finally, I carried out the major part of the performance measurements and analyses. I also took charge in the tests for the characterization of several fibers. This part was done in collaboration with two master students and in my case, I focused on the preparation of the optical set-up for the fibers test and of the analysis software.

Since 2008 a radial velocity (RV) monitoring of a sample of main sequence and giant stars in the open cluster (OC) M67 is on-going to detect signatures of giant planets around their parent stars. At my arrive in Munich I was involved in this project as part of my PhD project and I was in charge by the analysis of radial velocity (RV) measurements obtained with HARPS at ESO (La Silla), SOPHIE at OHP and HRS at HET. Additional RV data came from CORALIE at the Euler Swiss Telescope.

Chapter 4 is dedicated to a complete description of the stars sample and the cluster characteristics. Technical details of the different facilities used and their configurations employed for the acquisition of the high-resolution spectra are discussed. The description of the pipelines dedicated to the reduction of the high-resolution spectra and their following analysis for the computation of the RVs is also given. Finally, the chapter presents the estimation the offset of the all RV values with respect to the HARPS data, the radial velocity distribution of the stars, and how the most likely planetary host candidates have been individuated.

Our long-standing program to search for massive planets around main sequence and evolved stars of the Open Cluster M67, has been rewarded by success and we detected the first three exoplanets in this cluster: two in orbit around the two G dwarfs YBP1194 and YBP1514, and one around the evolved star S364. The complete analysis of the RV measurements is outlined in Chapter 5. The orbital solution for YBP1194 yields a period of 6.9 days, an eccentricity of 0.24, and a minimum mass of 0.34 M_J. YBP1514 shows periodic RV variations of 5.1 days, a minimum mass of 0.40 M_J, and an eccentricity of 0.39. The best Keplerian solution for S364 yields a period of 121.7 days, an eccentricity of 0.35 and a minimum mass of 1.54 M_J. A study of Hα core flux measurements as well as of the line bisectors spans revealed no correlation with the RV periods, indicating that the RV variations are best explained by the presence of a planetary companion. Remarkably, YBP1194 is one of the best solar twins identified so far, and YBP1194b is the first planet found around a solar twin that belongs to a stellar cluster.

The detection of these 3 planets sheds new light on our understanding of the planet formation in open clusters and the dependence of this on stellar mass. With our discovery in M67 (Brucalassi et al., 2014), the detection of two hot-Jupiters in the Praesepe open cluster in 2012 (Quinn et al., 2012) and of two sub-Neptune planets in the cluster NGC6811 (Meibom et al., 2013), and the new announcement of a hot-Jupiter in the Hyades (Quinn et al., 2013), it is now clear that giant planets can form and migrate in a dense cluster environment. This has been an open question for several years and the lack of detected planets with previous exoplanet surveys, in both open and globular clusters, triggered the hypothesis that the frequency of planet-hosting stars in clusters was lower than in the

field. Thus, studying the formation of giant planets in Open Clusters (OCs) will help to understand how a different environment, such as a rich cluster, might affect the planet formation process, the frequency, and the evolution of planetary systems with respect to field stars.

The second part of Chapter 5 reported the results about a series of simulations based on a similar Monte Carlo approach carried out to evaluate the detectability and the occurrence of giants planets in our Radial Velocity Survey. In contrast with early reports and in agreement with recent findings, our study show that massive planets around stars of open clusters are as frequent as those around field stars.

For the future work, the immediate objective is to obtain new radial velocity data, to refine the orbits parameter of the three detected planets, essential for studying formation and migration scenarios. Second, we purpose to continue the monitoring of a number of interesting candidates for hosting planets, whose RVs baseline is not yet long enough to determine the nature of the companion. In particular, 3 stars show significant hints for the presence of Jovian-mass companions.

Furthermore, once completed our RV survey, we aim to compare the chemical composition of stars with and without planets in detail. Stars in OCs indeed share age and chemical composition (Randich et al., 2005), so it is possible to control strictly the sample and to limit the parameter space in a better way than when studying field stars. Thus, a significant number of planets discovered around stars in OCs would provide the perfect sample to answer still open questions about the frequency of planets with respect to stellar properties.

Finally, search of planets around giants in OCs with HARPS and the spectrograph FEROS (Kaufer et al., 1999) spanning a large range of stellar masses are ongoing. This will enable us to study the dependence of planet formation on stellar mass. However, only with the new generation of spectrographs, such as ESO-ESPRESSO (Pepe et al., 2010), will make this search more effective and precise.

This instruments, that will be commissioned at the Very Large Telescope (VLT), using up to four of the 8.2-m telescopes, is designed to achieve a precision and long-term stability better than 0.1m s^{-1}(Pepe et al., 2010). At this level of precision, detection (and confirmation) of Earth-sized planets around Sun-like stars will be possible. Thus, giant planets around lower mass stars and low mass planets around M67 solar stars will be discovered.

Beyond the scientific interest, it was also good fun. Discovering a new planet, finding something no one knows exist else than you is quite exciting. The missions in the beautiful region of the southern Atacama (Chile) have a been great : the sky is so gorgeous, the Milky Way so evident in the night sky, than returning there is always a pleasure.

To conclude, a consideration regarding a future strategy for the study of giants planets in open clusters with RV technique. Large amount and dedicated observing time is essential for a scientific success in this kind of astronomical research and small optical observatories equipped with competitive high-resolution spectrographs can play an important role due to their different operational approach and minor schedule pressure with respect to large facilities. This one of the reasons to push the construction of a competitive high-resolution optical spectrograph as FOCES on the 2m-class telescope at the Wendelstein Observatory.

Appendix A

Fundamentals in Fiber Optics ‡

The basic structure of an optical fiber is shown in figure A.1. It consists of a inner most part referred as *core* surrounded by a layer of material called *cladding* with a slightly lower refractive index. The material of standard glass fibers is in both cases mostly fused silica glass (SiO_2) with a refractive index of the order of $n = 1.459$ and is doped with different elements to adjust the refractive index. The difference between core and cladding refractive index is usually expressed by the parameter

$$\Delta = \frac{n_1^2 - n_2^2}{2n_1^2}; \tag{A.1}$$

where n_1 and n_2 are the refractive index of the core and the cladding respectively. This value is usually of the order of ~ 0.01. The last outer layer is the *buffer*, generally a plastic material used to protect an optical fiber from physical damage. The concept of light propagation, that is the transmission of light along an optical fiber, can be described by two theories: the Ray Theory and the Mode Theory.

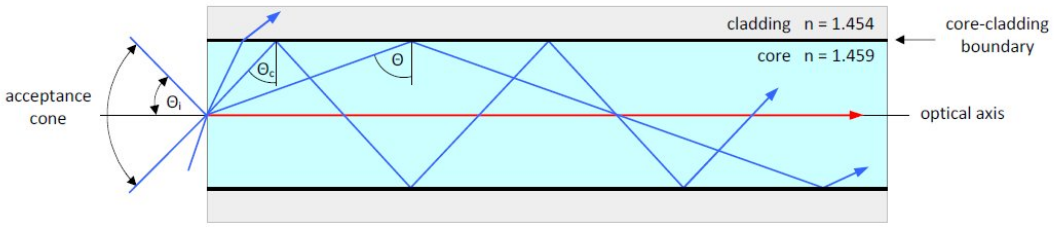

Figure A.1: Structure of a circular optical fiber. Adapted from Thyagarajan K. et al.1997

A.1 Ray Theory

According to this theory, light is described using an optical ray model, based on geometrical optics. The advantage of the ray approach is that you get a clearer picture of the propagation of light along a fiber. The ray theory is used to approximate the light acceptance and guiding properties of optical fibers.

Two types of rays can propagate along an optical fiber. The first type is called meridional rays and they pass through the axis of the optical fiber. Meridional rays are used to illustrate the basic transmission properties of optical fibers. The second type is called skew rays and they travel through an optical fiber without passing through its axis.

Light rays launched into the optical waveguides follow the principle of the total internal reflection and thus fulfill the Snell's law of refraction. However, total internal reflection only occurs if the angle of propagation is greater than the critical angle (θ_c). Only those rays that enter the fiber and strike the interface at these angles will propagate along the fiber. This means that the light ray incident on the fiber core must be within the acceptance cone defined by the acceptance angle (θ_i). This is the maximum angle with respect to the fiber axis that allows the propagation of light entering the fiber. The value of the angle of acceptance depends on fiber properties and transmission conditions and can be derived from the refractive indices of the core, cladding, and medium surrounding the fiber. Thus, the transmission can happen only if the following conditions are fulfilled:

$$\sin\theta > \frac{n_2}{n_1}; \quad \text{or} \quad \sin\theta_i < \frac{\sqrt{n_1^2 - n_2^2}}{n_0}; \tag{A.2}$$

where n_0 is often set to unity in air. The *numerical aperture* (NA) is a important parameter that measures the ability of an optical fiber to capture light, defining the acceptance cone of an optical fiber. It is given by

$$NA = \sin\theta_i = \sqrt{n_1^2 - n_2^2} = \frac{1}{2 \cdot f_\#} \tag{A.3}$$

where $f_\#$ is the focal ratio of the launched light cone. Typical values of NA range from 0.20 to 0.29 for glass fibers (fibers for astronomical purpose usually have around 0.22 for multi-mode fibers and 0.11 for single-mode fibers). Plastic fibers generally have a higher NA (higher than 0.50). With increasing the numerical aperture more light will collected by the fiber and faster is the accepted focal ratio.

A.2 Mode Theory

The mode theory uses electromagnetic wave behavior to describe the propagation of light along a fiber. The mode theory is useful in describing the optical fiber properties of

[‡]Based on *Fundamentals of Photonics*, B.E.A Saleh, M.C.Teich, 1991

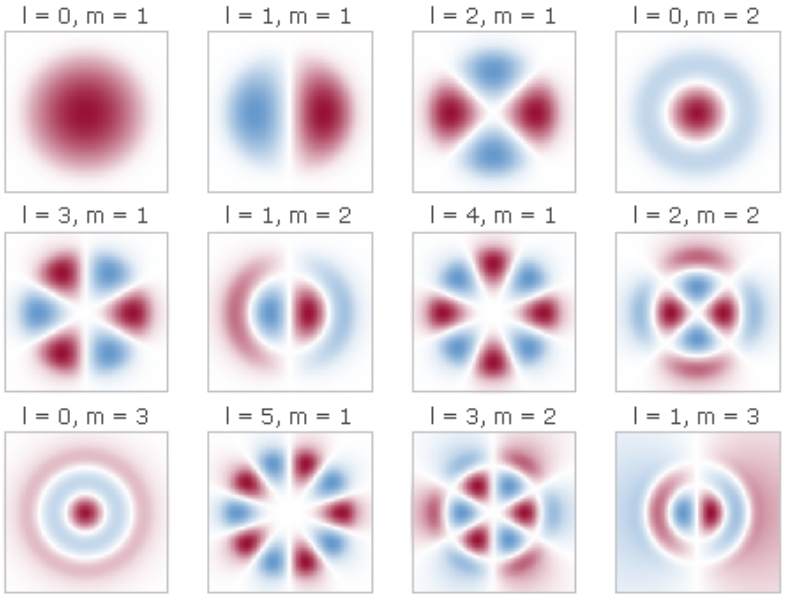

Figure A.2: Transversal modes in a circular waveguide. According to the Mode Theory, each mode is described by the indices l and m characterizing its azimuthal and radial distribution.

absorption, attenuation, and dispersion. Fibers modes can be described as a set of guided electromagnetic waves. A fiber in general can support one or several modes depending on their properties.

The mode theory suggests that a light wave can be represented as a plane wave, whose surfaces of constant phase, or wavefronts, are infinite parallel planes normal to the direction of propagation. A plane wave is described by its direction, amplitude, and wavelength of propagation.

Not only total internal reflection determines if modes are guided through on optical fiber. A further important factor that has to be considered is the phase-matching condition for the waves that superimpose constructively after each reflection at the core-cladding boundary. Wavefronts are required to remain in phase except for an integer number of 2π for light to be transmitted along the fiber. If propagating wavefronts are not in phase, they eventually disappear because of destructive interference. This interference is the reason why only a finite number of modes can propagate along the fiber (see fig. A.2).

For a given mode, a change in wavelength can prevent the mode from propagating along the fiber. The wavelength at which a mode ceases to be bound is called the cutoff wavelength for that mode. However, an optical fiber is always able to propagate at least one mode. This mode is referred to as the fundamental mode of the fiber.

An optical fiber that operates above the cutoff wavelength (at a longer wavelength) is called a single mode fiber. An optical fiber that operates below the cutoff wavelength is called a multimode fiber.

Appendix B

Keplerian orbit model[†]

A single planet orbiting a star causes this star to undergo a reflex motion around the star-planet center of mass. As in all orbiting systems, both star and planet orbit the common system barycenter with a closed elliptical orbit in inertial space, with the center of mass at one focus. For exoplanets studies, a specific reference frame is commonly used to describe the Keplerian orbit in three dimensions (see Figure B.1). It uses a *sky-plane* (*i.e.* a plane perpendicular to the line of sight and tangent to the celestial sphere) as the reference plane that intercepts the *orbital plane* along the *line of nodes* with an angle i, denoted *orbital inclination*. The x-axis is taken along line of nodes with direction chosen toward the *descending node*, the y-axis is also tangent to the celestial sphere, such that the resulting system is right-handed, the z-axis is directed along the line of sight, away from the observer.

Starting from the expression for the position and velocity vectors of the planet in an astrocentric reference frame (see Murray and Dermott, 2000 for details), we can pass to the new reference frame with an opportune coordinates transformation and then move to barycenter coordinates. To calculate the velocity actually detected by the observer, we must add the velocity γ of the barycenter itself with respect to the background stars.

The complete expression for the radial velocity (RV) of a star due to the presence of a single orbiting planet is:

$$V_r = \frac{2\pi a}{P\sqrt{1-e^2}} \frac{m_p sin(i)}{(M_\star + M_p)} \left[cos(\nu + \omega) + e \cdot cos\omega\right] + \gamma \tag{B.1}$$

where a is the semi-major axis of the orbit of the planet, P is the orbital period, m_p is the mass of the planet, $M_\star$ is the mass of the star, i is the inclination of the orbital plane, e is the eccentricity of the orbit, $\nu(t)$ is the true anomaly, ω is the argument of the periastron and γ is the systemic velocity off-set of the star-planet system.

In order to fit the data, the RV is usually parametrized as a function of the time t as follow:

$$V_r(t) = K \cdot \left[cos(\nu(t) + \omega) + e \cdot cos(\omega)\right] + \gamma \tag{B.2}$$

[†]Based on Beaugé et al. (2007)

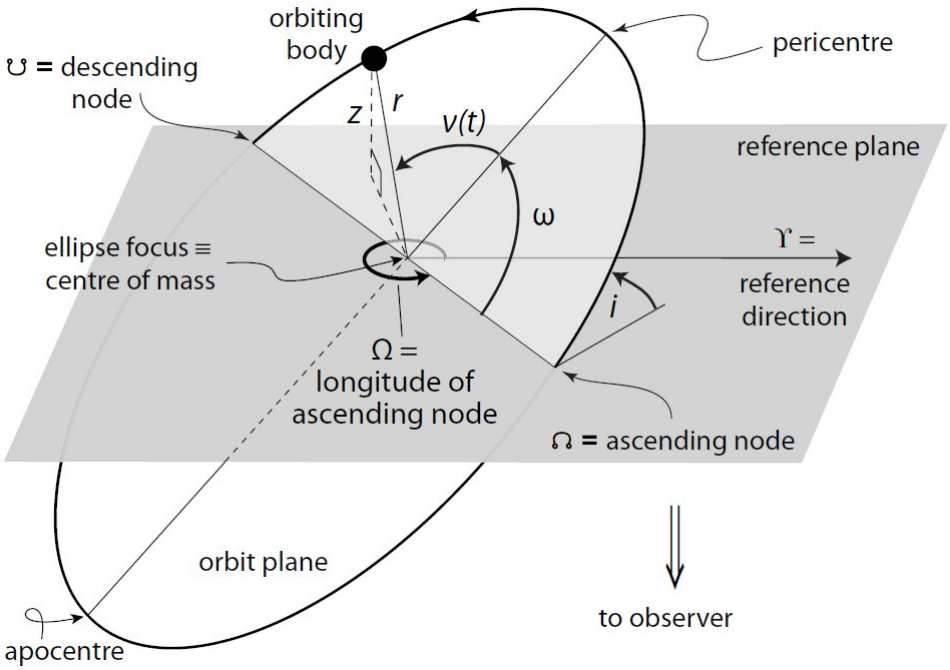

Figure B.1: An elliptical orbit in three dimensions. The reference plane is tangent to the celestial sphere. i is the inclination of the orbit plane. The nodes are the points where the orbit and reference planes intersect. Ω defines the longitude of the ascending node, measured in the reference plane. ω is the fixed angle defining the object's argument of pericenter relative to the ascending node. The true anomaly, $\nu(t)$, is the time-dependent angle characterizing the object's position along the orbit.

where:

$$K = \frac{m_p sin(i)}{(M_\star + m_p)} \frac{2\pi a}{P\sqrt{1-e^2}} \tag{B.3}$$

In Eq. B.2 only the true anomaly ν results to be a function of the time t. In the case of circular orbits (e=0), it results to be a linear function of time, while in the general elliptic case, it is the mean anomaly l to be a linear function of the time: l=$\frac{2\pi}{P}$(t-τ) where τ is the time of passage through the periastron. The relation between the true anomaly ν and the mean anomaly l is derived through the intermediate eccentric anomaly u, and is expressed by the following equations:

$$tan(\nu/2) = \sqrt{\frac{1+e}{1-e}} \cdot tan(u/2); \qquad l = u - e \cdot sin(u) \tag{B.4}$$

The latter is the classical Kepler equation, and must be solved iteratively. The position of an object along its orbit at any time can be estimated by calculating l at that time,

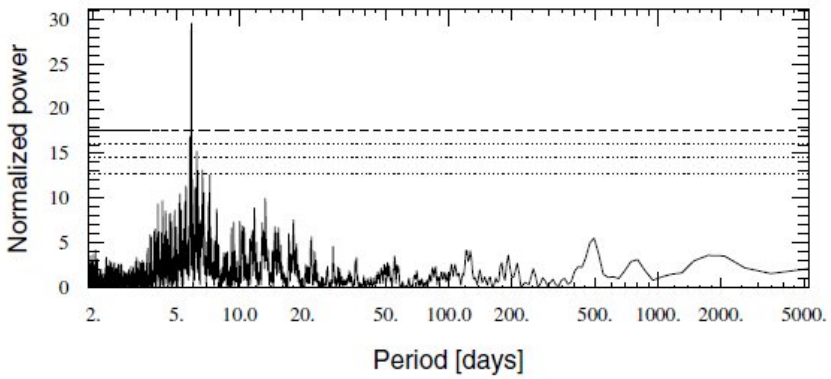

Figure B.2: Example of periodogram using the RV data for HD 103774. A significant peak is visible at ∼5.9 days. The topmost dashed line is the 10^{-4} false alarm probability, the lower dotted lines correspond to 10^{-3}, 10^{-2}, and 10^{-1} false-alarm probabilities. Adapted from Lo Curto et al. (2013).

solving iteratively for the eccentric anomaly u and then deriving the true anomaly ν that appears in Eq. B.2.

B.1 The Lomb-Scargle algorithm[‡]

The Lomb-Scargle algorithm is a modified periodogram analysis, equivalent to a least-squares fitting of sine waves, which aims to the efficient detection of a periodic signal in the case of unevenly-spaced observation times and in presence of noise. However, the original concept of the periodogram did not take into account measurement errors. This problem was solved by Gilliland & Baliunas (1987) introducing weighted sums. Additionally, the data was assumed to have no offset (the mean of the data and the mean of the sinewave were both assumed zero). Zechmeister & Kürster (2009) generalized the concept of the periodogram to fit a full sine wave, including an offset and weights: the General Lomb-Scargle periodogram (GLS). In our case, we computed the Lomb-Scargle periodogram according to the definition of Scargle (1982) and Horne & Baliunas (1986), that here below we summarize. For fast computation of trigonometric sums, we refer to Press & Rybicki (1989). Briefly, given a set of data points $h_i \equiv h(t_i)$, $i = 1, ..., N$ at respective observations times t_i, the mean and the variance of the data are computed by

$$\bar{h} \equiv \frac{1}{N}\sum_{1}^{N} h_i, \qquad \sigma^2 \equiv \frac{1}{N-1}\sum_{1}^{N}(h_i - \bar{h})^2 \tag{B.5}$$

The resulting Lomb-Scargle normalized periodogram $P_N(\omega)$ (spectral power as a function of the frequency, or period) is defined (according to Scargle (1982) and Horne & Baliunas

[‡]Based on Scargle (1982) and Horne & Baliunas (1986))

(1986)) by:

$$P_N(\omega) \equiv \frac{1}{2\sigma^2} \left\{ \frac{\left[\sum_j (h_i - \bar{h}) \cos \omega(t_j - \tau)\right]^2}{\sum_j \cos^2 \omega(t_j - \tau)} + \frac{\left[\sum_j (h_i - \bar{h}) \sin \omega(t_j - \tau)\right]^2}{\sum_j \sin^2 \omega(t_j - \tau)} \right\} \tag{B.6}$$

where τ is a time-offset that makes $P_N(\omega)$ completely independent of shifting all the t_i by any constant and is defined by the relation

$$\tan(2\omega\tau) = \frac{\sum_j \sin 2\omega t_j}{\sum_j \cos 2\omega t_j} \tag{B.7}$$

Lomb (1976) shows that this particular choice of offset has the further effect to make eq. B.6 identical to the equation that one would obtain by linear least-squares fitting of sine curves with the form

$$h(t) = A \cos \omega t + B \sin \omega t \tag{B.8}$$

Practically, we evaluate $P_N(\omega)$ for a range of frequencies (or periods), and look for the maximum (see fig. B.2). The significance of the peak depends on the *false alarm probability* (FAP) level, *i.e.* how often a periodogram power as large as the observed power would arise purely due to noise alone. The FAP level can be determined analytically following (Horne & Baliunas, 1986). It is shown that in case of data values being independent Gaussian random values, $P_N(\omega)$, with the σ^2 normalization, has an exponential e^{-z} probability distribution with unit mean. This means that for any frequency ω_0, the probability that $P_N(\omega_0)$ is of hight z or higher is $Prob[P_N(\omega_0) > z] = e^{-z}$. It follows that, if we can scan M *independent* frequencies, the probability that none give values larger than z is $(1 - e^{-z})^M$. Thus

$$FAP = 1 - (1 - e^{-z})^M \tag{B.9}$$

is the false alarm probability of the null Hypothesis, that is the significance level of any peak. The false alarm probability tells us the probability that a peak of height z or higher will occur, assuming that the data are pure noise. A small value for the FAP indicates a highly significant periodic signal. Finally, to evaluate this significance, we need to calculate the number of independent frequencies M. Horne & Baliunas (1986) used extensive Monte Carlo simulations for determining M in various cases, and found an empirical formula for M as function of N:

$$M = -6.362 + 1.193N + 0.000098N^2 \tag{B.10}$$

Alternatively the significance of a peak in the periodogram can be determined by *boost-rapping* methods (Mortier et al., 2012, references hereafter).

B.2 The Levenberg-Marquardt method[‡]

Since the equations describing the RV orbit are nonlinear, dedicated tools for the parameters search are requested to avoid computational problems and the presence of many false local χ^2 minima. The Levenberg-Marquardt method (LM) is a standard technique used to solve nonlinear least squares problems, that arise especially in least squares curve fitting, *i.e.* when one has to fit a parameterized function to a set of measured data points by minimizing the sum of the squares of the errors between the data points and the function. It has been widely adopted for both RV and astrometric orbiting fitting (Press et al. 1982). In case the function is not linear in the parameters, nonlinear least squares methods involve an iterative improvement of the parameter values in order to reduce the sum of the squares of the errors between the function and the measured data points. The Levenberg-Marquardt curve-fitting method is actually a combination of two minimization methods: the gradient descent method and the Gauss-Newton method. In the gradient descent method, the sum of the squared errors is reduced by updating the parameters with perturbation steps proportional to the negative of the gradient of the function at the current point, moving thus in the direction of the greatest reduction of the least squares function. In the Gauss-Newton method, the sum of the squared errors is reduced by assuming the least squares function is locally quadratic, and finding the minimum of the quadratic. The Levenberg-Marquardt method acts more like a gradient-descent method when the parameters are far from their optimal value, and acts more like the Gauss-Newton method when the parameters are close to their optimal value.

Considering a set of m data points (t_i, y_i) that must to be fitted with a function $f(t, \mathbf{p})$ of an independent variable t and a vector of n parameters $\mathbf{p}$. It is convenient to minimize the sum of the weighted squares of the errors (or weighted residuals) between the measured data $y(t_i)$ and the curve-fit function $f(t_i, \mathbf{p})$, given by

$$\chi^2 = \sum_i^m \left[\frac{y(t_i) - f(t_i, \mathbf{p})}{w_i} \right]^2 \tag{B.11}$$

$$= (\mathbf{y} - \mathbf{f}(\mathbf{p}))^T W (\mathbf{y} - \mathbf{f}(\mathbf{p})) \tag{B.12}$$

where the weighting matrix is diagonal with $W_{ii} = 1/w_i^2$ where $\mathbf{f}$ and $\mathbf{y}$ are vectors with ith component $f(t_i, \mathbf{p})$ and $y(t_i)$, respectively. If the function $f(t, \mathbf{p})$ is nonlinear in the model parameters $\mathbf{p}$, then the minimization of χ^2 with respect to the parameters $\mathbf{p}$ must be carried out iteratively. The goal of each iteration is to find a perturbation $\boldsymbol{\delta}$ to the parameters $\mathbf{p}$ that reduces χ^2.

To start a minimization, the user has to provide an initial guess for the parameter vector $\mathbf{p}$. In each iteration step, $\mathbf{p}$ is replaced by a new estimate, $\mathbf{p}+\boldsymbol{\delta}$. To determine $\boldsymbol{\delta}$, the functions $\mathrm{f}(t_i,\mathbf{p}+\boldsymbol{\delta})$ are approximated by their linearizations $\mathrm{f}(t_i,\mathbf{p}+\delta) \sim \mathrm{f}(t_i,\mathbf{p}) + J_i\boldsymbol{\delta}$

[‡]Based on *The Levenberg-Marquardt method for nonlinear least squares curve-fitting problems*, Henri P. Gavin, 2013

where $J_i = \partial f(t_i, \mathbf{p})/\partial \mathbf{p}$ is the gradient of f with respect to $\mathbf{p}$. At the minimum of the χ^2, the gradient of χ^2 with respect to $\boldsymbol{\delta}$ has to be zero. Replacing the linearization for f(t_i,$\mathbf{p}$+δ) in the eq. B.11 , taking the derivative with respect to $\boldsymbol{\delta}$ and setting the result to zero gives in the damped version proposed Levenberg:

$$\left[\mathbf{J^T W J} + \lambda \mathbf{I}\right] \boldsymbol{\delta} = \mathbf{J^T W}(\mathbf{y} - \mathbf{f}(\mathbf{p})) \tag{B.13}$$

where $\mathbf{I}$ is the identity matrix, $\mathbf{J}$ is the Jacobian matrix whose ith row equals J_i and the algorithmic parameter, λ, is adjusted at each iteration. Small values of λ bring the algorithm closer to the Gauss-Newton method and large values of λ result in a gradient descent update. A large value of λ is usually initialized. If an iteration results in a worse approximation, λ is increased. As the solution approaches the minimum, λ is decreased, the Levenberg-Marquardt method approaches the Gauss-Newton method, and the solution typically converges rapidly to the local minimum. Marquardt replaced the identity matrix, $\mathbf{I}$, with the diagonal matrix consisting of the diagonal elements of $\mathbf{J}^T\mathbf{W}\mathbf{J}$, to avoid slow convergence in the direction of small gradient. The resulting the Levenberg-Marquardt algorithm is:

$$\left[\mathbf{J^T W J} + \lambda diag(\mathbf{J^T W J})\right] \boldsymbol{\delta} = \mathbf{J^T W}(\mathbf{y} - \mathbf{f}(\mathbf{p})) \tag{B.14}$$

MPFIT

As concrete example of the application of the Levenberg-Marquardt method, we refer to the IDL implementation MPFIT (Markwardt, 2009) described by Wright & Howard (2009). This was the tool used for the analysis of the our RV measurements. MPFIT requires a user-defined function that accepts, as an argument, trial values for the parameters, evaluates the model at those values, and returns the corresponding residuals to the data. These informations are used to step through parameter space and to find the minimum χ^2. Uncertainties in these parameters can be calculated by mapping χ^2 space near the minimum (Wright et al., 2007) or by error *boostrapping* (Butler et al., 2006).

Wright & Howard (2009) present a method of efficiently fitting multi-Keplerian models to high RV and astrometric data separating the parameters into linear and nonlinear components in the content of LM algorithm and provide the explicit derivatives used in such a fit. The formulated linearization reduces the search space for n_p planets from $5n_p + 1$ Keplerian parameters to $3n_p$ non-linear variables (corresponding to e, P, t_p for each planet) In this approach, Eq. B.2, generalized to the case of n_p planets, is rearranged as

$$v_r(t) = \sum_{j}^{n_p} \left[h_j \cos \nu_j(t) + c_j \sin \nu_j(t)\right] + V_0 + d(t - t0) \tag{B.15}$$

where

$$h_j = K_j \cos \omega_j, \tag{B.16}$$

$$c_j = -K_j \sin \omega_j, \tag{B.17}$$

$$V_0 = \gamma + \sum_{j}^{n_p} K_j e_j \cos \omega_j, \tag{B.18}$$

The non-linear terms (e, P, t_p) are then searched for algorithmically (e.g. using the LM method), with the linear parameters (h, c, v_0), which are transformable back to (ω, K, γ), solved for analytically at each search step. For the specific calculation of the explicit derivative to be used in the LM alalgorithm we refer to Wright & Howard (2009)

Acknowledgements

This thesis is the result of four intense years as a PhD-student. Without the help and support of many people, this work would not have been realized and here I would like to take the opportunity to thank them.

My greatest thanks go to my supervisors Roberto Saglia, Luca Pasquini and Frank Grupp. They are remarkable persons of great scientific expertise, always available whenever I burst in their office, patiently answering my questions, teaching and encouraging me.

Special thanks go to my unofficial co-supervisors, Johannes Koppenhöfer and Florian Lang-Bardl and Gerardo Avila for working with me, explaining me tricks of astronomy and technical issues and helping me on a huge number of occasions.

The Wendelstein instrumental team at the University Observatory of Munich is an extraordinary fun team to work in. This young and dynamic group of people always made me comfortable to speak my mind and ask for help. Over the years I have worked with most of you and all of you have contributed in making me the researcher that I am today. I would like to thank also Tobias and Christian for the valuable discussions on fiber optics and the good time in the lab during the fibers test. Furthermore, special thanks go to Adolf Karasz and Anton Mittermeier from USM helped a lot with their skills in building mechanical parts for the test setup.

I could not have done this work without the help of Michele who introduces me with infinite patience to the world of spectral analysis and now is one of the my best friends together with Alessandro, Annalisa, Viola, Barbara, Giancarlo, Anna. *Grazie bimbetti! Grazie per aver sopportato i mie pasticci e le mie strane parole toscane. Grazie per le fughe in macchina a prendere il treno, per le fantastiche cene di Natale, per le pause caffe', per le gite della domenica, per le serate di D&D e per tutti i momenti stupendi passati insieme. Siete diventati per me come fratelli e ho sempre potuto contare su di voi in qualunque occasione.*

A huge thanks to Daniela, my special friend and my flatmate, for her advices, for her *"19:30 at Norbad??!!"* and *"Ehi ciao, come va?"* when I came back late from work, for saving me several times when I forgot my keys and for suffering all the times I was speaking up by my self.

Living in a foreign country is not always easy, but thanks to a lot of crazy colleagues and friends, I've always felt at home. A great thanks to Marie and Achim, our Salsa teachers and to all the people of the dancing class. Thanks to Fabiana, Matteo il Perugino, Giulia, Angela, Lodo, Ugo, Giulia di Roma, Matteo and all the members of the good company of

people regularly going out for drinking, eating, dancing, laughing...

Thanks for the guys that share my office and suffer my instant bursts of enthusiasm at any random new result, article or email appearing on my screen (sorry for the ever growing mess in the FOCES lab). I would like to specifically thank Alessia, for the very big help during the final phase of printing and assembling this Thesis. *Grazie Alessia per essere rimasta in ufficio con me a fino a tardissimo per stampare la tesi. Mi hai salvata!*

I would like to thank my mum Lorenza, my sister Chiara and all the friends back home for always supporting me. *Grazie per gli abbracci quando torno a casa, perche' siete sempre in pena quando viaggio, per i vostri "Annucci, ma come e' andato il viaggio?? sei arrivata??", e perche' mi tenete aggiornata su tutto quello che succede nel piccolo paese di S.Agata. Vi porto sempre con me.*

Finally, really special thanks go to 'Ciaps', my boyfriend at the begin of my PhD and now my husband. *Grazie per tutte le volte che mi sei venuto a prendere alla stazione, per le chiaccherate su Skype, per le decisioni prese a distanza, perche' ti ho sentito sempre vicino sebbene fossi a migliaia di chilometri di distanza, ma soprattutto per avermi supportato e aiutato in ogni momento di questa pazza esperienza della nostra vita insieme. Questa lavoro e' dedicato a te. Grazie davvero infinite per quello che e' stato e per quello che ci attende.*

Bibliography

Absil, O. & Mawet, D. (2010). Formation and evolution of planetary systems: the impact of high-angular resolution optical techniques. *A&AR*, **18**, 317–382.

Adams, F. C. & Laughlin, G. (2003). Migration and dynamical relaxation in crowded systems of giant planets. *ICARUS*, **163**, 290–306.

Adibekyan, V. Z., González Hernández, J. I., Delgado Mena, E., Sousa, S. G., Santos, N. C., Israelian, G., Figueira, P., & Bertran de Lis, S. (2014). On the origin of stars with and without planets. T_c trends and clues to Galactic evolution. *A&A*, **564**, L15.

Aigrain, S., Irwin, J., Hodgkin, S., Alapini, A., Hebb, L., Moraux, E., Irwin, M., & Monitor Collaboration (2006). Transiting planets and brown dwarfs in star forming regions and young open clusters. In L. Arnold, F. Bouchy, and C. Moutou, editors, *Tenth Anniversary of 51 Peg-b*, pages 181–183.

Alibert, Y., Mordasini, C., & Benz, W. (2004). Migration and giant planet formation. *A&A*, **417**, L25–L28.

Armitage, P. J. (2010). *Astrophysics of Planet Formation*.

Avila, G. (2012). FRD and scrambling properties of recent non-circular fibres. In *Society of Photo-Optical Instrumentation Engineers (SPIE) Conference Series*, volume 8446 of *Society of Photo-Optical Instrumentation Engineers (SPIE) Conference Series*.

Avila, G. & Singh, P. (2008). Optical fiber scrambling and light pipes for high accuracy radial velocities measurements. In *Society of Photo-Optical Instrumentation Engineers (SPIE) Conference Series*, volume 7018 of *Society of Photo-Optical Instrumentation Engineers (SPIE) Conference Series*.

Avila, G., Singh, P., & Albertsen, M. (2006). Photometrical scrambling gain and focal ratio degradation in fibers for astronomical instruments. In *Society of Photo-Optical Instrumentation Engineers (SPIE) Conference Series*, volume 6269 of *Society of Photo-Optical Instrumentation Engineers (SPIE) Conference Series*.

Ballard, S., Fabrycky, D., Fressin, F., Charbonneau, D., Desert, J.-M., Torres, G., Marcy, G., Burke, C. J., Isaacson, H., Henze, C., Steffen, J. H., Ciardi, D. R., Howell, S. B.,

Cochran, W. D., Endl, M., Bryson, S. T., Rowe, J. F., Holman, M. J., Lissauer, J. J., Jenkins, J. M., Still, M., Ford, E. B., Christiansen, J. L., Middour, C. K., Haas, M. R., Li, J., Hall, J. R., McCauliff, S., Batalha, N. M., Koch, D. G., & Borucki, W. J. (2011). The Kepler-19 System: A Transiting 2.2 R Planet and a Second Planet Detected via Transit Timing Variations. *ApJ*, **743**, 200.

Baraffe, I., Chabrier, G., & Barman, T. (2008). Structure and evolution of super-Earth to super-Jupiter exoplanets. I. Heavy element enrichment in the interior. *A&A*, **482**, 315–332.

Baranne, A. (1988). White pupil story or evolution of a spectrographic mounting. In *Very Large Telescopes and their Instrumentation, Vol. 2*, volume 2, pages 1195–1206.

Baranne, A., Queloz, D., Mayor, M., Adrianzyk, G., Knispel, G., Kohler, D., Lacroix, D., Meunier, J.-P., Rimbaud, G., & Vin, A. (1996). ELODIE: A spectrograph for accurate radial velocity measurements. *A&AS*, **119**, 373–390.

Basri, G. & Brown, M. E. (2006). Planetesimals to Brown Dwarfs: What is a Planet? *Annual Review of Earth and Planetary Sciences*, **34**, 193–216.

Baumann, P., Ramírez, I., Meléndez, J., et al. (2010). Lithium depletion in solar-like stars: no planet connection. *A&A*, **519**, A87.

Beaugé, C., Ferraz-Mello, S., & Michtchenko, T. A. (2007). *Planetary Masses and Orbital Parameters from Radial Velocity Measurements*, page 1.

Belloni, T., Verbunt, F., & Mathieu, R. D. (1998). X-rays from old open clusters: M 67 and NGC 188. *A&A*, **339**, 431–439.

Bonfils, X., Mayor, M., Delfosse, X., Forveille, T., Gillon, M., Perrier, C., Udry, S., Bouchy, F., Lovis, C., Pepe, F., Queloz, D., Santos, N. C., & Bertaux, J.-L. (2007). The HARPS search for southern extra-solar planets. X. A m sin i = 11 M_øplus planet around the nearby spotted M dwarf ¡ASTROBJ¿GJ 674¡/ASTROBJ¿. *A&A*, **474**, 293–299.

Bonnell, I. A., Smith, K. W., et al. (2001). Planetary dynamics in stellar clusters. *MNRAS*, **322**, 859–865.

Borucki, W. J. & for the Kepler Team (2010). Characteristics of Kepler Planetary Candidates Based on the First Data Set: The Majority are Found to be Neptune-Size and Smaller. *ArXiv e-prints*.

Borucki, W. J., Agol, E., Fressin, F., Kaltenegger, L., Rowe, J., Isaacson, H., Fischer, D., Batalha, N., Lissauer, J. J., Marcy, G. W., Fabrycky, D., Désert, J.-M., Bryson, S. T., Barclay, T., Bastien, F., Boss, A., Brugamyer, E., Buchhave, L. A., Burke, C., Caldwell, D. A., Carter, J., Charbonneau, D., Crepp, J. R., Christensen-Dalsgaard, J., Christiansen, J. L., Ciardi, D., Cochran, W. D., DeVore, E., Doyle, L., Dupree,

A. K., Endl, M., Everett, M. E., Ford, E. B., Fortney, J., Gautier, T. N., Geary, J. C., Gould, A., Haas, M., Henze, C., Howard, A. W., Howell, S. B., Huber, D., Jenkins, J. M., Kjeldsen, H., Kolbl, R., Kolodziejczak, J., Latham, D. W., Lee, B. L., Lopez, E., Mullally, F., Orosz, J. A., Prsa, A., Quintana, E. V., Sanchis-Ojeda, R., Sasselov, D., Seader, S., Shporer, A., Steffen, J. H., Still, M., Tenenbaum, P., Thompson, S. E., Torres, G., Twicken, J. D., Welsh, W. F., & Winn, J. N. (2013). Kepler-62: A Five-Planet System with Planets of 1.4 and 1.6 Earth Radii in the Habitable Zone. *Science*, **340**, 587–590.

Boss, A. P. (1997). Formation of giant gaseous protoplanets by gravitational instability. In *Lunar and Planetary Science Conference*, volume 28 of *Lunar and Planetary Science Conference*, page 137.

Boss, A. P. (2003). Rapid Formation of Outer Giant Planets by Disk Instability. *ApJ*, **599**, 577–581.

Bottke, W. F., Durda, D. D., Nesvorný, D., Jedicke, R., Morbidelli, A., Vokrouhlický, D., & Levison, H. F. (2005). Linking the collisional history of the main asteroid belt to its dynamical excitation and depletion. *ICARUS*, **179**, 63–94.

Bouchy, F. & Sophie Team (2006). SOPHIE: the successor of the spectrograph ELODIE for extrasolar planet search and characterization. In L. Arnold, F. Bouchy, and C. Moutou, editors, *Tenth Anniversary of 51 Peg-b: Status of and prospects for hot Jupiter studies*, pages 319–325.

Bouchy, F., Hébrard, G., Udry, S., Delfosse, X., Boisse, I., Desort, M., Bonfils, X., Eggenberger, A., Ehrenreich, D., Forveille, T., Lagrange, A. M., Le Coroller, H., Lovis, C., Moutou, C., Pepe, F., Perrier, C., Pont, F., Queloz, D., Santos, N. C., Ségransan, D., & Vidal-Madjar, A. (2009). The SOPHIE search for northern extrasolar planets . I. A companion around HD 16760 with mass close to the planet/brown-dwarf transition. *A&A*, **505**, 853–858.

Bramich, D. M., Horne, K., Bond, I. A., Street, R. A., Collier Cameron, A., Hood, B., Cooke, J., James, D., Lister, T. A., Mitchell, D., Pearson, K., Penny, A., Quirrenbach, A., Safizadeh, N., & Tsapras, Y. (2005). A survey for planetary transits in the field of NGC 7789. *MNRAS*, **359**, 1096–1116.

Bromley, B. C. & Kenyon, S. J. (2011). A New Hybrid N-body-coagulation Code for the Formation of Gas Giant Planets. *ApJ*, **731**, 101.

Brucalassi, A., Feger, T., Grupp, F., Lang-Bardl, F., Hu, S. M., Hopp, U., & Bender, R. (2012). Pressure and temperature stabilization of an existing Echelle spectrograph III. In *Society of Photo-Optical Instrumentation Engineers (SPIE) Conference Series*, volume 8446 of *Society of Photo-Optical Instrumentation Engineers (SPIE) Conference Series*.

Brucalassi, A., Grupp, F., Lang-Bardl, F., Liang, W., Franik, C., Kellerm, H., Hu, S. M., Hopp, U., & Bender, R. (2013). Pressure and temperature stabilization of an existing Echelle spectrograph IV. In *Society of Photo-Optical Instrumentation Engineers (SPIE) Conference Series*, volume 8864 of *Society of Photo-Optical Instrumentation Engineers (SPIE) Conference Series*.

Brucalassi, A., Pasquini, L., Saglia, R., Ruiz, M. T., Bonifacio, P., Bedin, L. R., Biazzo, K., Melo, C., Lovis, C., & Randich, S. (2014). Three planetary companions around M 67 stars. *A&A*, **561**, L9.

Bruntt, H., Grundahl, F., Tingley, B., Frandsen, S., Stetson, P. B., & Thomsen, B. (2003). A search for planets in the old open cluster NGC 6791. *A&A*, **410**, 323–335.

Burke, C. J., Gaudi, B. S., DePoy, D. L., & Pogge, R. W. (2006). Survey for Transiting Extrasolar Planets in Stellar Systems. III. A Limit on the Fraction of Stars with Planets in the Open Cluster NGC 1245. *AJ*, **132**, 210–230.

Burrows, A., Sudarsky, D., & Hubeny, I. (2004). Spectra and Diagnostics for the Direct Detection of Wide-Separation Extrasolar Giant Planets. *ApJ*, **609**, 407–416.

Butler, R. P., Wright, J. T., Marcy, G. W., Fischer, D. A., Vogt, S. S., Tinney, C. G., Jones, H. R. A., Carter, B. D., Johnson, J. A., McCarthy, C., & Penny, A. J. (2006). Catalog of Nearby Exoplanets. *ApJ*, **646**, 505–522.

Campbell, B., Walker, G. A. H., & Yang, S. (1988). A search for substellar companions to solar-type stars. *ApJ*, **331**, 902–921.

Capobianco, C. C., Duncan, M., & Levison, H. F. (2011). Planetesimal-driven planet migration in the presence of a gas disk. *ICARUS*, **211**, 819–831.

Cappetta, M., Saglia, R. P., & et al. (2012). The first planet detected in the WTS: an inflated hot-Jupiter in a 3.35 day orbit around a late F-star.

Charbonneau, D., Brown, T. M., Latham, D. W., & Mayor, M. (2000). Detection of Planetary Transits Across a Sun-like Star. *ApJ*, **529**, L45–L48.

Chazelas, B., Pepe, F., Wildi, F., Bouchy, F., Perruchot, S., & Avila, G. (2010). New scramblers for precision radial velocity: square and octagonal fibers. In *Society of Photo-Optical Instrumentation Engineers (SPIE) Conference Series*, volume 7739 of *Society of Photo-Optical Instrumentation Engineers (SPIE) Conference Series*.

Ciesla, F. J. (2008). Radial transport in the solar nebula: Implications for moderately volatile element depletions in chondritic meteorites. *Meteoritics and Planetary Science*, **43**, 639–655.

Corbett, J. C. W. & Allington-Smith, J. (2006). Fibre modal noise issues in astronomical spectrophotometry. In *Society of Photo-Optical Instrumentation Engineers (SPIE) Conference Series*, volume 6269 of *Society of Photo-Optical Instrumentation Engineers (SPIE) Conference Series*.

Cumming, A., Butler, R. P., Marcy, G. W., Vogt, S. S., Wright, J. T., & Fischer, D. A. (2008). The Keck Planet Search: Detectability and the Minimum Mass and Orbital Period Distribution of Extrasolar Planets. *PASP*, **120**, 531–554.

Debes, J. H. & Jackson, B. (2010). Too Little, Too Late: How the Tidal Evolution of Hot Jupiters Affects Transit Surveys of Clusters. *ApJ*, **723**, 1703–1710.

Delgado Mena, E., Israelian, G., González Hernández, J. I., Sousa, S. G., Mortier, A., Santos, N. C., Adibekyan, V. Z., Fernandes, J., Rebolo, R., Udry, S., & Mayor, M. (2014). Li depletion in solar analogues with exoplanets. Extending the sample. *A&A*, **562**, A92.

Döllinger, M. P., Hatzes, A. P., Pasquini, L., Guenther, E. W., Hartmann, M., Setiawan, J., Girardi, L., de Medeiros, J. R., & da Silva, L. (2011). Exoplanets around G–K Giants. In S. Schuh, H. Drechsel, and U. Heber, editors, *AIP Conf. Series*, volume 1331 of *AIP Conf. Series*, pages 79–87.

Dumusque, X., Udry, S., Lovis, C., Santos, N. C., & Monteiro, M. J. P. F. G. (2011). Planetary detection limits taking into account stellar noise. I. Observational strategies to reduce stellar oscillation and granulation effects. *A&A*, **525**, A140.

Eggenberger, A. (2010). Detection and Characterization of Planets in Binary and Multiple Systems. In K. Gożdziewski, A. Niedzielski, and J. Schneider, editors, *EAS Publications Series*, volume 42 of *EAS Publications Series*, pages 19–37.

Eisner, J. A., Plambeck, R. L., Carpenter, J. M., Corder, S. A., Qi, C., & Wilner, D. (2008). Proplyds and Massive Disks in the Orion Nebula Cluster Imaged with CARMA and SMA. *ApJ*, **683**, 304–320.

Esposito, L. W. (2002). Planetary rings. *Reports on Progress in Physics*, **65**, 1741–1783.

Fabricius, M. H., Barnes, S., Bender, R., Drory, N., Grupp, F., Hill, G. J., Hopp, U., & MacQueen, P. J. (2008). VIRUS-W: an integral field unit spectrograph dedicated to the study of spiral galaxy bulges. In *Society of Photo-Optical Instrumentation Engineers (SPIE) Conference Series*, volume 7014 of *Society of Photo-Optical Instrumentation Engineers (SPIE) Conference Series*.

Figueira, P., Marmier, M., Bonfils, X., di Folco, E., Udry, S., Santos, N. C., Lovis, C., Mégevand, D., Melo, C. H. F., Pepe, F., Queloz, D., Ségransan, D., Triaud, A. H. M. J., & Viana Almeida, P. (2010). Evidence against the young hot-Jupiter around BD +20 1790. *A&A*, **513**, L8.

Fischer, D. A. & Valenti, J. (2005). The Planet-Metallicity Correlation. *ApJ*, **622**, 1102–1117.

Ford, E. B. & Rasio, F. A. (2006). On the relation between hot-Jupiters and the Roche limit. In L. Arnold, F. Bouchy, and C. Moutou, editors, *Tenth Anniversary of 51 Peg-b: Status of and prospects for hot Jupiter studies*, pages 303–310.

Ford, E. B. & Rasio, F. A. (2008). Origins of Eccentric Extrasolar Planets: Testing the Planet-Planet Scattering Model. *ApJ*, **686**, 621–636.

Ford, E. B., Kozinsky, B., & Rasio, F. A. (2000). Secular Evolution of Hierarchical Triple Star Systems. *ApJ*, **535**, 385–401.

Ford, E. B., Havlickova, M., & Rasio, F. A. (2001). Dynamical Instabilities in Extrasolar Planetary Systems Containing Two Giant Planets. *ICARUS*, **150**, 303–313.

Ford, E. B., Rasio, F. A., & Yu, K. (2003). Dynamical Instabilities in Extrasolar Planetary Systems. In D. Deming and S. Seager, editors, *Scientific Frontiers in Research on Extrasolar Planets*, volume 294 of *Astronomical Society of the Pacific Conference Series*, pages 181–188.

Fortier, A., Benvenuto, O. G., & Brunini, A. (2007). Oligarchic planetesimal accretion and giant planet formation. *A&A*, **473**, 311–322.

Fregeau, J. M., Chatterjee, S., & Rasio, F. A. (2006). Dynamical Interactions of Planetary Systems in Dense Stellar Environments. *ApJ*, **640**, 1086–1098.

Freire Ferrero, R., Frasca, A., Marilli, E., & Catalano, S. (2004). Magnetic activity in HD 111456, a young F5-6 main-sequence star. *A&A*, **413**, 657–667.

Fressin, F., Torres, G., Rowe, J. F., Charbonneau, D., Rogers, L. A., Ballard, S., Batalha, N. M., Borucki, W. J., Bryson, S. T., Buchhave, L. A., Ciardi, D. R., Désert, J.-M., Dressing, C. D., Fabrycky, D. C., Ford, E. B., Gautier, I. T. N., Henze, C. E., Holman, M. J., Howard, A., Howell, S. B., Jenkins, J. M., Koch, D. G., Latham, D. W., Lissauer, J. J., Marcy, G. W., Quinn, S. N., Ragozzine, D., Sasselov, D. D., Seager, S., Barclay, T., Mullally, F., Seader, S. E., Still, M., Twicken, J. D., Thompson, S. E., & Uddin, K. (2012). Two Earth-sized planets orbiting Kepler-20. *Nature*, **482**, 195–198.

Ghezzi, L., Cunha, K., Smith, V. V., & de la Reza, R. (2010). Lithium Abundances in a Sample of Planet-hosting Dwarfs. *ApJ*, **724**, 154–164.

Gilliland, R. L. & Baliunas, S. L. (1987). Objective characterization of stellar activity cycles. I - Methods and solar cycle analyses. *ApJ*, **314**, 766–781.

Gilliland, R. L., Brown, T. M., Duncan, D. K., Suntzeff, N. B., Lockwood, G. W., Thompson, D. T., Schild, R. E., Jeffrey, W. A., & Penprase, B. E. (1991). Time-resolved CCD photometry of an ensemble of stars in the open cluster M67. *AJ*, **101**, 541–561.

Gilliland, R. L., Brown, T. M., Guhathakurta, P., Sarajedini, A., Milone, E. F., Albrow, M. D., Baliber, N. R., Bruntt, H., Burrows, A., Charbonneau, D., Choi, P., Cochran, W. D., Edmonds, P. D., Frandsen, S., Howell, J. H., Lin, D. N. C., Marcy, G. W., Mayor, M., Naef, D., Sigurdsson, S., Stagg, C. R., Vandenberg, D. A., Vogt, S. S., & Williams, M. D. (2000). A Lack of Planets in 47 Tucanae from a Hubble Space Telescope Search. *ApJ*, **545**, L47–L51.

Girard, T. M., Grundy, W. M., Lopez, C. E., & van Altena, W. F. (1989). Relative proper motions and the stellar velocity dispersion of the open cluster M67. *AJ*, **98**, 227–243.

Girardi, L., Bressan, A., Bertelli, G., & Chiosi, C. (2000). Low-mass stars evolutionary tracks & isochrones (Girardi+, 2000). *VizieR Online Data Catalog*, **414**, 10371.

Goldreich, P. & Tremaine, S. (1980). Disk-satellite interactions. *ApJ*, **241**, 425–441.

Goldreich, P. & Ward, W. R. (1973). The Formation of Planetesimals. *ApJ*, **183**, 1051–1062.

Gomes, R., Levison, H. F., Tsiganis, K., & Morbidelli, A. (2005). Origin of the cataclysmic Late Heavy Bombardment period of the terrestrial planets. *Nature*, **435**, 466–469.

Gonzalez, G., Carlson, M. K., & Tobin, R. W. (2010). Li abundances vsini for star-planet systems . *VizieR Online Data Catalog*, **740**, 31368.

González Hernández, J. I., Delgado-Mena, E., Sousa, S. G., Israelian, G., Santos, N. C., & Udry, S. (2013). Volatile and Refractory Abundances of Solar Analogs with Planets. In M. Chavez, E. Bertone, O. Vega, and V. De la Luz, editors, *New Quests in Stellar Astrophysics III: A Panchromatic View of Solar-Like Stars, With and Without Planets*, volume 472 of *Astronomical Society of the Pacific Conference Series*, page 97.

Gössl, C., Bender, R., Grupp, F., Hopp, U., Lang-Bardl, F., Mitsch, W., Altmann, W., Ayres, A., Clark, S., Hartl, M., Kampf, D., Sims, G., Thiele, H., & Toerne, K. (2010). A 64 Mpixel camera for the Wendelstein Fraunhofer Telescope Nasmyth wide-field port: WWFI. In *Society of Photo-Optical Instrumentation Engineers (SPIE) Conference Series*, volume 7735 of *Society of Photo-Optical Instrumentation Engineers (SPIE) Conference Series*.

Grupp, F. (2003). The nature of the fiber noise with the FOCES spectrograph. Nature, modeling and a way to achieve S/N ¿ 400. *A&A*, **412**, 897–902.

Grupp, F. (2004). MAFAGS-OS: New opacity sampling model atmospheres for A, F and G stars. I. The model and the solar flux. *A&A*, **420**, 289–305.

Grupp, F., Lang-Bardl, F., Bender, R., Gössl, C., & Hopp, U. (2008). A multi-instrument focal station for a 2m-class robotic telescope. In *Society of Photo-Optical Instrumentation Engineers (SPIE) Conference Series*, volume 7014 of *Society of Photo-Optical Instrumentation Engineers (SPIE) Conference Series*.

Grupp, F., Udem, T., Holzwarth, R., Lang-Bardl, F., Hopp, U., Hu, S.-M., Brucalassi, A., Liang, W., & Bender, R. (2010). Pressure and temperature stabilization of an existing Echelle spectrograph. In *Society of Photo-Optical Instrumentation Engineers (SPIE) Conference Series*, volume 7735 of *Society of Photo-Optical Instrumentation Engineers (SPIE) Conference Series*.

Grupp, F., Brucalassi, A., Lang, F., Hu, S. M., Holzwarth, R., Udem, T., Hopp, U., & Bender, R. (2011). Pressure and temperature stabilization of an existing chelle spectrograph II. In *Society of Photo-Optical Instrumentation Engineers (SPIE) Conference Series*, volume 8151 of *Society of Photo-Optical Instrumentation Engineers (SPIE) Conference Series*.

Guillot, T., Santos, N. C., Pont, F., Iro, N., Melo, C., & Ribas, I. (2006). A correlation between the heavy element content of transiting extrasolar planets and the metallicity of their parent stars. *A&A*, **453**, L21–L24.

Hahn, J. M. & Malhotra, R. (1999). Orbital Evolution of Planets Embedded in a Planetesimal Disk. *AJ*, **117**, 3041–3053.

Haisch, J. K. E., Lada, E. A., & Lada, C. J. (2001). Disk Frequencies and Lifetimes in Young Clusters. *ApJ*, **553**, L153–L156.

Hanuschik, R. W. (2003). A flux-calibrated, high-resolution atlas of optical sky emission from UVES. *A&A*, **407**, 1157–1164.

Hartman, J. D., Gaudi, B. S., Holman, M. J., McLeod, B. A., Stanek, K. Z., Barranco, J. A., Pinsonneault, M. H., Meibom, S., & Kalirai, J. S. (2009). Deep MMT Transit Survey of the Open Cluster M37 IV: Limit on the Fraction of Stars with Planets as Small as 0.3R_J. *ApJ*, **695**, 336–356.

Hekker, S. & Meléndez, J. (2007). Precise radial velocities of giant stars. III. Spectroscopic stellar parameters. *A&A*, **475**, 1003–1009.

Henry, G. W. & Fekel, F. C. (2002). Five New Delta Scuti Stars. *PASP*, **114**, 999–1005.

Henry, G. W., Marcy, G., Butler, R. P., & Vogt, S. S. (1999). HD 209458. *ApJ*, page 1.

Herbig, G. H. (1985). Chromospheric H-alpha emission in F8-G3 dwarfs, and its connection with the T Tauri stars. *ApJ*, **289**, 269–278.

Hill, G. J., Gebhardt, K., Komatsu, E., Drory, N., MacQueen, P. J., Adams, J., Blanc, G. A., Koehler, R., Rafal, M., Roth, M. M., Kelz, A., Gronwall, C., Ciardullo, R., & Schneider, D. P. (2008). The Hobby-Eberly Telescope Dark Energy Experiment (HETDEX): Description and Early Pilot Survey Results. In T. Kodama, T. Yamada, and K. Aoki, editors, *Panoramic Views of Galaxy Formation and Evolution*, volume 399 of *Astronomical Society of the Pacific Conference Series*, page 115.

Hopp, U., Bender, R., Goessl, C., Mitsch, W., Barwig, H., Riffeser, A., Lang, F., Wilke, S., Ries, C., Grupp, F., & Relke, H. (2008). Improving the Wendelstein Observatory for a 2m-class telescope. In *Society of Photo-Optical Instrumentation Engineers (SPIE) Conference Series*, volume 7016 of *Society of Photo-Optical Instrumentation Engineers (SPIE) Conference Series*.

Hopp, U., Bender, R., Grupp, F., Barwig, H., Gössl, C., Lang-Bardl, F., Mitsch, W., Thiele, H., Aniol, P., Schmidt, M., Hartl, M., Kampf, D., & Schöggl, R. (2010). The compact, low scattered-light 2m Wendelstein Fraunhofer Telescope. In *Society of Photo-Optical Instrumentation Engineers (SPIE) Conference Series*, volume 7733 of *Society of Photo-Optical Instrumentation Engineers (SPIE) Conference Series*.

Hopp, U., Bender, R., Grupp, F., Thiele, H., Ageorges, N., Aniol, P., Barwig, H., Gössl, C., Lang-Bardl, F., Mitsch, W., & Ruder, M. (2012). First tests of the compact low scattered-light 2m-Wendelstein Fraunhofer Telescope. In *Society of Photo-Optical Instrumentation Engineers (SPIE) Conference Series*, volume 8444 of *Society of Photo-Optical Instrumentation Engineers (SPIE) Conference Series*.

Horne, J. H. & Baliunas, S. L. (1986). A prescription for period analysis of unevenly sampled time series. *ApJ*, **302**, 757–763.

Ida, S. (2004). Planetary Mass-Period Distribution. In *KITP Conference: Planet Formation: Terrestrial and Extra Solar*.

Ida, S., Larwood, J., & Burkert, A. (2000). Evidence for Early Stellar Encounters in the Orbital Distribution of Edgeworth-Kuiper Belt Objects. *ApJ*, **528**, 351–356.

Inaba, S., Wetherill, G. W., & Ikoma, M. (2003). Formation of gas giant planets: core accretion models with fragmentation and planetary envelope. *ICARUS*, **166**, 46–62.

Israelian, G., Delgado Mena, E., Santos, N. C., Sousa, S. G., Mayor, M., Udry, S., Domínguez Cerdeña, C., Rebolo, R., & Randich, S. (2009). Enhanced lithium depletion in Sun-like stars with orbiting planets. *Nature*, **462**, 189–191.

Jackson, B., Barne, R., & Greenberg, R. (2009). Planetary Transits and Tidal Evolution. In F. Pont, D. Sasselov, and M. J. Holman, editors, *IAU Symposium*, volume 253 of *IAU Symposium*, pages 217–229.

Janson, M., Bonavita, M., Klahr, H., Lafrenière, D., Jayawardhana, R., & Zinnecker, H. (2011). High-contrast Imaging Search for Planets and Brown Dwarfs around the Most Massive Stars in the Solar Neighborhood. *ApJ*, **736**, 89.

Johnson, J. A., Aller, K. M., et al. (2010). Giant Planet Occurrence in the Stellar Mass-Metallicity Plane. *PASP*, **122**, 905–915.

Kalas, P., Graham, J. R., Chiang, E., Fitzgerald, M. P., Clampin, M., Kite, E. S., Stapelfeldt, K., Marois, C., & Krist, J. (2008). Optical Images of an Exosolar Planet 25 Light-Years from Earth. *Science*, **322**, 1345–.

Kaufer, A., Stahl, O., Tubbesing, S., Nørregaard, P., Avila, G., Francois, P., Pasquini, L., & Pizzella, A. (1999). Commissioning FEROS, the new high-resolution spectrograph at La-Silla. *The Messenger*, **95**, 8–12.

Kennedy, G. M. & Kenyon, S. J. (2008). Planet Formation around Stars of Various Masses: The Snow Line and the Frequency of Giant Planets. *ApJ*, **673**, 502–512.

Kirsh, D. R., Duncan, M., Brasser, R., & Levison, H. F. (2009). Simulations of planet migration driven by planetesimal scattering. *ICARUS*, **199**, 197–209.

Kjeldsen, H. & Bedding, T. R. (1995). Amplitudes of stellar oscillations: the implications for asteroseismology. *A&A*, **293**, 87–106.

Kobayashi, H. & Ida, S. (2001). The Effects of a Stellar Encounter on a Planetesimal Disk. *ICARUS*, **153**, 416–429.

Kokubo, E. & Ida, S. (2002). Formation of Protoplanet Systems and Diversity of Planetary Systems. *ApJ*, **581**, 666–680.

Lagrange, A.-M., Kasper, M., Boccaletti, A., Chauvin, G., Gratadour, D., Fusco, T., Ehrenreich, D., Apai, D., Mouillet, D., & Rouan, D. (2009). Constraining the orbit of the possible companion to β Pictoris. New deep imaging observations. *A&A*, **506**, 927–934.

Lagrange, A.-M., Bonnefoy, M., Chauvin, G., Apai, D., Ehrenreich, D., Boccaletti, A., Gratadour, D., Rouan, D., Mouillet, D., Lacour, S., & Kasper, M. (2010). A Giant Planet Imaged in the Disk of the Young Star β Pictoris. *Science*, **329**, 57–.

Lang-Bardl, F., Hodapp, K., Jacobson, S., Bender, R., Gössl, C., Fabricius, M., Grupp, F., Hopp, U., & Mitsch, W. (2010). 3kk: the Optical-NIR Multi-Channel Nasmyth Imager for the Wendelstein Fraunhofer Telescope. In *Society of Photo-Optical Instrumentation Engineers (SPIE) Conference Series*, volume 7735 of *Society of Photo-Optical Instrumentation Engineers (SPIE) Conference Series*.

Latham, D. W. (2006). Spectroscopic Binaries in M67. In *IAU Joint Discussion*, volume 14 of *IAU Joint Discussion*.

Latham, D. W., Mathieu, R. D., Milone, A. A. E., & Davis, R. J. (1992). Spectroscopic Binaries in the Open Cluster M67. In H. A. McAlister and W. I. Hartkopf, editors, *IAU Colloq. 135: Complementary Approaches to Double and Multiple Star Research*, volume 32 of *Astronomical Society of the Pacific Conference Series*, page 155.

Lee, Y. S., Beers, T. C., Sivarani, T., Johnson, J. A., An, D., Wilhelm, R., Allende Prieto, C., Koesterke, L., Re Fiorentin, P., Bailer-Jones, C. A. L., Norris, J. E., Yanny, B., Rockosi, C., Newberg, H. J., Cudworth, K. M., & Pan, K. (2008). The SEGUE Stellar Parameter Pipeline. II. Validation with Galactic Globular and Open Clusters. *AJ*, **136**, 2050–2069.

Levison, H. F. & Agnor, C. (2003). The Role of Giant Planets in Terrestrial Planet Formation. *AJ*, **125**, 2692–2713.

Lin, D. N. C. & Ida, S. (1997). On the Origin of Massive Eccentric Planets. *ApJ*, **477**, 781.

Lin, D. N. C. & Papaloizou, J. (1986). On the tidal interaction between protoplanets and the protoplanetary disk. III - Orbital migration of protoplanets. *ApJ*, **309**, 846–857.

Lissauer, J. J., Marcy, G. W., Bryson, S. T., Rowe, J. F., Jontof-Hutter, D., Agol, E., Borucki, W. J., Carter, J. A., Ford, E. B., Gilliland, R. L., Kolbl, R., Star, K. M., Steffen, J. H., & Torres, G. (2014). Validation of Kepler's Multiple Planet Candidates. II. Refined Statistical Framework and Descriptions of Systems of Special Interest. *ApJ*, **784**, 44.

Livio, M. & Pringle, J. E. (2003). Metallicity, planetary formation and migration. *MNRAS*, **346**, L42–L44.

Lo Curto, G., Mayor, M., Benz, W., Bouchy, F., Hébrard, G., Lovis, C., Moutou, C., Naef, D., Pepe, F., Queloz, D., Santos, N. C., Segransan, D., & Udry, S. (2013). The HARPS search for southern extra-solar planets . XXXII. New multi-planet systems in the HARPS volume limited sample: a super-Earth and a Neptune in the habitable zone. *A&A*, **551**, A59.

Lomb, N. R. (1976). Least-squares frequency analysis of unequally spaced data. *Astroph. Sp. Sci.*, **39**, 447–462.

Lovis, C. & Mayor, M. (2007). Planets around evolved intermediate-mass stars. I. Two substellar companions in the open clusters NGC 2423 and NGC 4349. *A&A*, **472**, 657–664.

Macintosh, B., Graham, J., Palmer, D., Doyon, R., Gavel, D., Larkin, J., Oppenheimer, B., Saddlemyer, L., Wallace, J. K., Bauman, B., Evans, J., Erikson, D., Morzinski, K., Phillion, D., Poyneer, L., Sivaramakrishnan, A., Soummer, R., Thibault, S., & Veran, J.-P. (2006). The Gemini Planet Imager. In *Society of Photo-Optical Instrumentation Engineers (SPIE) Conference Series*, volume 6272 of *Society of Photo-Optical Instrumentation Engineers (SPIE) Conference Series*.

Magic, Z., Serenelli, A., Weiss, A., & Chaboyer, B. (2010). On Using the Color-Magnitude Diagram Morphology of M67 to Test Solar Abundances. *ApJ*, **718**, 1378–1387.

Malhotra, R. (1995). The Origin of Pluto's Orbit: Implications for the Solar System Beyond Neptune. *AJ*, **110**, 420.

Malmberg, D., de Angeli, F., Davies, M. B., Church, R. P., Mackey, D., & Wilkinson, M. I. (2007). Close encounters in young stellar clusters: implications for planetary systems in the solar neighbourhood. *MNRAS*, **378**, 1207–1216.

Markwardt, C. B. (2009). Non-linear Least-squares Fitting in IDL with MPFIT. In D. A. Bohlender, D. Durand, and P. Dowler, editors, *Astronomical Data Analysis Software and Systems XVIII*, volume 411 of *Astronomical Society of the Pacific Conference Series*, page 251.

Marois, C., Macintosh, B., Barman, T., Zuckerman, B., Song, I., Patience, J., Lafrenière, D., & Doyon, R. (2008). Direct Imaging of Multiple Planets Orbiting the Star HR 8799. *Science*, **322**, 1348–.

Marois, C., Zuckerman, B., Konopacky, Q. M., Macintosh, B., & Barman, T. (2010). Images of a fourth planet orbiting HR 8799. *Nature*, **468**, 1080–1083.

Marsh, K. A., Kirkpatrick, J. D., & Plavchan, P. (2010). A Young Planetary-Mass Object in the ρ Oph Cloud Core. *ApJ*, **709**, L158–L162.

Martínez Fiorenzano, A. F., Gratton, R. G., Desidera, S., Cosentino, R., & Endl, M. (2005). Line bisectors and radial velocity jitter from SARG spectra. *A&A*, **442**, 775–784.

Marzari, F. & Weidenschilling, S. J. (2002). Eccentric Extrasolar Planets: The Jumping Jupiter Model. *ICARUS*, **156**, 570–579.

Mathieu, R. D., Latham, D. W., Griffin, R. F., & Gunn, J. E. (1986). Precise radial velocities of late-type stars in the open clusters M11 and M67. *AJ*, **92**, 1100–1117.

Mathieu, R. D., Latham, D. W., & Griffin, R. F. (1990). Orbits of 22 spectroscopic binaries in the open cluster M67. *AJ*, **100**, 1859–1881.

Mayer, L., Quinn, T., Wadsley, J., & Stadel, J. (2002). Formation of Giant Planets by Fragmentation of Protoplanetary Disks. *Science*, **298**, 1756–1759.

Mayor, M. & Queloz, D. (1995). A Jupiter-mass companion to a solar-type star. *Nature*, **378**, 355–359.

Mayor, M., Pepe, F., Queloz, D., Bouchy, F., Rupprecht, G., Lo Curto, G., Avila, G., Benz, W., Bertaux, J.-L., Bonfils, X., Dall, T., Dekker, H., Delabre, B., Eckert, W., Fleury, M., Gilliotte, A., Gojak, D., Guzman, J. C., Kohler, D., Lizon, J.-L., Longinotti, A., Lovis, C., Megevand, D., Pasquini, L., Reyes, J., Sivan, J.-P., Sosnowska, D., Soto, R., Udry, S., van Kesteren, A., Weber, L., & Weilenmann, U. (2003). Setting New Standards with HARPS. *The Messenger*, **114**, 20–24.

Mayor, M., Marmier, M., Lovis, C., Udry, S., Ségransan, D., Pepe, F., Benz, W., Bertaux, J. ., Bouchy, F., Dumusque, X., Lo Curto, G., Mordasini, C., Queloz, D., & Santos, N. C. (2011). The HARPS search for southern extra-solar planets XXXIV. Occurrence, mass distribution and orbital properties of super-Earths and Neptune-mass planets. *ArXiv e-prints*.

Meibom, S., Torres, G., Fressin, F., Latham, D. W., Rowe, J. F., Ciardi, D. R., Bryson, S. T., Rogers, L. A., Henze, C. E., Janes, K., Barnes, S. A., Marcy, G. W., Isaacson, H., Fischer, D. A., Howell, S. B., Horch, E. P., Jenkins, J. M., Schuler, S. C., & Crepp, J. (2013). The same frequency of planets inside and outside open clusters of stars. *Nature*, **499**, 55–58.

Meléndez, J., Asplund, M., Gustafsson, B., & Yong, D. (2009). The Peculiar Solar Composition and Its Possible Relation to Planet Formation. *ApJ*, **704**, L66–L70.

Melo, C. H. F., Pasquini, L., & De Medeiros, J. R. (2001). Accurate Vsin i measurements in M 67: The angular momentum evolution of 1.2 M_*sun* stars. *A&A*, **375**, 851–862.

Mermilliod, J.-C. & Mayor, M. (2007). Red giants in open clusters. XII. Six old open clusters NGC 2112, 2204, 2243, 2420, 2506, 2682. *A&A*, **470**, 919–926.

Mochejska, B. J., Stanek, K. Z., Sasselov, D. D., Szentgyorgyi, A. H., Bakos, G. Á., Hradecky, J., Devor, V., Marrone, D. P., Winn, J. N., & Zaldarriaga, M. (2005). Planets in Stellar Clusters Extensive Search. III. A Search for Transiting Planets in the Metal-rich Open Cluster NGC 6791. *AJ*, **129**, 2856–2868.

Montgomery, K. A., Marschall, L. A., & Janes, K. A. (1993). CCD photometry of the old open cluster M67. *AJ*, **106**, 181–219.

Montmerle, T., Augereau, J.-C., Chaussidon, M., Gounelle, M., Marty, B., & Morbidelli, A. (2006). From Suns to Life: A Chronological Approach to the History of Life on Earth 3. Solar System Formation and Early Evolution: the First 100 Million Years. *Earth Moon and Planets*, **98**, 39–95.

Mordasini, C., Alibert, A., Benz, W., & Naef, D. (2007). Extrasolar Planet Population Synthesis - Predictions for RV and Transit Surveys. In *JENAM-2007, "Our Non-Stable Universe"*.

Mordasini, C., Alibert, Y., Klahr, H., & Henning, T. (2012). Characterization of exoplanets from their formation. I. Models of combined planet formation and evolution. *A&A*, **547**, A111.

Mortier, A., Santos, N. C., Sozzetti, A., Mayor, M., Latham, D., Bonfils, X., & Udry, S. (2012). The frequency of giant planets around metal-poor stars. *A&A*, **543**, A45.

Mortier, A., Santos, N. C., Sousa, S., Israelian, G., Mayor, M., & Udry, S. (2013). On the functional form of the metallicity-giant planet correlation. *A&A*, **551**, A112.

Moutou, C. & Pont, F. (2006). Detection and characterization of extrasolar planets: the transit method. *Ecole de Goutelas*, **28**, 55–79.

Nascimbeni, V., Bedin, L. R., Piotto, G., De Marchi, F., & Rich, R. M. (2012). An HST search for planets in the lower main sequence of the globular cluster NGC 6397. *A&A*, **541**, A144.

Nicholson, M., Guido, E., & Sostero, G. (2008). Comet Observations [H06 RAS Observatory, Mayhill]. *Minor Planet Circulars*, **63322**, 3.

Önehag, A., Korn, A., Gustafsson, B., et al. (2011). M67-1194, an unusually Sun-like solar twin in M67. *A&A*, **528**, A85.

Önehag, A., Gustafsson, B., & Korn, A. (2014). Abundances and possible diffusion of elements in M 67 stars. *A&A*, **562**, A102.

Pace, G. & Pasquini, L. (2004). The age-activity-rotation relationship in solar-type stars. *A&A*, **426**, 1021–1034.

Pace, G., Pasquini, L., & François, P. (2008). Abundances of four open clusters from solar stars. *A&A*, **489**, 403–412.

Papaloizou, J. C. B., Nelson, R. P., Kley, W., Masset, F. S., & Artymowicz, P. (2007). Disk-Planet Interactions During Planet Formation. *Protostars and Planets V*, pages 655–668.

Pasquini, L. & Belloni, T. (1998). Optical identification of ROSAT sources in M 67: activity in an old cluster. *A&A*, **336**, 902–910.

Pasquini, L. & Pallavicini, R. (1991). H-alpha absolute chromospheric fluxes in G and K dwarfs and subgiants. *A&A*, **251**, 199–209.

Pasquini, L., Randich, S., & Pallavicini, R. (1997). Lithium in M 67: evidence for spread in a solar age cluster. *A&A*, **325**, 535–541.

Pasquini, L., Döllinger, M. P., Weiss, A., Girardi, L., Chavero, C., Hatzes, A. P., da Silva, L., & Setiawan, J. (2007). Evolved stars suggest an external origin of the enhanced metallicity in planet-hosting stars. *A&A*, **473**, 979–982.

Pasquini, L., Biazzo, K., Bonifacio, P., et al. (2008). Solar twins in M 67. *A&A*, **489**, 677–684.

Pasquini, L., Cristiani, S., García López, R., Haehnelt, M., Mayor, M., Liske, J., Manescau, A., Avila, G., Dekker, H., Iwert, O., Delabre, B., Lo Curto, G., D'Odorico, V., Molaro, P., Viel, M., Vanzella, E., Bonifacio, P., di Marcantonio, P., Santin, P., Comari, M., Cirami, R., Coretti, I., Zerbi, F. M., Spanò, P., Riva, M., Rebolo, R., Israelian, G., Herrero, A., Zapatero Osorio, M. R., Tenegi, F., Carswell, B., Becker, G., Udry, S.,

Pepe, F., Lovis, C., Naef, D., Dessauges, M., & Mégevand, D. (2010). Codex. In *Society of Photo-Optical Instrumentation Engineers (SPIE) Conference Series*, volume 7735 of *Society of Photo-Optical Instrumentation Engineers (SPIE) Conference Series*.

Pasquini, L., Melo, C., Chavero, C., Dravins, D., Ludwig, H.-G., Bonifacio, P., & de La Reza, R. (2011). Gravitational redshifts in main-sequence and giant stars. *A&A*, **526**, A127.

Pasquini, L., Brucalassi, A., Ruiz, M. T., Bonifacio, P., Lovis, C., Saglia, R., Melo, C., Biazzo, K., Randich, S., & Bedin, L. R. (2012). Search for giant planets in M 67. I. Overview. *A&A*, **545**, A139.

Paulson, D. B., Saar, S. H., Cochran, W. D., & Henry, G. W. (2004). Searching for Planets in the Hyades. III. The Quest for Short-Period Planets. *AJ*, **127**, 1644–1652.

Pepe, F., Mayor, M., Galland, F., Naef, D., Queloz, D., Santos, N. C., Udry, S., & Burnet, M. (2002). The CORALIE survey for southern extra-solar planets VII. Two short-period Saturnian companions to HD 108147 and HD 168746. *A&A*, **388**, 632–638.

Pepe, F., Lovis, C., Ségransan, D., Benz, W., Bouchy, F., Dumusque, X., Mayor, M., Queloz, D., Santos, N. C., & Udry, S. (2011). The HARPS search for Earth-like planets in the habitable zone. I. Very low-mass planets around HD 20794, HD 85512, and HD 192310. *A&A*, **534**, A58.

Pepe, F. A., Cristiani, S., Rebolo Lopez, R., Santos, N. C., Amorim, A., Avila, G., Benz, W., Bonifacio, P., Cabral, A., Carvas, P., Cirami, R., Coelho, J., Comari, M., Coretti, I., de Caprio, V., Dekker, H., Delabre, B., di Marcantonio, P., D'Odorico, V., Fleury, M., García, R., Herreros Linares, J. M., Hughes, I., Iwert, O., Lima, J., Lizon, J.-L., Lo Curto, G., Lovis, C., Manescau, A., Martins, C., Mégevand, D., Moitinho, A., Molaro, P., Monteiro, M., Monteiro, M., Pasquini, L., Mordasini, C., Queloz, D., Rasilla, J. L., Rebordão, J. M., Santana Tschudi, S., Santin, P., Sosnowska, D., Spanò, P., Tenegi, F., Udry, S., Vanzella, E., Viel, M., Zapatero Osorio, M. R., & Zerbi, F. (2010). ESPRESSO: the Echelle spectrograph for rocky exoplanets and stable spectroscopic observations. In *Society of Photo-Optical Instrumentation Engineers (SPIE) Conference Series*, volume 7735 of *Society of Photo-Optical Instrumentation Engineers (SPIE) Conference Series*.

Perruchot, S., Bouchy, F., et al. (2011). Higher-precision radial velocity measurements with the SOPHIE spectrograph using octagonal-section fibers. In *SPIE Conf. Series*, volume 8151.

Petigura, E. A., Howard, A. W., & Marcy, G. W. (2013). Prevalence of Earth-size planets orbiting Sun-like stars. *Proceedings of the National Academy of Science*, **110**, 19273–19278.

Petit, J.-M., Morbidelli, A., & Chambers, J. (2001). The Primordial Excitation and Clearing of the Asteroid Belt. *ICARUS*, **153**, 338–347.

Pfeiffer, M. J., Frank, C., Baumueller, D., Fuhrmann, K., & Gehren, T. (1998). FOCES - a fibre optics Cassegrain Echelle spectrograph. *Astron. Astrophys. Suppl. Ser.*, **130**, 381–393.

Pietrinferni, A., Cassisi, S., Salaris, M., & Castelli, F. (2004). A Large Stellar Evolution Database for Population Synthesis Studies. I. Scaled Solar Models and Isochrones. *ApJ*, **612**, 168–190.

Pollack, J. B., Hubickyj, O., Bodenheimer, P., Lissauer, J. J., Podolak, M., & Greenzweig, Y. (1996). Formation of the Giant Planets by Concurrent Accretion of Solids and Gas. *Icarus*, **124**, 62–85.

Pont, F., Husnoo, N., Mazeh, T., & Fabrycky, D. (2011). Determining eccentricities of transiting planets: a divide in the mass-period plane. *MNRAS*, **414**, 1278–1284.

Povich, M. S., Giampapa, M. S., Valenti, J. A., Tilleman, T., Barden, S., Deming, D., Livingston, W. C., & Pilachowski, C. (2001). Limits on Line Bisector Variability for Stars with Extrasolar Planets. *AJ*, **121**, 1136–1146.

Press, W. H. & Rybicki, G. B. (1989). Fast algorithm for spectral analysis of unevenly sampled data. *ApJ*, **338**, 277–280.

Queloz, D. (1995). Echelle Spectroscopy with a CCD at Low Signal-To-Noise Ratio. In A. G. D. Philip, K. Janes, and A. R. Upgren, editors, *New Developments in Array Technology and Applications*, volume 167 of *IAU Symposium*, page 221.

Queloz, D., Henry, G. W., Sivan, J. P., Baliunas, S. L., Beuzit, J. L., Donahue, R. A., Mayor, M., Naef, D., Perrier, C., & Udry, S. (2001). No planet for HD 166435. *A&A*, **379**, 279–287.

Quinn, S. N., White, R. J., Latham, D. W., Buchhave, L. A., Cantrell, J. R., Dahm, S. E., Fűrész, G., Szentgyorgyi, A. H., Geary, J. C., Torres, G., Bieryla, A., Berlind, P., Calkins, M. C., Esquerdo, G. A., & Stefanik, R. P. (2012). Two "b"s in the Beehive: The Discovery of the First Hot Jupiters in an Open Cluster. *ApJ*, **756**, L33.

Quinn, S. N., White, R. J., Latham, D. W., Buchhave, L. A., Torres, G., Stefanik, R. P., Berlind, P., Bieryla, A., Calkins, M. C., Esquerdo, G. A., Fürész, G., Geary, J. C., & Szentgyorgyi, A. H. (2013). HD 285507b: An Eccentric Hot Jupiter in the Hyades Open Cluster. *ArXiv e-prints*.

Quintana, E. V., Barclay, T., Raymond, S. N., Rowe, J. F., Bolmont, E., Caldwell, D. A., Howell, S. B., Kane, S. R., Huber, D., Crepp, J. R., Lissauer, J. J., Ciardi, D. R., Coughlin, J. L., Everett, M. E., Henze, C. E., Horch, E., Isaacson, H., Ford, E. B., Adams, F. C., Still, M., Hunter, R. C., Quarles, B., & Selsis, F. (2014). An Earth-Sized Planet in the Habitable Zone of a Cool Star. *Science*, **344**, 277–280.

Ramírez, I., Meléndez, J., & Asplund, M. (2009). Accurate abundance patterns of solar twins and analogs. Does the anomalous solar chemical composition come from planet formation? *A&A*, **508**, L17–L20.

Ramírez, I., Asplund, M., Baumann, P., Meléndez, J., & Bensby, T. (2010). A possible signature of terrestrial planet formation in the chemical composition of solar analogs. *A&A*, **521**, A33.

Ramírez, I., Fish, J. R., Lambert, D. L., & Allende Prieto, C. (2012). Lithium Abundances in nearby FGK Dwarf and Subgiant Stars: Internal Destruction, Galactic Chemical Evolution, and Exoplanets. *ApJ*, **756**, 46.

Randich, S., Bragaglia, A., Pastori, L., Prisinzano, L., Sestito, P., Spano, P., Villanova, S., Carraro, G., Carretta, E., Romano, D., Zaggia, S., Pallavicini, R., Pasquini, L., Primas, F., Tagliaferri, G., & Tosi, M. (2005). FLAMES Observations of Old Open Clusters: Constraints on the Evolution of the Galactic Disc and Mixing Processes in Stars. *The Messenger*, **121**, 18–22.

Randich, S., Sestito, P., Primas, F., et al. (2006). Element abundances of unevolved stars in the open cluster M 67. *A&A*, **450**, 557–567.

Rasio, F. A. & Ford, E. B. (1996). Dynamical instabilities and the formation of extrasolar planetary systems. *Science*, **274**, 954–956.

Raymond, S. N., Quinn, T., & Lunine, J. I. (2006). High-resolution simulations of the final assembly of Earth-like planets I. Terrestrial accretion and dynamics. *ICARUS*, **183**, 265–282.

Raymond, S. N., Quinn, T., & Lunine, J. I. (2007). High-Resolution Simulations of The Final Assembly of Earth-Like Planets. 2. Water Delivery And Planetary Habitability. *Astrobiology*, **7**, 66–84.

Raymond, S. N., Armitage, P. J., Moro-Martín, A., Booth, M., Wyatt, M. C., Armstrong, J. C., Mandell, A. M., Selsis, F., & West, A. A. (2011). Debris disks as signposts of terrestrial planet formation. *A&A*, **530**, A62.

Rice, W. K. M., Armitage, P. J., Bonnell, I. A., & Bate, M. R. (2003). On the stability of self-gravitating protoplanetary discs. In M. Fridlund, T. Henning, and H. Lacoste, editors, *Earths: DARWIN/TPF and the Search for Extrasolar Terrestrial Planets*, volume 539 of *ESA Special Publication*, pages 555–560.

Riffeser, A., Fliri, J., Gössl, C. A., Bender, R., Hopp, U., Bärnbantner, O., Ries, C., Barwig, H., Seitz, S., & Mitsch, W. (2001). WeCAPP - Wendelstein Calar Alto pixellensing project I. Tracing dark and bright matter in M 31. *A&A*, **379**, 362–373.

Rodler, F., Lopez-Morales, M., & Ribas, I. (2012). Weighing the Non-transiting Hot Jupiter τ Boo b. *ApJ*, **753**, L25.

Rowe, J. F., Bryson, S. T., Marcy, G. W., Lissauer, J. J., Jontof-Hutter, D., Mullally, F., Gilliland, R. L., Issacson, H., Ford, E., Howell, S. B., Borucki, W. J., Haas, M., Huber, D., Steffen, J. H., Thompson, S. E., Quintana, E., Barclay, T., Still, M., Fortney, J., Gautier, I. T. N., Hunter, R., Caldwell, D. A., Ciardi, D. R., Devore, E., Cochran, W., Jenkins, J., Agol, E., Carter, J. A., & Geary, J. (2014). Validation of Kepler's Multiple Planet Candidates. III. Light Curve Analysis and Announcement of Hundreds of New Multi-planet Systems. *ApJ*, **784**, 45.

Ruden, S. P. (1999). The Formation of Planets. In C. J. Lada and N. D. Kylafis, editors, *NATO ASIC Proc. 540: The Origin of Stars and Planetary Systems*, page 643.

Saar, S. H., Butler, R. P., & Marcy, G. W. (1998). Magnetic Activity-related Radial Velocity Variations in Cool Stars: First Results from the Lick Extrasolar Planet Survey. *ApJ*, **498**, L153.

Safronov, V. S. & Zvjagina, E. V. (1969). Relative Sizes of the Largest Bodies during the Accumulation of Planets. *ICARUS*, **10**, 109–115.

Sanders, W. L. (1977). Membership of the open cluster M67. *A&AS*, **27**, 89–116.

Sandquist, E. L. (2004). Blue Stragglers in Low-Mass Globular Clusters. In *American Astronomical Society Meeting Abstracts*, volume 36 of *Bulletin of the American Astronomical Society*, page 1382.

Sandquist, E. L. & Shetrone, M. D. (2003). Time Series Photometry of M67: W Ursae Majoris Systems, Blue Stragglers, and Related Systems. *AJ*, **125**, 2173–2187.

Sandquist, E. L., Latham, D. W., Shetrone, M. D., & Milone, A. A. E. (2003). The Blue Straggler RS Canum Venaticorum Star S1082 in M67: A Detailed Light Curve and the Possibility of a Triple. *AJ*, **125**, 810–824.

Santerne, A., Díaz, R. F., Moutou, C., Bouchy, F., Hébrard, G., Almenara, J.-M., Bonomo, A. S., Deleuil, M., & Santos, N. C. (2012). SOPHIE velocimetry of Kepler transit candidates. VII. A false-positive rate of 35% for Kepler close-in giant candidates. *A&A*, **545**, A76.

Santos, N. C., Mayor, M., Naef, D., Pepe, F., Queloz, D., Udry, S., Burnet, M., Clausen, J. V., Helt, B. E., Olsen, E. H., & Pritchard, J. D. (2002). The CORALIE survey for southern extra-solar planets. IX. A 1.3-day period brown dwarf disguised as a planet. *A&A*, **392**, 215–229.

Santos, N. C., Israelian, G., Mayor, M., Rebolo, R., & Udry, S. (2003). Statistical properties of exoplanets. II. Metallicity, orbital parameters, and space velocities. *A&A*, **398**, 363–376.

Santos, N. C., Israelian, G., & Mayor, M. (2004). Spectroscopic [Fe/H] for 98 extra-solar planet-host stars. Exploring the probability of planet formation. *A&A*, **415**, 1153–1166.

Sato, B., Izumiura, H., Toyota, E., Kambe, E., Takeda, Y., Masuda, S., Omiya, M., Murata, D., Itoh, Y., Ando, H., Yoshida, M., Ikoma, M., Kokubo, E., & Ida, S. (2007). A Planetary Companion to the Hyades Giant ϵ Tauri. *ApJ*, **661**, 527–531.

Scargle, J. D. (1982). Studies in astronomical time series analysis. II - Statistical aspects of spectral analysis of unevenly spaced data. *ApJ*, **263**, 835–853.

Schroeder, D. J. (1987). *Astronomical optics*.

Setiawan, J., Pasquini, L., da Silva, L., Hatzes, A. P., von der Lühe, O., Girardi, L., de Medeiros, J. R., & Guenther, E. (2004). Precise radial velocity measurements of G and K giants. Multiple systems and variability trend along the Red Giant Branch. *A&A*, **421**, 241–254.

Shaver, P. (2006). Report on the XXXVIth IAU General Assembly (held in Prague, Czech Republic, 14-25 August 2006). *The Messenger*, **125**, 51.

Silvotti, R., Schuh, S., Janulis, R., Solheim, J.-E., Bernabei, S., Østensen, R., Oswalt, T. D., Bruni, I., Gualandi, R., Bonanno, A., Vauclair, G., Reed, M., Chen, C.-W., Leibowitz, E., Paparo, M., Baran, A., Charpinet, S., Dolez, N., Kawaler, S., Kurtz, D., Moskalik, P., Riddle, R., & Zola, S. (2007). A giant planet orbiting the 'extreme horizontal branch' star V391 Pegasi. *Nature*, **449**, 189–191.

Smolinski, J. P., Lee, Y. S., Beers, T. C., An, D., Bickerton, S. J., Johnson, J. A., Loomis, C. P., Rockosi, C. M., Sivarani, T., & Yanny, B. (2011). The SEGUE Stellar Parameter Pipeline. IV. Validation with an Extended Sample of Galactic Globular and Open Clusters. *AJ*, **141**, 89.

Sousa, S. G., Santos, N. C., Israelian, G., Mayor, M., & Udry, S. (2011). Spectroscopic stellar parameters for 582 FGK stars in the HARPS volume-limited sample. Revising the metallicity-planet correlation. *A&A*, **533**, A141.

Sozzetti, A. (2012). Astrometry and Exoplanet Characterization: Gaia and Its Pandora's Box. In F. Arenou and D. Hestroffer, editors, *Proceedings of the workshop "Orbital Couples: Pas de Deux in the Solar System and the Milky Way". Held at the Observatoire de Paris, 10-12 October 2011. Editors: F. Arenou, D. Hestroffer. ISBN 2-910015-64-5, p. 25-31*, pages 25–31.

Spiegel, D. S., Burrows, A., & Milsom, J. A. (2010). Planet or Brown Dwarf? Bringing the Deuterium-Burning Criterion into Focus. In *AAS/Division for Planetary Sciences Meeting Abstracts #42*, volume 42 of *AAS/Division for Planetary Sciences Meeting Abstracts*, page 27.

Spronck, J. F. P., Kaplan, Z. A., Fischer, D. A., Schwab, C., & Szymkowiak, A. E. (2012). Extreme Doppler precision with octagonal fiber scramblers. In *Society of Photo-Optical Instrumentation Engineers (SPIE) Conference Series*, volume 8446 of *Society of Photo-Optical Instrumentation Engineers (SPIE) Conference Series*.

Spurzem, R., Giersz, M., Heggie, D. C., & Lin, D. N. C. (2009). Dynamics of Planetary Systems in Star Clusters. *ApJ*, **697**, 458–482.

Steinmetz, T., Wilken, T., Araujo-Hauck, C., Holzwarth, R., Hänsch, T. W., Pasquini, L., Manescau, A., D'Odorico, S., Murphy, M. T., Kentischer, T., Schmidt, W., & Udem, T. (2008). Laser Frequency Combs for Astronomical Observations. *Science*, **321**, 1335–.

Strassmeier, K. G., Woche, M., Ilyin, I., Popow, E., Bauer, S.-M., Dionies, F., Fechner, T., Weber, M., Hofmann, A., Storm, J., Materne, R., Bittner, W., Bartus, J., Granzer, T., Denker, C., Carroll, T., Kopf, M., DiVarano, I., Beckert, E., & Lesser, M. (2008). PEPSI: the Potsdam Echelle Polarimetric and Spectroscopic Instrument for the LBT. In *Society of Photo-Optical Instrumentation Engineers (SPIE) Conference Series*, volume 7014 of *Society of Photo-Optical Instrumentation Engineers (SPIE) Conference Series*.

Street, R. A., Horne, K., Lister, T. A., Penny, A. J., Tsapras, Y., Quirrenbach, A., Safizadeh, N., Mitchell, D., Cooke, J., & Collier Cameron, A. (2003). Searching for planetary transits in the field of open cluster NGC 6819 - I. *MNRAS*, **340**, 1287–1297.

Takeda, Y. & Kawanomoto, S. (2005). Lithium Abundances of F-, G-, and K-Type Stars: Profile-Fitting Analysis of the Li I 6708 Doublet. *PASJ*, **57**, 45–63.

Takeda, Y., Honda, S., Kawanomoto, S., Ando, H., & Sakurai, T. (2010). Behavior of Li abundances in solar-analog stars. II. Evidence of the connection with rotation and stellar activity. *A&A*, **515**, A93.

Tanaka, H., Takeuchi, T., & Ward, W. R. (2002). Three-Dimensional Interaction between a Planet and an Isothermal Gaseous Disk. I. Corotation and Lindblad Torques and Planet Migration. *ApJ*, **565**, 1257–1274.

Taylor, B. J. (2007). The Benchmark Cluster Reddening Project. II. A Reddening Value for M67. *AJ*, **133**, 370–386.

Thiele, H., Ageorges, N., Kampf, D., Hartl, M., Egner, S., Aniol, P., Ruder, M., Abfalter, C., Hopp, U., Bender, R., Gössl, C., Grupp, F., Lang-Bardl, F., & Mitsch, W. (2012). New Fraunhofer Telescope Wendelstein: assembly, installation, and current status. In *Society of Photo-Optical Instrumentation Engineers (SPIE) Conference Series*, volume 8444 of *Society of Photo-Optical Instrumentation Engineers (SPIE) Conference Series*.

Thommes, E. W., Duncan, M. J., & Levison, H. F. (1999). The formation of Uranus and Neptune in the Jupiter-Saturn region of the Solar System. *Nature*, **402**, 635–638.

Thommes, E. W., Duncan, M. J., & Levison, H. F. (2003). Oligarchic growth of giant planets. *ICARUS*, **161**, 431–455.

Trilling, D. E., Lunine, J. I., & Benz, W. (2002). Orbital migration and the frequency of giant planet formation. *A&A*, **394**, 241–251.

Tsiganis, K., Gomes, R., Morbidelli, A., & Levison, H. F. (2005). Origin of the orbital architecture of the giant planets of the Solar System. *Nature*, **435**, 459–461.

Tull, R. G., MacQueen, P. J., Good, J., Epps, H. W., & HET HRS Team (1998). High Resolution Spectrograph for the Hobby-Eberly Telescope. **30**, 1263.

Udry, S. & Santos, N. C. (2007). Statistical Properties of Exoplanets. *ARAA*, **45**, 397–439.

Unwin, S., Boden, A., & Shao, M. (1997). Space Interferometry Mission. In M. S. El-Genk, editor, *Space Technology and Applications*, volume 387 of *American Institute of Physics Conference Series*, pages 63–72.

van den Berg, M., Tagliaferri, G., et al. (2004). A Chandra observation of the old open cluster M 67. *A&A*, **418**, 509–523.

van Saders, J. L. & Gaudi, B. S. (2011). Ensemble Analysis of Open Cluster Transit Surveys: Upper Limits on the Frequency of Short-period Planets Consistent with the Field. *ApJ*, **729**, 63.

Veras, D. & Armitage, P. J. (2006). Predictions for the Correlation between Giant and Terrestrial Extrasolar Planets in Dynamically Evolved Systems. *ApJ*, **645**, 1509–1515.

Ward, W. R. (1997). Protoplanet Migration by Nebula Tides. *ICARUS*, **126**, 261–281.

Weldrake, D. T. F., Sackett, P. D., Bridges, T. J., & Freeman, K. C. (2005). An Absence of Hot Jupiter Planets in 47 Tucanae: Results of a Wide-Field Transit Search. *ApJ*, **620**, 1043–1051.

Weldrake, D. T. F., Sackett, P. D., & Bridges, T. J. (2008). The Frequency of Large-Radius Hot and Very Hot Jupiters in ω Centauri. *ApJ*, **674**, 1117–1129.

Wolszczan, A. & Frail, D. A. (1992). A planetary system around the millisecond pulsar PSR1257 + 12. *Nature*, **355**, 145–147.

Wolszczan, A. & Kuchner, M. (2011). *Planets Around Pulsars and Other Evolved Stars: The Fates of Planetary Systems*, pages 175–190.

Woolfson, M. M. (1993). The Solar - Origin and Evolution. *QJRAS*, **34**, 1–20.

Wright, J. T. & Howard, A. W. (2009). Efficient Fitting of Multiplanet Keplerian Models to Radial Velocity and Astrometry Data. *ApJS*, **182**, 205–215.

Wright, J. T., Marcy, G. W., Fischer, D. A., Butler, R. P., Vogt, S. S., Tinney, C. G., Jones, H. R. A., Carter, B. D., Johnson, J. A., McCarthy, C., & Apps, K. (2007). Four New Exoplanets and Hints of Additional Substellar Companions to Exoplanet Host Stars. *ApJ*, **657**, 533–545.

Wright, J. T., Marcy, G. W., Howard, A. W., Johnson, J. A., Morton, T. D., & Fischer, D. A. (2012). The Frequency of Hot Jupiters Orbiting nearby Solar-type Stars. *ApJ*, **753**, 160.

Wu, Y., Luo, A.-L., Li, H.-N., Shi, J.-R., Prugniel, P., Liang, Y.-C., Zhao, Y.-H., Zhang, J.-N., Bai, Z.-R., Wei, P., Dong, W.-X., Zhang, H.-T., & Chen, J.-J. (2011). Automatic determination of stellar atmospheric parameters and construction of stellar spectral templates of the Guoshoujing Telescope (LAMOST). *RAA*, **11**, 924–946.

Yadav, R. K. S., Bedin, L. R., Piotto, G., Anderson, J., Cassisi, S., Villanova, S., Platais, I., Pasquini, L., Momany, Y., & Sagar, R. (2008). Ground-based CCD astrometry with wide-field imagers. II. A star catalog for M 67: WFI@2.2 m MPG/ESO astrometry, FLAMES@VLT radial velocities. *A&A*, **484**, 609–620.

Zechmeister, M. & Kürster, M. (2009). The generalised Lomb-Scargle periodogram. A new formalism for the floating-mean and Keplerian periodograms. *A&A*, **496**, 577–584.